Adiabatic Effectiveness Measurements of Leakage Flows near the Hub Region of Gas Turbine Engines

William W. Ranson

Thesis submitted to the Faculty of the
Virginia Polytechnic Institute and State University
in partial fulfillment of the requirements for the degree of

Master of Science
in
Mechanical Engineering

Dr. K. A. Thole, Chair
Dr. W. F. O'Brien
Dr. B. Vick

May 11, 2004
Blacksburg, VA

Keywords: endwall, gas turbine, adiabatic effectiveness
leakage flows, featherseal, microcircuit

Adiabatic Effectiveness Measurements of Hub Leakage Flows near the Hub Region of Gas Turbine Engines

William W. Ranson

Abstract

To prevent melting of turbine blades, numerous cooling schemes have been developed to cool the blades using cooler air from the compressor. Unfortunately, the clearance gap between adjacent hub sections allows coolant to leak into the hub region. Coolant flow also leaks into the hub region through gaps between individual stages. The results of a combined experimental and computational study of cooling along the hub of a first stage turbine blade caused by leakage flows are discussed in detail. Additionally, this study examines a novel cooling feature, called a microcircuit, which combines internal convective cooling with external film cooling.

For the experimental investigation, scaled up blades were tested in a low speed wind tunnel. Adiabatic effectiveness measurements were made with infrared thermography of the entire hub region for a range of leakage flow conditions. For the computations, a commercially available computational fluid dynamics (CFD) code, FLUENT 6.0, was used to simulate the various flows.

Results show that featherseal leakage flows provide small cooling benefits to the hub. Increases in featherseal flow provide no additional cooling to the hub region. Unlike the featherseal, leakage flows from the front rim provide ample cooling to the hub region, especially the leading edge of the blade passage. None of the leakage flows provide significant cooling to the pressure side region of the hub or trailing edge suction side. With the addition of the hub microcircuits, there is improved hub cooling of the suction side of the blades. Though the coolant exit uniformity was low and affected by the featherseal flow, the microcircuits were shown to provide more cooling along the hub region. Good agreements were observed between the computational and experimental results, though computations over-predicted front rim cooling and microcircuit uniformity.

Acknowledgments

First and foremost, I would like to thank my parents for supporting me through my college career. It has been a wonderful six years at Virginia Tech, and I would not have experienced any of it without their help.

I owe thanks to my advisor, Dr. Karen Thole. She has been there to provide help and guidance when needed. She was always able to keep me level, providing encouragement when I was frustrated and keeping me grounded when I was overly optimistic. She also threw some really good parties.

I would also like to thank our sponsors, Pratt & Whitney. Their support, both financially and technically, made all of this work possible.

I would not have had as much fun in lab without the people working beside me. Many thanks to Eric Couch, Jesse Christophel, Erik Hohlfeld, Andrew Gratton, Will Colban, Dan Knost, Jeff Prausa, Joe Scrittore, and Chris Ebeling for helping me out when I first started working in VTExCCL. Through my year and a half adventures, Scott Walsh, Erin Elder, Nik Cardwell, Sundar, and Paul Sanders have joined lab as well, adding to the fun memories. I am lucky to have had such good co-workers. We always seemed to be laughing about something, or someone.

I would also like to thank the professors I've had throughout the years. I've been lucky to take classes with some of VT's best engineering professors.

I would also like to thank Sub Station II for providing my lunch just about every day. I also extend thanks to PKs, especially Larry's Knockout Punch, which not only helped me through the tough times, but also helped me celebrate the good times.

Lastly, I'd like to thank my friends and fraternity brothers. They were always there for me, ready to help me forget about work problems.

I only hope I have as much fun and success at DuPont as I have had at Virginia Tech. GO HOKIES!

Contents

Abstract ii
Acknowledgments iii
Nomenclature vi
List of Tables viii
List of Figures ix

1. Introduction 1
    1.1 Microcircuit Cooling Technology for Airfoils 3
    1.2 Research Objectives 4

2. Literature Review 10
    2.1 Platform Studies. 10
    2.2 Uniqueness of Current Study 15

3. Experimental Design and Construction 23
    3.1 Test Section Scaling Parameters 23
    3.2 Turbine Blade Design and Construction 24
    3.3 Platform Design 26
    3.4 Platform Construction 31
    3.5 Microcircuit Installation 34
    3.6 Top Endwall Design and Construction 36
    3.7 Wind Tunnel Facilities 39
    3.8 Additional Test Rig Features 42
    3.9 Instrumentation and Uncertainty 43

4. Test Matrix and Benchmarking Procedures 75
    4.1 Test Matrix for Hub Leakage Flows 75
    4.2 Setting of the Passage Inlet Conditions 77

4.3 Setting of the Leakage Flow 82
4.4 Calibration of the Infrared Camera 85
4.5 Design of Thermal Field Measurements 89

5. Analysis of Results 100
5.1 Analysis of Public Cases 100
5.2 Analysis of Microcircuit Cases 106
5.3 Comparisons to Computational Cases 111
5.4 Analysis of Thermal Field Measurements 116

6. Conclusions 147
6.1 Summary of Results 147
6.2 Recommendations for Future Work 150

References 151
Appendix A: Blade Geometry and Pressure Tap Locations 155
Appendix B: Dimensions of Front and Aft Plenums 156
Appendix C: Locations of Thermocouples and Pressure Taps in Plenums 158
Appendix D: Hole Locations in Top Endwall 161
Appendix E: Locations of Thermocouples and Markers in Platform 162
Appendix F: Uncertainty Calculations 163
Vita 167

Nomenclature

A	= effective area
B_X	= axial chord
C	= true chord
C_p	= static pressure coefficient, $C_p = (P_{s,\,local} - P_{s,\,inlet}) / P_{dyn}$
C_d	= discharge coefficient
f	= friction factor
f_o	= normalized friction factor
HFOV	= horizontal field of view of infrared camera
I	= momentum flux ratio
k	= thermal conductivity
L	= distance from camera lens to tip surface
M	= blowing ratio
$\dot{m}$	= mass flow
P	= blade pitch
$P_{d,\,in}$	= dynamic pressure at the test section inlet
$P_{s,\,in}$	= static pressure at the test section inlet
$P_{s,\,local}$	= local static pressure
Re	= Reynolds Number
Re_d	= Reynolds Number based upon diameter
S	= span
s	= surface distance along the blade from stagnation point
T	= temperature
Tu	= average turbulence levels
t	= thickness
U, V	= velocity components for the blade coordinate system
u, v	= velocity components for the wind tunnel coordinate system
VFOV	= vertical field of view of the infrared camera
w	= width of feature
X, Y, Z	= wind tunnel coordinate system

Greek

η	= adiabatic effectiveness, $\eta = (T_\infty - T_{aw}) / (T_\infty - T_c)$
θ	= thermal effectiveness = $(T_\infty - T) / (T_\infty - T_c)$
ρ	= density
ΔP	= measured pressure drop between two locations (e.g. across a venturi)

Subscripts and Superscripts

$\overline{\quad}$	= lateral average value at a given axial location
aw	= adiabatic wall conditions
av	= averaged value
c	= coolant conditions
j	= jet conditions into the mainstream
max	= maximum value
∞	= mainstream conditions
rms	= root mean square value
e	= engine scale, conditions
t	= test scale, conditions

List of Tables

Table 3.1 Summary of cooling flow from each geometric feature 45

Table 3.2 Blade Parameters used in the experimental testing.....45

Table 3.3 Dimensions of leakage flow geometries 46

Table 3.4 Dimensions of microcircuit geometries 46

Table 3.5 Flow versus pressure drop for the venturi.....47

Table 3.6 Pressure transducers used in experimental testing.....47

Table 4.1a Test matrix for public cases 91

Table 4.1b Test matrix for the microcircuit cases.....91

Table 4.2 The total exit area of each leakage feature.....91

Table 4.3 Leakage flow conditions used for thermal field measurements.....91

Table A1. Coordinates of test blades 155

Table A2. Locations of pressure taps on blades.....155

Table C1. Coordinates of pressure taps corresponding to the numbers in Figure C2.....159

Table C2. Coordinates for thermocouples shown in Figure C3.....160

Table D1. Coordinates of holes in top plate.....161

Table E1. Coordinates of thermocouples and pressure taps in platform 162

List of Figures

Figure 1.1 Picture of Whittle Engine test rig (http://www.visitcumbria.com) 5

Figure 1.2 Picture of Heinkel He-178 airplane (http://www.allstar.fiu.edu/aero/ohain.htm) 5

Figure 1.3 Drawing of a turbojet (Rolls Royce, 1992) 6

Figure 1.4 Diagram of Brayton Cycle (Cengel and Boles, 1998).....6

Figure 1.5 Cut-away view of 1st row of turbine blades (Weidemer, 2003) 7

Figure 1.6 Picture of assembled stator ring (Gas Turbine Theory, 2001) 7

Figure 1.7 Illustration of turbine blade used in the current research (Weidemer, 2003) 8

Figure 1.8a Picture of the suction side microcircuit 8

Figure 1.8b Picture of pressure side microcircuit 8

Figure 1.9 Top view of platform 9

Figure 2.1a Horseshoe vortex patterns as described by Langston [1980] 16

Figure 2.1b Horseshoe vortex patterns as described by Sharma [1987].....16

Figure 2.1c Horseshoe vortex patter as described by Goldstein [1988] 16

Figure 2.2 Test geometry used by Aunapu et al. [2000].....17

Figure 2.3 Oil and dye visualization by Friedrichs et al. [1996] 17

Figure 2.4 Cooling geometry used by Oke et al. [2000].....18

Figure 2.5 Cooling geometry used by Burd et al. [2000] 18

Figure 2.6 Cooling geometry used by Nicklas [2001].....19

Figure 2.7 Results from Nicklas [2001].....19

Figure 2.8a Test configuration used by Colban and Thole [2003] 20

Figure 2.8b Side view of Colban and Thole [2003] slot 20

Figure 2.9 Cooling configuration used by Knost and Thole [2003] 21

Figure 2.10 Cooling results from Knost and Thole [2003].....22

Figure 2.11 Cooling configuration used by Yu and Chyu [1998] 22

Figure 3.1 Side view of 1st stage gas turbine blade.....48

Figure 3.2 Blade geometry redefined by Pratt & Whitney 48

Figure 3.3 Picture of individual foam pieces of test blade.....49

Figure 3.4 Picture showing the location of the pressure taps on test blade 49

Figure 3.5 Picture showing the assembled test blade.....50

Figure 3.6a Side view drawing of blade fillet.....50

Figure 3.6b Top view drawing of blade fillet 50

Figure 3.7 Schematic of cooling benefits of microcircuits 51

Figure 3.8a Top view suction side microcircuit 51

Figure 3.8b Isometric view suction side microcircuit.....51

Figure 3.8c Top view pressure side microcircuit.....51

Figure 3.8d Isometric view pressure side microcircuit.....51

Figure 3.9a Schematic showing public leakage features 52

Figure 3.9b Schematic showing microcircuit leakage features 53

Figure 3.10 Schematic of platform showing locations of plenums.....53

Figure 3.11a Drawing of side view of backwards facing front step 54

Figure 3.11b Drawing of top view of backwards facing front step 54

Figure 3.12 Side view of the front rim and aft rim plenums.....55

Figure 3.13a Top view of sliding gate 56

Figure 3.13b Front view of sliding gate.....56

Figure 3.14 Picture of front of test section....56

Figure 3.15 Drawing of the plenums that feed the microcircuit....57

Figure 3.16 Top view piping to the five internal plenums....57

Figure 3.17 Drawing of the top view of platform....58

Figure 3.18 Top view of the sliding gate mechanism being installed....59

Figure 3.19 Picture of plenums being constructed....59

Figure 3.20 Side view of featherseal and suction side microcircuit plenum....60

Figure 3.21 Picture of seven finished plenums....60

Figure 3.22 Picture of five PVC valves for each of the plenums....61

Figure 3.23 Picture of foam blade cut-out on top of the plenums....61

Figure 3.24a Picture of the mold for the pressure side microcircuit....62

Figure 3.24b Picture of the mold for the suction side microcircuit....62

Figure 3.25 Picture of molded microcircuit....63

Figure 3.26 Picture of platform during microcircuit installation....63

Figure 3.27 Picture of finished platform....64

Figure 3.28 Picture of ThermalCam® infrared camera....64

Figure 3.29 Top and side views of viewport covers....65

Figure 3.30 19 field of view rectangles for IR camera view....66

Figure 3.31 Picture of underside of top plate....67

Figure 3.32 Locations of markers and thermocouples in platform....68

Figure 3.33 Picture of platform with the thermocouples and markers installed....69

Figure 3.34 Schematic of the wind tunnel facilities....69

Figure 3.35 Picture of PVC supply of coolant flow....70

Figure 3.36 Plot of venturi flow versus pressure drop 70

Figure 3.37 Percent difference between LFE and venturi 71

Figure 3.38 Picture the completed test section 71

Figure 3.39 Schematic top view of tunnel 72

Figure 3.40a Side bleed gates in open position 73

Figure 3.40b Side bleed gates in closed position 73

Figure 3.41 Picture looking upstream from the test section exit 73

Figure 3.42 Picture of the exterior of the flexible walls 74

Figure 3.43 Picture of the pressure tap scanivalve 74

Figure 4.1 Location of inlet velocity measurements 92

Figure 4.2 Plot of inlet velocity distribution 92

Figure 4.3 Picture of strings attached to leading edge of blades 93

Figure 4.4 Plot of the matched pressure distribution around the blades 93

Figure 4.5 Schematic showing s/s_{max} for the blades 94

Figure 4.6 Top view drawing of instrumented blade passage 95

Figure 4.7 Plot of the friction factor for the leakage features 96

Figure 4.7 Plot of normalized friction factor, f/f_o 96

Figure 4.9 Screen shot of ThermalCam® software 97

Figure 4.10 Screen shot of MatLab software 97

Figure 4.11 Schematic of the thermocouple rake 98

Figure 4.12 Drawing showing the locations of thermal field measurements 99

Figure 5.1 Adiabatic effectiveness measurements for 1.5% front rim flow, 0.25% featherseal flow, and 1.5% aft rim flow 121

Figure 5.2 Adiabatic effectiveness measurements of a repeat of Figure 5.1 121

Figure 5.3a Adiabatic effectiveness measurements for 1.5% front rim, 0.25% featherseal and 1.5% aft rim flow.....122

Figure 5.3b Adiabatic effectiveness measurements for 1.5% front rim, 0.5% featherseal, and 1.5% aft rim flow.....122

Figure 5.3c Adiabatic effectiveness measurements for 1.5% front rim, 0.75% featherseal, and 1.5% aft rim flow.....122

Figure 5.4 Schematic illustrating the averaged adiabatic effectiveness.....123

Figure 5.5 Plot of average adiabatic effectiveness values for three featherseal flow conditions.....123

Figure 5.6a Adiabatic measurements with 0.5% front rim, 0.25% featherseal, and 1.5% aft rim.....124

Figure 5.6b Adiabatic measurements with 1.5% front rim, 0.25% featherseal, and 1.5% aft rim.....124

Figure 5.6c Adiabatic measurements with 2.0% front rim, 0.25% featherseal, and 1.5% aft rim.....124

Figure 5.7 Laterally averaged adiabatic effectiveness values for 0.5%, 1.5%, and 2.0% front rim with 0.25% featherseal, and 1.5% aft rim 125

Figure 5.8a Adiabatic effectiveness contours for 0.25% microcircuit only flow. 126

Figure 5.8b Adiabatic effectiveness contours for 0.25% microcircuit only flow with a conduction correction.....126

Figure 5.9 Adiabatic effectiveness contours of 1.5% front rim, 0.25% featherseal 0.25% microcircuit flow, and 1.5% aft rim flow 127

Figure 5.10a Adiabatic effectiveness contours with 2.0% front rim, 0.25% featherseal 0.25% microcircuit, and 1.5% aft rim flow 128

Figure 5.10b Adiabatic effectiveness contours with 2.0% front rim, 0.25% featherseal 0.5% microcircuit, and 1.5% aft rim flow 128

Figure 5.11 Zoom of adiabatic effectiveness contours around the suction side microcircuit for 2.0% front rim, 0.25% featherseal, 0.25% microcircuit, and 1.5% aft rim flow 129

Figure 5.12 Adiabatic effectiveness measurements taken 1 slot width downstream

of the suction side microcircuit for mass fluxes of 0.08-0.47.....129

Figure 5.13 Adiabatic effectiveness contours at the pressure side microcircuit exit for mass fluxes of 0.28, 0.48 only.....130

Figure 5.14 Plot of adiabatic effectiveness from the pressure side microcircuit for four mass flux ratios, 0.28, 0.34, 0.42, 0.48.....130

Figure 5.15 Zoom of adiabatic effectiveness of the pressure side microcircuit with 1.5% front rim, 0.0%-0.5% featherseal, 0.25% microcircuit, and 1.5% aft rim flow 131

Figure 5.16 Plot of adiabatic effectiveness values one slot width downstream of pressure side microcircuit for 1.5% front rim flow, 0.0%-0.5% featherseal, 0.34-0.42 microcircuit mass flux, and 1.5% aft rim.....132

Figure 5.17 Plot of average eta values for microcircuit and public cases with 1.5%-2.0% front rim, 0.25% featherseal, 0.0%-0.25% microcircuit and 1.5% aft rim flow 133

Figure 5.18a Top view schematic of computational domain.....134

Figure 5.18b Side view schematic of computational domain.....134

Figure 5.19a Repeat of Figure 5.1 (1.5% front and aft rim, 0.25% featherseal) 135

Figure 5.19b Adiabatic effectiveness predictions of 1.5% front rim, 0.25% featherseal, and 1.5% aft rim flow 135

Figure 5.19c Adiabatic effectiveness predictions of 2.0% front rim, 0.25% featherseal, and 1.5% aft rim flow 136

Figure 5.19d Adiabatic effectiveness predictions of 2.0% front rim, 0.75% featherseal, and 1.5% aft rim flow 136

Figure 5.20a Computational predictions of temperature-colored streamlines released from the featherseal for 1.5% front rim, 0.25% featherseal, and 1.5% aft rim flow 137

Figure 5.20b Computational predictions of height-colored streamlines released from the featherseal for 1.5% front rim, 0.25% featherseal, and 1.5% aft rim flow 137

Figure 5.21a Adiabatic effectiveness contours of experimental case, 2.0% front rim, 0.25% featherseal, 0.25% microcircuit, and 1.5% aft rim.....138

Figure 5.21b Adiabatic effectiveness contours of computational case, 2.0% front rim, 0.25% featherseal, 0.25% microcircuit, and 1.5% aft rim 138

Figure 5.22a Adiabatic effectiveness contours of experimental case of only 0.25% microcircuit.....139

Figure 5.22b Adiabatic effectiveness contours of computational case of only 0.25% microcircuit.....139

Figure 5.23 Average adiabatic effectiveness plots for computational and experimental data of the public cases 140

Figure 5.24 Average adiabatic effectiveness plots for computational and experimental data of 0.25% only microcircuit flow 140

Figure 5.25 Computationally predicted pressure distribution across the hub [Hohlfeld, 2003].....141

Figure 5.26a Thermal rake measurements on the leading edge of the featherseal for 1.5% front rim flow and 0.25% featherseal flow.....142

Figure 5.26b Thermal rake measurements on the leading edge of the featherseal for 1.5% front rim flow and 0.75% featherseal flow.....142

Figure 5.27a Thermal rake measurements on the trailing edge of the featherseal for 1.5% front rim flow and 0.25% featherseal flow.....143

Figure 5.27b Thermal rake measurements on the trailing edge of the featherseal for 1.5% front rim flow and 0.75% featherseal flow.....143

Figure 5.28a Thermal rake measurements along the suction side microcircuit for 0.4% microcircuit flow only.....144

Figure 5.28a Thermal rake measurements along the suction side microcircuit for 0.2% microcircuit flow only.....144

Figure 5.29a Computational predictions of a thermal plane above the leading edge featherseal for 1.5% front rim flow and 0.25% featherseal flow.....145

Figure 5.29b Computational predictions of a thermal plane above the leading edge featherseal for 1.5% front rim flow and 0.25% featherseal flow.....145

Figure 5.30a Computational predictions of a thermal plane above the trailing edge featherseal for 1.5% front rim flow and 0.25% featherseal flow.....146

Figure 5.30b Computational predictions of a thermal plane above the trailing edge featherseal for 1.5% front rim flow and 0.75% featherseal flow.....146

Figure B1. Drawing of a top view of the front rim plenum.....156

Figure B2. Drawing of a front view of the front rim plenum.....156

Figure B3. Drawing of a top view of the aft rim plenum.....157

Figure B4. Drawing of a front view of the aft rim plenum.....157

Figure C1. Top view of the numbered plenums (reference for instrumentation).....158

Figure C2. Numbered locations of pressure taps in the plenums.....158

Figure C3. Numbered locations of thermocouples in the plenums.....160

Chapter 1: Introduction

Whether propelling aircraft through the sky, ships through the ocean or providing power to the electrical grid, gas turbine engines have become incorporated into our daily lives. As society moves towards a higher dependence on technology, there will be an increased demand for gas turbine engines to produce electricity at higher efficiencies. The effects of globalization and continued military actions will further the need for more efficient, faster gas turbine engines for propulsion. These requirements will be met only through detailed research of the specific components within gas turbines.

Although there has been research on turbo propulsion since before the 20th century, the first gas turbines to be developed that bare resemblance to modern technology were designed in the 1930s. Working independently of each other, both Sir Frank Whittle and Dr. Hans Joachim Pabst von Ohain both built working gas turbine engines. In 1939, Sir Whittle unveiled the first gas turbine demonstration engine, shown in Figure 1.1. At the same time, Dr. von Ohain put his engine on a Heinkel He-178, shown in Figure 1.2, producing the world's first gas turbine airplane (http://www.allstar.fiu.edu/aero/ohain.htm). Both of their designs contain the three main parts found within all modern gas turbine engines: a compressor, a combustion chamber and a turbine. Figure 1.3 shows a schematic diagram of a turbojet engine that illustrates the relationship between the compressor, combustion chamber, and turbine. The compressor takes the inlet air and through numerous stages compresses the air to facilitate the propulsion. Fuel is added to the air mixture and ignited in the combustion chamber. Work to drive the compressor is removed from the heated flow in the turbine section. For aircraft, little work is removed in the turbine section as thrust is desired. However, in electrical generation, the work removed from the flow by the turbines is maximized.

The interaction between the compressor, combustion chamber and turbine can be modeled by the Brayton cycle, shown in Figure 1.4. The efficiency of gas turbine engines is the work output divided by the heat input. From analysis using the Brayton cycle, the efficiency of a gas turbine is:

$$\eta_{th,Brayton} = \frac{w_{net}}{q_{in}} = 1 - \frac{T_4 - T_1}{T_3 - T_2} \tag{1.1}$$

where T_4 is the exit gas temperature from the turbine, T_1 is the entry gas temperature to the compressor, T_3 is the entry gas temperature to the turbine and T_2 is the exit temperature from the compressor. From equation (1.1), increasing the turbine inlet temperature (T_3) increases the efficiency of the gas turbine engine. Since the turbine inlet temperature is directly related to the combustion chamber temperature, engine designers have continually pushed the combustion temperatures higher to gain increased efficiencies. Currently, the typical inlet gas temperature to the turbine section is approximately 3000^o F /1650 C [Hohlfeld, 2003]. Since this temperature exceeds the melting point of the turbine blade materials (2200^o F / 1205 C) [Hohlfeld, 2003], cooling schemes are required to prevent blade degradation.

In nearly all gas turbine engines, cooler air (1250^o F / 675 C) [Hohlfeld,2003] from the compressor bypasses the combustion chamber and is used to cool the turbine blades. Numerous techniques have been used to cool turbine blades such as impingement cooling, film cooling, and convective cooling. Unfortunately, the bearings and seals inherent to rotating machinery result in leakage points for the cooling flow to leak into other regions. Figure 1.5 shows a cut-away schematic of typical gas turbine stages consisting of a row of blades between rows of stator vanes. The seals between the blades and vanes allow for some coolant to leak through into the mainstream hot gasses. In addition to gaps between rows of blades, the construction and installation of the individual blades produces gaps where coolant can leak into the mainstream. Figure 1.6 shows a row of assembled first stage turbine blades in a gas turbine engine. One of the most common gaps between blades, called the featherseal, allows coolant to leak into the mainstream. The featherseal gap exists on the turbine blades as well as the stator vanes.

Elimination of leakage flows in turbines through improved sealing results in lower fuel consumption and thus increased efficiencies (Lattime, 2002). Fuel consumption is increased by leakage flow because the engine has to work harder (i.e. hotter) to produce the same thrust. Minimization of leakage flows in gas turbine engines has been shown to increase efficiencies by as much as 1% and reduce the unit heat rate by 0.6% (Aksit, 2002). In addition to efficiency effects, leakage flows also cause component damage. As leakage flows cause the engine to run hotter, components degrade faster, which causes more leakages and thus requires the engine to run even hotter. This

cycle eventually degrades the turbine components to the point of required removal and maintenance. Maintenance costs for current gas turbine engines can easily exceed millions of dollars.

Similar to efficiency effects, leakage flows also affect the cooling of the turbine, especially the hub region. Conventional wisdom suggests elimination of leakage flows would provide more cooling flow to other parts of the blade which have been designed to provide maximum cooling. However, since leakage flows do provide some cooling, this tradeoff of leakage flow cooling is not well understood. It is important to understand the effect of leakage flows in order to identify any positive or negative effects on the cooling of turbine blades. This work attempts to quantify the effects of coolant leakage and to measure the gain, if any, of cooling effectiveness on the hub region.

The first part of this study describes the effects of coolant leakage flow on the hub region of a first stage gas turbine engine blade. Figure 1.7 shows an illustration of a typical turbine blade used in this study and the locations of possible leakage points. The cooling effectiveness on the platform (hub) of leakage flows from the front rim, aft rim and featherseal are examined. Infrared images of the hub region were taken for various configurations of flow through the three leakage points. Comparisons to baseline cases and computational predictions are presented.

1.1 Microcircuit Cooling Technology for Turbine Airfoils

In addition to studying any possible benefits of leakage flows, the effects of platform microcircuits will also be analyzed. Microcircuits are an innovative approach to blade cooling that has been designed by Pratt & Whitney, a sponsor of this work. A microcircuit is a series of passages internal to the blade that ultimately eject coolant through a film cooling hole or slot. Microcircuits are able to cool turbine blades and vanes through both internal convective cooling and external film cooling. Though these cooling techniques are currently used in some other designs, the ability to manufacture intricate internal passages within the thin walls of blades is what makes microcircuits unique.

For this study, two slightly different microcircuits will be tested. Figures 1.8a and 1.8b show both the suction side microcircuit and the pressure side microcircuit used in

this research. The suction side microcircuit, in Figure 1.8a, is located in the hub next to the suction side of the blade, which is the convex side of the blade. The suction side is thus named because the pressure distribution around the blade on the convex side is lower, which tends to draw flow towards that side. Conversely, the concave side of the blade is named the pressure side because of the relatively higher pressures on that side. Figure 1.9 shows a top view of the geometry tested in this research and the location of the two microcircuits relative to the blades. Both of the microcircuits are designed to remove heat through interval convection and conduction along the body of the microcircuit as well as film cooling at the slot exit of the microcircuit. It is important to note the microcircuits shown in Figures 1.8a-b are actually within the wall of the platform during testing, and only the exit slot at the top left of both figures is visible. The design and functionality of the microcircuits is further described in section 3.5 of this thesis.

1.2 Research Objectives

There are two main objectives to this research: to analyze the effects leakage flows have on cooling of the hub region and to analyze the effect hub microcircuits have on platform cooling. The microcircuits were tested both with and without leakage flows to document any differences between the two cases. The hub region was tested in a large scale, low speed recirculation wind tunnel with an inlet Reynolds number of 3.0×10^5 (based upon axial chord). Spatially resolved temperature measurements were made on the platform for five different leakage flows and three different microcircuit flows. Thermal contours were measured of the featherseal leakage flows near the leading and trailing edges to document the leakage effects in the main stream flow.

Literature relevant to heat transfer and cooling schemes on the hub region are presented in Chapter 2. A detailed description of the experimental test section design and construction is given in Chapter 3. The test matrix, test procedures and benchmarking procedures are described in Chapter 4. A detailed analysis of the results from the experimental testing are explained in Chapter 5, which is followed by conclusions and recommendations for future work in Chapter 6.

Figure 1.1 Picture of Whittle Engine test rig which successfully proved the feasibility of turbojet propulsion. (http://www.visitcumbria.com)

Figure 1.2 Picture of Heinkel He-178 airplane, the first aircraft to fly using a gas turbine engine for propulsion. (http://www.allstar.fiu.edu/aero/ohain.htm)

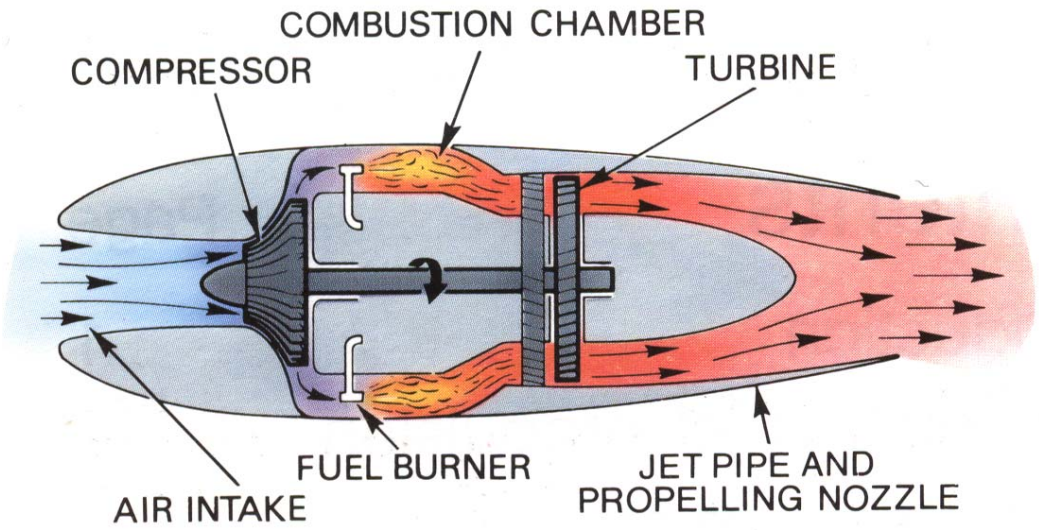

Figure 1.3 Drawing of a turbojet, illustrating the interaction between the compressor, combustion chamber and the turbines (Rolls Royce, 1992)

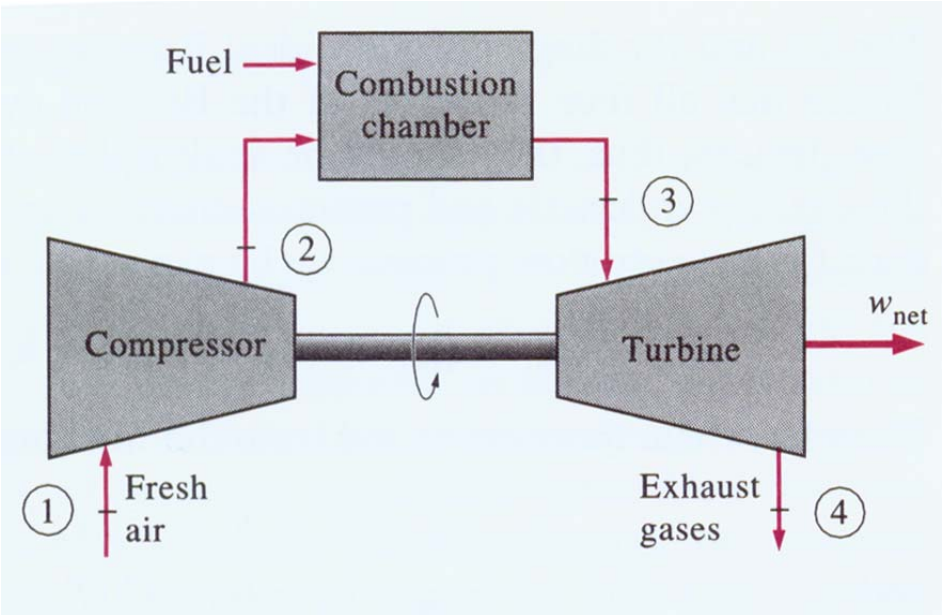

Figure 1.4 Diagram of Brayton Cycle, from which the equation for gas turbine efficiency (1.1) is derived. (Cengel and Boles, 1998)

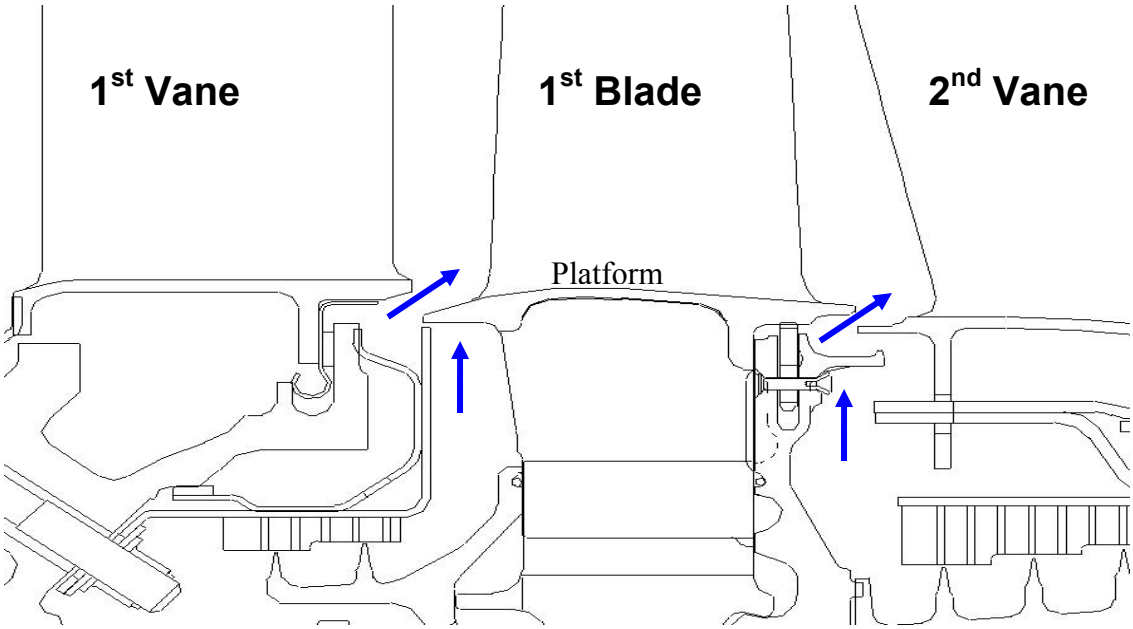

Figure 1.5 Cut-away view of 1st row of turbine blades, showing the internal seals and locations on the platform where leakage occurs. (Weidemer, 2003)

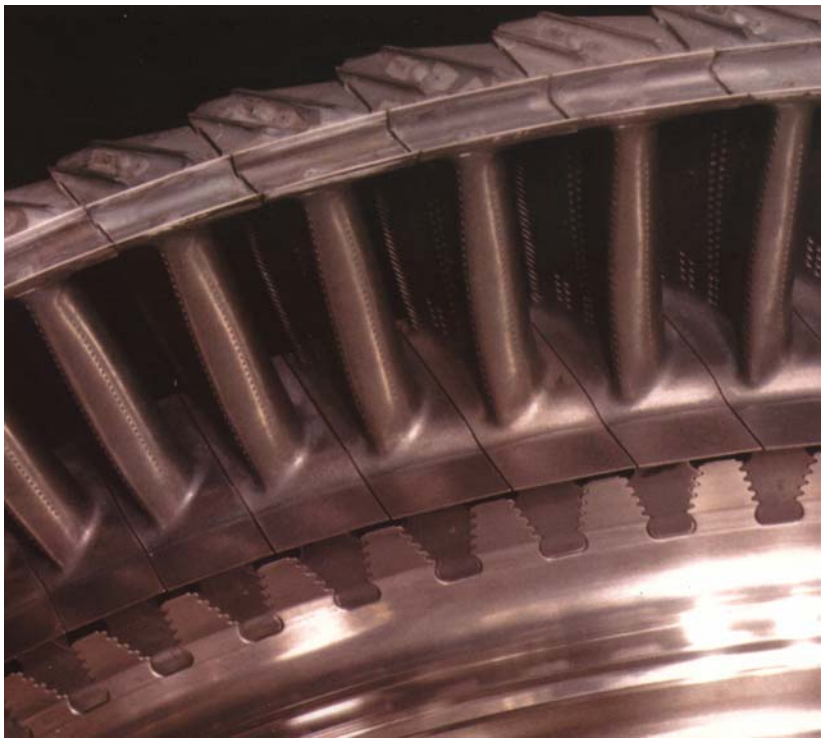

Figure 1.6 Picture of assembled turbine blade rig, showing the featherseal gap at the hub between blades. (Gas Turbine Theory, 2001)

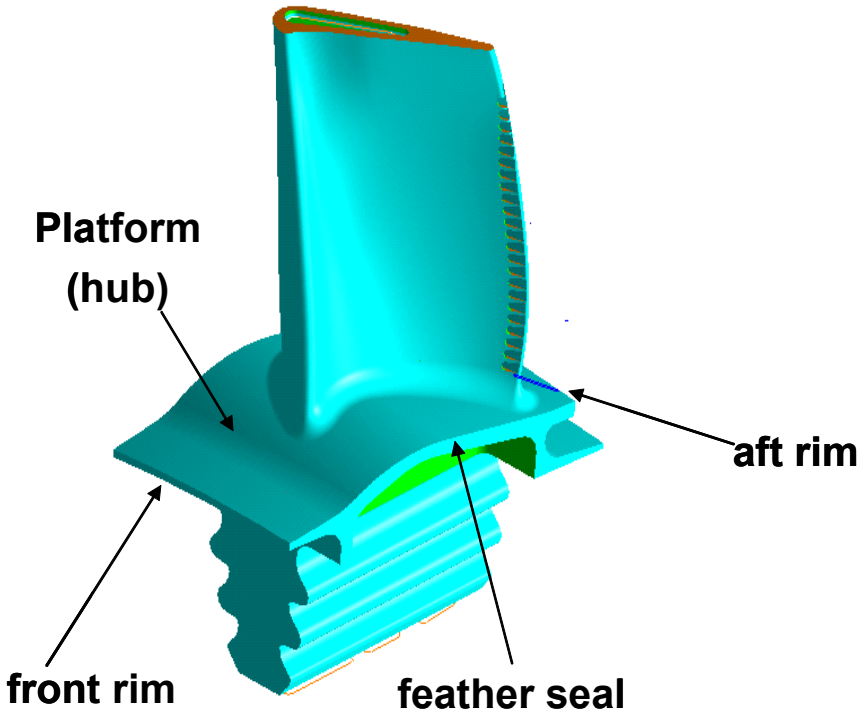

Figure 1.7 Illustration of turbine blade used in the current research with locations of possible hub leakage flows indicated. (Weidemer, 2003)

a) b)

Figure 1.8 Pictures of the microcircuits from the a)suction side and b) pressure side before they are molded and installed within the platform

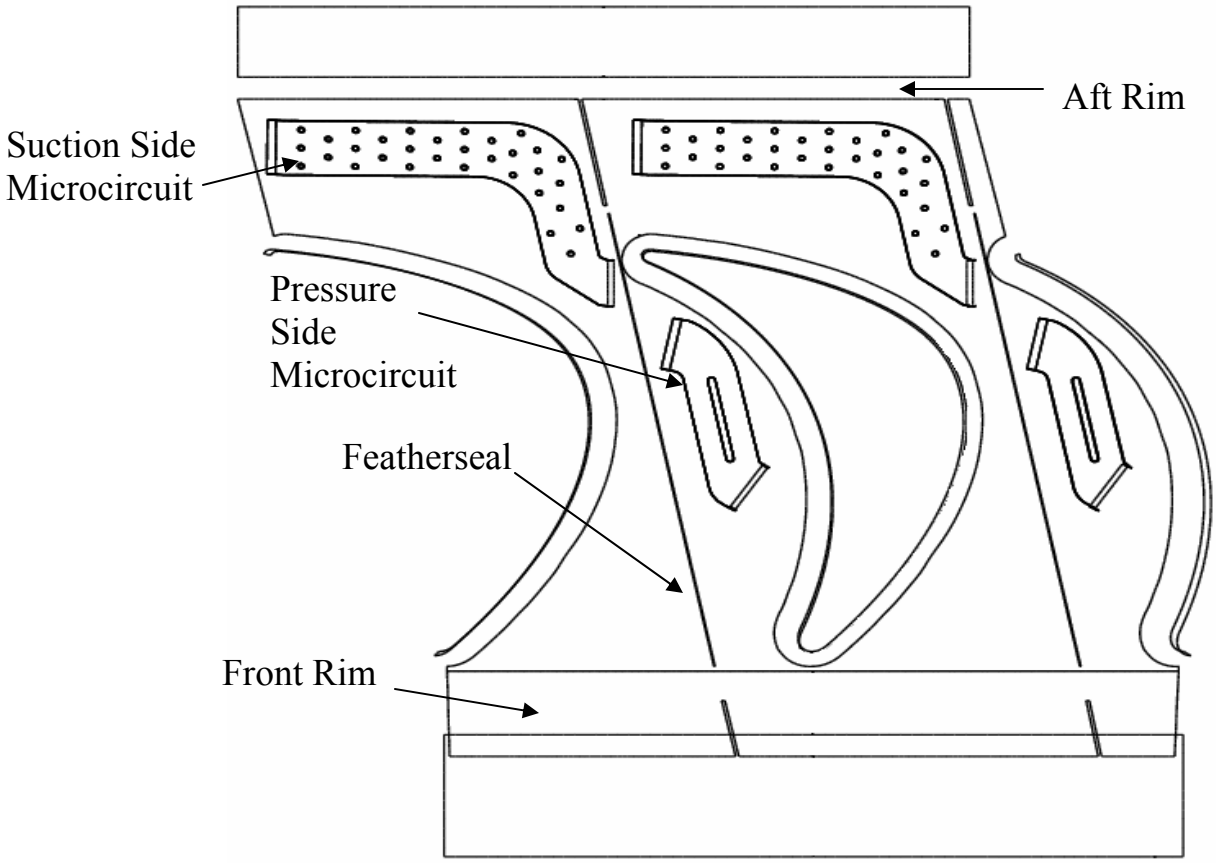

Figure 1.9 Top view of platform showing locations of pressure side and suction side microcircuits relative to the blades and other leakage geometries.

Chapter 2: Literature Review

Cooling within the turbine section of gas turbine engines has been the focus of research for the past half century. As designers push the combustion chamber exit temperature higher and higher, fundamental understanding of turbine cooling is critical to prevent blade degradation. Specifically, there has been considerable research dedicated to cooling the hub region of gas turbine engines. Numerous papers have worked to benchmark the secondary flow fields and their affects on heat transfer in the hub region in both radial test rigs and linear cascades, as well as computationally. A very small sample representation of these studies include: [Goldstein et al., 1995; Graziani et al., 1980; Hermanson 1999]. Additionally, there has been considerable hub research related to the affects of fillets around the base of the blades [Zess and Thole, 2001; Shih and Lin 2002; Lethander and Thole, 2003].

Though these studies have yielded fundamental understanding of the complex flows along the hub region, the papers detailed in the first section of this chapter focus on the prior work most related to leakage cooling of the hub region. Studies of both turbine blades and vanes are presented, as there are similarities between the two. Turbine blades typically have a higher angle of attack, since the flow into stator vanes is normal to the vanes. Additionally, vanes turn the flow while blades extract work, which sets up different aerodynamic flows. However, results of platform studies in both vanes and blades are relevant to this research. The second section of this chapter describes the uniqueness of the current study.

2.1 Platform Studies

Some of the earliest work related to the cooling of the hub region was performed by Blair [1974]. To study the possible advantages of film cooling on the hub region, a slot was placed upstream of walls representing guide vanes. Though he only examined three blowing ratios, Blair observed increasing cooling effectiveness as the flow from the slots was increased.

Though not directly related to slot cooling, one of the most influential studies of the hub region was performed by Langston et al. [1977]. Their research focused on the

formation of horseshoe vortices in front of a vane-endwall junction. A drawing of the vortices first proposed by Langston [1980] is shown in Figure 2.1a. The vortices are caused by the deceleration of the boundary layer as it approaches the stagnation point. The endwall pressure gradients cause the boundary layer to roll up, creating two vortices, one that travels down the passage side of the blades and one that travels down the suction side. Their model is important to research dealing with leakage flows along the hub region because the passage vortex causes reduction in cooling effectiveness as coolant is pulled off the platform. Two other models of vortex formation along the hub region have been presented by Sharma and Butler [1987] and Goldstein and Spores [1988], which are shown in Figures 2.1b and 2.1c, respectively. All three models differently describe the location of the suction side leg of the vortex. The Sharma and Butler [1987] model predicts the suction side leg of the vortex does not adhere to the suction side of the model. Goldstein and Spores [1988] proposed the suction side leg stays above the passage vortex. Though each model differs slightly, all three models are sited as reasons for decreases in film cooling across the hub region.

In an attempt to reduce the decreased cooling effectiveness caused by the passage vortex, Aunapu et al. [2000] used blowing along the hub region. They hypothesized endwall blowing in the blade passage would have a similar affect seen by Chung and Simon [1993] who used a fence in the middle of the passage to lift the passage vortex. Figure 2.2 shows both the location of the endwall blowing studied by Aunapu et al. [2000] and the location of the fence used by Chung and Simon [1993]. Aunapu et al. [2000] observed that endwall jets in the center of the blade passage effectively altered the path of the pressure side leg of the vortex. Through using flow conditions comparable to those used for film cooling, the migration of the pressure side vortex was partially blocked. Unfortunately, the increased blowing caused higher turbulence and thus higher secondary losses. Though Aunapu et al. [2000] did not study temperatures on the hub region, their work represents the only known literature studying the effects of blowing from a featherseal-like slot in the blade passage.

Though little open research has focused on cooling from a slot within the blade passages, several studies have been performed on coolant from holes within the blade passage. Friedriches et al. [1996] studied the effectiveness of film cooling holes on a

turbine endwall. Through using an ammonia and diazo coating technique on the hub surface, they were able to measure the adiabatic film cooling effectiveness in a large scale, low speed linear blade cascade. The researchers showed the horseshoe vortices in the blade passage can act as barriers to the coolant trajectories. Figure 2.3 shows oil and dye surface flow visualization of their test configuration, which marks the locations of the vortices in the passage. They showed that coolant ejected near the indicated vortex path lines in Figure 2.3 is inefficient, since most of the coolant is pulled off the platform. However, coolant injected away from these lift off lines provides cooling to the hub region. They additionally showed that with the addition of the cooling holes, the lift off lines shown in Figure 2.3 were moved downstream as the coolant ejection delayed the boundary layer separation.

In addition to coolant holes in the hub region between the blades, studies have been performed using film cooling holes upstream of airfoil cascades. Oke et al. [2000] studied hub cooling in a vane cascade with upstream film cooling holes. Figure 2.4 shows the cooling hole pattern they used to study endwall cooling. Oke used staggered, 45° holes with flow rates between 1.5% and 3.0%. They found at lower flow rates, coolant was drawn across the platform towards the suction side of the blades. Additionally, they observed that higher coolant flow rates increased the coolant momentum and decreased the migration of the coolant towards the suction side of the blades.

In a similar study of coolant upstream of a vane passage, Burd et al. [2000a,b] studied the effects of an upstream cooling slot. The flush, 45° slot used in the study is shown in Figure 2.5, which included a break in the slot between the vanes. The slot studied by Burd is very similar in design to a front rim leakage point. By using coolant flows as high as 6% of the inlet flow, good cooling was observed over the endwall and both sides of the vanes. These results were only achieved when the slot coolant flow was high enough to overcome the effects of near wall secondary flows. Burd also showed the high coolant flows also reduced the secondary flow effects.

Combining the effects of a leading slot and film hole cooling in the blade passage, Nicklas [2001] measured film cooling effectiveness and heat transfer on the hub region. Figure 2.6 shows the endwall cooling arrangement studied by Nicklas [2001]. Through

analysis using an infrared camera, Nicklas [2001] observed the effects of the passage vortex on the hub region temperature distribution. Figure 2.7 shows the film cooling effectiveness results obtained with coolant out of all of the slots and holes. While high cooling was observed in the front part of the passage due to the slot injection, the effects of the passage vortex decrease the cooling effectiveness, especially near the pressure side corner. Additionally, Nicklas showed the coolant injection increased the horseshoe vortex, which caused a strong increase in heat transfer coefficients near the leading edge.

An experimental study by Colban et al. [2003] measured effectiveness levels along the endwall of a first stage turbine vane. Figure 2.8 shows their experimental test section, in which they measured the effects of changing the combustor liner film-cooling and junction slot flows. The results show the coolant from the slot was not uniform across the exit. Instead, coolant accumulated along the endwall near the suction side of the vane. Additionally, increasing the slot cooling reduced the endwall temperatures, which was not true with increases in film-cooling from the liner. Coolant injection from the upstream combustor liner causes different total pressure profiles entering the vane passage. Their measurements showed that as a result of the modified inlet pressure profiles, coolant was ingested in the front rim for several of their flow conditions. Colban and Thole [2003] also observed coolant was swept towards the suction side of the vane by cross flow within the passage.

In a similar study of both leading edge slot cooling and film hole cooling, Knost and Thole [2003] studied two different cooling hole patterns in turbine vane passages with leading edge slot cooling. Figure 2.9 shows the two cooling hole patterns studied. Additionally, room was left in the cooling hole patterns for the location of a featherseal gap, but no featherseal flow was modeled. Figure 2.10 shows the measured adiabatic effectiveness results for both slot and film cooling hole cooling. High cooling of the front part of the passage was observed with the slot flow, and the flow was swept towards the suction side of the blades in the passage. Additionally, it was shown that with the addition of film cooling holes in the passage, the hub cooling was dramatically increased. Just as in the Nicklas [2001] studies, the ample cooling in the leading part of the passage did not provide a significant amount of cooling to the pressure side of the blades. The

results in Figure 2.9 also show a gap of cooling in the platform, where hopefully featherseal flow would provide additional cooling.

Though not directly studying the flows within turbine blade passages, Yu and Chyu [1998] studied the influences of gap leakages downstream of injection cooling holes. Figure 2.12 shows the geometry of used in this study. Using liquid crystal measurements, they observed the film effectiveness of combined slot and film cooling hole effectiveness without the secondary flow fields present in the previous studies. Yu and Chyu [1998] observed that for a moderate level of film cooling upstream of a coolant slot, the combined presence of the gap promotes better coolant film protection. Coolant from the first injection seemed to suppress the second injection from overshooting into the freestream. However, stronger secondary injection from the gap seems to lift the boundary layer from the wall, decreasing the effectiveness. Additionally, they showed the gap effectiveness can be affected by increasing the flow from the cooling holes. They showed the effects of the upstream coolant holes on the gap cooling depends on the ratio of downstream to upstream mass flow ratio (m_2/m_1). When the m_2/m_1 ratio was near 0.5, increases in the first blowing rate caused reduction the second coolant effectiveness, since the coolant from the gap lacked sufficient momentum to penetrate the boundary layer. However, as the m_2/m_1 is increased, the overall cooling effectiveness increases as the gap coolant is able to penetrate the boundary layer. Their results correlate well with the previously mentioned studies showing the increased cooling with combined slot and cooling hole flows.

Also studying cooling holes placed upstream of turbine vanes, Zhang and Jaiswal [2001] studied endwall surface film cooling effectiveness. Using cooling flows ranging from 0.5% to 3.0% of the mainstream flow, they examined a double staggered row of holes and a single row of slots. Their results indicated cooling effectiveness did not linearly increase with coolant flow rate. This result suggests an interference between cooling jets, such as the results of Yu & Chyu [1998]. Additionally, the cooling was affected by the secondary flows within the vane passage. They showed that low cooling rates were ineffective because secondary flows dominated the region near the wall. However, at higher coolant flow rates, the coolant momentum was able to overcome the near wall flow and provide ample cooling to the platform.

2.2 Uniqueness of Current Study

The main objective of this research was to study the effects of leakage flows near the hub region, including the effects of microcircuits placed within the platform. Though several previous studies have analyzed the effects of a leading edge slot similar to a front rim, there is no known literature that has studied the cooling benefits of a featherseal. Though room was left in the cooling hole pattern for the featherseal in Knost and Thole [2003], no featherseal flow was tested. Though the results of Yu & Chyu [1998] suggest the interaction of front rim and featherseal flow could provide increased cooling, this result has yet to be analyzed.

Additionally, there is no public literature discussing the effects of microcircuits in the hub region. Since microcircuits are a proprietary design by Pratt & Whitney, it is not surprising there is no open literature describing their effects. There has been three previous thesis works studying microcircuits. Couch [2003] and Christophel [2003] studied the effects of microcircuits in the tip of a turbine blade. Prausa [2004] studied the internal and external cooling of a microcircuit designed for the main body of a turbine blade. There has been no research, public or private, studying the adiabatic effectiveness of microcircuit cooling of the hub region.

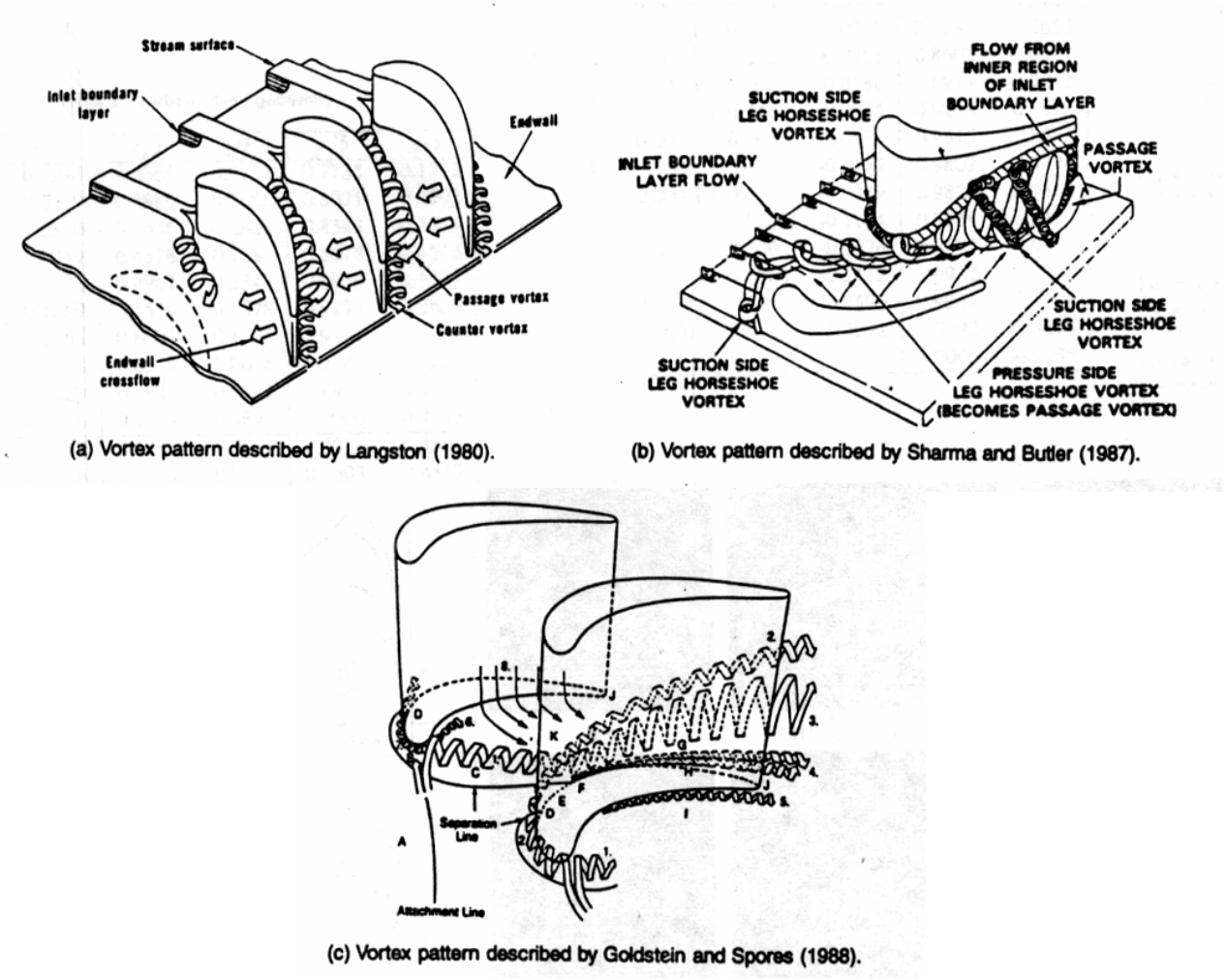

(a) Vortex pattern described by Langston (1980).

(b) Vortex pattern described by Sharma and Butler (1987).

(c) Vortex pattern described by Goldstein and Spores (1988).

Figure 2.1 Horseshoe vortex patterns as described by a)Langston [1980], b)Sharma and Butler [1987] and c) Goldstein and Spores [1988]

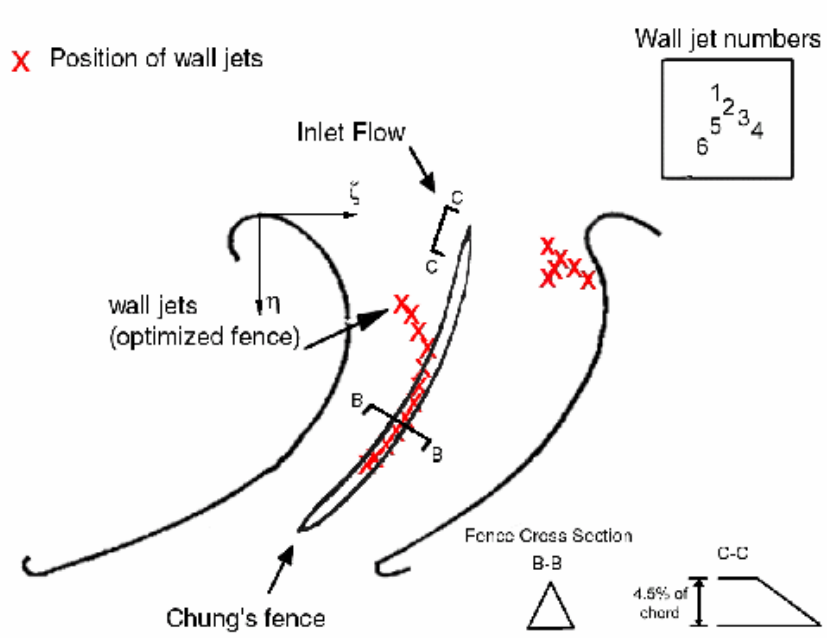

Figure 2.2 Test geometry used by Aunapu et al.[2000]. Blowing from a slot in the center of the channel was used to lift the passage vortex, based upon the fence location of Chung and Simon [1993].

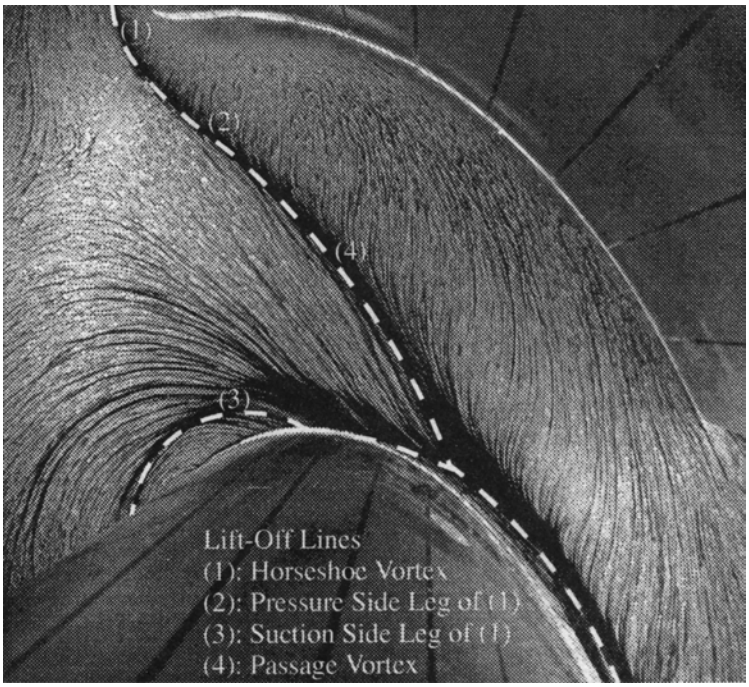

Figure 2.3 Oil and dye visualization of the blade passage used by Friedriches et al. [1996], showing the locations of the vortices in the passage.

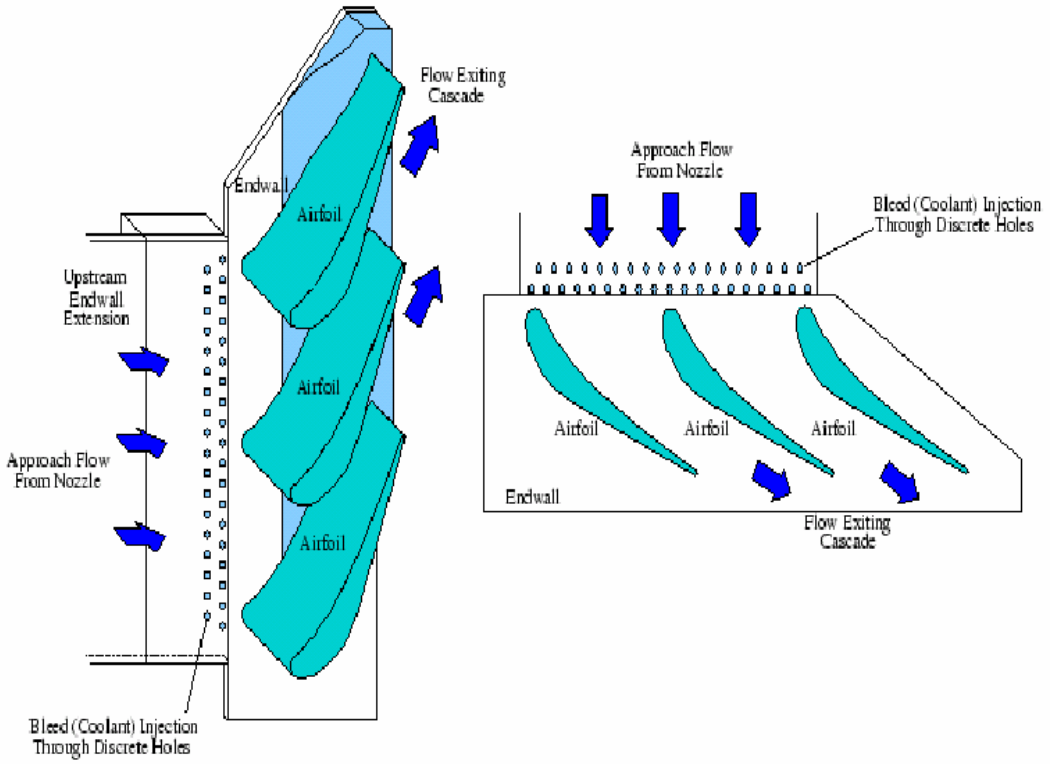

Figure 2.4 Cooling geometry used by Oke et al. [2000]. Film cooling holes were used upstream of the airfoil passage.

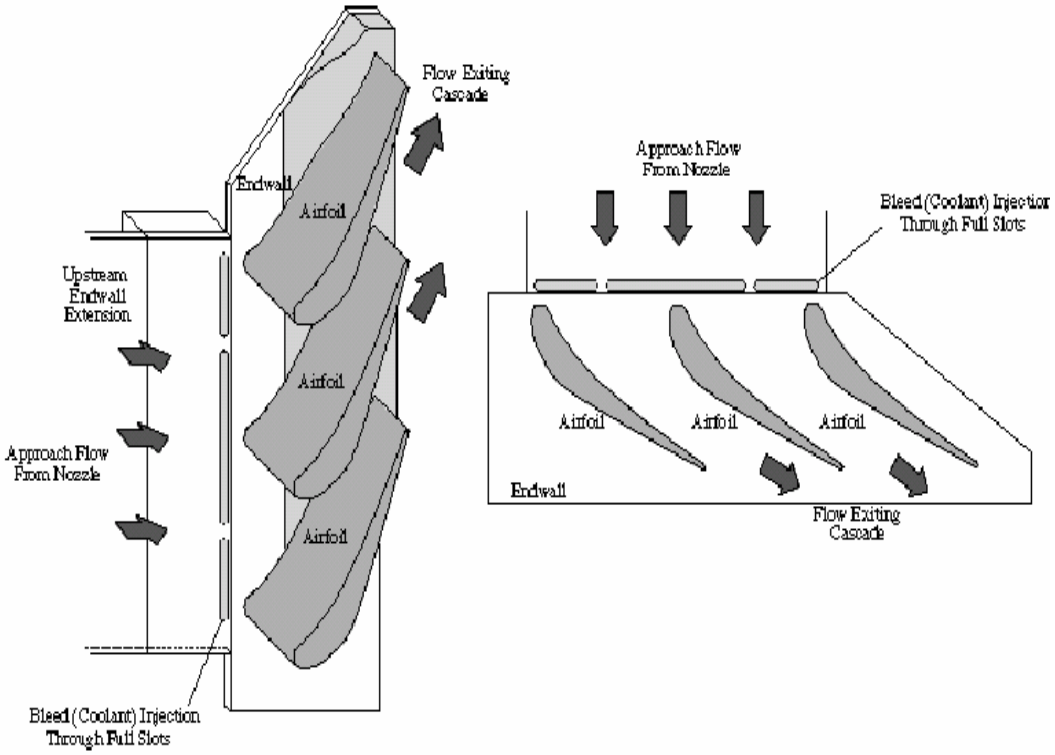

Figure 2.5 Cooling geometry used by Burd et al. [2000a,b].

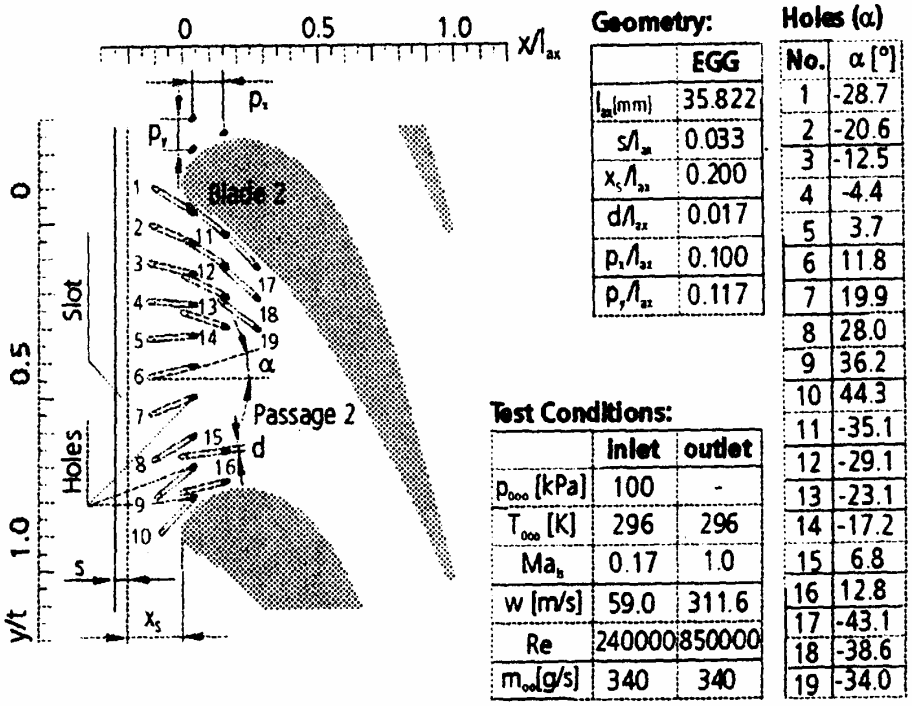

Geometry:

	EGG
l_{ax}[mm]	35.822
s/l_{ax}	0.033
x_s/l_{ax}	0.200
d/l_{ax}	0.017
p_x/l_{ax}	0.100
p_y/l_{ax}	0.117

Holes (α)

No.	α [°]
1	-28.7
2	-20.6
3	-12.5
4	-4.4
5	3.7
6	11.8
7	19.9
8	28.0
9	36.2
10	44.3
11	-35.1
12	-29.1
13	-23.1
14	-17.2
15	6.8
16	12.8
17	-43.1
18	-38.6
19	-34.0

Test Conditions:

	inlet	outlet
$p_{0\infty}$ [kPa]	100	-
$T_{0\infty}$ [K]	296	296
Ma_s	0.17	1.0
w [m/s]	59.0	311.6
Re	240000	850000
m_{∞}[g/s]	340	340

Figure 2.6 Cooling geometry used by Nicklas [2001]. Both slot cooling and film hole cooling in the blade passage were analyzed.

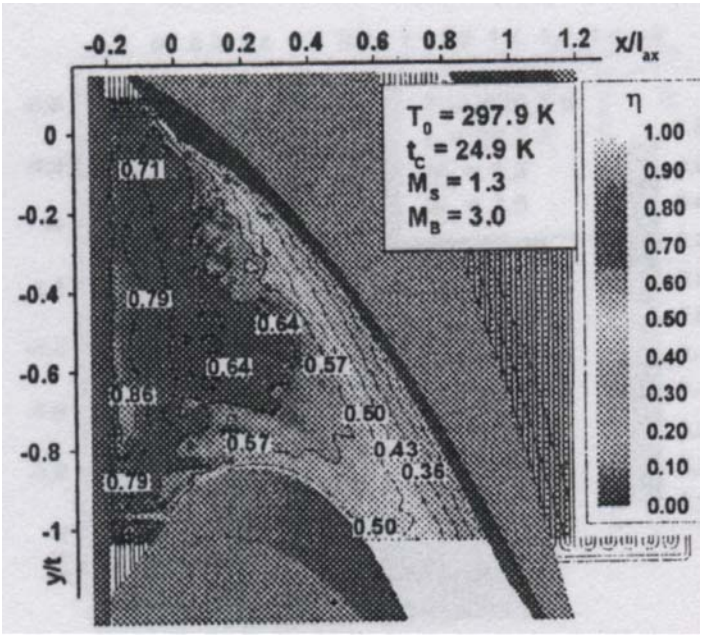

Figure 2.7 Results from Nicklas [2001], showing adiabatic effectiveness between the blades. Cooling from both the front rim and cooling holes is present.

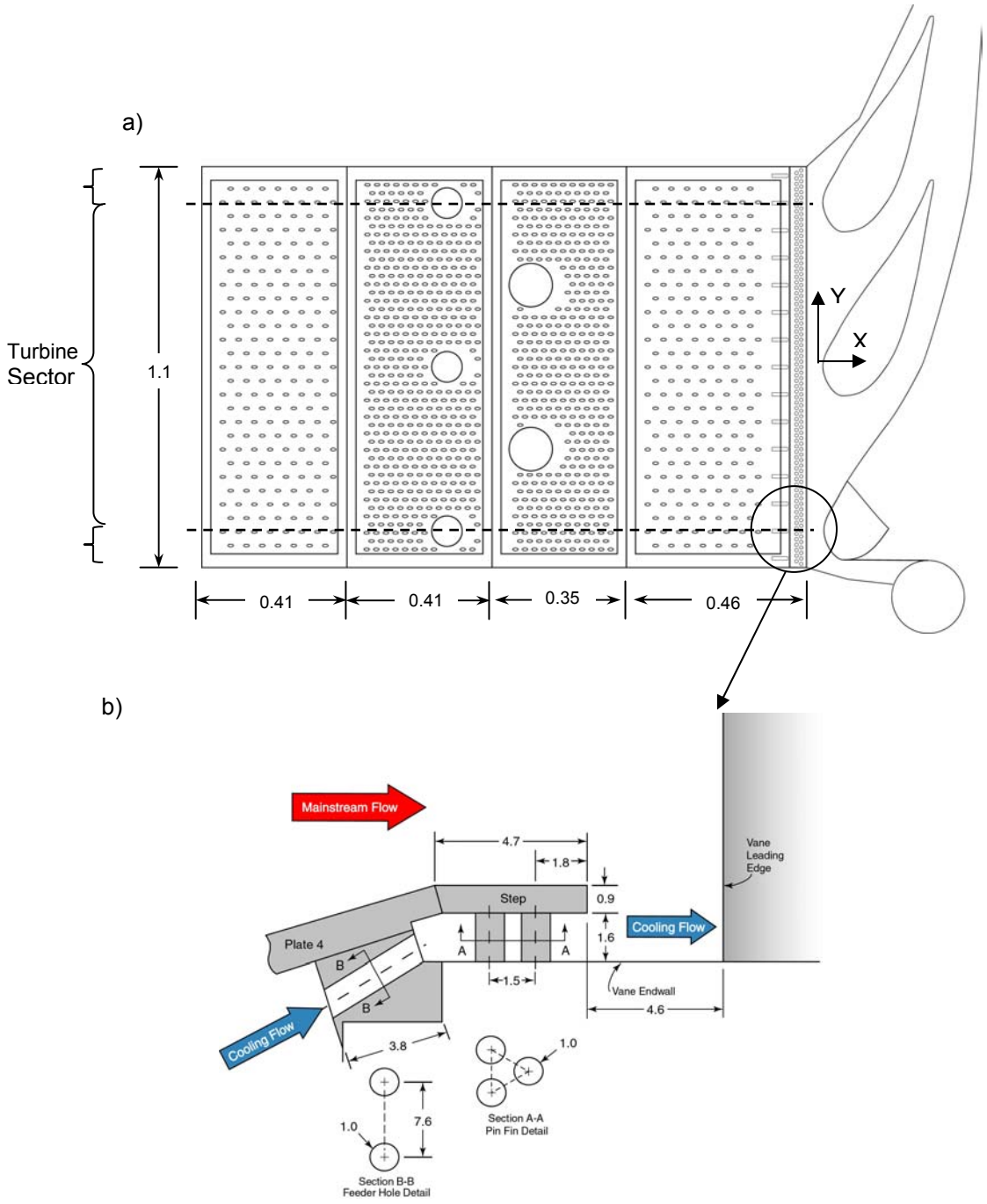

Figure 2.8a-b. Diagram of experimental test configuration used by Colban and Thole [2003]. The slot and cooling hole configuration is shown from a) top view and b) side view, detailing the slot configuration.

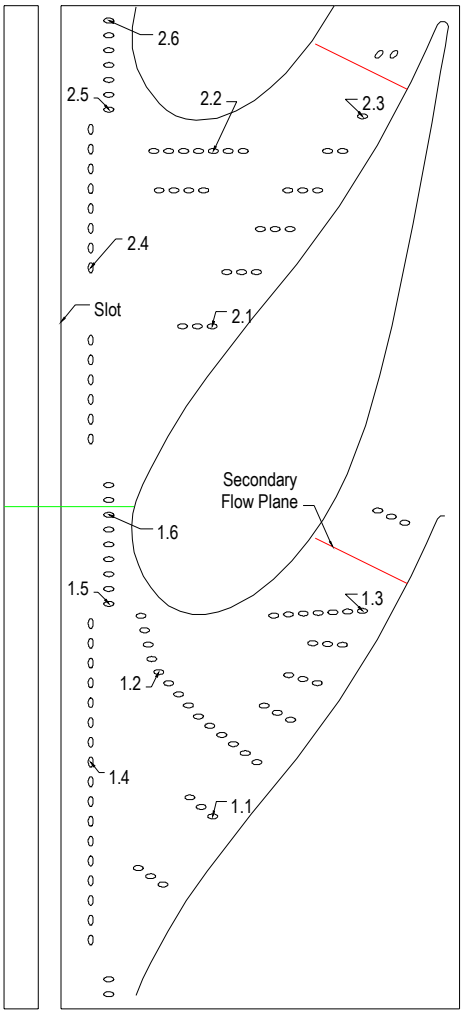

Figure 2.9 Cooling configuration used by Knost and Thole [2003]. Similar to Nicklas [2001], hub cooling was achieved with both slot and film hole cooling.

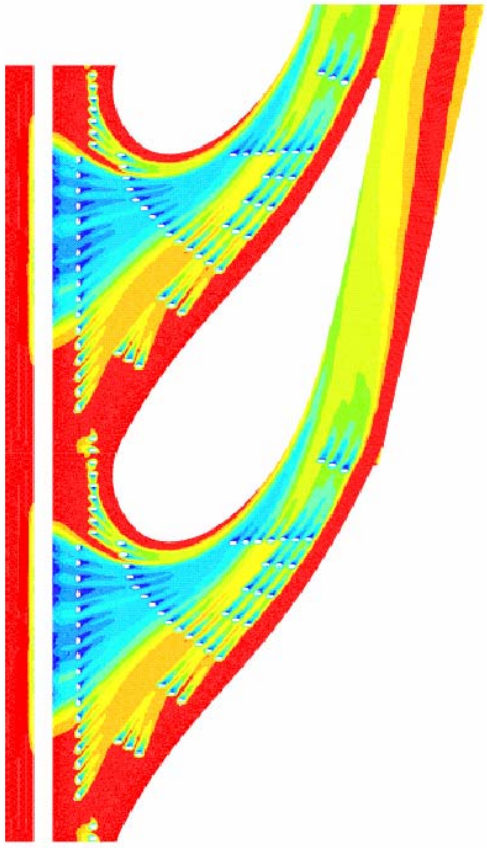

Figure 2.10 Cooling results from Knost and Thole [2003]. Leading edge slot flow does not provide cooling to the pressure side of the blades.

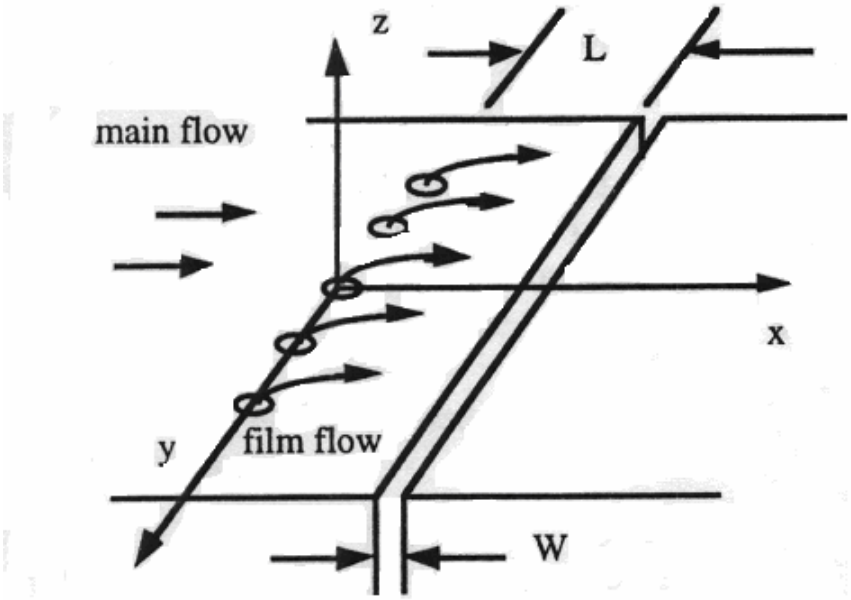

Figure 2.11 Cooling configuration used by Yu and Chyu [1998].

Chapter 3: Experimental Design and Construction

The flow field near the hub region of gas turbine blades is a three-dimensional flow that would be very difficult to quantify at the actual engine size. To spatially resolve thermal details, large scale testing was performed on the leakage flows representative of the flows around the hub region of a gas turbine engine. The design and construction of the large scale test rig is described in this chapter. First, the design parameters for scaling the engine geometries and flow conditions are given. The next section describes the blade, platform and microcircuit designs, and construction procedures. Explained in the next section are the wind tunnel facilities and instrumentation of the test section. The final section of this chapter presents the uncertainty analysis of the measurements..

3.1 Test Section Scaling Parameters

Based upon the size limitations of the current experimental facilities, the scaling factor for the geometric features was set at 11X engine scale. This scale was large enough to maximize the spatial resolution of both the surface temperature measurements and the thermal field measurements, but at the same time, small enough to allow room for a four blade, three passage linear cascade. Ideally, it is desirable to run experiments that match the inlet Reynolds number of the gas turbine engines. Unfortunately, the test facility inlet velocity is limited, which prevents direct matching of the Reynolds number. However, the test inlet Reynolds number could be matched to one half the engine inlet Reynolds number. Based upon the axial chord length of 0.45 m and an inlet velocity of 10.3 m/s, the test inlet Reynolds number was 3×10^5 . For consistency, the internal Reynolds number was also matched to one half the internal Reynolds number at engine scale.

Calculations by Pratt & Whitney [Blair, as documented in Hohlfeld, 2003] showed that if the external Reynolds number for the test section was set to one half the engine conditions, then the ratio of the blowing ratios was equal to:

$$\frac{M_t}{M_e} = \frac{\rho_{ct} U_{ct} \Big/ \rho_t U_t}{\rho_{ce} U_{ce} \Big/ \rho_e U_e} = 1.79 \qquad (3.1)$$

where M is the blowing ratio, ρ is the density, U is the velocity, the subscript 't' is for test scale, the subscript 'e' is for engine scale, and the subscript 'c' is for cooling flow. The ratio given in equation (3.1) was used to scale all of the coolant mass flow settings from the engine scale to the test scale. Through rearrangement of equation (3.1), as shown in Hohlfeld, the mass flux of the coolant at test scale is defined by:

$$\rho_{ct} U_{ct} = \left(\frac{\rho_t U_t}{\rho_e U_e} \right) \frac{\dot{m}_{ce}}{A_{ce}} = 0.0219 \frac{\dot{m}_{ce}}{A_{ce}} \tag{3.2}$$

where $\dot{m}_{ce}$ is the mass flow of the coolant at engine scale and A_{ce} is the area of the coolant exit at engine scale. The coefficient in equation (3.2) was determined since all of the values of the free stream velocity and density are known at both engine and test scale. To determine the coolant mass flows at test scale, first the coolant mass flow at engine scale was divided by the area at engine scale. Next, the coolant mass flux at test scale was calculated by multiplying the coolant mass flux at engine scale by 0.0219, as shown in equation (3.2). Finally, the coolant mass flow at test scale was calculated by multiplying the coolant mass flux at test scale by the test area. The values used to calculate the coolant mass flow are shown in Table 3.1, which gives the resulting mass flow as a percent of the total inlet mass flow at test scale. Additionally listed in Table 3.1 are the ranges of coolant flows used during testing. Section 4.1 details the complete test matrix, which was designed based upon the ranges listed in Table 3.1. The design of each of these leakage features is explained in section 3.3, and the construction of each leakage feature is explained in section 3.4.

3.2 Turbine Blade Design and Construction

In addition to the 11X scaling of the turbine blades, the geometry of the test section blades varied from the actual engine blades by three modifications. First, the platform of actual turbine blades has a slight curvature. Figure 3.1 shows a side view of a typical turbine blade [Weidemer, 2004], illustrating the curvature of the platform as the leading edge is higher than the trailing edge of the blade. In the experimental test section, the blade was modeled with a completely flat platform. A flat platform simplifies the data collection process, allows for easier comparisons to prior experiments and computations, and does not significantly affect the overall flow fields since the curvature

of the hub is small compared to the curvature of the hub disk. The second difference between the test blades and engine blades is the lack of twist in the test blades. The engine blades are designed with twist to aid in the aerodynamics; however, the test blades were designed with the perimeter of hub region modeled throughout the entire span. Third and lastly, the geometry of the hub region was redesigned by Pratt & Whitney to accommodate the difference in pressure distribution around the blades.

Although the engine blades experience compressible speeds, the test blades in the wind tunnel are subjected to low speed conditions and thus very different pressure distributions. Figure 3.2 shows the blade geometry provided by Pratt & Whitney for our low speed testing. The compressible effects, density variations, and shocks associated with high speed flows are not accounted for with this redesigned blade geometry. However, as the heat transfer is dependant on the Reynolds number and geometry, which are both scaled to match the actual engine conditions, the resulting temperature distributions along the hub region will still accurately model the actual gas turbines. Some of the basic blade parameters, such as blade pitch, chord, and angle are shown on Figure 3.2 and summarized in Table 3.2. The data points of the scaled blade perimeter supplied by Pratt & Whitney are shown in Appendix A.

Since this research is only concerned with adiabatic thermal measurements, the blades were constructed out of foam with a thermal conduction coefficient of 0.04 W / m K (Tenneco, 2003). To construct each of the four blades, ten foam sections, each 5.08 cm thick, were cut out of the foam and glued together with epoxy glue. To accurately cut out each foam piece, an outline of the blade geometry was made out of 0.64 cm aluminum. The points were then cut out of the aluminum sheet using metal shears. Two aluminum blade shapes were created for the process of making the foam blade sections. A rectangular foam piece was sandwiched between two of the aluminum blade shapes. Next, a hot-wire with 10 mA of current was used to cut out the shape of each foam blade since the hot-wire would cut the foam but not the metal outline. Figure 3.3 shows the cut out foam blades as they are assembled.

During construction of the blades, one of the pieces of blade sections was hollowed so pressure taps could be instrumented around the perimeter. The hollowed out piece was put at the midspan of the blade during the assembly of the individual blade

pieces. Figure 3.4 shows a top view of the pressure tap locations on the pressure side and suction side of the blade. The dimensioned locations for each of the pressure taps is also listed in Appendix A. Each pressure tap consisted of hollow metal tube, 0.8 mm in diameter, connected to 1.6 mm vinyl tubing. The pressure measurements are described in detail in section 3.9 of this chapter.

Once all ten foam pieces were assembled, the entire blade structure was sanded to ensure smoothness of the whole blade. Then the blades were coated with 0.13 mm thick Teflon® film which was painted black. The film was used to both ensure a smooth, continuous surface on the blades and to allow the blades to be painted black. The blades were painted black to reduce any radiation errors in taking infrared images of the hub region. The blades could not be directly painted black as paint would have corroded the foam blades. Figure 3.5 shows a finished, coated blade.

After the blade was coated, it was attached to the base fillet that was provided by Pratt & Whitney. The fillets were manufactured using a stereo lithography (SLA) machine. The fillet height was 7.0% of the span, and the upstream extent of the fillet was 6.8% of the span, with a radius of curvature that is 23.1% of the span. The actual fillet is shown attached to the completed blade in Figure 3.5. Figure 3.6a shows a side drawing of the fillet around the blade and Figure 3.6b shows a top figure of the blade attached to the filet. Although the fillet was included in this study to see if there was any gain in platform cooling, previous work [Hermanson, 2000] has shown that manufacturing fillets have little effect on hub cooling.

3.3 Platform Design

The platform section was designed after the test blades had been constructed. As previously mentioned, the experimental facilities were designed to match the internal Reynolds number to one half the internal Reynolds number at engine scale. Unfortunately, calculations from Pratt & Whitney [Blair, as documented in Hohlfeld, 2003] show that if both the pressure side and suction side microcircuit are fed from the same source, each microcircuit would have a significantly different internal Reynolds number. If a supply pressure of 101,897 Pa (14.779 psia) was used for the pressure side microcircuit, the ratio of internal Reynolds number from test scale to engine scale would

be 0.5. The same supply pressure of 101,897 Pa (14.779 psia) for the suction side microcircuit would result in a ratio of internal Reynolds number from test scale to engine scale of 0.36. Since it was desired for both microcircuits to match one half the internal Reynolds number at engine scale, each microcircuit would require a different supply pressure.

Before the platform design is described, it is important to discuss the microcircuit design in more detail. Figure 3.7 shows a generic model of the two main forms of cooling generated by a microcircuit. As shown, cool air enters the microcircuit, which is within the wall thickness of the hub. Inside the microcircuit, convection will cool the outer walls of the microcircuit. Conduction through the wall will provide cooling to the hub. In addition to convective cooling, additional film cooling is gained once the flow exits the microcircuit.

The pressure side and suction side microcircuits used in this study are shown in top and isometric views in Figures 3.8a-d. There are several differences between the designs of the two microcircuits. The pressure side microcircuit is considerably shorter in length, because of limited space. In addition, there is a separating wall down the center of the pressure side microcircuit which divides the flow into two paths. The scaled exit slot dimensions of the pressure side microcircuit are 5.1 cm by 0.64 cm.

In contrast, the suction side microcircuit is nearly twice the length of the pressure side microcircuit. Instead of the separating wall, there are 32 staggered pedestals inside the rectangular area of the microcircuit. These pedestals both provide support for the microcircuit and help increase the turbulence, and thus heat transfer, within the microcircuit. Because of the additional length and numerous obstructions to the flow, the estimated pressure drop across the suction side microcircuit was higher than the pressure drop across the pressure side microcircuit. Determination of the experimental pressure drops across the microcircuits is detailed in section 4.3. The scaled exit slot dimensions of the suction side microcircuit are 5.7 cm by 0.64 cm.

In addition to designing separate pressure supplies for each of the microcircuits, each of the remaining leakage features was designed to have their own supply pressure. Thus all seven leakage features (front rim, aft rim, feather seal, 2 pressure side microcircuits, 2 suction side microcircuits) required a plenum that could be independently

controlled. Figure 3.9a shows a top view drawing of the three main leakage features inherent to gas turbines: the front rim, featherseal, and aft rim. The studies involving these three leakage features are referred to as the public cases. The featherseal gap width, which in this experiment is 0.46 mm, was taken as the average thickness between gaps that exist at hot and cold conditions. The gap width of the featherseal increases to 6.35 mm as it connects to the front and aft rims, as shown in Figure 3.9a. The sections where the featherseal connects to the front and aft rim have been termed the front gutter and aft gutter. The dimensions of these leakage features are summarized in Table 3.3. In addition to the public cases, testing of the microcircuits also studied the effects of the front rim, aft rim, and featherseal. Figure 3.9b shows a top view of the leakage features used when testing the pressure side and suction side microcircuits. As previously mentioned, each leakage feature shown in Figure 3.9b required a separate plenum to allow for independent control of the leakage flow. Figure 3.10 shows a top view of the platform with boxes representing the plenums for each of the seven leakage features.

While the featherseal, aft gutter and aft rim were simply 90° slots cut into the flat hub region, the front rim and front gutter were designed as a backwards facing front step. Figure 3.11a shows a dimensioned side view of the backwards facing front step for the front rim leakage geometry. The 6.35 cm long front gutter is actually within the step at an angle of 17^{o}. Also shown in Figure 3.11a is the location of the fillet relative to the backwards facing front step. Figure 3.11b shows a top view of the backwards facing front step and the location of the front gutter within the step.

In designing plenums, the front gutter and front rim were fed from the same plenum, just as the aft rim and aft gutter were fed from the same plenum. The front and aft plenums were designed based upon two constraints. First, each plenum needed to be sufficiently large so the velocity inside each plenum was near zero. A near zero velocity was required to create a uniform supply and to ease the calculations of exit velocity from the plenum. Secondly, each plenum was designed to be fed from a source that provided enough pressure to overcome friction losses. For the front and aft rim plenums, the calculated pressure loss across the slot was 62.2 kPa for a mass flow rate of 2.5% of the inlet flow. Because the bottom passage of the wind tunnel (explained in section 3.7) provides more than 80 kPa, the front and aft rims were designed to be fed from the

bottom passage. Figure 3.12 shows a side view of the test section design with both the front and aft rim plenums marked. Shown in Figure 3.12, the flow for the aft rim plenum passes underneath the front rim plenum. The space between the front and aft rim plenums underneath the blades allows room for the remaining plenums. Each of the front and aft rim plenums are fed by slots in the front of the test section, which are connected to the bottom passage of the wind tunnel.

To analyze the effects of the front and aft rim leakage flows, it was desired to vary the amount of flow out of the front and aft rim plenums. Since both plenums were attached to the bottom passage of the tunnel, a flow control device was needed in each plenum to change the amount of flow entering each plenum. To independently control the flow into each slot from the tunnel, sliding gates were installed in the entrance area to each plenum. The sliding gates consist of two main parts, a fixed front gate and a rear moveable gate. Each gate piece was identical, with four rectangular slots cut in the middle. When the two pieces were aligned, the rectangular slots would allow for maximum flow. As the rear piece was moved, the open area between the two slots was decreased, which reduced the flow into the plenum. Since both plenums were fed from the same source, by closing one of the gates and thus reducing the flow to one plenum, the flow would be increased to the other plenum. Figure 3.13a shows a drawing of one of the slide gates from a top view, and Figure 3.13b shows a front view of the sliding gate. The coolant air in the bottom section of the wind tunnel passes through two slots in the front of the test section to enter the plenums as shown in the side view in Figure 3.14. The two slots shown in Figure 3.14 attach to matching slots in the bottom section of the wind tunnel (which is further described in section 3.7).

In designing the remaining plenums, the total pressure required to feed each of the four microcircuit plenums was calculated based upon microcircuit losses given by Pratt & Whitney. It was calculated each pressure side microcircuit would need 102 kPa and each suction side microcircuit would need 103 kPa, based upon a dump pressure of 101 kPa. Additionally, because of the size of the featherseal gap, the required pressure to overcome frictional losses for a mass flow rate of 1.5% was nearly 90 kPa . Since these pressure requirements were higher than the pressure supplied by the bottom of the wind tunnel (80 kPa), the other five plenums needed to be supplied from an external source.

This problem of supplying coolant air at a higher pressure has been overcome in previous studies(Couch [2003] and Christophel [2003]) by using a compressed air source. In those previous studies, coolant air was supplied from a compressor in 5.1 cm diameter polyvinyl chloride (PVC) pipes. Since the majority of the piping from the previous studies still existed, the plenums for each the five other leakage features were each designed to be fed from the existing PCV piping. The compressed air source is described in more detail in section 3.7.

Each of the five remaining plenums was designed as a large box, using a factor of twenty between the plenum area and the area of the leakage feature. This scaling factor resulted in each microcircuit plenum having a minimum exit area of approximately 70 cm^2. In order to have a velocity inside a plenum of near zero, the depth of the plenums was designed to be ten times the entrance PVC pipe diameter. The depth scaling of the microcircuits resulted in each plenum having a depth of approximately 50 cm. Figure 3.15 shows the design drawing of one of the plenums to feed a microcircuit. The PVC piping was designed to attach to the side of the plenum instead of the bottom in an attempt to reduce any entrance velocity affects. It was feared that if the PVC was attached to the bottom of the plenums, the assumption of near zero velocity inside the plenums would no longer be valid. The featherseal plenum was designed similarly to the other four plenums, except in a rectangular shape instead of square. The featherseal plenum was designed with the area scaled up five times, resulting in an area of 90 cm^2 and the same depth of 50 cm.

Just as a flow control device was designed for the front and aft rim plenums, each of the five plenums fed by the compressor required a way to change the amount of flow into the plenum. Instead of the flow control device being designed within the plenums, the flow was designed to be controlled through valves placed within the PVC piping. Using commercially available valves for controlling the flow made the plenum construction easier and ensured accurate control over the flow. Unfortunately, since all five plenums were designed to be fed from a single compressor, by closing the valve to one of the plenums, the flow to the other four plenums was increased. This interaction between the five plenums made setting the proper flows to each plenum more complicated, but was the best design solution economically. Figure 3.16 shows a

schematic of the plenums and piping to each plenum underneath the platform. In Figure 3.16, the PVC piping for two of the plenums passes underneath the feather seal plenum. For reference, each of the plenums shown in Figure 3.16 correspond to the shaded areas in Figure 3.10.

The last step in the design of the platform was to determine the blade spacing and orientation to set the correct inlet angle to the test section. The blades were spaced correctly to ensure the correct pitch of 0.34 m, and inlet angle of 19.2°. Figure 3.17 shows a top view of a drawing of the platform with the blade locations clearly identified. Also included in Figure 3.17 are the locations for the for microcircuit pieces, including inlet and outlet slots, that were specified by Pratt & Whitney

3.4 Platform Construction

The first step in the platform construction was building the support frame out of 4.12 cm Unistrut channels. The support frame defines the total dimensions of the test stand and supports the platform surface. The overall dimensions of the support from are 2.51 m long, 1.3 m wide and 0.93 m high with 7.6 cm casters. After the support frame was constructed, a large box of medium density fiberboard (MDF) was built to contain all of the plenums. The exterior walls of the plenums feeding the front rim and aft rim are also the walls of the large containment box. The two slots that feed the front and aft rim were cut into the containment box, as previously shown in Figure 3.14. Each slot is 0.83 m long by 10.1 cm high. The bottom slot in feeds the aft rim, while the top slot feeds the front rim.

As mentioned in the previous section, the flow through each of the slots was controlled by sliding gate mechanisms. Figure 3.18 shows the sliding gate mechanism being installed in the plenum feeding the aft rim. The sliding gate mechanism was a 81.2 cm long, 8.2 cm high piece of 0.635 cm thick Lexan. Each Lexan piece had two rectangular squares, each 16.5 by 3.8 cm, cut out from the middle. Attached to the rear sliding piece were two threaded aluminum blocks used to open and close the gate. Also shown in Figure 3.18 are the side walls of the aft plenum that passes underneath the front rim plenum.

The front and aft rim plenums were built into the area defined by the containment box. Both plenums were constructed out of 1.3 cm MDF pieces, with the aft rim plenum passing underneath the front rim plenum. Refer to Figure 3.12 for a schematic of the aft plenum passing underneath the front rim plenum. The gap between the two plenums creates room for the other plenums to feed the microcircuits and featherseal. Detailed dimensions of the front and aft rims are shown in Appendix B.

The remaining five plenums built were all fed by the compressed air lines instead of the bottom passage of the tunnel. All of the remaining plenums were constructed with 1.3 cm thick MDF pieces. All four of the microcircuit plenums were of identical size to facilitate setting of the flows during testing. Figure 3.19 shows a picture of the five plenums: the front rim, the aft rim, the featherseal, a pressure side microcircuit plenum, and a suction side microcircuit plenum. The four microcircuit plenums and the featherseal plenum each had a 5.1 cm diameter hole cut in one side to connect the compressed air lines to the plenum. Figure 3.20 shows a side view of the 5.1 cm diameter hole in the side of the featherseal and suction side microcircuit plenums. The PVC was secured in each plenum using silicone to seal the connection. To prevent any leakages out of the tops of the plenums, each plenum was sanded to ensure a smooth fit with the bottom of the platform test section. Each plenum was also sealed on the inside with silicone to ensure they were air tight.

After the plenums were constructed, they were instrumented with thermocouples and pressure taps. All seven of the plenums had pressure taps placed both near the entrance to the plenum and near the platform surface. The pressure taps were the same style as the pressure taps used on the blade surface (0.8 mm metal tubing connected to 1.6 mm vinyl tubing). Appendix C lists the exact location of the pressure taps on all seven of the plenums. The pressure taps were installed flush with the interior sides of the plenums to measure static pressure; but since the plenums were designed to have a near zero velocity, the taps actually measured the total pressure inside the plenums. Each plenum also had type E thermocouples near the plenum entrance and near the platform region. Spherical thermocouple beads of approximately 1 mm were placed in each plenum protruding 1.3 cm into the plenum. The transmission and calibration of the thermocouples is discussed in section 3.9 of this chapter. The locations of the

thermocouples in each plenum is documented in Appendix C as well. The readings from the two thermocouples were averaged to provide an accurate measurement of the temperature inside the plenum during testing. The actual difference in temperature measurements between the two thermocouples in a single plenum was 0.3 ± 0.1° C. While the plenums were set so the coolant leakage flow temperature was identical in all the plenums, in actuality the average coolant temperature variation from plenum to plenum was 0.2 ± 0.1°C.

Once all of the plenums were built and instrumented, the PVC piping was connected from the plenums to the compressor. Figure 3.21 shows a picture of the seven finished, instrumented plenums with the PVC connections. A 5.1 cm PVC ball valve was attached to each of the individual lines to allow independent control over the flow entering each plenum. After the ball valve in the PVC lines, each of the lines were connected into the one line from the compressor tank. The 5 ball valves and joining of the 5 PVC pipes into one is shown in Figure 3.22. The one main line from the compressor has a 6.4 cm diameter venturi in the line to measure the total mass flow entering each of the five plenums. The use of this mass flow meter in setting the flows in each plenum is discussed in section 4.3 of the next chapter.

After the supporting structures under the platform were completed, construction of the hub region began. First, three parallelogram panels with a length of 64.7 cm and width of 33 cm were cut out of General Plastic 1.9 cm thick Elasta-foam, which has a thermal conductivity of 0.021 W/ m K. The parallelogram shapes were designed as previously shown in the drawing in Figure 3.17. Next, blade outlines were cut into the Elasta-foam so the blade fillet could be secured into the platform. Figure 3.23 shows one of the cut-out blade panels placed next to the featherseal plenum. The space needed for the front rim and aft rim gaps were cut out of the parallelogram panels first. The space required to place the microcircuit piece in the platform was cut out of each blade panel. The space needed for each microcircuit piece is shown in Figure 3.17 and also discussed in section 3.5 of this chapter. To attach each piece to the supporting plenums, both 6.4 mm thick window sealant and silicone were placed on the top surfaces of all the plenums. Each foam piece was painted black with X-O 19 flat black paint to reduce the errors in infrared thermography of the hub.

Although the locations for the other leakage features were cut out of the platform foam, the featherseal gap was not cut into the foam directly since the gap size of 0.46 mm is smaller than the thickness of most cutting tools. Instead, the featherseal gap was created by placing spacers between two of the blade panels to ensure the correct gap size. Precision metal strips, 0.46mm thick, were placed near the front, middle and end of the featherseal. Double sided 3M tape was applied to the edges of both panels next to the featherseal, however the non-adhesive tape was left on the exterior. The tape was used to ensure a smooth featherseal gap, as any imperfections in the foam would cause a significant effect in such a thin gap. The sides of two of the foam parallelograms were pushed together, with the metal strips insuring the correct gap thickness along the length of the featherseal. Once the foam pieces were secured with window sealant and silicone, the metal strips were removed from the featherseal. 20 measurements of the gap thickness along the featherseal with dial calipers showed the featherseal thickness to be 0.46 mm ±0.02 mm.

While the aft rim geometry was simply cut out of the panels, the front rim was assembled in two pieces. Recalling Figure 3.11, the backwards facing step piece at 17^{o} was cut as a single piece and glued at the correct angle to the existing platform. Then, the raised step section was attached above the backwards facing piece. The backwards facing front step pieces were painted with X-O 19 flat black paint.

3.5 Microcircuit Installation

The microcircuits were molded into the platform after the front rim was constructed. The microcircuits were manufactured at Pratt & Whitney using a stereo lithography (SLA) machine. In addition to the two microcircuits, molds for both designs were designed and fabricated at Pratt & Whitney. Figures 3.24a-b show the pressure side mold and suction side mold. The molds were designed so each microcircuit could be molded into foam to fit within the 1.9 cm thick foam panels described in the previous section. The foam used was manufactured by the Stepan Company and shipped to Virginia Tech's Experimental and Computational Convection Laboratory in two liquid parts. To obtain a uniform solid foam, equal volumes of part A (Stepanfoam AM-9451 polymeric diisocyanate) and part B (Stepanfoam RM-9137 polyol) were mixed. After

thoroughly mixing for thirty seconds, the mixture begins to exothermically expand rapidly. Previous studies (Couch [2003]) determined that 118 mL of part A mixed with 118 mL of part B yields 473 mL of foam. To form the microcircuit molds, each SLA part was placed in the mold and the foam was allowed to expand around the part within the mold.

In preparation for the molding process, the SLA microcircuits were fabricated at Pratt & Whitney with the entrance and exit slots sealed off to prevent foam from leaking into the passage. This additional SLA material, which protruded out of the foam mold at each microcircuit entrance and exit, was cut off with a rotary tool after the molding was complete. Since the foam has a tendency to bond to the mold and the microcircuit, all of the mold surfaces in contact with the foam were lined with Seal Fast Teflon coated fiberglass tape and then lightly covered with Dee-Rax resin mold release. Because the foam expands with a high pressure, four relief holes were drilled into each side of the microcircuit molds near the top. These holes allowed any excess foam to be pushed out of the mold and thus alleviate pressure inside the mold that could crush the microcircuits. To determine the volume of foam needed, the molds were filled with water to determine their volume. The volume of the pressure side microcircuit mold was measured to be 650 mL and the volume of the suction side mold was measured to be 1.18 L. Based upon the expansion of the foam and the volumes of the mold, 79 mL of parts A and B were mixed for the pressure side mold and 158 mL of parts A and B were mixed for the suction side mold. After the foam was poured into the molds, the top piece of the mold was attached and two cinderblocks were placed on top of the mold to force any internal pressure out the relief holes instead of pushing the top off. Though the initial expansion takes approximately ten minutes, the molds sat overnight before being opened. Figure 3.25 shows a picture of a molded pressure side microcircuit piece produced from the molding process. The top of the molded piece in Figure 3.25 has been cut away to show the microcircuit within the foam. Just as the blade cut-outs, these molded pieces were painted black with X-0 19 flat black paint.

As previously mentioned, the shape of the microcircuit molds were cut out of the foam platform sections. Each microcircuit piece was first attached to the supporting plenums using 0.64 cm window sealant and silicone. Once the silicone underneath the

mold had set, any gaps between the microcircuit mold and adjacent blade cut-out were filled with small amounts of the molding foam. Figure 3.26 shows a picture of the platform with one of the pressure side microcircuits installed and the area cut out for the second pressure side microcircuit. Once the foam between the mold and blade cut-outs dried, the whole platform section was sanded repeatedly to ensure a smooth surface. This process was repeated for the installation of each of the microcircuits. Figure 3.27 shows a finalized picture of the platform with all of the microcircuits installed. The backwards facing front step, aft rim and aft gutter are also shown in Figure 3.27.

3.6 Top Endwall Design and Construction

The top endwall was designed after the platform construction was completed. To take thermal data of the hub region, infrared images were taken from holes cut in the top of the platform test section. The design of the top plate was critical to the final hub construction since the location of the infrared camera ports in the top plate dictates the location of thermocouples and markers in the platform. Thermocouples and markers were needed in the platform to calibrate and orient the infrared images.

The first step in the design of the top plate was sizing of the holes required for the infrared camera. The infrared camera used in this research is a model P20 Flir Systems Thermacam infrared camera, shown in Figure 3.28. The diameter of the lens on the camera is 7.6 cm. A 10 cm diameter hole in the top endwall was determined to be the optimal size to allow slight adjustment of the camera but at the same time limit leakage out of the holes. The infrared camera could not take accurate pictures through the lexan top piece because the infrared wavelengths do not transmit through the lexan. To accurately take pictures of the hub region, the infrared camera needed to take pictures without any obstructions in front of the lens. To prevent ambient air from flowing into these view ports for the camera, covers were designed seal each view port when not in use. Covers for each of the four inch viewing holes were designed and built, as shown in Figure 3.29.

Once the hole size was determined, the viewing area of the camera had to be calculated. Each view port hole location was determined by the field of view of the

camera. The camera viewing angles of 20^o and 15^o were used to determine the size of a rectangular viewing area by using the equations:

$$\mathrm{HFOV} = 2\mathrm{L}\sin\left(10^o\right) \tag{3.3}$$

$$\mathrm{VFOV} = 2\mathrm{L}\sin\left(7.5^o\right) \tag{3.4}$$

where HFOV is the horizontal field of view, VFOV is the vertical field of view, and L is the distance from the platform to the camera lens. As dictated by the blade span, the camera lens was positioned 55 cm from the hub surface. From equations 3.3 and 3.4, the resulting viewing area was 19 cm by 14.5 cm. The infrared camera records each picture as a 240 x 320 pixel image, with a temperature value assigned to each pixel. This image size results in a resolution of 278 pixels/ cm^2. In other words, each pixel represents a temperature reading on a 0.6 mm by 0.6 mm area.

Once the viewing area was established, the location of each of the viewing holes was determined. Using the drawing of the platform, correctly sized rectangles were drawn to match the viewing plane of the infrared camera. Each rectangle was placed on the platform drawing to determine the camera view port locations. When placing each rectangle, they were slightly overlapped to allow for any camera movement. Slight overlap of the viewing areas also facilitated orientation of the images (see Section 4.4) Figure 3.30 shows a top drawing of the platform, with each of the camera field of view locations marked. The view port hole in the top plate was cut at the center point of each of the field of view locations. Based upon the locations of the view ports from the drawing, the holes were cut in the top plate at Worley Machine Company in Floyd, Virginia. Figure 3.31 shows a view of the top plate with the holes cut for the infrared images. The locations of the view ports cut in the top plate are given in Appendix D.

After the locations of the view ports was determined, the platform was instrumented with markers. Since each picture was combined into one large picture, the location and orientation of each picture had to be determined using markers. To orient the pictures, metallic markers were placed in the platform section. For each viewing area of the camera, two markers were placed in the platform. The markers were metallic circular tubing with an outside diameter of 1.3 mm. Two markers were needed in each viewing area to define the orientation of each picture. By overlapping the viewing area, one marker was used for two different viewing areas, which both reduces the number of

markers in the platform and made it easier to align the pictures with identical reference points. Figure 3.32 shows a top view drawing of the platform with the markers indicated in each camera viewing plane.

Just as markers were needed in the platform to align the pictures, thermocouples were needed in the platform to calibrate the infrared images. Although the infrared camera can accurately capture temperature variations, the camera can not accurately measure temperature directly without proper calibration. To have accurate measurements of temperatures and temperature variations, thermocouple readings were used to calibrate each image. The calibration of infrared images is further explained in Section 4.4. Type E thermocouples were embedded in the surface of the platform in locations also shown in Figure 3.32. In Figure 3.32, the thermocouples are shown with squares and the markers are shown with circles. Just like the markers, an attempt was made to put thermocouples in the overlapping viewing areas to reduce the number of thermocouples and aid in the accuracy of image calibration. A table of the X and Y locations of each thermocouple and marker is shown Appendix E. To install the thermocouples, a 1.6 mm drill bit was used to dill holes through the platform. The thermocouples were inserted from underneath the platform and then sealed with silicone to prevent any leakage around the thermocouples.

Because the expected boundary layer on the platform was very thin, any surface defects would cause disturbances in the boundary layer and result in incorrect measurements. After the platform was sanded, there were several sections of the platform where air trapped during the microcircuit molding created air bubbles approximately 2-4 mm in diameter on the platform surface. Even though the air bubble cavities are relatively small, their size was significant enough to cause disturbances in the boundary layer. These small cavities were filled with Squadron molding putty, which had a very similar thermal conductivity (0.03 W / m K) to that of the foam platform.

In addition to markers and thermocouples on the platform surface, pressure taps were needed for calculations of the mass flow out of each of the plenums. To calculate the mass flow for a particular leakage feature, measurement of the pressure drop from the plenum to the platform was required. To measure this pressure drop, pressure taps identical to those used in the blades were installed in the hub region downstream of each leakage feature. The pressure taps were installed 2 mm downstream of each leakage

feature to accurately capture the static exit pressure on the hub that the feature was discharging into. Since the front rim and featherseal would experience different platform pressures across their length, three pressure taps were used for each of these leakages. Two pressure taps were used at the exit of each microcircuit. The methodology for determining the discharge coefficient using these pressure taps is described in section 4.3.

Finally, each of the constructed blades were installed in the platform. Since the blade area had already been cut out in the platform panels, the blades were simply glued into these cutout panels. Figure 3.33 shows the finished platform with one of the blades installed in the platform. Before discussing the specific flow setting devices on the test section, it is important to understand the facilities the test rig was designed for.

3.7 Wind Tunnel Facilities

The test section described in the previous sections was tested in a large scale, low speed wind tunnel as shown in Figure 3.34. The air was pushed through the wind tunnel by a 50 hp, 0-60 hertz Joy Technologies axial fan. As shown in Figure 3.34, air exiting the fan was cooled by the primary heat exchanger, which used water cooled by a 38 kW chiller. A description of the fan, chiller and heat exchanger settings used during testing is given in section 4.2. After the primary heat exchanger, the flow split into three passages. A perforated plate with an open area of 0.27 m^2 was placed over the center passage to create a pressure drop and force the flow into all three passages.

In the center passage, the flow was heated by a 55 kW heater bank, which consisted of three sections that could be independently controlled. The upper and lower passages were cooled by secondary heat exchangers that were fed by the same chiller as the main heat exchanger. The cooling of the lower passage was of special interest since the flow from the lower section of the wind tunnel was used as the leakage flow feeding the front rim and aft rim of the test section. The settings and controls used for the secondary heat exchangers are discussed in section 4.2. In addition to supplying coolant to the test section, the split in the wind tunnel provides the necessary flows to feed the combustion simulator. The combustor simulator models the film and injection cooling schemes common to actual gas turbine engines. The cooler flow from the outside two passages is reintroduced into the main, hotter, passage flow. The design and

benchmarking of the combustor simulator are presented in Barringer [2002]. Although the cooling within the combustor section was not analyzed in this study, the turbulence generated within the combustor was required to accurately match the inlet turbulence to the turbine blades.

For these experiments, flow from both the top and bottom passages was injected into the passage through six 8.5 cm diameter dilution holes. The holes were spaced 25.4 cm from the side walls of the combustor simulator and the middle hole was spaced 30.4 cm from the other two holes. The dilution holes on the top of the combustion simulator were spaced identically to those on the bottom. All six of these holes were 2.4 chord lengths upstream of the test section inlet. The center combustion holes were located in the center of the tunnel directly upstream of the middle passage in the test section. The setting of each of the flows from the dilution holes and the measurement of the resulting turbulence is described in section 4.2.

Towards the exit of the combustor simulator, the height of the test section contracted at an angle of 15.4° from 72.6 cm to 55.4 cm while maintaining the same width of 1.1 m. The test rig used in this research was attached to the exit of the combustor simulator, completing the closed loop of the wind tunnel. Thus, the entrance area to the test rig was 55.4 cm by 110 cm. Since the thermal measurements were along the floor of the test rig, a smooth transition between the wind tunnel and test rig was important to achieve accurate results. To smoothly transition the decrease in area, a 1.6 mm thick piece of Formica was used to connect the platform section to the angled wind tunnel exit. The Formica was thin enough to bend into a smooth transition but rigid enough to not move during testing.

In addition to the wind tunnel facilities, external compressors were used to supply the necessary coolant flow. A tank located at the Virginia Tech Power Plant provided compressed air at a supply pressure of 551 kPa. The average temperature of this compressed air was 21^{o} C. The temperature of the compressed air was dictated by ambient temperature and thus the temperature could not be adjusted during testing. Instead, the temperature of the coolant supplied by the tunnel was matched to the temperature of the compressed air. The settings used to match these temperatures are discussed in section 4.4. The compressed air was supplied to the Virginia Tech

Experimental and Computational Laboratory through 5.1 cm PVC piping. To measure the amount of compressed air, a model CV-150 6.3 cm diameter venturi from Lambda Square Incorporated was installed within the PVC lines. To ensure accurate pressure measurements within the venturi, the diameter of the PVC piping was kept constant for a length of 38 cm upstream and downstream of the venturi. Figure 3.35 shows a picture of the venturi and PVC piping above the wind tunnel that supplied coolant flow to the five plenums. A 0-2.49 kPa transducer displayed the pressure drop across the venturi. Lambda Square provided a table of flow and the resulting pressure drop across the transducer. Table 3.3 shows the data from Lambda Square for the model CV-150 venturi, which gives the flow in ft^3/min (CFM) and the resulting pressure drop across the venturi in inches of water pressure. Since the density of the coolant was calculated from the temperature and pressure of the fluid, the mass flow, in kg/s, could be calculated from the flow parameters given in Table 3.3. The resulting correlation for mass flow through the venturi based upon the pressure drop was:

$$\dot{m} = \left(-2x10^{-5}\right)(\Delta P)^6 + \left(4x10^{-4}\right)(\Delta P)^5 - \left(3.5x10^{-3}\right)(\Delta P)^4 + 0.014(\Delta P)^3 - 0.029(\Delta P)^2 + 0.037(\Delta P) \quad (3.5)$$

where m is the mass flow in kg/s, and ΔP is the measured pressure drop across the venturi in inches of water. Figure 3.36 shows a plot of the resulting equation (3.4) against the data points provided by Lambda Square.

The venturi was benchmarked against a Merian model 50MC2-2 laminar flow element (LFE) to ensure the accuracy of the venturi. The venturi was used for mass flow measurement instead of the LFE because the laminar flow element causes a pressure drop three times higher than the venturi. If the laminar flow element was used during testing, there would not be enough supply pressure to feed all of the leakage features. To benchmark the venturi, both the venturi and the laminar flow element were connected in the same PVC piping. Figure 3.37 shows the percent difference in measured mass flow between the laminar flow element and the venturi. From the data shown in Figure 3.37, the venturi and laminar flow element both measure the same volumetric flow within less than 1.0% error for high flows. However, as the flowrate is decreased, the discrepancy between the two readings increases. Since the laminar flow element has a higher accuracy, it was determined from the data in Figure 3.37 that the venturi does not

accurately measure the flows at conditions less than 55 CFM (26 L/s). Thus, the venturi was used during testing only when the coolant flow was higher than 60 CFM (28.3 L/s). For the lower flow conditions, which occurred during benchmarking of the plenums, the laminar flow element was used to measure the mass flow. A description of the benchmarking process of each of the plenums using the laminar flow element is given in section 4.3.

3.8 Additional Test Rig Features

As previously mentioned, the test section was designed to be a four blade, three passage rig. Figure 3.38 shows a picture of the completed test section looking downstream from the exit of the combustor simulator. After the hub section was constructed, the side and rear walls were built. The main purpose of these walls was to ensure the periodicity of the flow around the blades. To control the pressure distribution around the blades, side bleed gates and flexible walls were constructed. Figure 3.39 shows a top view schematic of the test section that highlights the three blade passages, the inlet angle and some of the combustor simulator geometry. The upper two passages in section 3.39 were used for data collection, with the instrumented blade indicated.

The side bleed gates allow control over the amount of flow passing though the blade test section. There are side bleed gates on both sides of the test section entrance. Figure 3.40a shows the side bleed gate in the open position, and Figure 3.40b shows the same gate in a closed position. By opening the gates, more flow passes around the test section than through the test section, altering the velocity and thus changing the pressure distribution around the blades. In addition to pressure changes, by opening and closing the side bleed gates, the location of the stagnation point of the flow on the blades can be moved. The location of the side bleed gates is also shown in the top view schematic in Figure 3.39.

While the side bleed gates have a slight affect on the pressure distribution around the blades, the adjustable rear walls have the largest effect on the pressure distribution. The adjustable walls were designed to follow the contour of the blades to ensure periodic conditions within the test section. The rear flexible wall is made of two 0.32 cm thick Lexan pieces. Figure 3.41 shows a view from the exit of the test section looking back

upstream. The two Lexan pieces are connected with rubber padding to allow for maximum mobility. By pushing these flexible walls into and out of the flow path, the area is changed and thus the velocity and pressure distribution. To push the walls, a device known as a flexible wall adjust mechanism (FWAM), was installed on both walls. As described in Couch [2003], multiple FWAMS are placed on the flexible wall to allow more contouring of the wall. Figure 3.42 shows a view from the outside of the test section of the FWAMs attached to the flexible rear wall. Additionally shown in Figure 3.42 are the access covers on the exterior of the test section. These two panels allowed access to the FWAMs if they needed to be repaired during testing.

3.9 Instrumentation and Uncertainty

As previously mentioned, numerous pressure and temperature measurements were taken throughout the test section. To record all of the pressure measurements, all of the pressure taps were connected to a Scanivalve VINL-063 wafer through 1.6 mm vinyl tubing. The wafer, shown in Figure 3.43, allows different pressure channels to be read simple by switching a knob. Three scanivalve wafers, each with 24 outputs, were used for the pressure measurements. The outputs from the scanivalve wafers were connected to the Omega pressure transducers. Each of the transducers converted the input pressure into a digital signal in voltage that was recorded in LabView. All of the pressure transducers expressed the measured pressure in a 0-5 volt range. Table 3-4 lists each of the pressure transducers used in this study with their ranges and serial numbers. Each of the pressure transducers required a high and low pressure input to record a pressure difference. For the pressure around the blade, the stagnation point pressure was used as the reference high pressure. The pressure inside each plenum was measured in two ways, both against atmospheric pressure and against the static pressure at the hub region near the exit of that particular plenum. The methodology of using the plenum pressures to calculate a discharge coefficient is discussed in section 4.3.

Voltage signals from both the pressure transducers and type E thermocouples were processed by a National Instruments SCXI-1100 data acquisition board, which was set to read a 0-10 volt analog input. The data acquisition board was connected to the computer 12 bit analog to digital (A/D) board, which were then displayed on the National

Instruments LabView software. The LabView software was set to sample 5,140 data points at a rate of 1,028 scans per second with a gain of 1.

The infrared camera used in this research is a model P20 Flir Systems Thermacam infrared camera, as previously shown in Figure 3.28. The infrared camera measured the total radiation heat flux from the hub surface, from which the temperature can be calculated by knowing the background temperature and emissivity. Each of the images were calibrated, using ThermaCam Researcher software, by adjusting the emissivity and background temperature until the temperature measured by the infrared camera matched the temperature measured by the thermocouples in the hub. Five images were taken at each location, and after each image was calibrated individually, the five images were averaged into one image to reduce the uncertainty of the infrared measurements. The image calibration and alignment is discussed further in Section 4.4.

The scan rates chosen for both the pressure and temperature measurements helped reduce the uncertainty of each of the measurements. For the pressure measurements, the total uncertainty was calculated to be 7.5% of the high pressures and 7.6% of the low pressures. For the temperature measurements, all of the thermocouples were calibrated in an ice bath to have an uncertainty of 0.2 degrees, which is 0.4% of the mainstream temperature measurement and 0.95% of the coolant measurement. This uncertainty in the temperature measurement yields an uncertainty in the non-dimensional temperature measurements (eta) of 0.03, which is 2.6% of a high value (1.0) and 12.5% of the low values (0.2). The inlet turbulence intensity uncertainty was 1.8%. The uncertainty in the density calculation, which depended on temperature and pressure measurements, was 0.016 kg/m^3, or 1.5% of the density of 1.1 kg/m^3. The velocity uncertainty, which depended on pressure and density uncertainties, was 0.63 m/s, which was 6.1% of the low values (10.3 m/s) and 1.8% of the high values (35 m/s). The mass flow uncertainty, which depended on the velocity and density uncertainties, was 0.0042 kg/s, which was 10.1% of the low values (0.041 kg/s), and 8.6% of the high values (0.048 kg/s). The detailed calculations for each of these uncertainties are shown in Appendix F.

Table 3.1 Summary of Cooling Flow from Each Geometric Feature

	Engine coolant mass flow	Engine Area	Test coolant mass flux	Test Area	Test coolant mass flow as a percent of total inlet mass flow	Coolant Range Tested
	m_{ce}	A_{ce}	$\rho_{ct}U_{ct}$	A_{ct}	m_{ct}/m_{total}	m_{ct}/m_{total}
	kg/s	cm^2	kg/m^2 s	cm^2	%	%
Pressure Side Microcircuit	0.0023	0.026	0.0279	3.1	0.27	0.0-0.5
Suction Side Microcircuit	0.0002	0.026	0.0021	3.3	0.21	0.0-0.5
Featherseal	0.0030	0.019	0.0477	2.5	0.37	0.25-0.75
Front Rim	0.0148	0.677	0.0068	81.8	1.71	0.75-2.5
Aft Rim	0.0159	0.684	0.0072	83.1	1.85	1.5

Table 3.2 Blade Parameters used in the Experimental Testing

Blade Parameter	Symbol	Value
Scaling Factor	Xt/Xe	11
Inlet Angle	Θ	19.2°
Blade Angle	Φ	20°
Axial Chord	Bx	0.43m
True Chord	C	0.45m
Pitch	P	0.34m
Span	S	0.55m

Table 3.3 Dimensions of Leakage Flow Geometries

	Length	Thickness
	cm	cm
Front Rim	35	2.4
Aft Rim	35	2.4
Feather Seal	73	0.046
Front Gutter	6.3	0.28
Aft Gutter	11.4	0.28

Table 3.4 Dimensions of Microcircuit Geometries as supplied by Pratt & Whitney

	Length	Internal Width	Internal Features	Exit length	Exit width
	(cm)	(mm)		(mm)	(mm)
Pressure Side	17.8	5.5	2 passages	51	6.4
Suction Side	43.8	5.5	31 pedistals	57	6.4

Table 3.5 Table of Flow and the Resulting Pressure Drop across the Venturi (supplied by the Lambda Square company)

Flow	Pressure Drop
cubic ft/min	inches H2O
0	0.0000
5	0.0158
10	0.0631
15	0.1419
20	0.2523
25	0.3942
30	0.5676
35	0.7726
40	1.0091
45	1.2772
50	1.5768
55	1.9079
60	2.2705
65	2.6647
70	3.0904
75	3.5477
80	4.0365
85	4.5568
90	5.1087
95	5.6921
100	6.3070

Table 3.6 Values for Pressure Transducers

Transducer	Manufacturer	Serial #	Range (Pa)	Range (in H20)
1	Omega	605181167	0-125	0-0.5
2	Setra	17536379	0-1245	0-5.0
3	Setra	1753678	0-623	0-2.5
4	Setra	1083664	0-125	0-0.5
5	Meriam	779780-P2	0-4980	0-20.0

Figure 3.1 Side view of 1st stage gas turbine blade showing the curvature of the hub region typical to most blades.

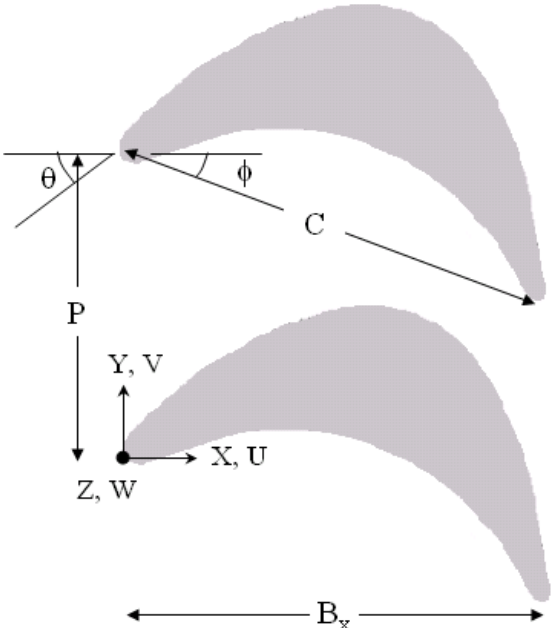

Figure 3.2 Blade geometry redefined by Pratt & Whitney, showing some of the important blade features such as the pitch, chord, and entrance angle.

Figure 3.3 Picture of individual foam pieces as they are assembled into the final blade by using both glue and metal rods for strength.

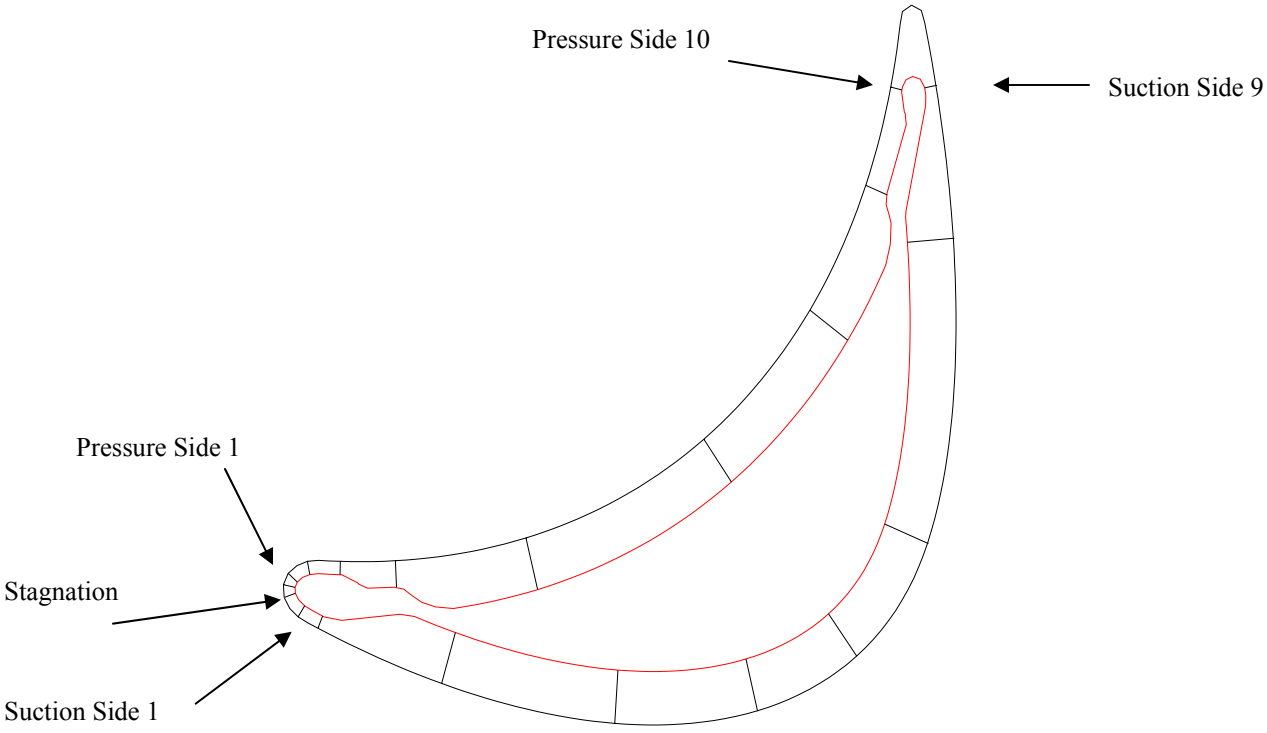

Figure 3.4 Picture showing the location of the pressure taps around the pressure side and suction side of the blade (indicated by the lines in the thickness of the blade).

Figure 3.5 Picture showing the assembled foam pieces coated with black Teflon® film to provide a smooth surface, attached to the LSA fillet.

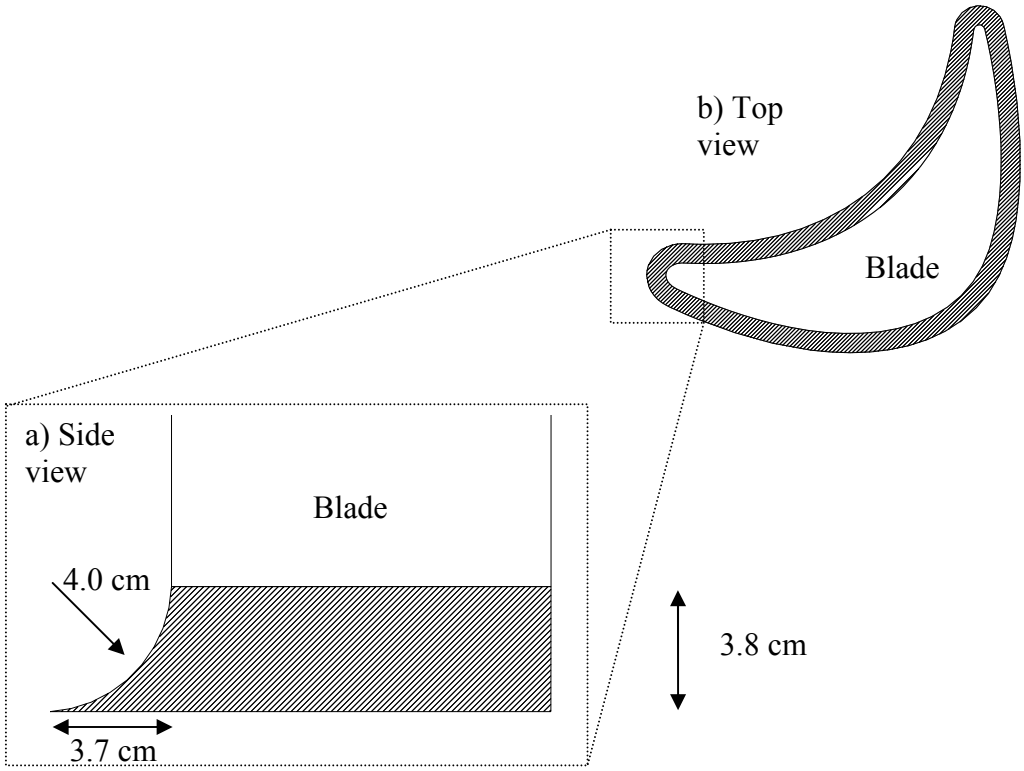

Figure 3.6a,b Drawing of a) side view and b)top view of blade with the fillet around the perimeter of the blade shaded.

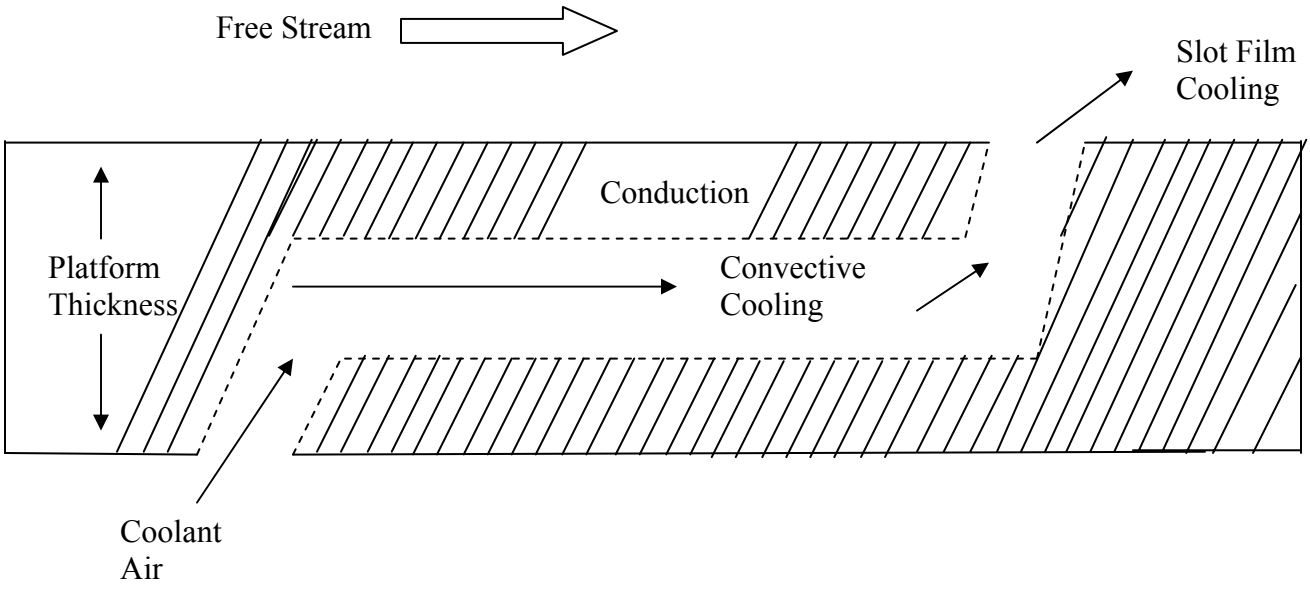

Figure 3.7 Schematic of cooling benefits of microcircuits: internal convective cooling, conduction cooling and exit slot film cooling.

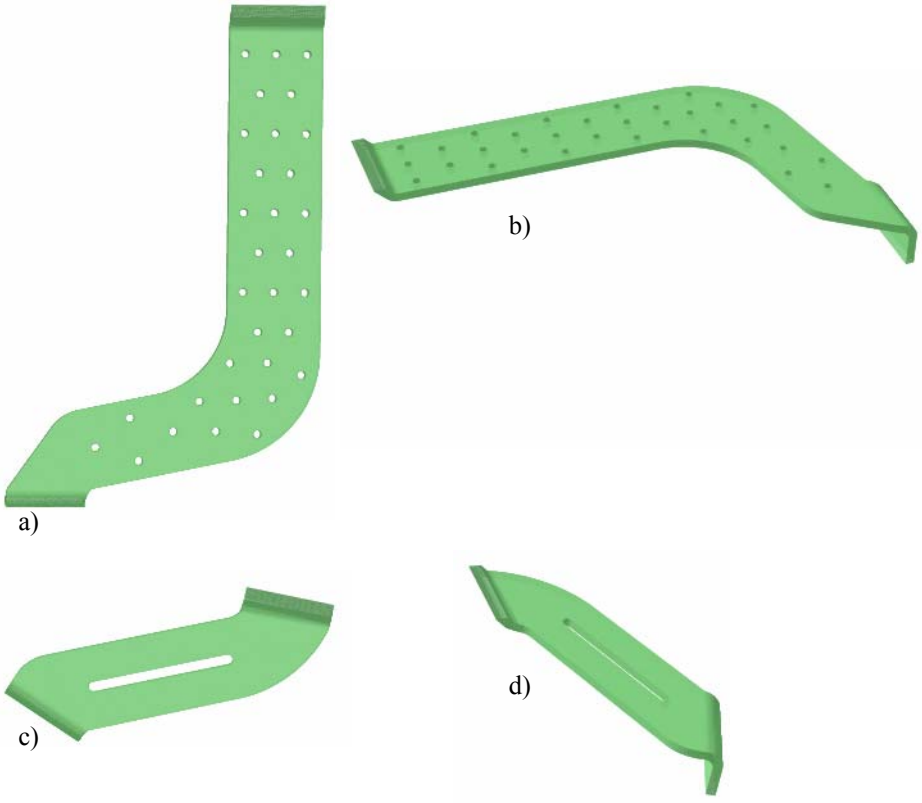

Figure 3.8 The platform microcircuits from the a) top view, and b) isometric view of the suction side microcircuit and c)top view, d) isometric view of the pressure side microcircuit.

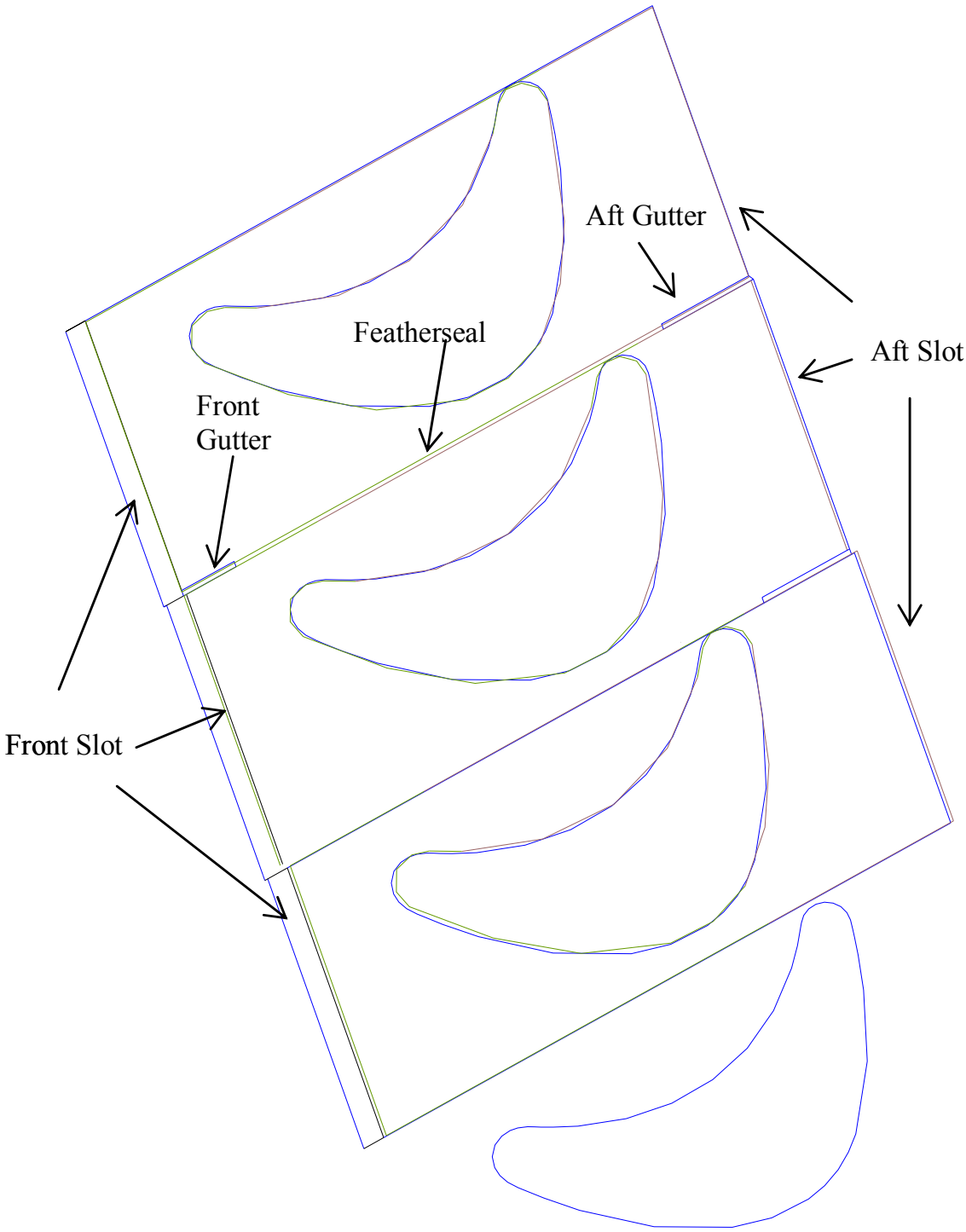

Figure 3.9a Schematic showing the front rim, front gutter, feather seal, aft gutter, and aft rim.

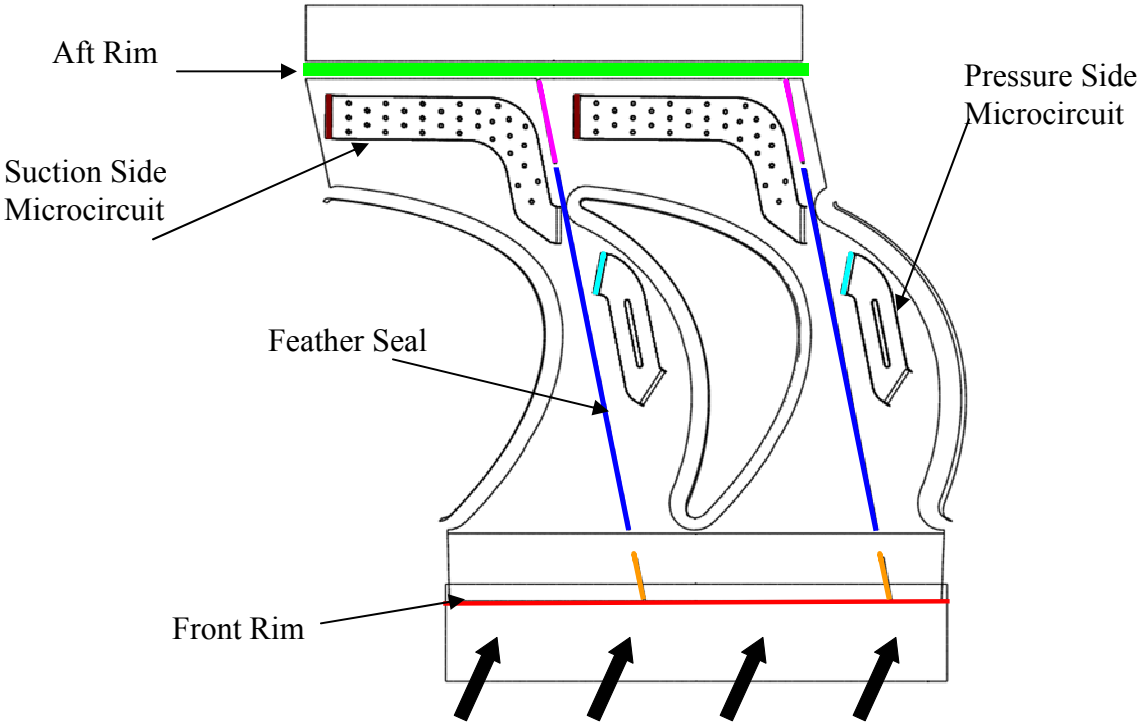

Figure 3.9b Schematic of the main leakage features modeled in this study, including the locations of the pressure side and suction side microcircuits.

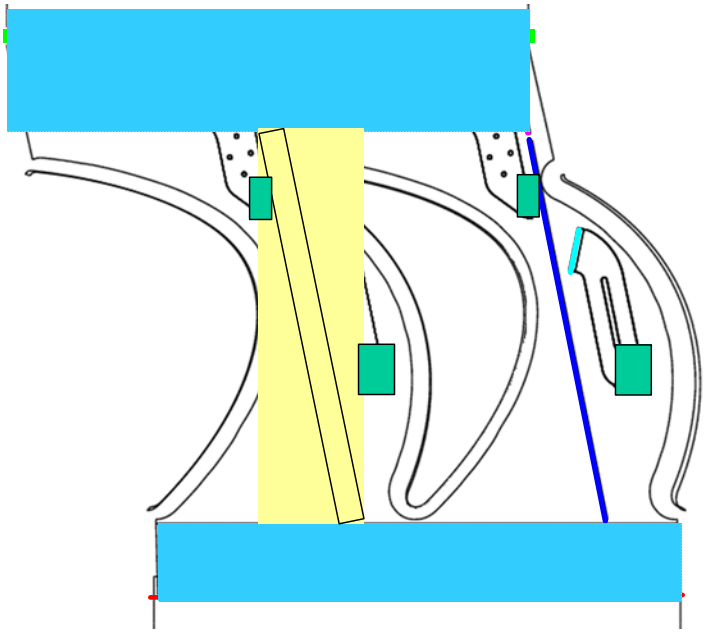

Figure 3.10 Schematic of platform showing the front and aft rim plenums (blue), the four microcircuit plenums (green), and the feather seal plenum (yellow).

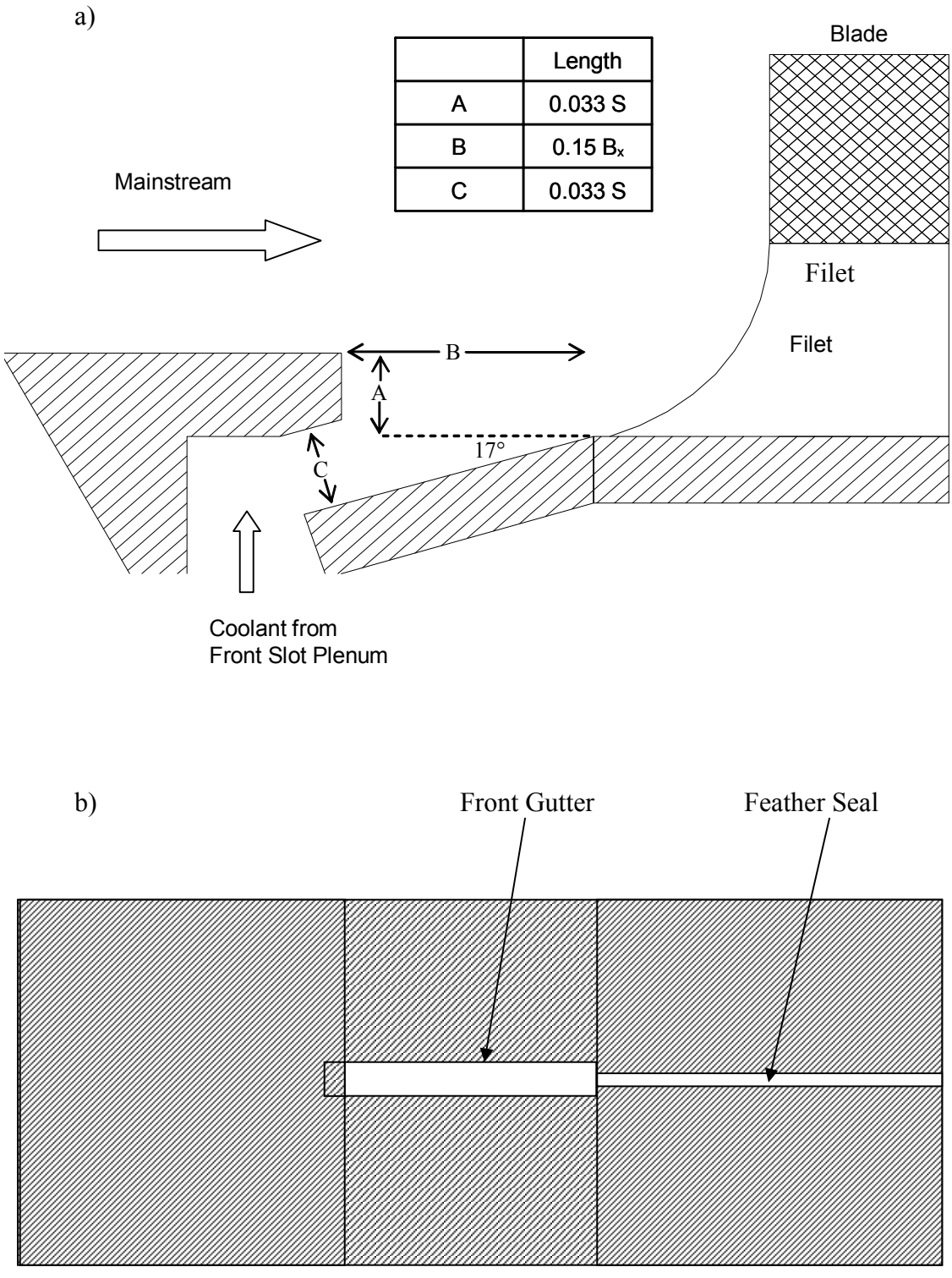

Figure 3.11a Drawing of a)side and b)top view of backwards facing front step leakage geometry for the front rim, showing the front gutter slot cut into the step.

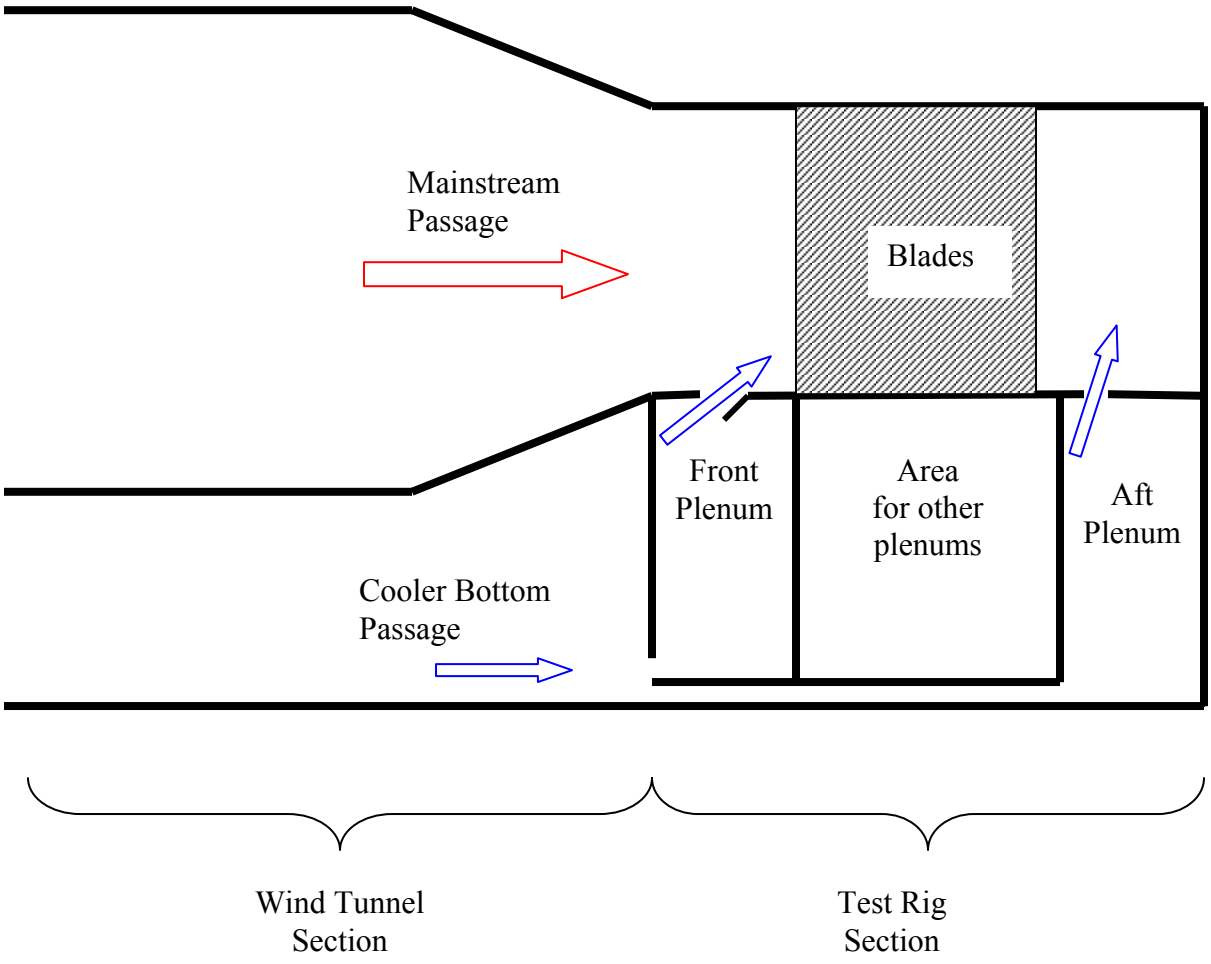

Figure 3.12 Figure showing a side view illustrating the front rim and aft rim being fed from the secondary passage within the wind tunnel.

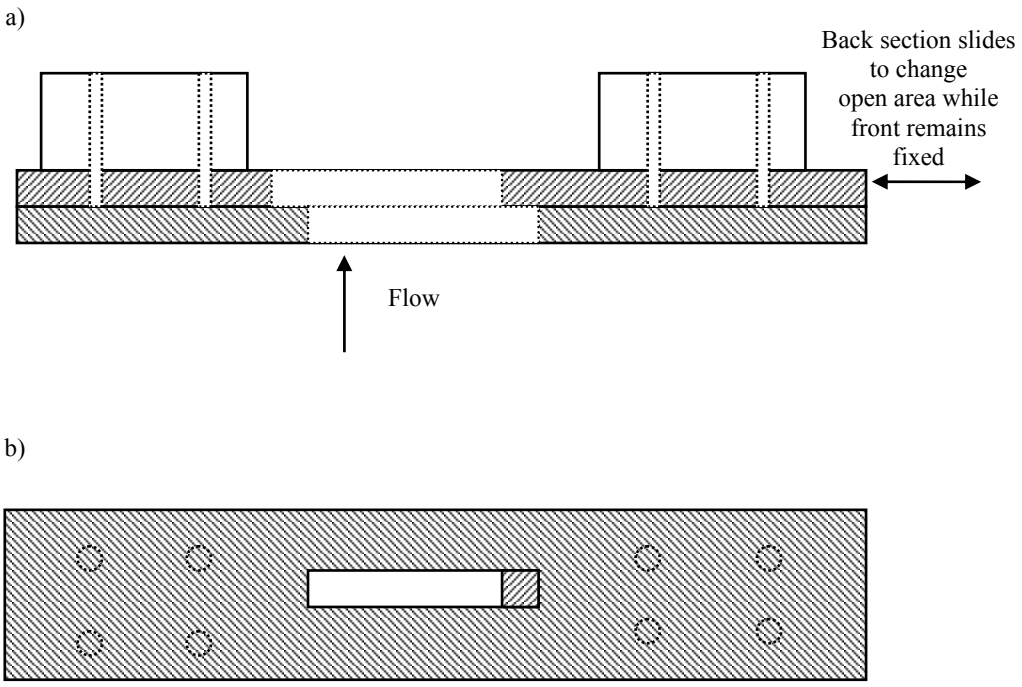

Figure 3.13 Drawing of a) top and b) front view of sliding gate, where the front section is fixed while the back section slides to change the inlet area.

Figure 3.14 Picture of front of test section, showing the two slots that feed the front and aft rim plenums from the wind tunnel.

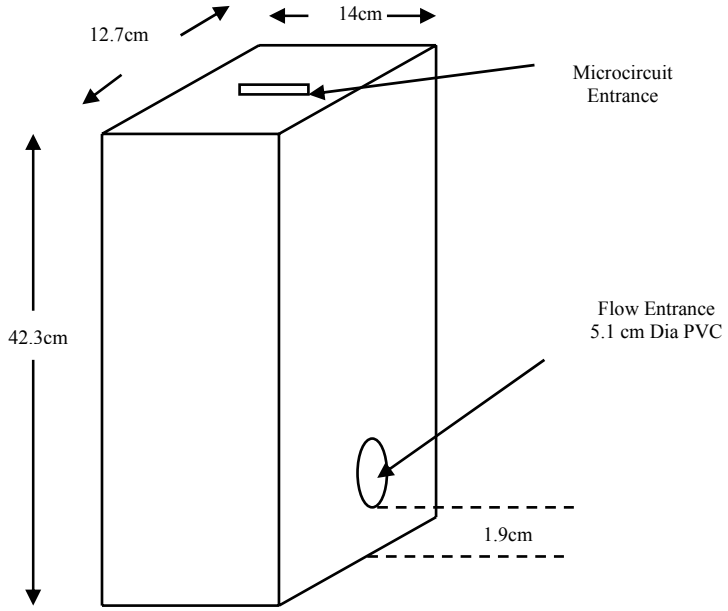

Figure 3.15 Drawing of the plenums that feed the microcircuit, showing the piping entrance and location of microcircuit entrance, centered over the plenum.

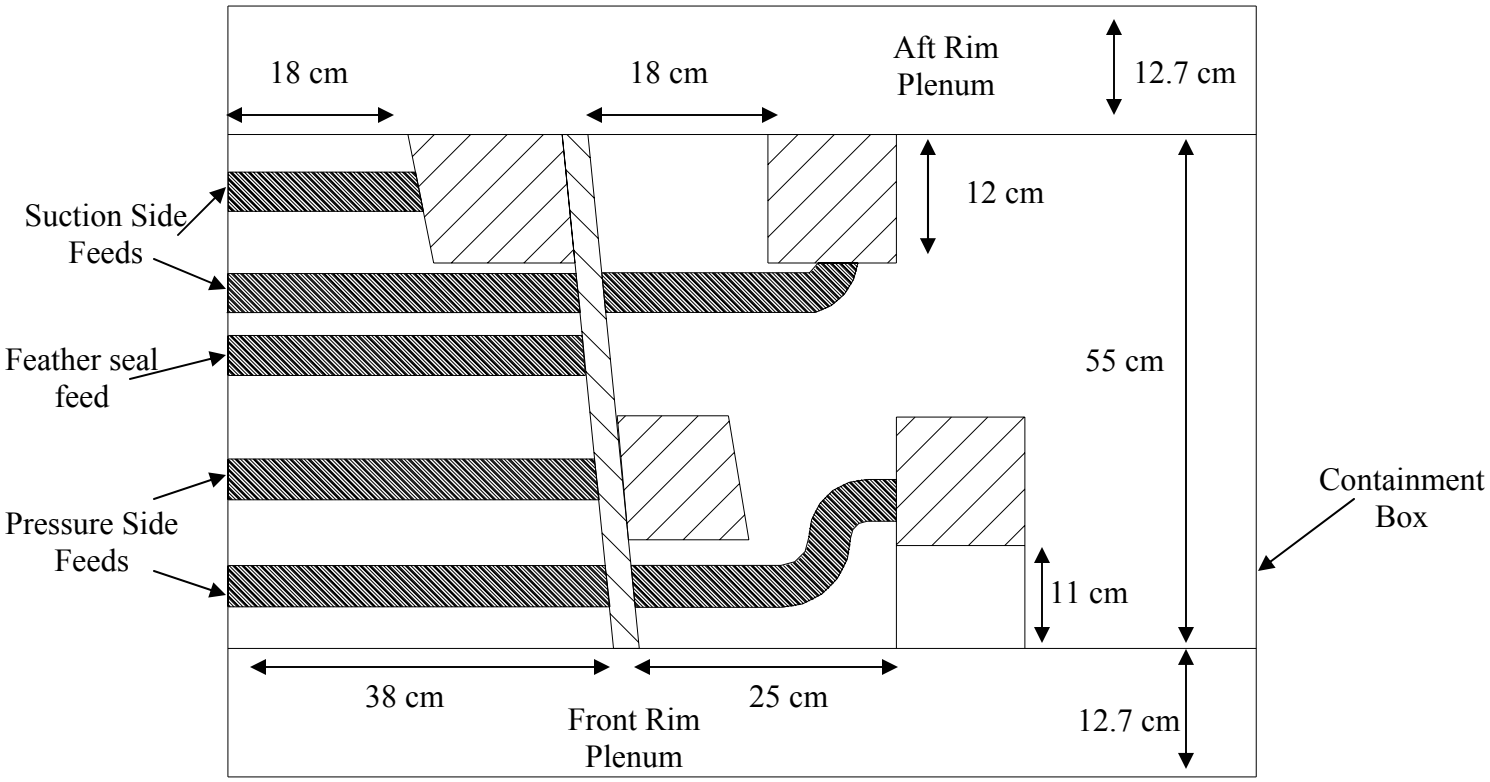

Figure 3.16 Top view drawing showing the five internal plenums (shown hatched),and the PVC piping connections underneath the platform.

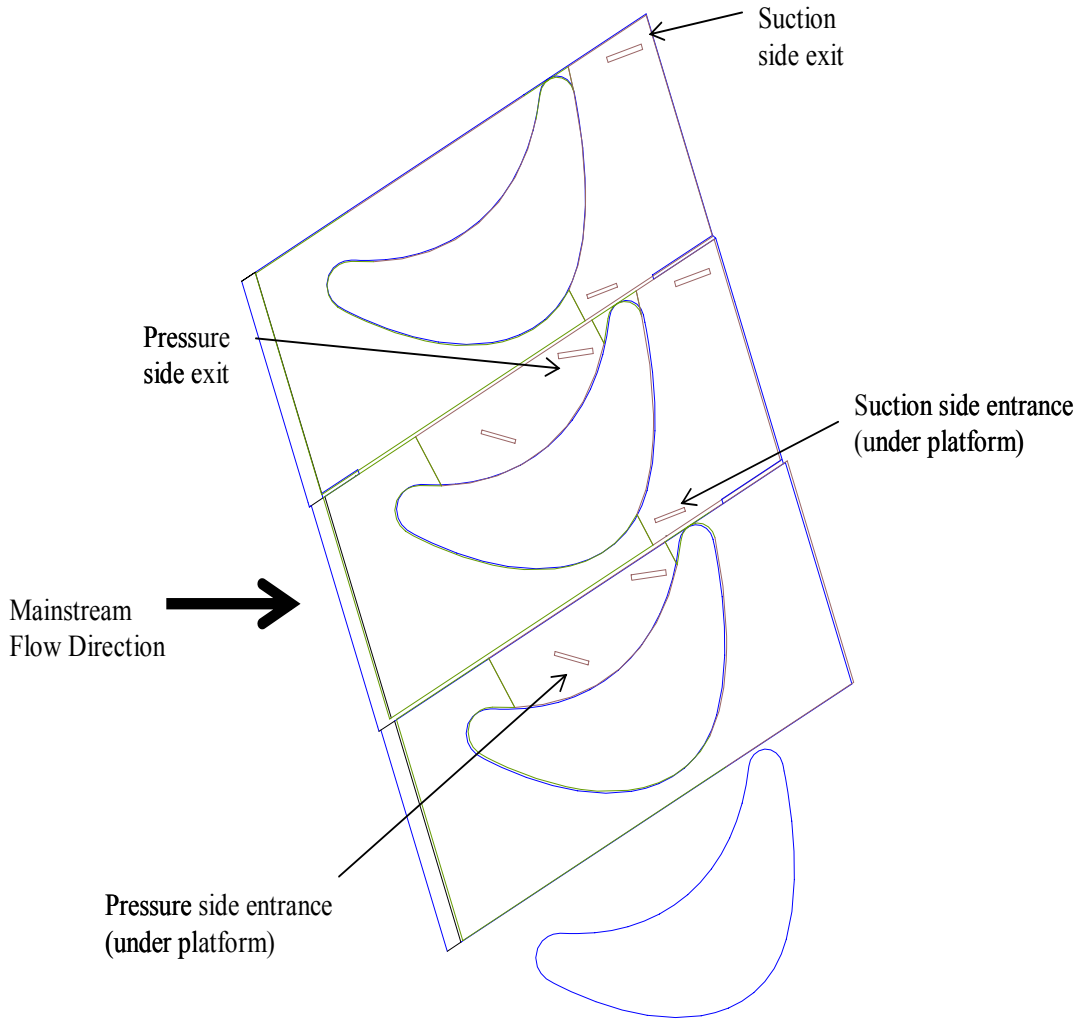

Figure 3.17 Drawing of the top view of platform, showing the three parallelogram panels and the inlet and exit locations of the microcircuits.

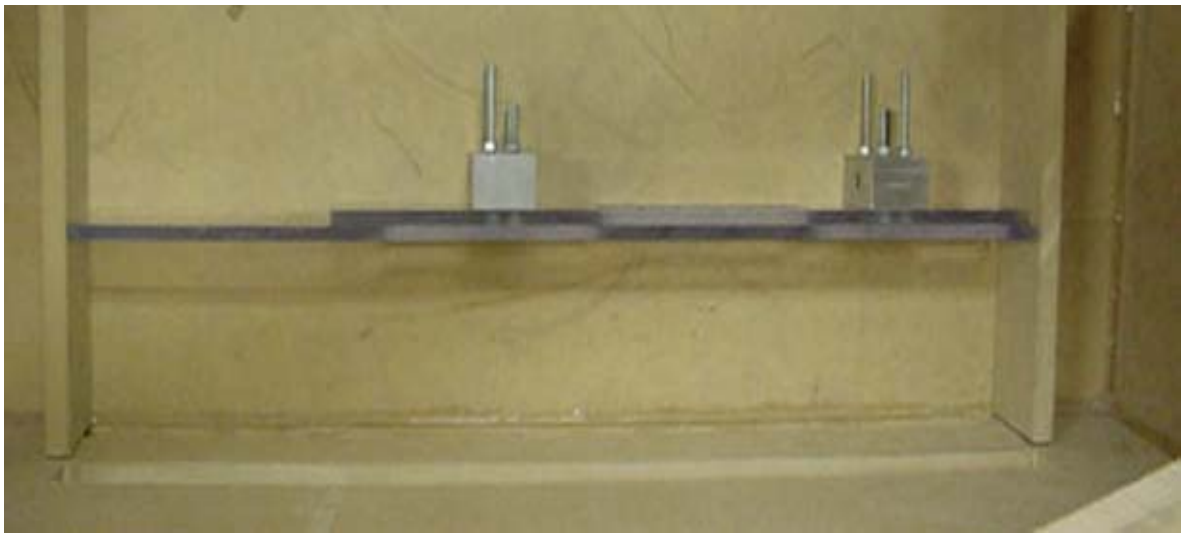

Figure 3.18 Top view of the sliding gate mechanism being installed in the plenum for the aft rim, the rod to move the blocks has not been attached in this picture.

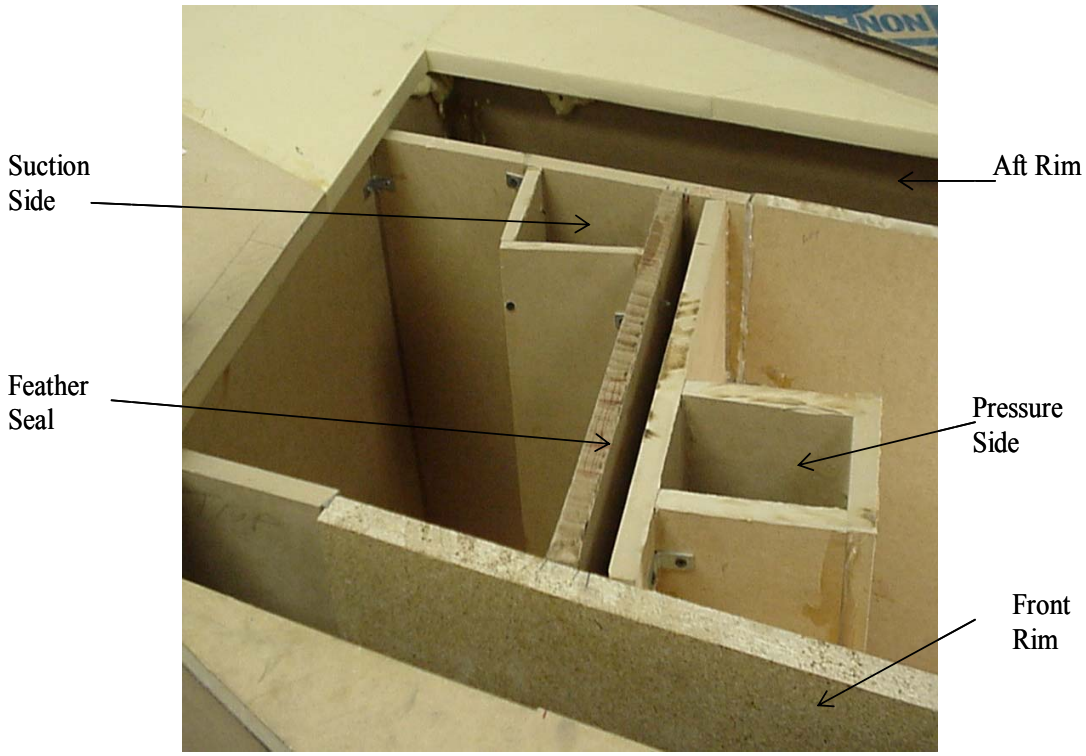

Figure 3.19 Picture of front rim, aft rim, featherseal, pressure side microcircuit and suction side microcircuit plenums.

Figure 3.20 Side view of featherseal and suction side microcircuit plenum, showing 2" holes for the coolant flow though 2" PVC pipes.

Figure 3.21 Picture of seven plenums after installing all the PVC piping, thermocouples and pressure taps.

Figure 3.22 Picture of five PVC valves for each of the plenums fed by one compressed air line.

Figure 3.23 Picture of foam blade cut-out on top of the plenums, showing half of the feather seal gap, and the pressure side microcircuit plenum.

a)

b)

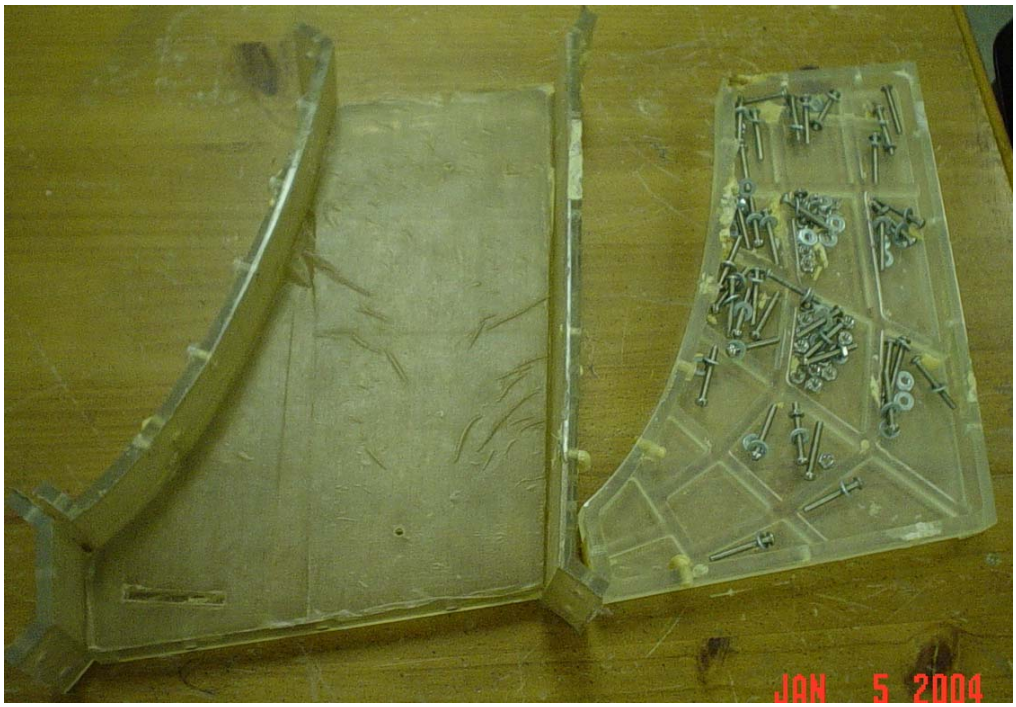

Figure 3.24 Pictures of the molds for the a) pressure side microcircuit and b) suction side microcircuit provided by Pratt & Whitney.

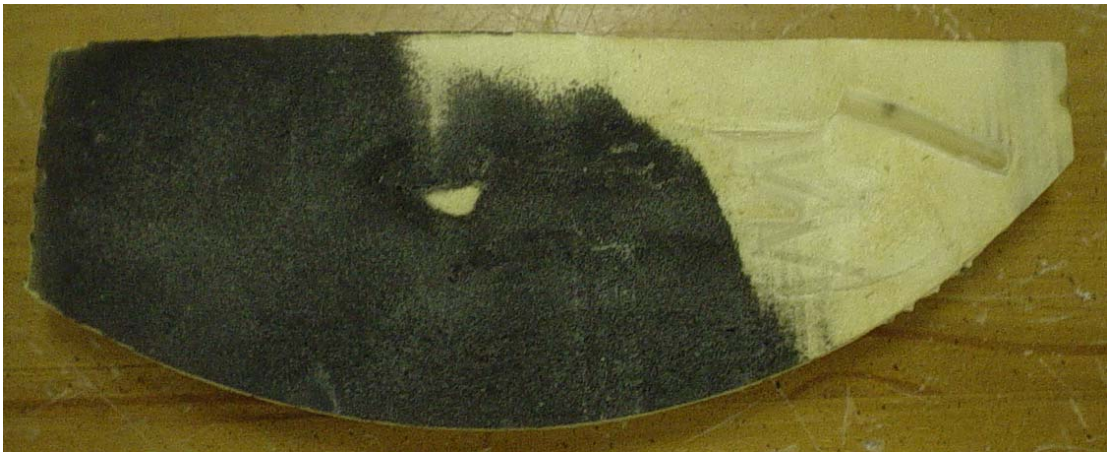

Figure 3.25 Pictures of the resulting mold of the pressure side microcircuit, the right side has been sanded to show the microcircuit within the foam.

Figure 3.26 Picture of platform during installation of molded microcircuits, one pressure side microcircuit has been installed and the area for the second is visible.

Figure 3.27 Picture of finished platform section, showing installed microcircuits and the backwards facing front step.

Figure 3.28 Picture of ThermalCam® infrared camera used to collect hub temperature data.

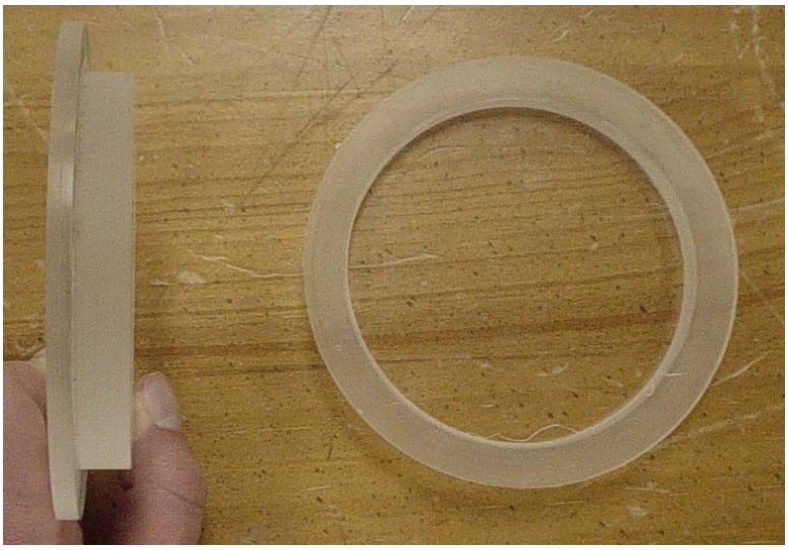

Figure 3.29 Top and side views of the machined ports to cover each of the infrared camera holes in the top plate of the test section.

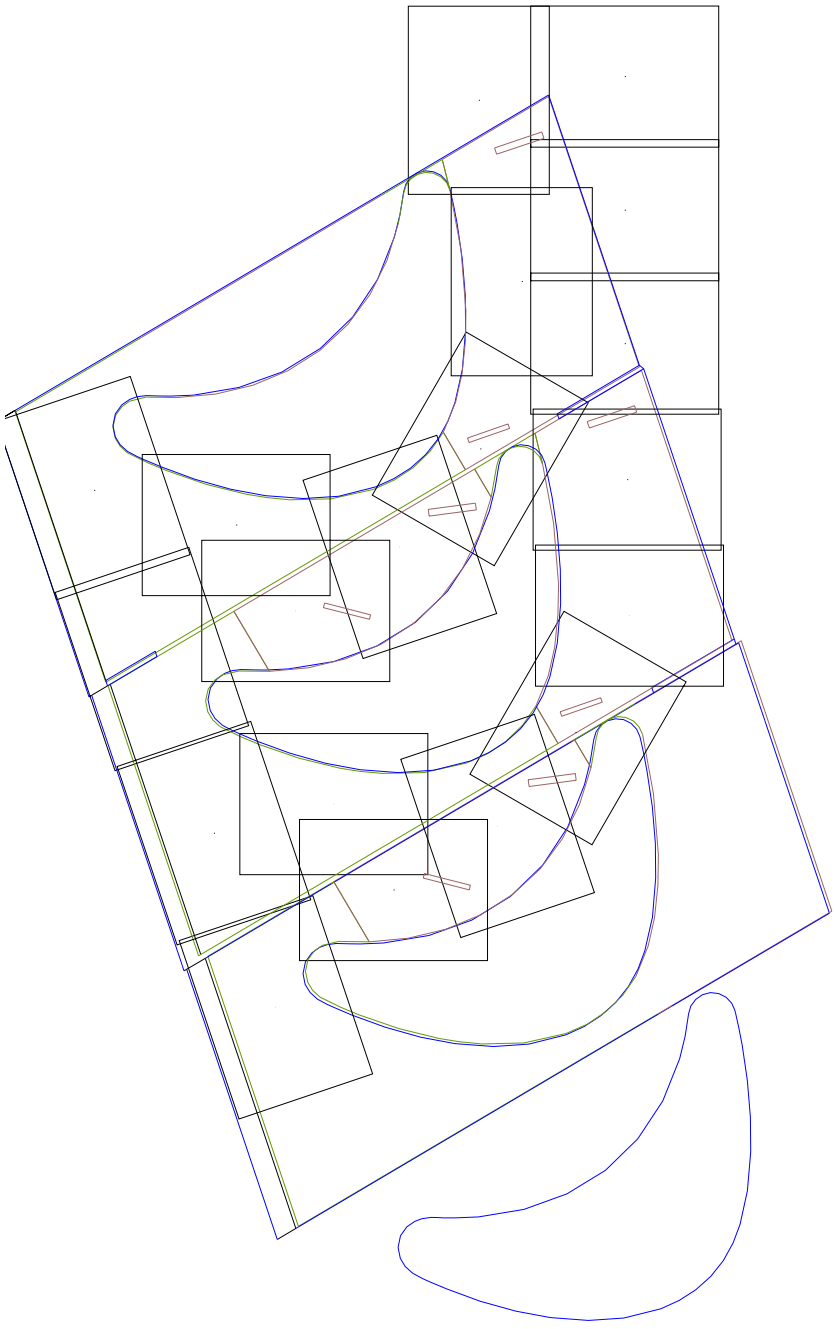

Figure 3.30 Drawing of top of platform, showing the 19 field of view rectangles for each of the infrared camera ports.

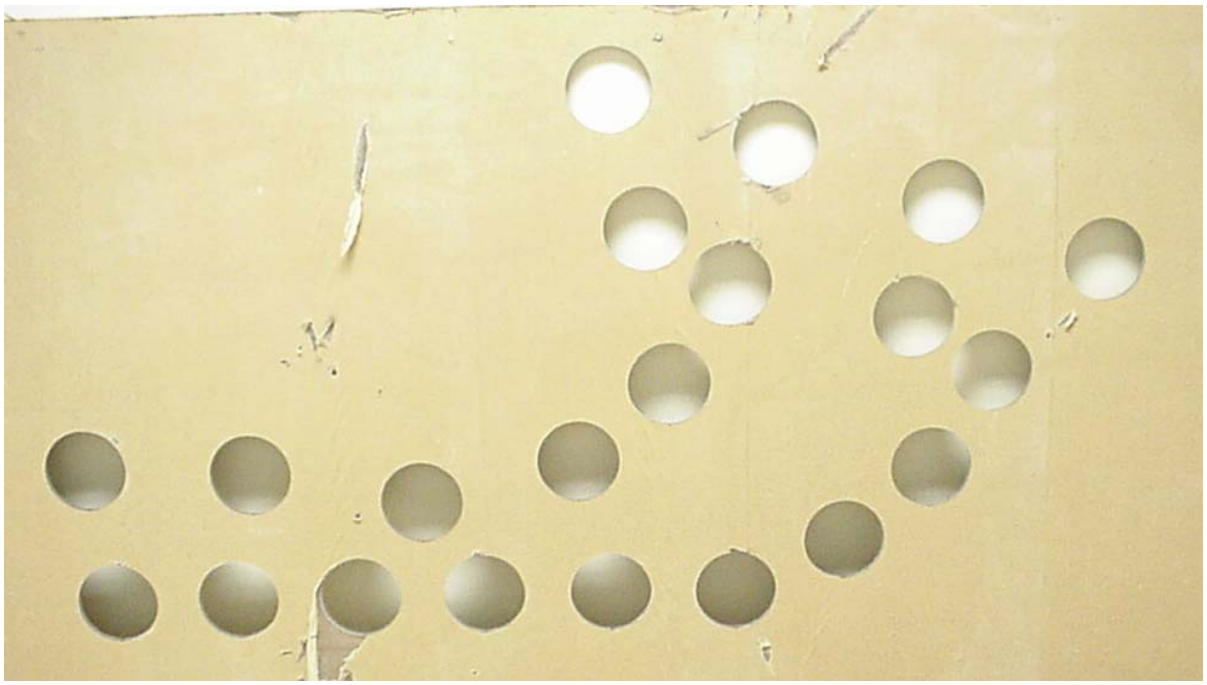

Figure 3.31 Picture of underside of top plate, showing the holes cut for the infrared camera view ports.

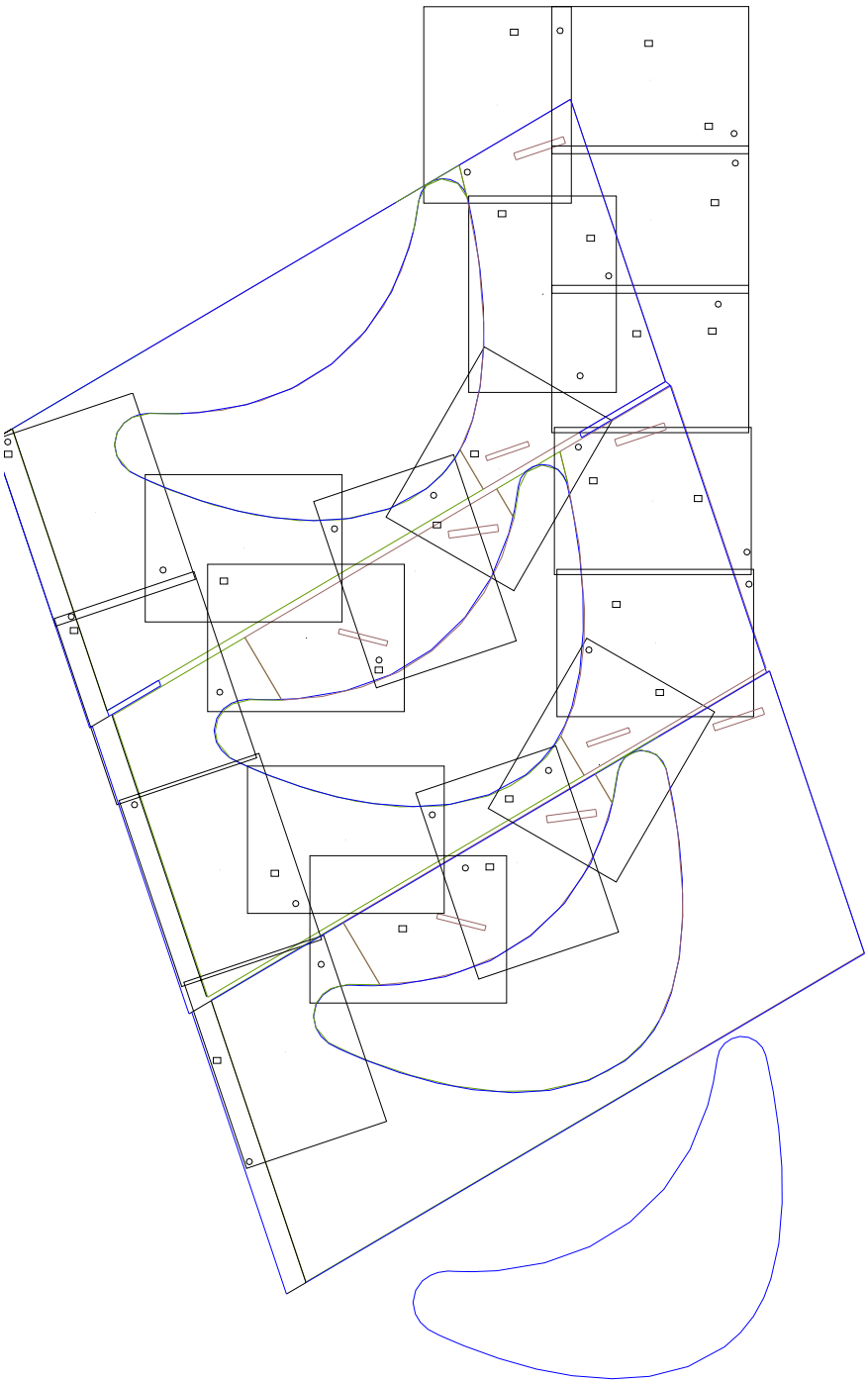

Figure 3.32 Drawing of top of platform, showing location of markers (circles) and thermocouples (square) in the platform for each infrared image.

Figure 3.33 Picture of platform with the thermocouples and markers installed, as well as the first blade attached on the left.

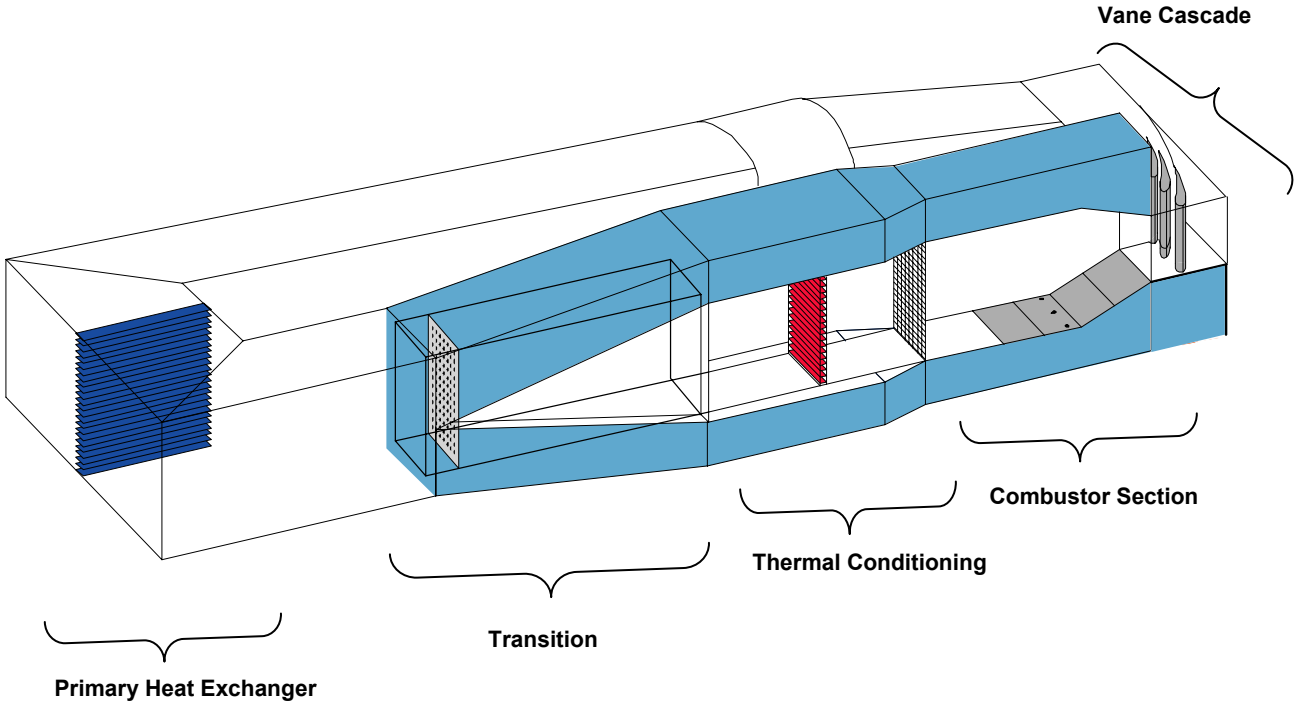

Figure 3.34 Schematic of the wind tunnel facilities, showing the location of the test section downstream of the combustor simulator.

Figure 3.35 Picture of PVC supply of coolant flow through a venturi on top of the wind tunnel, flow goes from left to right.

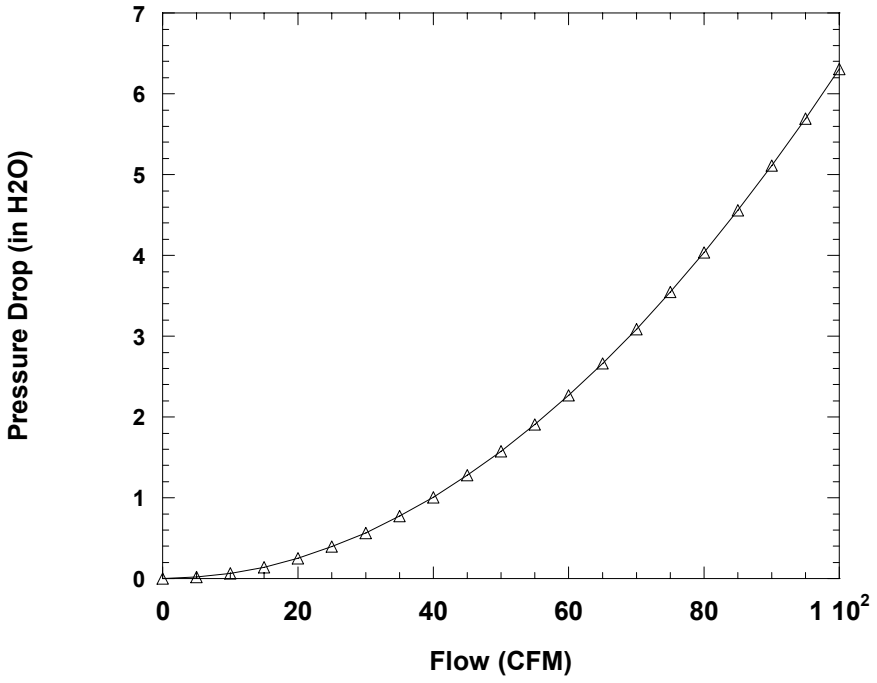

Figure 3.36 Plot of flow through the venturi and resulting pressure drop across the venturi (Lambda Square, 2003).

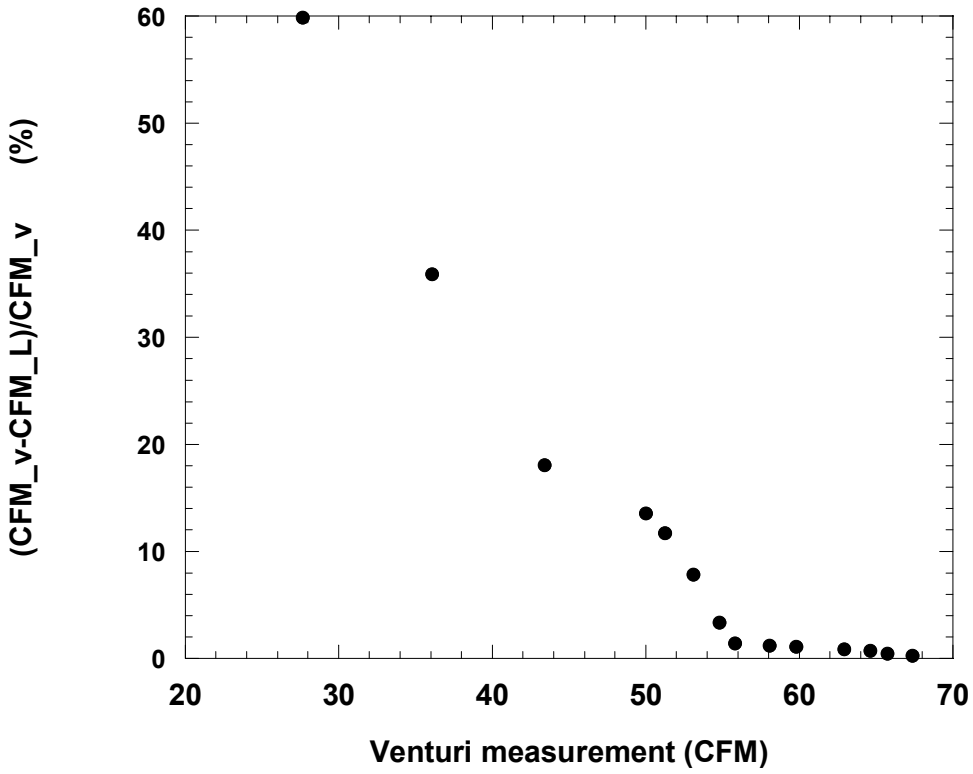

Figure 3.37 Plot showing the percent difference between venturi and LFE measurements of flow decreases as the flow is increased.

Figure 3.38 Picture the completed test section looking downstream from the combustor simulator exit, showing the three passage, four blade linear cascade.

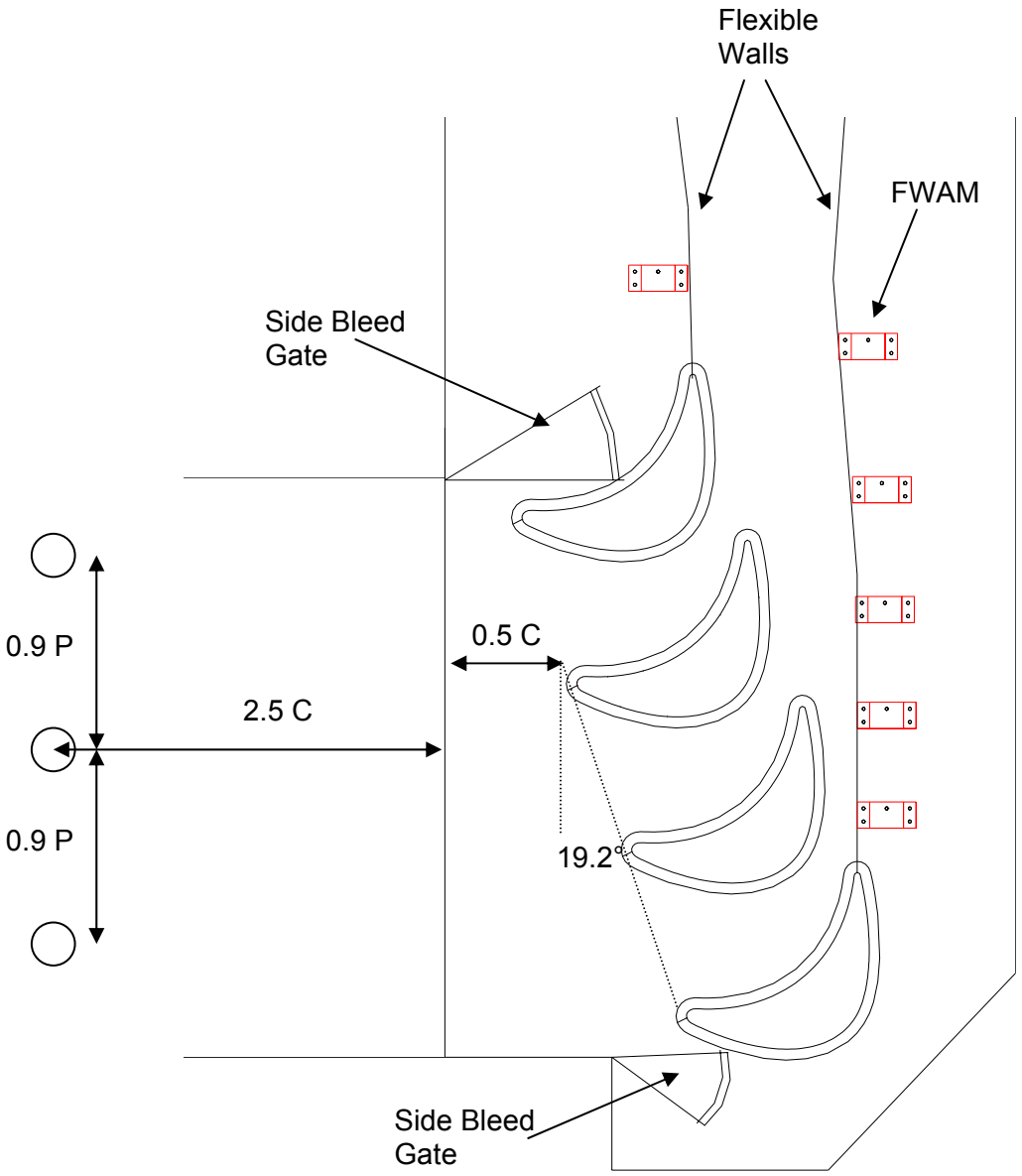

Figure 3.39 Schematic top view of tunnel, showing blade location, FWAM spacing and combustor simulator holes upstream of the test section. Lengths are given based upon chord length (C) or pitch length (P).

a) b)

Figure 3.40 Design of the side bleed gates, shown in the a) open and b) closed position.

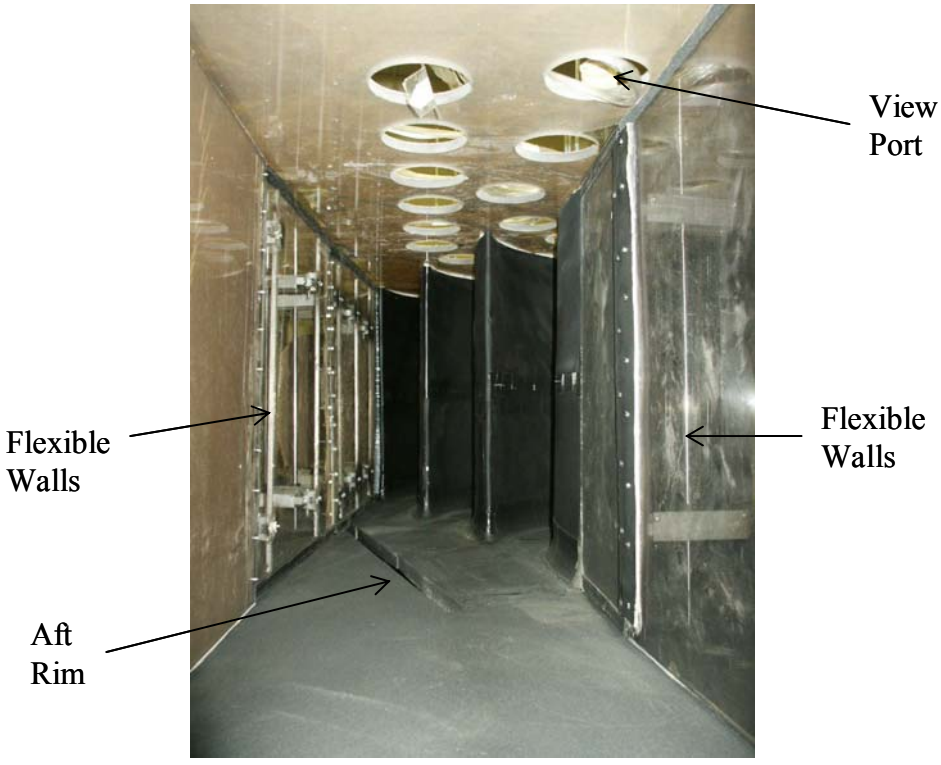

Figure 3.41 Picture looking upstream from the test section exit, showing the trailing edges of the blades, the aft rim, the holes in the top plate for the infrared camera, and the flexible side walls.

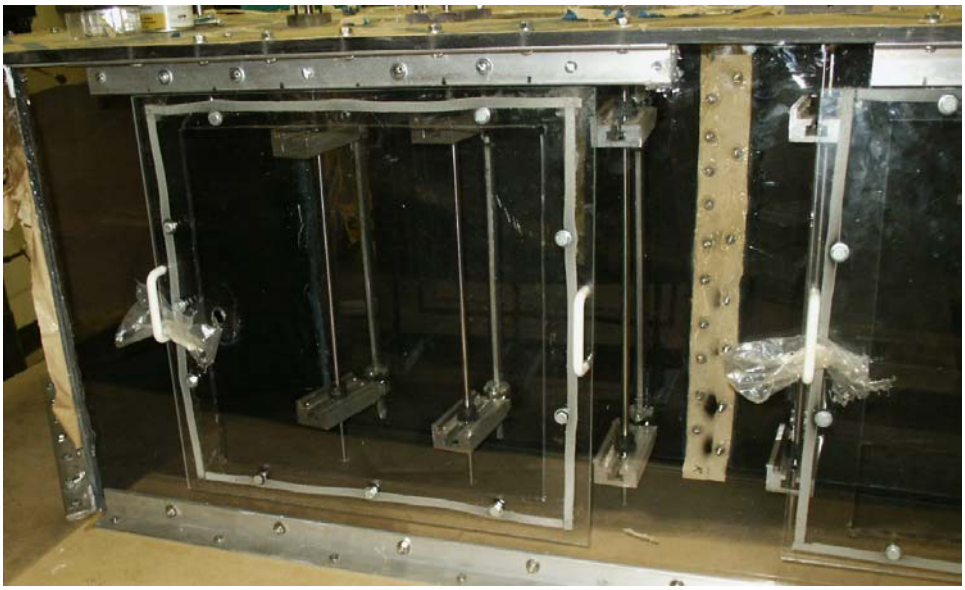

Figure 3.42 Picture of the exterior of the flexible walls, showing the FWAMs attached to the outer walls and the panels that allow access to the FWAMs.

Figure 3.43 Picture of the pressure tap scanivalve wafer used to select one pressure to measure from 24 inputs.

Chapter 4: Test Matrix and Benchmarking Procedures

Once the test section was designed and built, the test rig needed to be benchmarked and calibrated before test data could be collected. The test scenarios and benchmarking of the test rig are described in this chapter. The test matrix is explained first. Next, the methodology for setting the inlet test conditions is explained. Described next is the method for setting the leakage flows is described. Next, the infrared camera calibration and picture orientation is explained. Lastly, the thermal field measurements are described.

4.1 Test Matrix for Hub Leakage Flows

The test matrix for the cooling flow was designed to show the effects of various levels of leakage flow through the feather seal, front and aft rim, and microcircuits. To accurately analyze an effect from a specific leakage point, the test matrix was designed to have just one variable change between runs. Since the microcircuits were a proprietary design by Pratt & Whitney, the results of the microcircuit testing could not be published. To allow the data in this thesis to be published, one test matrix was created for the microcircuits and another test matrix was created for the leakage geometries excluding the microcircuits. The test cases not involving the microcircuits are referred to as the 'public cases' throughout this thesis because those cases did not involve proprietary material and could be published. The public test matrix is shown in Table 4.1a, and the microcircuit test matrix is shown in Table 4.1b. The flows are listed in the two tables as a percentage of the total inlet mass flow in the mainstream.

As shown for the public cases in Table 4.1a, the first three cases keep the front and aft rim leakage flows constant while varying the amount of flow through the featherseal. These cases were designed to show the effect of increasing featherseal flow on the hub region. The fourth public case was designed to show any effect increasing the front rim leakage from the third case. The fifth case was designed to show relatively low leakage from the front rim, as some other gas turbine engines have significantly smaller front rim gaps than the current Pratt & Whitney geometry being studied.

The public cases were not only designed to have one variable changed between runs, but each case was designed to match the some of the computational work done by

Hohlfeld [2003]. The first four public cases listed in Table 4.1a were also computationally modeled. Additionally, the microcircuit cases were computationally modeled that matched the same conditions as the first four public cases, but with a microcircuit cooling flow of 0.5%. Section 5.4 shows a comparison between the computational and experimental results.

For the cases involving the microcircuits, each case was designed to allow comparison to one of the public cases. The cases listed under 'Constant Microcircuit' were designed to be compared directly to runs A-C as the featherseal coolant flow was incremented from 0.25% to 0.75%. However, in addition to effects the featherseal and front rim have on the microcircuits, the effects of increasing only the microcircuit flows were analyzed. During testing, the flows through the microcircuits were increased in increments large enough to affect the local region, but too small to effect the overall hub platform. These flow increments through the microcircuit range from 0.15% to 0.5% in increments of 0.05%. Because of these small increases, many of the microcircuit cases listed in Table 4.1b were analyzed only near the region around the microcircuit. Since over twenty-five flow conditions were tested involving the microcircuits, the specific cases are not listed in Figure 4.1b. Instead, the ranges of the flows are listed for each of the leakage features. More flows through the microcircuits were analyzed than the other features because this geometry has never been tested before and a significant amount of data was needed to evaluate the microcircuit's effectiveness in an engine.

To ensure the repeatability of the experimental data, the first public case (run A) was designed to be repeated one week after the first set of data was taken. Additionally, the first microcircuit case (0.25% flow in microcircuits, 0.25% flow in featherseal, 1.5% flow in front, aft rim) was repeated one week later. Performing repeatability measurements ensured the accuracy of the experimental measurements and showed changes in ambient temperature and pressure had no effect on the results. These repeated cases are analyzed in chapter 5, section 5.1 for the public repeated cases, and section 5.2 for the microcircuit repeated cases.

4.2 Setting of the Passage Inlet Conditions

To correctly set the flows around the test section, we needed to match four parameters in the wind tunnel: inlet turbulence, inlet temperature, inlet velocity, and blade passage velocity. The setting of each of these four parameters is described in this section.

The first step in benchmarking the flows through the test rig was to set the inlet velocity, temperature, and turbulence. The inlet velocity was set first since it was the simplest parameter to modify. From scaling of the Reynolds number, as discussed in section 3.1, the required inlet velocity was 10.3 m/s. This inlet velocity resulted in an inlet passage mass flow of 2.28 kg/s. To measure the inlet velocity, we took total and static pressure measurements at the test section entrance with a pitot probe. The pitot probe extended 8.5 inches into the combustor exit section from above the wind tunnel, which was 39% of the span. By knowing the density of the air, the velocity at the inlet was calculated by the equation

$$V = \sqrt{2\Delta P / \rho} \tag{4.1}$$

where ΔP is the pressure measured by the pitot probe, and ρ is the density of air. This velocity was controlled by adjusting motor controller of the wind tunnel fan. For this experiment, the proper inlet velocity was achieved by setting the fan frequency at 37.5 Hz. Although the velocity was ideally changed by adjusting only the fan speed, changes of the air temperature in the wind tunnel also caused velocity changes. These changes are discussed in the next few sections.

Inlet Turbulence Setting

Once the inlet velocity was set, we then matched the inlet turbulence. For the specifications from Pratt & Whitney, inlet turbulence levels of 10% were desired. From previous calculations [Couch, 2003], the momentum flux ratio of the combustor simulator dilution holes to the mainstream flow was 8.4. This momentum flux ratio is defined as follows:

$$I = \frac{\rho_j U_j^2}{\rho_\infty U_\infty^2} \tag{4.2}$$

where ρ is the density of air, U is the velocity, the subscript 'j' refers to the dilution hole exit, and the subscript '∞' refers to the free stream. To set this momentum flux ratio to 8.4, we measured the velocity of the flow out of each combustor dilution hole with the pitot probe. By adjusting the flow though each of the six dilution holes, the momentum flux ratio for each dilution hole was set to 8.4 while a constant free stream velocity was maintained.

Once all of the dilution hole velocities were set, we measured the inlet turbulence using fiber optic laser doppler velocimetry (LDV). LDV measurements were taken by using a four-component beam focused on one location within the free stream. To measure the turbulence, we seeded the entire wind tunnel with finely dispersed olive oil. As the fine oil droplets passed through the focal point of the laser beam, the droplets caused a disruption in the beam that was used to calculate the u and v velocities of the free stream flow. The resulting turbulence, Tu, was calculated by using the following equation:

$$Tu = \frac{\sqrt{\frac{1}{2}\left(u_{rms}^2 + v_{rms}^2\right)}}{u_{av}} \tag{4.3}$$

where u_{rms} is the streamwise velocity, v_{rms} is the spanwise velocity, and u_{av} is the streamwise velocity averaged over the tunnel height. These measurements were repeated in nine locations within the free stream. Each measurement was taken one half a chord length upstream of the turbine blades. In the spanwise direction, the bottom measurement was taken at 12.7 cm from the platform surface. Each measurement point in the spanwise direction was evenly spaced 12.7 cm apart. In the pitchwise direction, the measurements were evenly spaced 5.1 cm apart and aligned with the passage between the blades. The average of these nine turbulence measurements was 9.8% inlet turbulence.

Inlet Temperature Setting

After the turbulence was set, we set the temperature of the inlet flow. Three heater banks, as previously shown in Figure 3.32, heated the main flow. A high temperature variation between the free stream flow and coolant flow was desired, to reduce the uncertainty of the thermal measurements on the platform. However, to prevent damage to the blades, the temperature of the free stream was limited to 50° C.

To achieve the maximum temperature of 50° C , we set the lower heat bank to 99% of its full power, the middle heat bank was set to 90% of its full power, and the upper heat bank to 78% of its full power. These power settings resulted in the thermocouples in each of the three heater banks reading exactly 50°C. To chill the coolant flow, the chiller was used to supply both the main heat exchanger and the heat exchanger on the lower passage of the wind tunnel with chilled water. The main heat exchanger was set to 22.7 L/min (5.0 gal/min) of flow, and the lower passage heat exchanger was set to 6.8 L/min (1.5 gal/min). The main heat exchanger was used to prevent the wind tunnel from over heating because the fan heats up the flow in addition to the heaters.

We chose the setting for the heat exchanger in the lower passage to chill the coolant supply to 23° C, which matched the temperature of the coolant supplied using the compressed air. By measuring the temperature of the coolant supply from both the compressor and the bottom of the wind tunnel, we assured the same temperature coolant was supplied to the test section. The temperature difference of the coolant in the plenums fed by the wind tunnel and compressed air was less than 0.3 °C. By changing the amount of flow from the chiller into the lower heat exchanger, the temperature of the coolant from the wind tunnel changed to match the temperature of the coolant supplied from the compressed air. The coolant flow temperature of 23°C in the plenums resulted in a temperature difference of 25°C between the mainstream (50° C) and coolant flow entering the mainstream (25° C). The temperature difference of 2° C between the coolant in the plenum and at the plenum exit was attributed to heat losses through the plenums, which were not insulated.

Inlet Velocity Setting

After we set the inlet turbulence and temperature, the velocity was re-verified across the entire inlet. Since the temperature increase caused a decrease in density and thus increase in velocity, the fan speed was adjusted. Generally, the velocity changes caused by temperature effects were less than ±0.1 m/s. However, it was important to benchmark the velocity distribution across the inlet in the pitchwise direction.

We took measurements of the inlet velocity in seven locations across the test section inlet using the pitot probe. Figure 4.1 shows a top view schematic of the test section, illustrating the locations of the velocity measurements. Each of the inlet velocity

measurement points are evenly spaced 15.3 cm apart in the pitchwise direction. Figure 4.2 shows the resulting velocity at each of these seven locations for the benchmarking procedures. The two slightly lower velocity measurements in Figure 4.2 can be attributed to the free stream velocity slowing down as it nears the blades. The locations of these two blades are marked in Figure 4.2. Interestingly, unlike the first two blades, the third blade in the cascade does not reduce the measured inlet velocity. The velocity measurements that were affected by the blades were taken 0.23 chord lengths upstream of the first blade and 0.52 chord lengths upstream of the second blade. The unaffected velocity measurement was taken 0.81 chord lengths upstream of the third blade, showing the blades have an affect on the inlet velocity approximately 0.6 to 0.8 chord lengths upstream.

Blade Passage Flow Setting

Once the inlet turbulence, temperature, and velocity were set to their specified conditions, we verified the correct flow around the blades. To accurately model the flows around actual gas turbine engine blades, we matched the pressure distribution around the pressure and suction sides of the blades to the pressure distributions from periodic CFD computations [Hohlfeld, 2003]. To set the flows around the blades, first the stagnation point needed to be set in the correct location on the blades. To visualize the location of the stagnation point on the blade, we attached tufts of strings near the designed stagnation point at the mid span of the blades. Figure 4.3 shows these black strings attached to the stagnation point on one of the blades. The exact location of the stagnation point was determined at the point where the strings were pulled in opposite directions. The location of the stagnation point is clearly marked in Figure 4.3. The location of the stagnation point on the blades was set in the correct location by opening and closing of the side bleed gates (shown in Figures 3.40a-b). By opening the gate on the pressure side of the outer left blade (Blade 1) and closing the gate on the suction side of the outer right blade (Blade 4), the stagnation point on the blades would be moved slightly towards the pressure side of the blades. Though adjustment of the side bleed gates, we oriented the stagnation point in the correct blade location. For the correct stagnation point location, the right bleed gate on the suction side was completely closed and the left bleed gate on the pressure side was 80% closed.

Once the stagnation point was located in the correct position on the blades, we set the pressure distribution around the blades. This pressure distribution was determined computationally and matched to the predictions of Pratt & Whitney [Hohlfeld, 2003]. The pressure distribution around the blades is shown in Figure 4.4. Here the pressure is shown in non-dimensional terms, by the following equation :

$$C_p = \frac{P_{s,in} - P_{s,loc}}{P_{d,in}} \tag{4.4}$$

where $P_{s,loc}$ is the local static pressure, $P_{s,in}$ is the static inlet pressure measured with the pitot probe, and $P_{d,in}$ is the dynamic inlet pressure calculated from the inlet velocity using equation (4.1). These non-dimensional pressures are plotted as distance around the blade normalized by the total distance (s/s_{max}). Positive values of s/s_{max} denote the suction side of the blade and negative values denote the pressure side of the blade. Figure 4.5 shows a top view of the blades, with the stagnation point and s/s_{max} distances indicated. The value of s/s_{max} is 0.0 at the stagnation point, and increases along the pressure side to a value of 1.0 at the trailing edge. Conversely, the value of s/s_{max} decreases along the suction side from 0.0 at the stagnation point to -1.0 at the trailing edge.

As described in section 3.2, pressure taps were installed around the pressure side and suction side of the blades. However, since the passage between the blades was the main area of interest, pressure taps were used on the pressure side of one blade and the suction side of the other. By placing pressure taps only the passage sides of the blades, the number of pressure taps required was halved while still allowing accurate measurement of the flow. Figure 4.6 shows a top view of the blades with the pressure taps on each of the blade passages indicated. As shown in Figure 4.6, the first blade (blade 1) was instrumented with three pressure taps on the pressure side and nine on the suction side. The second blade (blade 2) was instrumented with ten pressure taps on the pressure side and three pressure taps on the suction side. All four blades in the cascade were instrumented with pressure taps at the stagnation point.

To set the flows around the blade, we adjusted the flexible walls to achieve the correct pressure at each tap location. By pushing the flexible wall towards the blades, the passage area was reduced, which increased the velocity and thus lowered the pressure at the blade. Through a process of adjusting the flexible wall, measuring the pressure

distribution, and then re-adjusting the wall, we acheived the correct pressure distribution around the blades. The pressure measurements at each tap for two test cases are shown plotted on the computational pressure curve in Figure 4.4. The first set of pressure distribution measurements was from the public case A, and the second set of measurements was from public case E. These two cases were taken two months apart. As shown in Figure 4.4, the pressure distribution matched around the pressure side of the blade, but it was difficult to match the lowest pressure on the suction side of the blade. The measured pressure along the pressure side for the two shown cases did not vary, while the measured pressure along the suction side shows variation. However, the pressure distribution set around the blades still accurately models the flows around the actual gas turbine blades.

4.3 Setting of the Leakage Flows

Once the inlet conditions and blade pressure distributions were set, we calibrated each of the seven leakage flows. Since it was not feasible to use seven mass flow meters to measure the flow supplied to each leakage feature, each plenum was calibrated individually. Though calibration, the discharge coefficients were determined for each of the leakage features, as described in this section.

Since the front and aft rim were supplied by flow from the bottom passage of the wind tunnel, a mass flow measurement device could not be installed to measure the exact amount of flow into each plenum. However, since pressure taps were installed inside the plenum and on the platform surface downstream of the slot exits, we measured the pressure difference between the coolant in the plenum and the coolant on platform. By assuming the plenums were sufficiently large enough to have no velocity inside them, the exit velocity was calculated directly from the pressure measurement by using equation (4.1). However, since equation (4.1) does not take into account any losses, a discharge coefficient correction was used to calculate the actual mass flow. By knowing the density of the air and the slot exit area, the mass flow through each of the slots was determined by the equation:

$$\dot{m}_{actual} = C_d \rho_c V A \tag{4.5}$$

where C_d is the discharge coefficient, ρ_c is the density of the coolant, V is the exit velocity, and A is the area of the slot exit. The calculation of the discharge coefficient is discussed in the next paragraph. The velocity was calculated by using equation (4.1). The pressure difference used in equation (4.1) was the difference in static pressure between the exit of the leakage feature and within the plenum. The pressure taps inside the plenums and at the exterior of each leakage feature were discussed in section 3.6 of this thesis. The exit area of each of the leakage features is given in Table 4.2. The actual area fed by the front rim plenum was the sum of the front rim area and the front gutter area. This area summation was the same for the aft rim and aft gutter, since both were fed from the aft plenum.

Since the front and aft rim leakages were simply slot flow leakages, the discharge coefficient for each of these features was assumed to be 0.6 (Fox and McDonald [1998]). For the remaining five plenums, the discharge coefficient for each plenum was calculated directly. To calculate a discharge coefficient, all the plenums were closed except for one. With the tunnel running at the correct inlet velocity, temperature, and pressure distribution, the cooling flow was turned on to one plenum. The flow though the one plenum was measured in two ways. First, the flow was measured by the venturi in the PVC piping feeding the plenum. This flow measured by the venturi was termed the actual mass flow. Secondly, by using the pressure taps inside the plenum and downstream of the plenum exit, the velocity (and thus the mass flow) was calculated by using equation (4.1). The mass flow calculated from these pressure tap measurements was termed the ideal mass flow. The discharge coefficient for each plenum that was used in equation (4.5) was calculated by dividing the ideal mass flow from the actual mass flow.

By changing the supply pressure, numerous measurements of the discharge coefficient for a particular plenum were recorded. A friction factor, f, for each of the leakage features was calculated from the discharge coefficients by the equation:

$$f = \frac{2D\,\Delta P}{\rho L V^2} \tag{4.6}$$

where D is the hydraulic diameter, ΔP is the static pressure difference measured from inside the plenum to the platform, ρ is the coolant density, L is the length, and V is the velocity as calculated from the pressure difference using equation (4.1). Figure 4.7 shows a plot for the measured friction factor for the feather seal, pressure side, and suction side microcircuits at various supply pressures. As expected, the friction factor for the suction side microcircuit is higher, since the suction side microcircuit is considerably longer and thus causes a higher pressure loss. Also shown in Figure 4.7 are the calculations by Pratt & Whitney of the expected friction factors for the microcircuits. There is good agreement between the expected and calculated values of the friction factors for suction side microcircuit. For the pressure side microcircuit, the computationally predicted values were lower than the measured friction factor. After the difference in friction factors was noted with the computational values, the friction factor was remeasured. Since the experimental friction factor for the pressure side was measured as 0.029 from two different experiments, the experimental friction factor was taken as the correct value.

The data shown in Figure 4.7 was also compared to the friction factor based upon the Blasius correlation for turbulent flows in a smooth pipe. This friction factor, f_o, was calculated by the equation:

$$f_o = \frac{0.3164}{Re_d^{0.25}} \tag{4.7}$$

where Re_d is the internal Reynolds number based upon hydraulic diameter. Figure 4.8 shows a plot of f/f_o versus the internal Reynolds number. The data in Figure 4.8 shows the friction factor for the suction side microcircuit is nearly twice as high as the Blasius friction factor. The increase in friction factor for the suction side microcircuit is attributed to the pedestals inside the channel, the length of the microcircuit, and the 80° bend in the channel.

After the discharge coefficients were determined for all of the leakage features, the mass flow meter was no longer needed to set the leakage flows. By knowing the discharge coefficient for each leakage feature, the mass flow in each plenum was calculated directly using equation (4.5), using pressure measurements to determine the exit velocity. Thus, all of the leakage flows were set by balancing the correct pressure in

each microcircuit. However, to verify there were no leaks in the system, we measured the total mass flow at the venturi. By summing all the mass flows through the five plenums and comparing it to the measured mass flow at the venturi, the leakage flows were double checked and any unwanted leakages in the system could be discovered. For the majority of the testing, the percent difference between the venturi reading and the sum of the calculated mass flows through each of the plenums was 1.1%, ±0.3%. We attributed this variation to the uncertainty in the discharge coefficient calculations, which was affected by the uncertainty of the pressure measurements in the plenum.

4.4 Calibration of the Infrared Camera

After the inlet conditions and leakage flows were set, the test section needed to reach steady state before data was collected with the infrared camera. Although the velocity distribution reached equilibrium within several minutes, the time to reach steady state required over two hours, on average. The time to reach steady state was dependent upon the ambient temperature in the laboratory. To determine when the test section had reached thermal steady state, we monitored the temperatures of both the platform and the heater bank. Since the temperature reading of the wind tunnel heaters displayed one decimal point (in degrees Celsius), we determined the heaters to be at thermal equilibrium when the temperature reading did not change over 20 minutes. However, because the thermocouples inserted in the platform and plenums (see section 3.6) displayed temperature with two decimal points (in degrees Celsius), the test section was taken to be at thermal equilibrium when the temperature readings did not change by more than 0.02 °C over a 20 minute period. This steady state condition with a variance of less than 0.02 °C resulted in thermal variations on the platform less than 0.04 %. We chose a 20 minute time period to measure steady state because the time required to take a data set was approximately 20 minutes. Once the tunnel had reached steady state, the test section was ready to collect data with the infrared camera.

As described in section 3.6, 19 holes were drilled in the top plate of the test section to allow the infrared camera to capture images of the hub region. The Flir systems model P20 infrared camera, previously shown in Figure 3.28, was used to take all of the infrared images. The camera was able to automatically focus on the markers in

the hub region, assuring a clear picture. The camera output was hooked up to a television so we could clearly see if the camera was focused and in the correct position. As described in section 3.6, the camera resolution was one temperature reading for every 0.6 mm by 0.6 mm area.

To position the camera, pilot holes were drilled into the top plate to hold the camera in place at each location. While the wind tunnel was not running, we positioned the camera in each view port so the markers and thermocouples were visible. The correct amount of picture overlay between images was assured by using the pilot holes. The infrared camera was also prohibited from shifting during data collection by using the pilot holes. It was important to always have the infrared camera secured in the same place because five images were taken at each location. We took five images instead of one to reduce the precision uncertainty in the camera images because the five images were averaged into one picture. If the camera were to move during these five images, the resulting averaged image would be an incorrect average of the actual hub temperatures. Thus, 195 images were taken for each test case, five images at each of the 19 view ports.

After the images were taken, they needed to be calibrated. Although the infrared camera is able to precisely record temperature variations, the temperature measurement of the camera is not accurate unless the camera is calibrated. The infrared camera is greatly affected by both background temperature and local emissivity. To reduce the effect of emissivity on the camera, the entire interior of the test section was painted black. To reduce the effects of background temperature, we calibrated each of the 195 images by using the ThermaCam® imaging software. Figure 4.9 shows a screen snapshot of this software. To calibrate each image, a circular query icon is placed on the image. The software displays the temperature recorded at that exact circular point. One of these circular points is visible in Figure 4.9. To calibrate the picture, the query icon was placed over the location of the thermocouples in the platform. By adjusting the values of the background temperature and emissivity within the software, the resulting temperature at the query icon was changed. By increasing the background temperature, we reduced the local temperature. Although increasing the emissivity increased the local temperature, the emissivity was not adjusted as often as the background temperature.

Through changing the background temperature and emissivity, we changed the temperature of the image to match the measured temperature of the thermocouple. The temperature recorded by the thermocouples is actually an average of the thermocouple readings over the span of the data collection process. Typically, it would take 20 minutes to record all 195 infrared images. The LabView software was set up to record the temperature of the thermocouples every ten seconds. These 120 temperature measurements were then averaged to provide one temperature value for each of the thermocouples in the platform. The average variation of these 120 data points was calculated to be ± 0.015 ° C, based upon a 95% confidence interval. Fortunately, this calculated temperature variation matches the assumed steady state conditions, showing the test section was at thermal equilibrium.

During calibration, the background temperature used to calibrate each picture would vary slightly from image to image. For each of the images, we recorded the values used for the background temperature and emissivity. After all of the images were calibrated, these background temperatures and emissivities were averaged to produce one value for the whole data set. We used these averaged values in the final calibration of the images. The final averaged emissivity for all the data sets was 0.9 ± 0.02 , and the final averaged background temperature for all the data sets was 32.1 °C ± 4.4°C. The variance of the background temperature for all the data sets is high because the background temperature calibration was very sensitive to the ambient temperature in the laboratory. Depending on if data was taken in the morning or evening had a large effect on the background temperature calibration. However, for individual test cases, the background temperature variation was ±1.2°C. Through the adjustment of the background temperature and emissivities, for all of the data sets the agreement between the measured temperature at each of the thermocouples and the calibrated temperature was ±0.1° C.

Once each of the 195 images was individually calibrated, each of the five sets of images was averaged into one image using a MatLab code (developed and documented in Knost [2003]). Within the same code, the 19 averaged images were oriented and aligned to produce one large composite data image of the test section. This code used the location of the markers in the platform to orient the images. All of the marker locations were programmed into the MatLab code with X and Y distances from a fixed point. For

this experiment, the fixed point was taken as the corner of the test section. Since at least two markers were in each image, the orientation of each image was defined because only two points are needed to define a plane at a specific height. A snapshot of this MatLab code is shown in Figure 4.10. As shown in Figure 4.10, markers within the hub region are clearly visible with this code. In addition to markers, the X and Y positions of obvious features, such as leakage points, were programmed into the code. By selecting the appropriate marker and clicking on that marker in the image, we correctly oriented each of the images.

In addition to orienting the images, the MatLab code also averaged any overlap between images. Since slight overlap was designed in the construction of the top plate to facilitate image orientation, it was important any overlaps would not produce blotches of poor data. If two images contained a substantial amount of overlap, only the area of unique data from each image was selected. By reducing the amount of overlap in the final image, we reduced the uncertainty of the final image. To produce the final image, first the images would be correctly oriented using a low resolution to reduce computation time. Once all of the images were correctly oriented, the program was rerun using higher resolution to provide the final image.

After using the MatLab program to align the images into one composite, the resulting file was imported into TecPlot® for the final processing. TecPlot was chosen because of its high control over the contours and plotting functions. Although temperature in degrees Celsius was recorded by the infrared camera, we converted the data into the non-dimensional adiabatic effectiveness, η, which is defined as:

$$\eta = \frac{T_{aw} - T_{\infty}}{T_c - T_{\infty}} \tag{4.8}$$

where T_{∞} is the freestream temperature, T_{aw} is the adiabatic wall temperature measured by the infrared camera, and T_c is the coolant temperature measured inside the plenum near the leakage area. The temperature shown in the remainder of this thesis is shown as non-dimensional adiabatic effectiveness.

4.5 Design of Thermal Field Measurements

Although the infrared images illustrate an accurate measurement of the temperature distribution along the hub region, the images provide little information of the temperature distribution directly above the platform. To quantify the thermal distributions in the freestream near the platform, we took thermal field measurements along the platform. The thermal field measurements were taken with a thermal rake, which is shown in Figure 4.11. The thermal rake consists of 21 thermocouples, evenly spaced 5.1 mm apart. To quantify the thermal field near the platform, we took temperature data using the thermal rake at a position 1 mm above the platform surface. Then, the thermal rake was raised another 1 mm and data is taken again. By stepping through a total of 25 mm, taking data at each 1mm step, we quantified the thermal distribution above the platform.

Unfortunately, since the thermal rake is only 10.2 cm long, taking thermal rake measurements of every area above the platform was impractical. Instead, thermal field measurements were taken at specific locations along the hub region. The locations where thermal field measurements were taken are shown in Figure 4.12. An attempt was made to quantify the thermal field in the important areas of the hub leakages. As shown in Figure 4.10, we took thermal field measurements in two locations along the featherseal, near both the leading edge and trailing edge of the blades. The thermal field measurements were taken perpendicularly along the featherseal 4.0 cm (0.09 chord lengths) and 12.1 cm (0.27 chord lengths) from the front rim. Thermal field measurements were taken in these two locations to quantify and changes in the direction of the flow out of the featherseal.

Additionally shown in Figure 4.12, we took thermal field measurements at the exit of the suction side microcircuit. For the microcircuit, the thermal field measurements were taken 0.5 cm downstream of the microcircuit exit, parallel to the microcircuit. We measured the thermal field at these locations to observe how much of the coolant remains attached to the platform flow. For all of the locations shown in Figure 4.12, the coolant flow was varied to provide different thermal distributions above the platform. Table 4.3 lists each of the thermal rake measurement locations and the corresponding leakage flows

used for each measurement. The results of the thermal field measurements are detailed in section 5.3.

Table 4.1a Test Matrix for Public Cases

	Run A*	Run B*	Run C*	Run D*	Run E
	Percent of total inlet mass flow				
Featherseal	0.25%	0.50%	0.75%	0.75%	0.50%
Front Rim	1.50%	1.50%	1.50%	2.00%	0.50%
Aft Rim	1.50%	1.50%	1.50%	1.50%	1.50%
Total	3.25%	3.50%	3.75%	4.25%	2.50%

* denotes computational modeling

Table 4.1b Test Matrix for the Microcircuit Cases

	Constant microcircuit	Microcircuit variations
	Percent total inlet mass flow	
Suction Side Microcircuit	0.25%*	0.15% 0.2%* 0.25%* 0.3% 0.35% 0.4%* 0.45%0.5%
Pressure Side Microcircuit	0.25%*	0.15% 0.2%* 0.25%* 0.3% 0.35% 0.4%* 0.45%0.5%
Featherseal	0.25%* 0.5% 0.75*	0%,0.5%*
Front Rim	1.5%*,2.5%	0%*
Aft Rim	1.5%*	0%*

* denotes computational modeling

Table 4.2 The Total Exit Area of Each Leakage Feature.

	Area (cm^2)	Total Area (cm^2)
Front Rim	223.2	225
Front Gutter	1.8	
Aft Rim	223.2	226.4
Aft Gutter	3.2	
Featherseal	2.5	2.5
Pressure Side microcircuit	3.1	3.1
Suction Side microcircuit	3.3	3.3

Table 4.3 Leakage Flow Conditions used for thermal Field Measurements

	Featherseal Measurements	Microcircuit Measurements
Front Rim	0.5%,1.5%	0%
Featherseal	0.25%,0.75%	0.50%
Aft Rim	0%	1.50%
Microcircuits	0%	0.25%, 0.5%

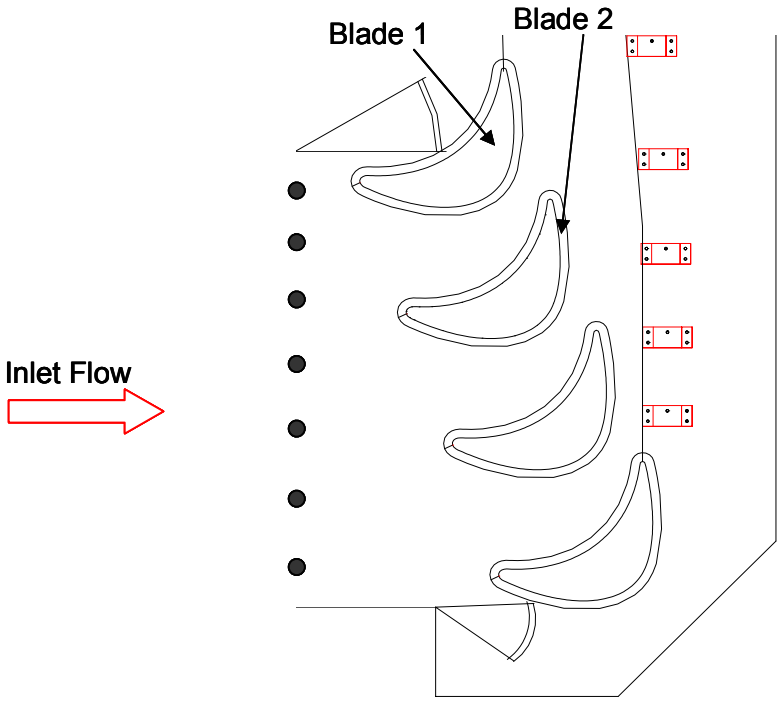

Figure 4.1 Location of inlet velocity measurements (shown by circles), taken in a line horizontal to the inlet flow.

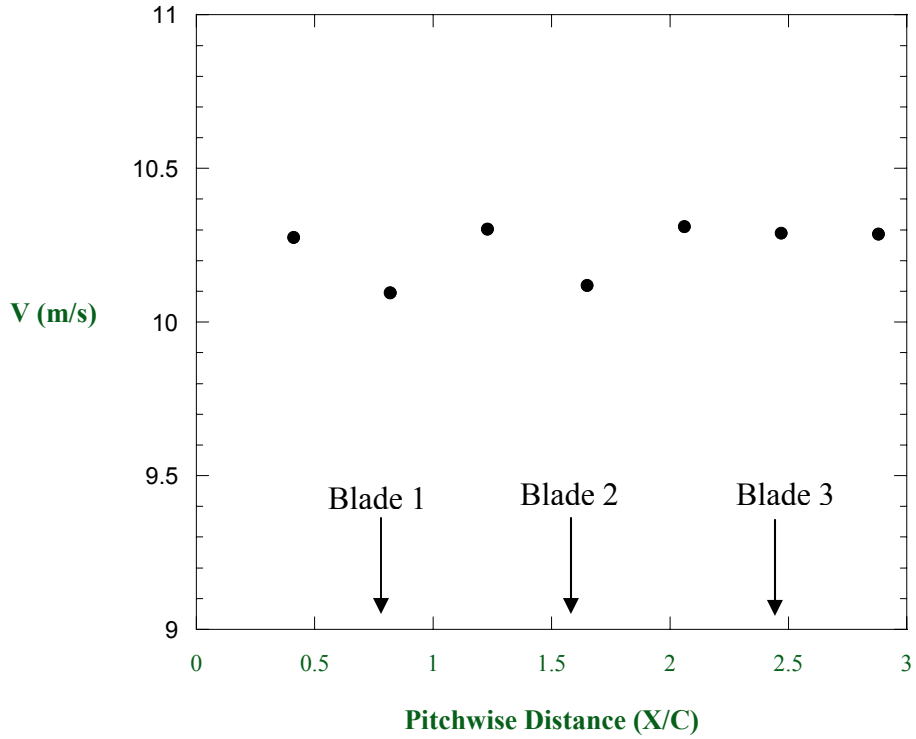

Figure 4.2 Plot of inlet velocity distribution as measured by the pitot probe at 38.5% of the span from the top plate into the combustor exit, at the plane of Figure 4.1.

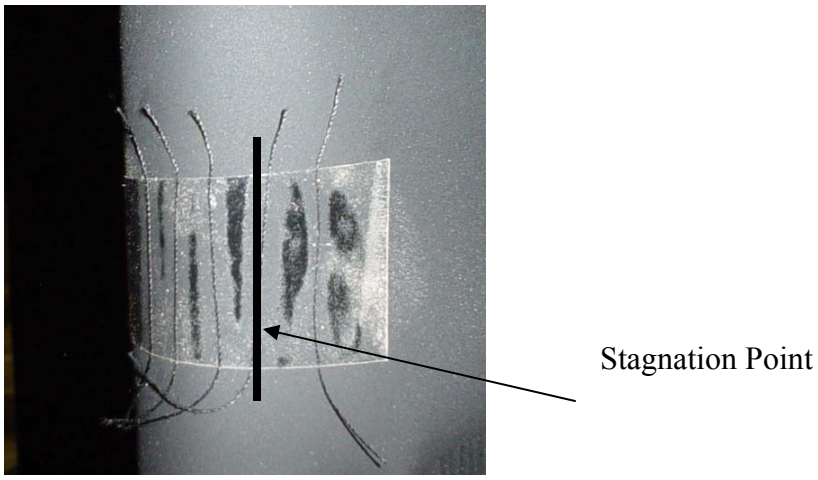

Figure 4.3 Picture of strings attached to leading edge of blades which were used to show the location of the stagnation point on the blades.

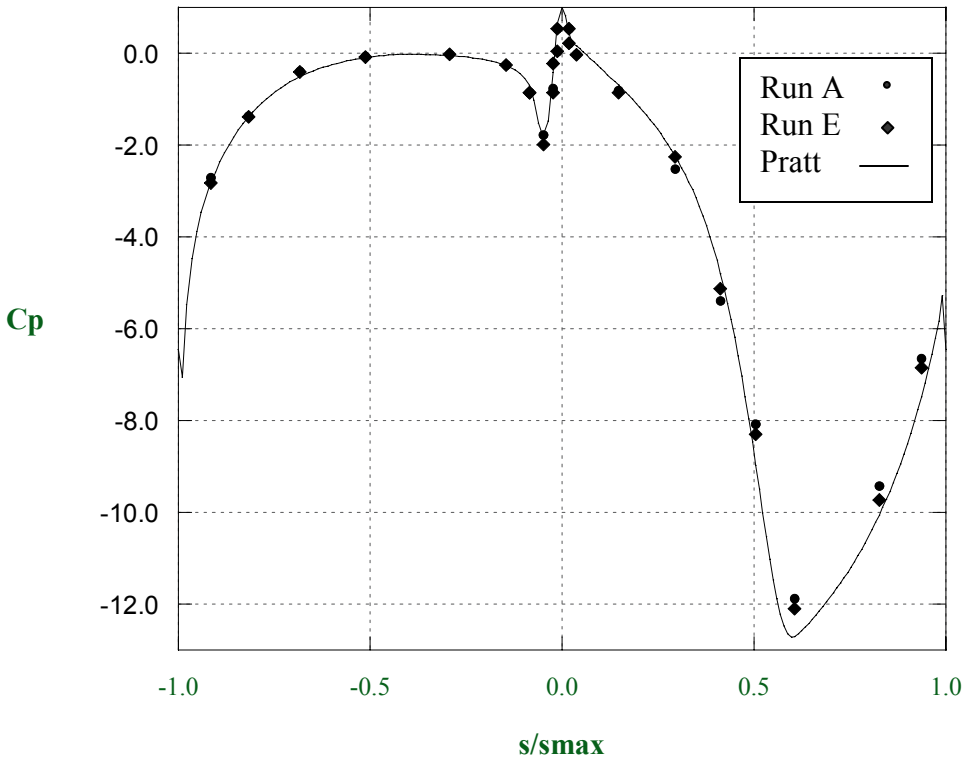

Figure 4.4 Plot of the matched pressure distribution around the blades with the value of each of the pressure taps at the blade mid chord indicated.

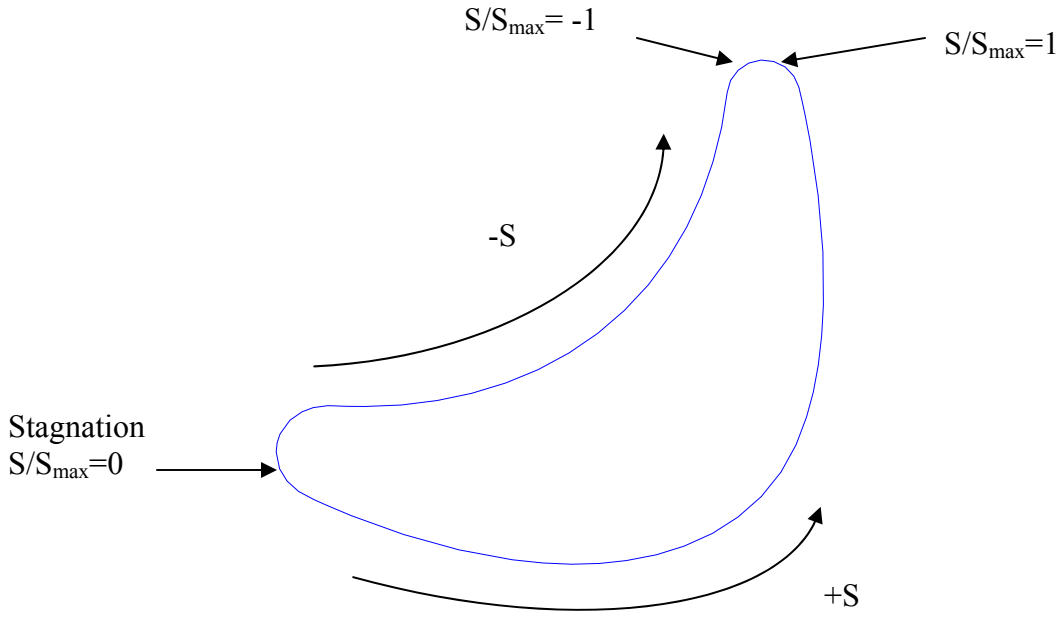

Figure 4.5 Top view drawing of the blades, showing the locations of positive and negative s/s_{max} relative to the stagnation point on the blade.

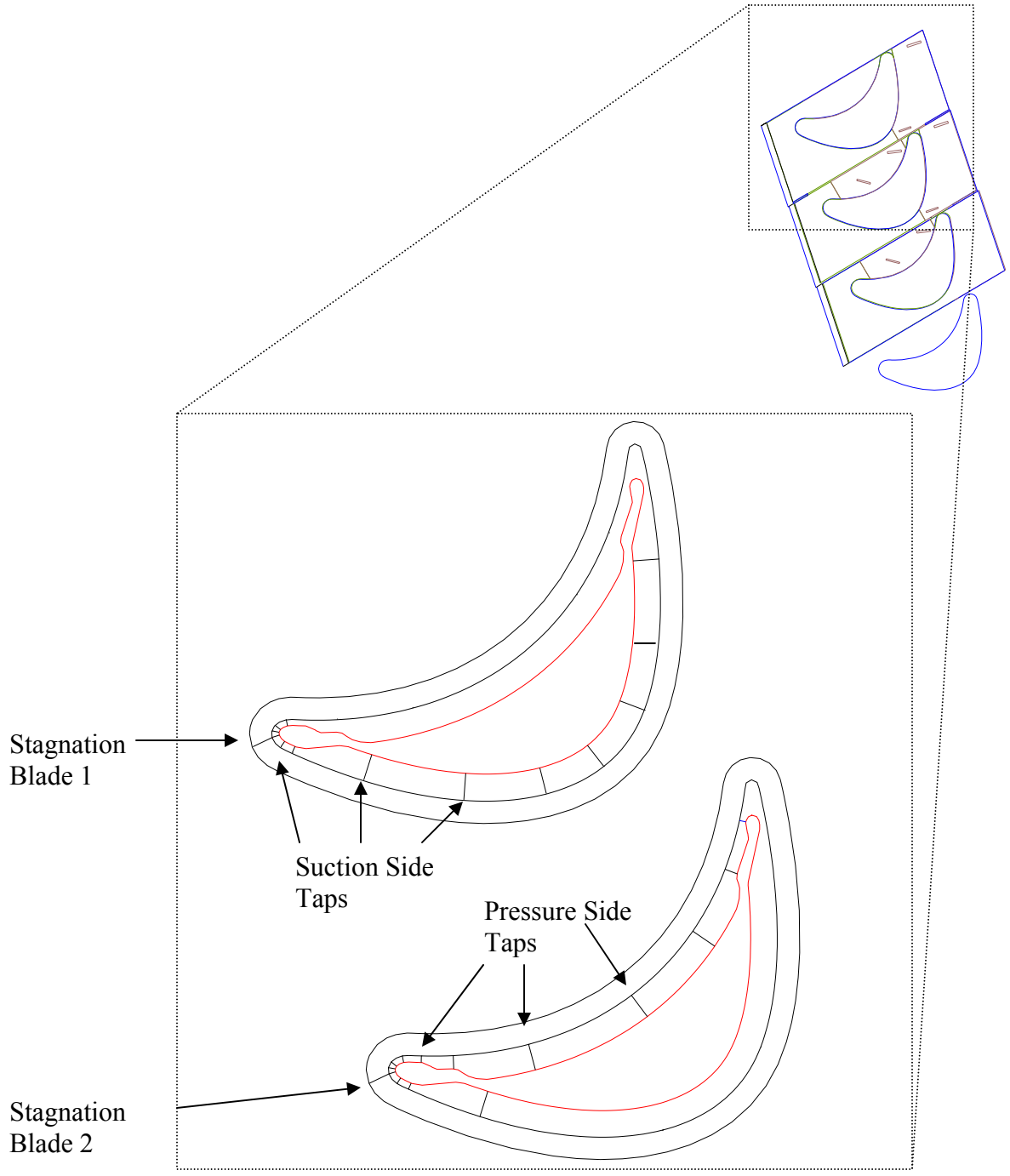

Figure 4.6 Top view drawing of blades, including the fillets, showing the pressure taps used on the two blades on either side of the main passage in the test section .

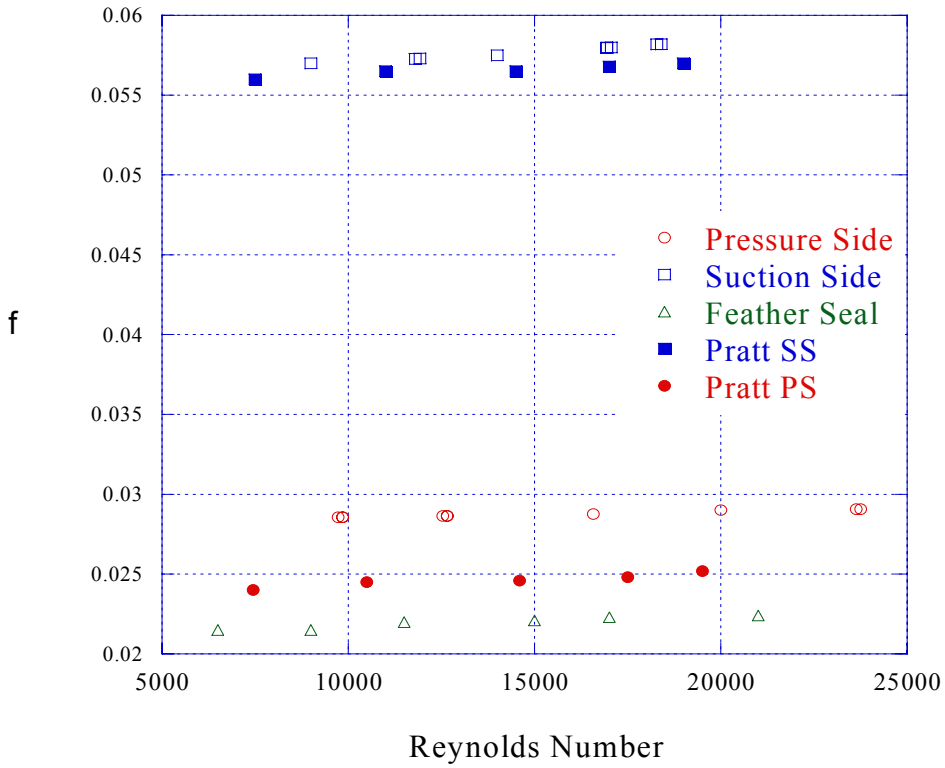

Figure 4.7 Plot of the friction factor for the pressure side, suction side microcircuits and the feather seal, as compared to Pratt & Whitney calculations.

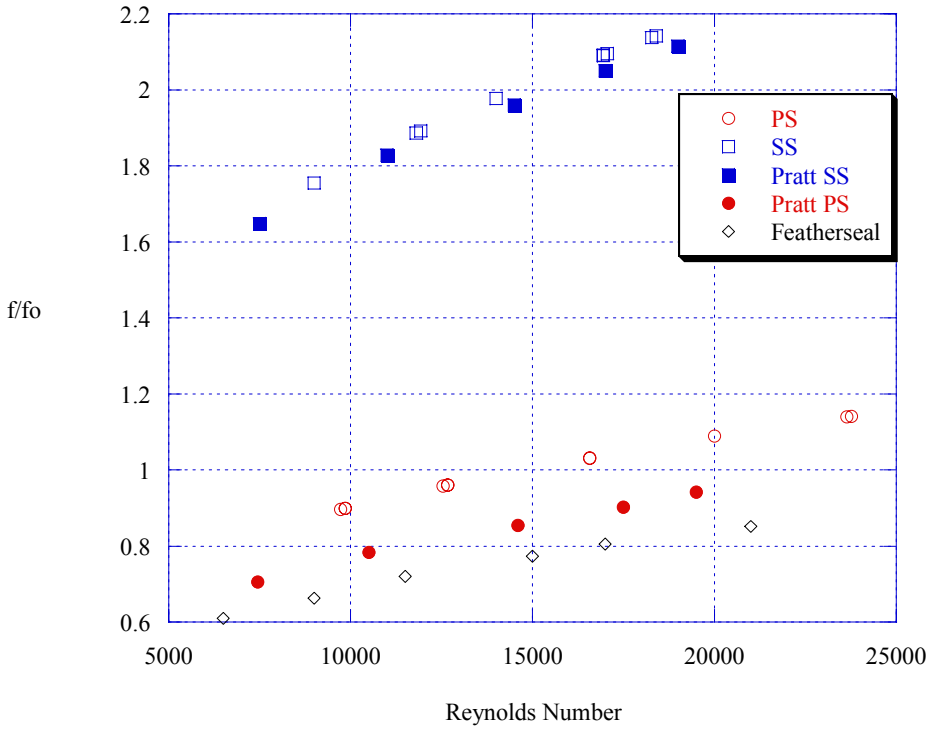

Figure 4.8 Plot of normalized friction factor, f/f_o, for the microcircuits and featherseal.

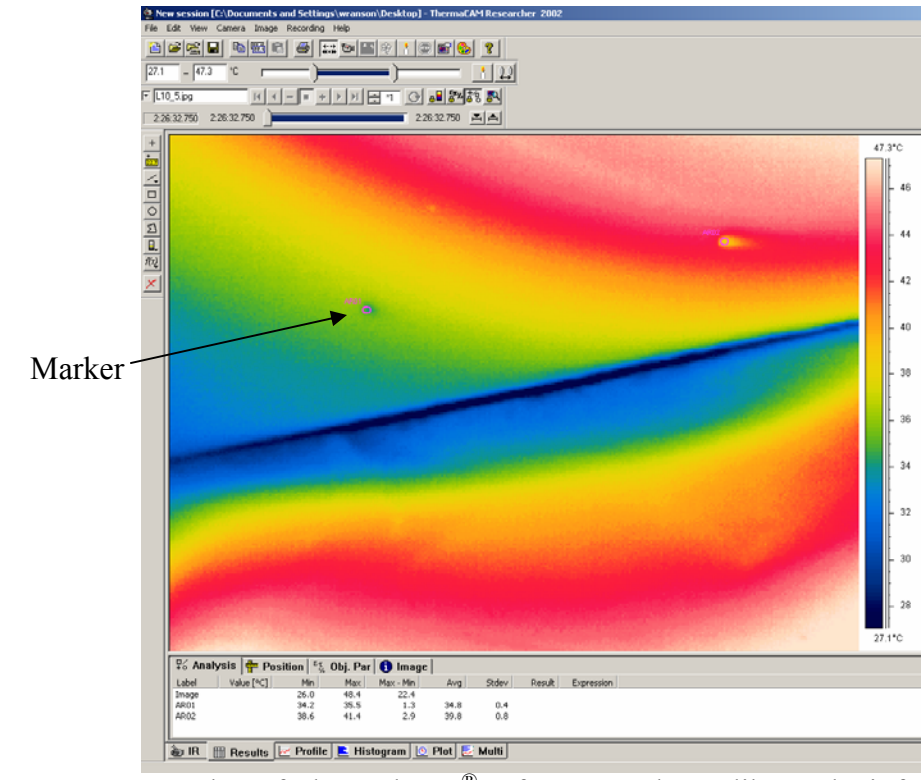

Figure 4.9 Screen shot of ThermalCam® software used to calibrate the infrared images, showing the circular icons on the picture an their temperature readings.

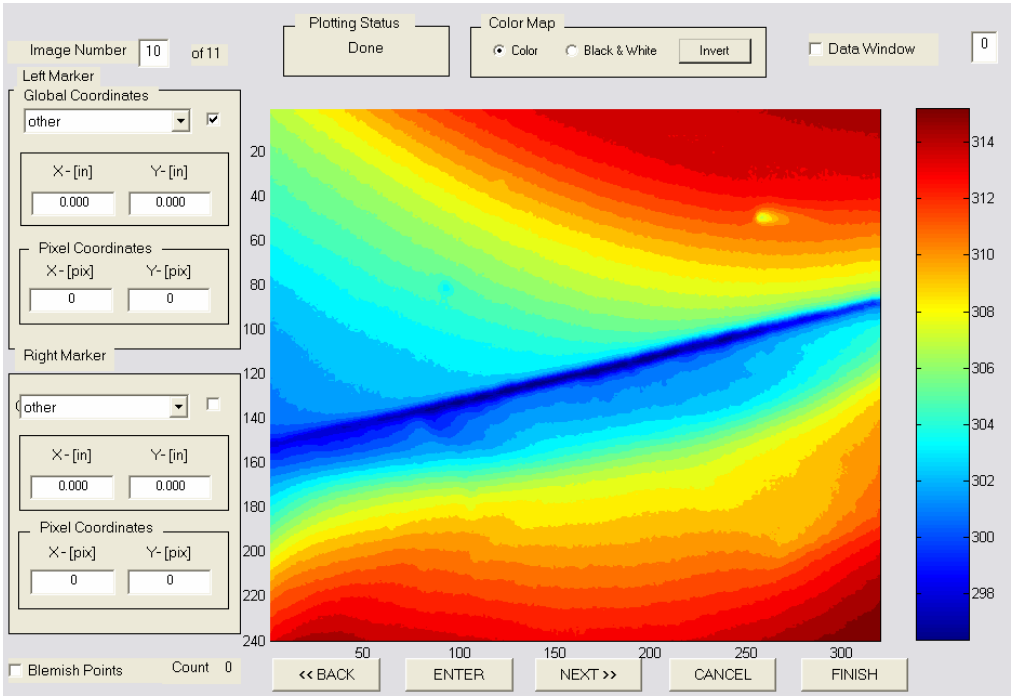

Figure 4.10 Screen shot of MatLab software used to orient the infrared images after calibration, using the same infrared image as shown in Figure 4.9.

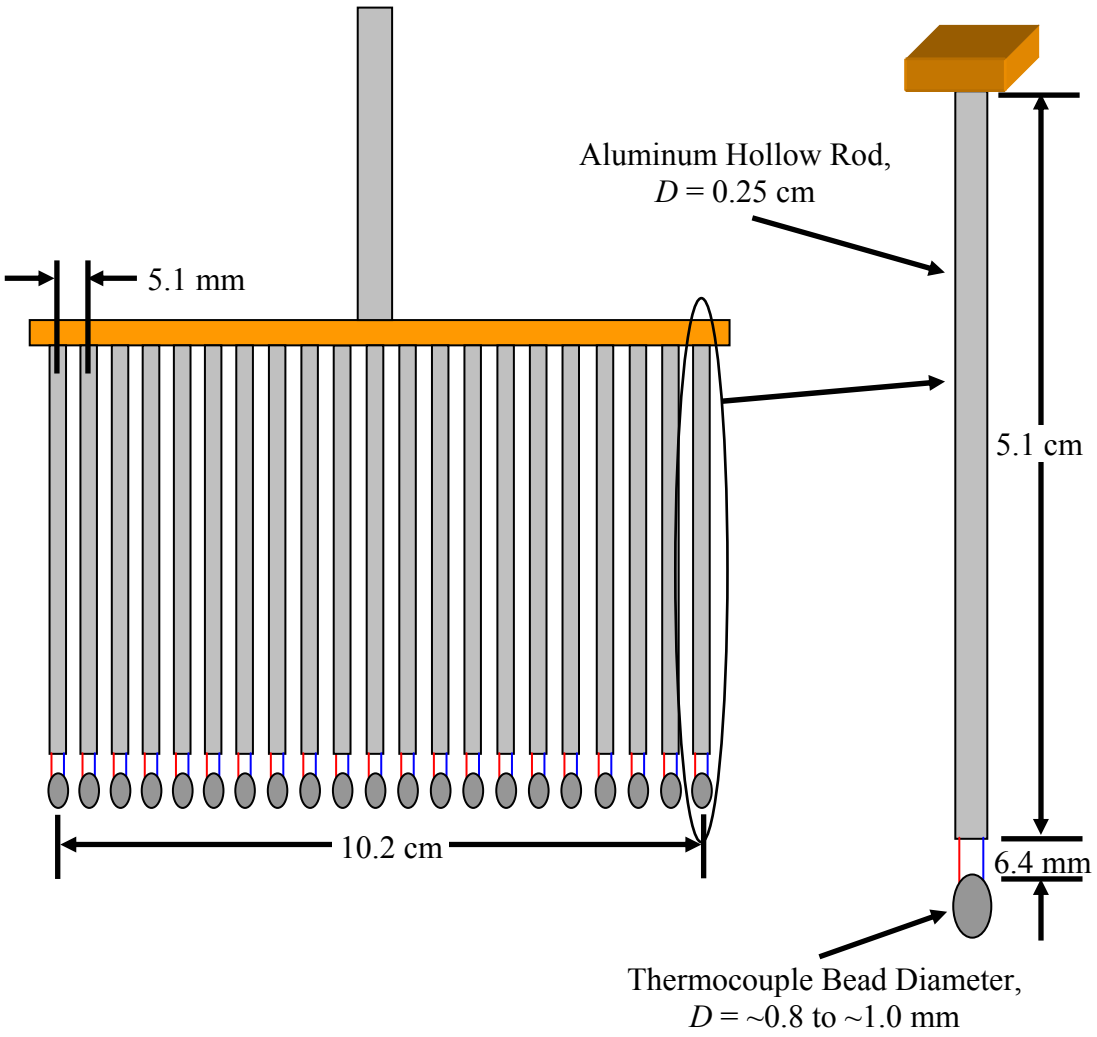

Figure 4.11 Schematic of the thermocouple rake used to take thermal field measurements of the flow above the platform.

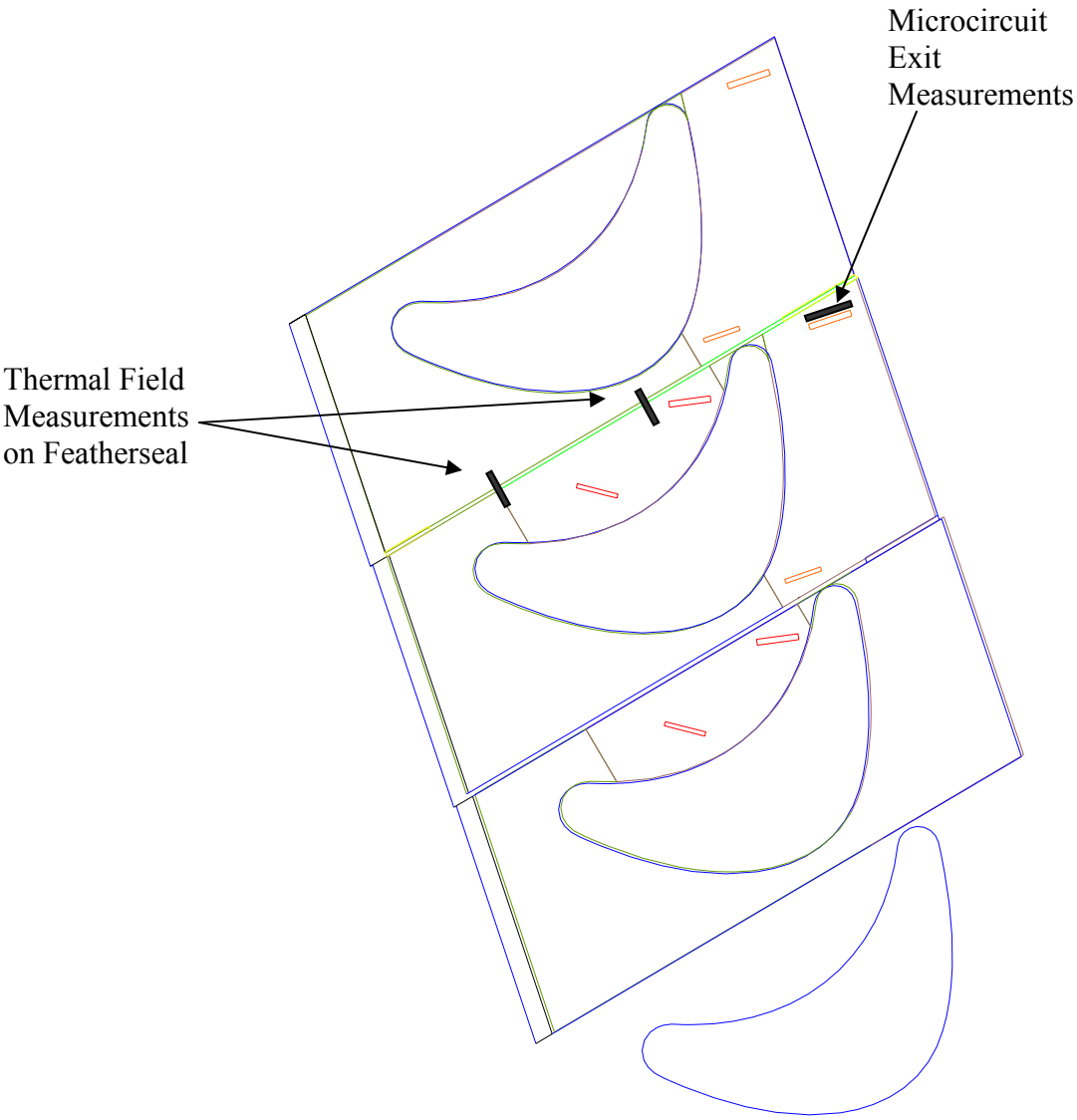

Figure 4.12 Drawing showing the four locations of thermal field measurements: two locations along the featherseal (green) and locations at the pressure side (red) and suction side (orange) .

Chapter 5: Analysis of Results

This chapter presents the results of the adiabatic effectiveness measurements of leakage flows on the hub region of a typical gas turbine engine. As previously described in Chapter 4, the temperature measurements are presented in the non-dimensional adiabatic effectiveness, η, which is described in equation (4.8). The value of adiabatic effectiveness ranges from zero to one, with zero corresponding to the freestream temperature, and one representing the coolant temperature. Presented first in this chapter are the results from the public cases with no proprietary microcircuit design. Analysis of these cases focuses on the effects of changing the featherseal and front rim flow. Next, we analyzed the results from the microcircuit cases and compared them with the computational predictions. The temperature distribution at the exit locations of the microcircuits are studied in detail The last section of this chapter describes the thermal rake measurements taken along the featherseal and microcircuit exit locations.

5.1 Analysis of Public Cases

The first public case analyzed, case A (see Table 4.1, as discussed in Section 4.1), was designed with the front rim flow at 1.5%, the featherseal at 0.25%, and the aft rim flow at 1.5%. Figure 5.1 shows the resulting thermal variations along the hub region for this leakage coolant configuration. In Figure 5.1, the front rim leakage dominates the cooling of the hub region. Just downstream of the front rim, the adiabatic effectiveness measurements are between 0.8 and 0.9. In Figure 5.1, the actual front rim slot has been covered with a blue rectangle because the 17° angle of the front step affects the results. The front step affects the results because as the images are calibrated and oriented (as discussed in Section 4.4), any three dimensional features will be skewed when viewed directly from above. Since the thermal profiles along the hub region are of main interest, ignoring the thermal variations along the backward facing front step did not affect the objectives of this research.

In addition to a patch over the backwards facing front step, there are patches over the blade locations. The size of the patches includes the size of the fillet at the blade-platform intersection. Since the curvature of the fillet distorts the thermal images when viewed from above, the fillet was not included in the adiabatic effectiveness contours.

The dotted lines in Figure 5.1 represent the actual blade shape within the gray patch over the blade-fillet area.

Although the coolant from the front rim provides ample cooling of the hub region downstream of the slot, the leading edges of the blades are not significantly cooled. Near the leading edges of the blades, the adiabatic effectiveness values are below 0.2. Although there is a large amount of coolant from the front rim, almost none of that coolant helps cool the leading edges of the blades, as the stagnation point flow prevents coolant from reaching the leading edge of the blades. Examination of the lower passage in Figure 5.1 shows the front rim coolant has almost no affect on cooling the pressure side of the blades either. The adiabatic effectiveness values near the trailing edge pressure side of the blades are close to zero. The lack of pressure side cooling from the front rim slot matches the results of Nicklas [2001], who also showed that even with ample cooling from the front rim, the film cooling effectiveness decreases towards the pressure side corner of the blades. Additionally, the high adiabatic effectiveness values at the front of the blade passage caused by the front rim cooling agree with the results observed by Burd et al. [2000], Knost and Thole [2003], and Colban et al. [2003].

Additionally shown in Figure 5.1, in the lower passage, the leading half of the suction side of the blades is cooled by the front rim leakage. However, towards the trailing edge of the blades, the front rim flow has no affect on the suction side of the blades. After 60% of the chord length, the adiabatic effectiveness values between the blades are below 0.2. In contrast to the lower passage in Figure 5.1, the coolant leakage out of the featherseal in the upper passage provides more cooling to the trailing edge suction side of the blades. Without the featherseal, the adiabatic effectiveness values near the trailing edge of the suction side are below 0.15, while the adiabatic effectiveness values near the trailing edge with the featherseal coolant are 0.55. However, the flow out of the featherseal does not have an effect on the cooling of the pressure side of the blades.

The featherseal flow has more of an effect on the suction side of the blades because the inherent pressure distribution in the blade passage tends to pull flow from the pressure side to the suction side of the blades. This flow from pressure side to suction side can be seen in the thermal variations of the lower passage in Figure 5.1, as warmer flow is pulled from the midchord of the pressure side of the blades to the trailing edge of

the suction side of the blades. Oke et al. [2000] also observed coolant flow drawn across the endwall towards the suction side of the blades because of the passage cross-flow from pressure side to suction side.

Additionally shown in Figure 5.1, the flow out of the featherseal is swept towards the pressure side of the blades near the leading edge of the passage. However, towards the mid-passage, the flow from the featherseal is swept back towards the suction side of the blades. The flow is initially swept towards the pressure side of the blades because the flow inlet angle pushes the flow towards the pressure side. However, as the pressure distribution in the blade passage overcomes the inlet flow momentum, the coolant from the featherseal crosses over itself and is then swept back towards the suction side of the blades.

There is actually more coolant leaking out of the featherseal in the trailing edge than the leading edge in Figure 5.1. There appears to be less featherseal flow on the trailing edge because the coolant is quickly swept away from the featherseal by the strong cross passage flow from pressure side to suction side. In the leading edge of the featherseal ,the combined presence of the featherseal and front rim coolant creates the illusion there is more coolant flowing from the featherseal. In actuality, there is more coolant from the trialing edge of the featherseal, as the flow from the featherseal is dictated by the static pressure on the hub surface. As the velocity in the passage increases, the static pressure on the hub decreases, allowing more flow out of the featherseal in the trailing edge.

Even though the coolant flow out of the featherseal near the trailing edge of the blades is not as visible as the flow from the leading edge, the overall effect of the featherseal on the hub cooling is more pronounced near the trailing edge. Near the end of the featherseal, the adiabatic effectiveness values on the hub increase by more than two times across the featherseal. As warmer air is swept from the pressure side of the blades to the suction side of the blades, the featherseal flow provides a layer of film cooling. The flow from the featherseal remains near the hub region, providing a thermal barrier between the hot mainstream and the platform. In contrast to the thermal variations near the trailing edge, the adiabatic effectiveness values are similar on both sides of the featherseal near the leading edge. Since the leading edge is dominated by coolant from

the front rim, the featherseal affects are difficult to distinguish from the front rim affects. In the mid-passage, the featherseal flow is affected by the secondary flow fields. As the featherseal flow crosses over from being swept towards the pressure side to being swept towards the suction side, the secondary flow affects are increased. Aunapu et al. [2000] also observed increased secondary flow fields when blowing was introduced from a slot in the mid-passage.

Lastly, the results in Figure 5.1 show the aft rim has less effect on the cooling of the hub region near the blades than either the front rim or featherseal. The majority of the flow out of the aft rim cools the hub region directly downstream, but the aft rim cooling is significantly less than the front rim cooling. Downstream of the aft rim, the adiabatic effectiveness values are in the range of 0.45-0.55. Downstream of the front rim, the adiabatic effectiveness values range from 0.75-0.95, showing the aft rim has less of a cooling effect. Additionally, since this study is only concerned with one blade row, the affects of aft rim cooling on the next blade row cannot be analyzed. In reality, the aft rim of this research is the front rim for the second row of stator vanes in an actual gas turbine engine.

As mentioned in the previous chapter, we repeated cases to ensure accurate measurements and to ensure there were periodic flows within the test section. The first case show in Figure 5.1 was taken September 29, 2003. One week later, on October 6, the first case was performed again. Figure 5.2 shows the results of repeating a test case inside the wind tunnel. Figure 5.2 shows there are no major differences between the two cases, as all of the trends discussed of Figure 5.1 are apparent in Figure 5.2.

To analyze the effects of the featherseal, we tested the flow out of the featherseal at three levels while keeping the other leakage flows constant. Figure 5.3 shows results from leakage flow out of the featherseal of 0.25%, 0.5%, and 0.75% with the front and aft rim flows at 1.5%. The first case in Figure 5.3 is the same case shown in Figure 5.1, repeated again for reference. Only the passage with the featherseal is shown for the remaining two cases because the flow in the bottom passage is identical for all three cases. In all three cases shown in Figure 5.3, there appears to be no affect in the overall cooling of the hub region, even though the flow though the featherseal is doubled and tripled. All three cases show the same trends and same adiabatic effectiveness values

around the featherseal. There is no additional cooling on the trailing edge suction side of the blades with the increased featherseal cooling. The results in Figure 5.3 indicate that as the flow out of the featherseal is increased, the momentum of the flow causes the coolant to be blown into the mainstream. Thus, increasing the amount of cooling though the featherseal does not provide any additional cooling to the hub region. Instead, cooling flow is wasted as it is ejected into the mainstream.

To quantify the lack of additional cooling from increasing the featherseal flow, we calculated laterally averaged adiabatic effectiveness values for the first three cases shown. Laterally averaged values were calculated based upon averages of all the adiabatic effectiveness values along a line perpendicular to the featherseal. Figure 5.4 shows a schematic of two blades with rectangles representing the regions between the blades, perpendicular to the featherseal, that were averaged into one value. For the actual calculations, the width of each averaged line was 0.83% of the blade axial chord, but the width of the rectangles in Figure 5.4 is exaggerated for clarity. Along each line, points were taken from the data in squares of size 3.5 mm. The square size of 3.5 mm is also shown in Figure 5.4, which shows that each point used in the line average is actually an average of individual data points. The size of the square and number of data points shown in Figure 5.4 has been exaggerated for clarity, since each square size of 3.5 mm encompasses between 16 and 25 actual data points.

Figure 5.5 shows a plot of average adiabatic effectiveness values for the first three public cases where the featherseal flow is increased from 0.25% to 0.75%. The average adiabatic effectiveness values start at the leading edges of the blades and end at the trailing edge of the blades. Figure 5.5 shows that the case of 0.75% featherseal flow actually has the lowest average adiabatic effectiveness value of all three cases, suggesting the increased blowing causes increases in the secondary flows, which pulls more coolant off the hub. However, within the uncertainty of the average adiabatic effectiveness values, Figure 5.5 shows there is no cooling increase when the flow out of the featherseal is increased. The decreasing trend of the averaged adiabatic effectiveness values while moving down the featherseal shows the decreasing effect of the front rim in the passage. The increase in the laterally averaged adiabatic effectiveness values near $x/Bx = 0.9$ is caused by the featherseal affects on the trailing edge suction side of the blades. At a

location of x/Bx = 0.8, a laterally averaged line will include the adiabatic effectiveness values below 0.15 on the pressure side of the blades. Near x/Bx = 0.9, a line perpendicular to the featherseal will average the low adiabatic effectiveness values on the pressure side with the higher adiabatic effectiveness values near the trailing edge of the suction side, which causes the increase in average adiabatic effectiveness.

Although increasing the featherseal flow does not significantly increase the cooling of the hub region, increasing the coolant from the front rim significantly increases cooling of the hub region. Figure 5.6 shows the cases where the front rim flow is changed from 0.5% to 1.5% and 2.0% while the featherseal remains at 0.25% and the aft rim remains at 1.5%. As shown in Figure 5.6a, there is considerably less leading edge cooling as a result of the 0.5% front rim cooling. Directly upstream of the blades, there is no visible coolant from the front rim for this case as the stagnation point flow prevents any flow from leakage out of the front rim. Increasing the leakage flows causes the coolant from the front rim to travel farther into the passage, as shown in Figure 5.6b, causing higher adiabatic effectiveness values. When the front rim flow is increased to 2.0%, the adiabatic effectiveness values near the trailing edge of the suction side passage without the featherseal are increased from 0.5 to 0.15, showing the coolant from the front rim stays near the hub region for the entire chord length of the blades. Additionally, the coolant from the front rim leakage of 2.0% in the lower passage appears to wrap around the suction side of the blades.

To further quantify the effects of increasing the front rim flow, we calculated laterally average adiabatic effectiveness values for these cases. Figure 5.7 shows laterally averaged adiabatic effectiveness values for the three cases analyzed in Figure 5.6. Throughout the entire blade passage, the average adiabatic effectiveness values are higher by 0.2 for the front rim leakage flow of 2.0% as compared to the 0.5% front slot case. The laterally averaged values show that increases in the amount of from rim cooling affect the entire blade passage. The three curves in Figure 5.7 show identical trends that seem to be shifted based upon the amount of from rim cooling.

5.2 Analysis of Microcircuit Cases

The microcircuit cases were analyzed once we completed the baseline public case work. Shown in Figure 5.8a is the first microcircuit case analyzed, with 0.25% coolant flow through each of the microcircuits and no flow out of the front rim, featherseal, or aft rim. In reality this test case could not exist; however, testing only the microcircuits eliminates affects from other leakage features. Unfortunately, the thermal results in Figure 5.8a show there was considerable conduction through the foam where the microcircuits are molded into the platform. This conduction error did not exist during testing of the public cases for two reasons. First, there was no coolant flow in the microcircuits, where the visible conduction error occurred. Secondly, the foam thickness in the platform (1.9 cm thick) provided enough insulation to prevent any measurable temperature change on the platform from the coolant in the featherseal plenum underneath the platform. However, because the microcircuits are molded into the platform foam, the thickness of foam between the top of the microcircuit and the platform was 0.32 cm. Because the foam was six times thinner above the microcircuits than in other areas of the platform, the temperature of the platform was cooled by the microcircuit through conduction.

Since the microcircuits were designed to cool the platform using conduction cooling, this conduction error showed the microcircuits do add additional cooling to the platform region through internal convective cooling. However, since the objective of this study was to quantify the cooling based upon an adiabatic assumption, a conduction correction was modeled into the analysis. To correct the adiabatic effectiveness measurements on the hub region, the resulting adiabatic effectiveness values were normalized to the corrected adiabatic effectiveness based upon the equation derived by Bogard et al [2000]:

$$\eta = \frac{1}{(1-\eta_o)}(\eta_{meas} - \eta_o) \tag{5.1}$$

where η_o is the conduction error, and η_{meas} is the adiabatic effectiveness value measured on the surface. Since the exact geometries of the microcircuits was known, by applying equation (5.1) to the areas of the microcircuits, the conduction error from the microcircuits was accounted for. Analysis of the conduction error showed almost no

lateral conduction in the foam. The value of η_o used for each case was based upon the adiabatic effectiveness values from the matching public case where there was no cooling though the microcircuits and thus no conduction error. The value of η_o was 0.05 for the low flow microcircuit cases (microcircuit cooling flow below 0.3% of the mainstream) and 0.1 for the high flow microcircuit cases.

Figure 5.8b shows the first microcircuit case once the conduction correction is applied to the results. Interestingly, the flow out of the microcircuits is not uniform across the exit area. Both the suction side microcircuit exit cooling patterns appear 'tooth-shaped', as more coolant exits from the edges than center of the microcircuit. Though more uniform that the suction side exits, the coolant exiting from the pressure side microcircuits is not uniform either. Interestingly, upstream of the microcircuits, the adiabatic effectiveness value on the platform is 0.05, not zero. The non-zero adiabatic effectiveness readings on the hub where no coolant is present are caused by a thermal boundary layer temperature profile from the upstream heaters to the test section.

By adding in leakage flows from the front rim and featherseal, we observed the additional affects of the microcircuit cooling on the platform. Figure 5.9 shows the test case of 1.5% front rim flow, 0.25% featherseal flow, 0.25% microcircuit flow, and 1.5% aft rim flow. For reference, the pressure side and suction side microcircuits are shown in the side of Figure 5.9 at their approximate size and orientation. Just like the microcircuit case shown in Figure 5.8b, the flow out of the suction side microcircuit is higher on the edges of the microcircuit that in the center. Additionally, compared to the pressure side microcircuits, the suction side microcircuits provide considerably less cooling.

Figure 5.9 also shows the pressure side microcircuit appears to be affected by the flow from the featherseal. With the addition of the featherseal in the top passage, the lack of uniform flow out of the pressure side microcircuit is more pronounced compared to the pressure side microcircuit flow without the featherseal in the bottom passage. Additionally, the flow from the microcircuit appears to entrain flow out of the featherseal. Downstream of the pressure side microcircuit, the additional flow from the microcircuit slot causes an increase in cooling effectiveness from the featherseal. The increase in featherseal flow at that location was not observed in the public cases without the featherseal. This result of increased effectiveness out of a slot caused by upstream

cooling matches previous literature results [Yu, 1998]. However, the results from Figure 5.9 led to two main issues regarding the microcircuit cooling. First, we needed to investigate the differences in coolant non-uniformities between the pressure side and suction side microcircuits. Second, we needed to investigate the interaction between the featherseal and pressure side microcircuit.

To further investigate the different uniformities of the coolant from the microcircuits, each microcircuit was inspected to ensure there were no blockages in the channels. After each microcircuit was checked, two more microcircuit cases were analyzed to observe the effects of increased flow through the microcircuits. The results from the second and third microcircuit cases are shown in Figures 5.10a-b, which both have 2.0% front rim flow, 0.25% featherseal flow, 0.25%-0.5% microcircuit flow, and 1.5% aft rim flow. These two additional cases show the cooling exiting from the microcircuits similarly to the case in Figure 5.9. Though the flow is increased through the microcircuits from 0.25% to 0.5%, the cooling exits in the tooth-shaped profile from the suction side microcircuits in both cases. This non-uniform distribution of flow from the suction side microcircuits shown in Figures 5.9, 5.10a-b is caused by the pedestals inside the channel, which block part of the flow in the center of the channel. Additionally, these cases show that although there is the same amount of flow through both the pressure side and suction side microcircuit, the higher pressure drop in the suction side microcircuit (see Section 4.3) causes there to be less flow out of the suction side microcircuit.

To further quantify the flow from the exits of the microcircuits, individual data points were plotted from a line perpendicular to the microcircuit exit. Figure 5.11 shows a close up view of the exit of the suction side microcircuit with a black line representing the region where adiabatic effectiveness values were taken. The case in Figure 5.11 has flow settings of 2.0% front rim flow, 0.25% featherseal flow, 0.25% microcircuit flow, and 1.5% aft rim flow. The line of interest is one slot width downstream of the suction side microcircuit and has a length of 1.5 slots, centered on the exit of the microcircuit. Figure 5.12 shows the resulting adiabatic effectiveness values that occur on the line for nine different cases. Each case is represented as the mass flux out of the microcircuit. The mass flux, M, is defined as:

$$M = \frac{\rho_j U_j}{\rho_\infty U_\infty} \tag{5.2}$$

where the velocity out of the microcircuit was calculated based upon equation (4.1) and ρ_∞, U_∞ are the respective inlet density and velocity. In Figure 5.12, which is the case of 2.0% front rim, 0.25% featherseal, 0.25% microcircuit flow, and 1.5% aft rim flow, the microcircuit width is from Z/W of -0.5 to 0.5, centered at Z/W = 0. As the mass flux out of the suction side microcircuit is increased, the resulting measured adiabatic effectiveness values on the platform are increased. However, increasing the mass flow out of the microcircuit does not change the uniformity of coolant out of the microcircuit. For all nine cases, the cooling at the edges of the microcircuit is two to three times higher than the cooling in the center of the microcircuit. These cases show that increasing the flow out of the suction side microcircuit does not add any additional flow out of the center of the microcircuit.

Although the distribution out of the suction side microcircuit is not affected by increasing the mass flux, the coolant distribution out of the pressure side microcircuit is affected by changing the mass flux. Figure 5.13a shows a close up view of the pressure side microcircuit cooling with a mass flux of 0.28, and Figure 5.13b shows the same view for a mass flux of 0.48 out of the microcircuits. There is no flow out of the front rim or featherseal for either case in Figure 5.13. By comparing the two cases, the coolant distribution appears more uniform for the higher mass flux. One would expect the lower mass flux case provides less cooling on the platform than the higher mass flux case. However, plots of adiabatic effectiveness values taken from a line one slot width downstream of the microcircuit show the highest mass flux does not provide the best cooling. Figure 5.14 shows a plot of the adiabatic effectiveness values taken from the black lines indicated in Figures 5.13. Figure 5.14 shows that a mass flux of both 0.42 and 0.34 provide at least as much cooling as the mass flux of 0.48. Unlike the suction side microcircuit, as the mass flow is increased, the amount of cooling provided is not increased. Because of the smaller size of the pressure side microcircuit, as the mass flux is increased, the additional coolant is blown off of the platform and into the freestream.

In addition to being affected by the mass flux, the pressure side microcircuit is also affected by the flow out of the featherseal. Figure 5.15a shows a close up view of

the pressure side microcircuit flow with 1.5% front rim flow, no featherseal flow, a microcircuit mass flux of 0.34, and 1.5% aft rim flow. Figure 5.15b shows the contours for 1.5% front rim flow, 0.5% featherseal flow, the same pressure side mass flux of 0.34, and 1.5% aft rim flow. The uniformity of the coolant exiting the microcircuit is decreased when combined with the featherseal. To further quantify the effect of the featherseal on the pressure side microcircuit, adiabatic effectiveness values were taken directly from the line shown in Figures 5.15. The resulting adiabatic effectiveness values from one slot width downstream of the microcircuit exit are shown in Figure 5.16. Figure 5.16 shows the featherseal decreases the cooling near the center of the microcircuit exit. Additionally, the adiabatic effectiveness values are lower near the edge of the featherseal (Z/W= -0.3). Since the featherseal flow acts as a barrier to the flow in the mainstream, the flow out of the pressure side microcircuit near the featherseal is decreased.

Additionally shown in Figure 5.16, the resulting adiabatic effectiveness values including the featherseal spike at Z/W= -0.7. This spike is actually the flow out of the featherseal, showing its proximity to the pressure side microcircuit. Interestingly, the measured adiabatic effectiveness directly over the featherseal only has a maximum adiabatic effectiveness of 0.6. Because the microcircuit coolant provides a relatively stable coolant boundary layer, an addition of coolant from the featherseal promotes better cooling. This increased cooling from the featherseal matches the results of Yu [1998], who observed the increase of flow from a gap affected by upstream cooling.

To show the overall effect of the microcircuits in externally cooling the platform, laterally averaged adiabatic effectiveness values were calculated for the microcircuit cases. Just as in the public cases, these averages were taken along lines perpendicular to the featherseal. Figure 5.17 shows average adiabatic effectiveness plots for two microcircuit cases and two public cases, where the front rim flow is varied from 1.5%-2.0%, the featherseal is 0.25%, the microcircuit is 0.25%, and the aft rim is 1.5%. These average adiabatic effectiveness plots show the same values of platform temperature upstream of the microcircuits, because the cooling patterns upstream of the microcircuits were the same. However, near x/Bx = 0.8, while the average adiabatic effectiveness

values for the public cases continue to decrease, the cooling on the platform is increased because of the microcircuits.

Through analysis of the microcircuit data, it was shown the slot cooling from the pressure side microcircuit helps cool the suction side of the blades. Unfortunately, the pressure side microcircuit is adversely affected by flow from the featherseal, which acts as a barrier to the microcircuit exit slot cooling. Though the pressure side microcircuit has a mass flux ratio that produces the best cooling, there is no such optimum for the suction side microcircuit. Unfortunately, for all mass flux ratios tested (which define the operating limits of the microcircuits), the uniformity of the suction side microcircuit did not improve. For all tests, more coolant flowed from the edges of the microcircuit than from the center.

5.3 Comparisons to Computational Studies

Many of the experimental cases presented in this chapter were also modeled computationally. Initial computational modeling was performed by Hohlfeld [2003] before the experimental test rig was constructed. After we analyzed the data, some of the coolant mass flow percentages were changed and re-modeled from the original computations. Although the computational design, mesh, and grid independence have previously been described in detail [Hohlfeld, 2003], the computational geometries and boundary conditions are shown in Figures 5.18a and 5.18b. The computational domain contained one blade passage with the featherseal, front and aft rim, and microcircuits. This domain corresponds to the top blade passage in the experimental test rig. A commercially available CFD code, Fluent 6.0, was used to perform the computational simulations.

Figure 5.19a shows the computational contours of cooling effectiveness, which correspond to the first experimental case of 1.5% front rim flow, 0.25% featherseal flow, and 1.5% aft rim flow. For comparison, the first experimental case (Figure 5.1) has been repeated in Figure 5.19b. By comparing the two cases shown in Figure 5.19a,b, the computations overpredict the cooling benefit from the front rim leakage. However, the computational predictions match the cooling trends shown in both the experimental data and open literature. For both cases, there is little cooling on the pressure side of the

blades, especially near the trailing edge. Both cases show there is not much cooling of the leading edge of the blades, even though there is plenty of coolant from the front rim.

Figures 5.19c and 5.19d show the computational cases for 2.0% front rim cooling with 0.25% featherseal flow, and 2.0% front rim coolant with 0.75% featherseal flow; both cases having 1.5% aft rim flow. These cases also show that compared to the experimental results, the computations overpredict the effects of the front rim cooling. The increased coolant from the front slot provides more coolant to the blade passage, shown by the increased cooling of the leading edges of the blades as compared to the previous computational case (Figure 5.19a). Figure 5.19d shows the computations predict no additional cooling with increased featherseal flow. The trailing section of the blade passage is predicted to be cooled more by the 0.25% featherseal flow conditions than the 0.75% featherseal flow conditions, as seen by a comparison of Figure 5.19a with Figure 5.19c and Figure 5.19d. As the featherseal flow is increased, the computations predict no additional hub cooling.

Additionally, the cases show similar cooling trends from the featherseal leakage. In both the computational and experimental testing, the featherseal coolant benefits are more pronounced near the trailing edge than the leading edge. The computational model slightly underpredicts the cooling benefit from the featherseal near the suction side trailing edge. Additionally, though the computational results underpredict the effect of the aft gutter, both cases show the aft gutter has little to no affect on the overall cooling of the hub region.

To clarify the computational predictions of the flow out of the featherseal, Figure 5.20a shows streamlines of temperature released from the featherseal. Though not shown in Figure 5.20a, there is also coolant flow from the front rim as the streamlines are from the same computational case shown in Figure 5.19b, which has 1.5% front rim flow, 0.25% featherseal flow, and 1.5% aft rim flow. The computational streamlines show the characteristics of the featherseal flow that were observed in the experimental testing. The streamlines are first swept towards the pressure side of the blades near the leading edge, then they are swept back towards the suction side of the blades near the trailing edge, matching the featherseal affects seen in the experimental cases.

The streamlines from the featherseal show the secondary flow fields have a large effect on the streamlines in the mid-passage, particularly the location where the featherseal flow crosses over from being swept towards the pressure side to being swept towards the suction side. To show these effects, Figure 5.20b shows the same featherseal streamlines as Figure 5.20a, but colored by height above of the hub. These streamlines show that near the location of featherseal coolant crossover in the middle of the blade passage, the resulting secondary flows pull the coolant off the hub. In contrast, the streamlines from the trailing edge of the featherseal remain on the platform, providing a coolant barrier for the suction side of the blades. The streamlines show how the featherseal flow cools the trailing edge of the blade passage more than the leading edge. These results match the results of Aunapu et al. [2000], who observed higher secondary flows in the passage as a results of blowing from a slot in the passage.

Just as the computational predications were able to capture the trends of cooling in the public cases, the computational results for the microcircuits showed similar trends as the experimental results. Figure 5.21a shows the computational effectiveness for a microcircuit case, and Figure 5.21b shows the experimental version of the same case containing 2.0% front rim flow, 0.25% featherseal flow, 0.25% microcircuit flow, and 1.5% aft rim flow. These figures illustrate that again, the front rim cooling is overpredicted by the computational modeling. However, the trends of the flow out of the pressure side microcircuit are similar to the trends observed in the experimental cases. The coolant out of the microcircuit is not uniform, and there appears to be a slight decrease in the effectiveness in the middle of the microcircuit exit. Just as in the experimental case, the flow out of the featherseal is increased in the region directly downstream of the pressure side microcircuit.

Though the computational models match the trends in the pressure side microcircuit, the modeled coolant out of the suction side microcircuit appears more uniform than experimentally observed. Though both cases show the flow out of the suction side microcircuit is less than the flow from the pressure side microcircuit, the predicted cooling from the suction side microcircuit is overpredicted. However, the computational prediction of suction side flow leads to questions of the experimental flow. Since conduction errors were visible in the experimental microcircuit flow, the coolant

inside the suction side microcircuit could have been heated by conduction. However, the contour plotted in Figure 5.11 shows that the adiabatic effectiveness values for the coolant exiting the microcircuit are 1.0. Thus, although the comparison between experimental and computational results suggest conduction errors could cause the differences in cooling from the suction side microcircuit, it appears the computational model still overpredicts the cooling.

Analysis was also performed on the microcircuit case to observe if any of the featherseal effects shown in the experimental tests were predicted. Figure 5.22a shows the predicted cooling when 0.25% cooling flow is released only from the microcircuits. The previously shown experimental results are shown again in Figure 5.22b for reference. Comparison between these two cases shows the cooling benefit from the microcircuits is slightly overpredicted. However, the predicted flow from the pressure side microcircuits is more uniform in Figure 5.22a than the predicted uniformity in Figure 5.21a, which contains 2.0% front rim flow, 0.25% featherseal flow, 0.25% microcircuit flow, and 1.5% aft rim flow. Thus, the computational models also predict the uniformity of the flow out of the pressure side microcircuits is decreased by the presence of the featherseal flow. However, unlike the experimental data, the predicted flow from the suction side microcircuits is uniform, regardless of other leakage flows.

To further compare the computational and experimental results, we calculated averaged adiabatic effectiveness values for both the public and microcircuit cases. Figure 5.23 shows a plot of the averaged values for both the predicted and experimental cases with flow ranges of 0.5%-2.0% front rim flow, 0.25%-0.75% featherseal flow, no microcircuit flow, and 1.5% aft rim flow. As expected, near the leading edge the computational values are higher since the front rim cooling was overpredicted. However, the trends for the cases show that the computational predictions were able to match the experimental flows within the blade passage. For the microcircuit only case of 0.25% flow, the averaged adiabatic effectiveness values shown in Figure 5.24 show there is very good agreement between the computational and experimental results. Although the computational adiabatic effectiveness values are slightly higher, the trends are nearly identical. The experimental values upstream of the microcircuit were not 0.0 because of the thermal entrance effects that were previously discussed.

Through the computational and experimental comparison, it was shown that although the computations slightly overpredicted cooling, the computations followed the same trends observed in the experiments. In regard to the microcircuits, the cooling predictions for the pressure side microcircuit were more accurate than the suction side microcircuit. However, these results show that CFD can be used as a first step in redesigning the location, shape and size of the microcircuits in the platform.

Additionally, Hohlfeld [2003] generated pressure distributions across the hub region. Though the pressure distribution across the entire hub region was out of the scope of this research experimentally, we took pressure measurements along the hub region to calculate the mass flows out of each of the plenums (see Section 4.3). Figure 5.25 shows the computationally predicted pressure distribution across the hub region. A comparison of the experimental pressure values along the hub region to the computationally predicted values shows good agreement within the blade passage. We calculated C_p values of -6.7 from the pressure taps directly downstream of the pressure side microcircuit exits, which matches the computational range of -6.6. However, based upon the pressure taps downstream of the suction side microcircuits, we calculated C_p values of -8.2 versus the computationally predicted values near -8.0. Thus, the computations seem to slightly overpredict the pressure along the hub region near the suction side microcircuits and aft gutter.

The pressure results from the computational work show that the platform pressure decreases towards the end of the blade passage. This decreasing pressure variation causes there to be more flow out of the featherseal near the trailing edge. With the aid of the computational pressure distribution around the hub region, the local momentum flux ratio was calculated at the two regions where the thermal rake measurements were taken for the case of 1.5% front rim flow, 0.25% featherseal flow, and 1.5% aft rim flow. Based upon the inviscid freestream velocity from the mid-chord and the local static pressure, the local momentum flux ratio out of the front section of the featherseal was calculated to be 1.24. We calculated the momentum flux out of the aft of the featherseal to be 1.3. Thus, changes in the velocity out of the featherseal do not account for the differences is hub cooling. Since the momentum flux is constant across the featherseal, secondary flow effects must be causing the observed flow patterns out of the featherseal,

especially in the blade passage near the crossover point. These calculations match the observed flow out of the featherseal in both the computational streamlines (Figures 5.20a-b), showing the featherseal flow is lifted off the hub in the blade passage by the increased secondary flows.

Though the trends in hub pressure appear similar, the results from the computational results were used to calculate if there was ingestion of the hot mainstream gasses into the plenums. The relatively high pressure readings near the trailing edge of the blades in the hub pressure distributions shown in Figure 5.25 are the most likely area for ingestion. A review of Figure 5.1 shows no cooling from the end of the featherseal and beginning of the aft gutter at this location, since the adiabatic effectiveness values are identical on both sides of the gutter. The computational pressures predict ingestion of the flow at this location. Two thermocouples that were placed within the aft gutter in an attempt to measure ingestion recorded a temperature increase of less than 0.4° C, which is barely above the thermocouple uncertainty. Additionally, just as computational predictions show no coolant from the aft gutter, experimentally there was a slight cooling advantage from the aft gutter as the adiabatic effectiveness values are increased downstream of the aft gutter.

5.4 Analysis of Thermal Field Measurements

To quantify the thermal variations above the platform region, we took thermal rake measurements at three locations along the platform: near the leading edge of the featherseal, near the trailing edge of the featherseal, and above the suction side microcircuit. The locations of these measurements are detailed in section 4.5. For all of the featherseal measurements, the front rim was set at 1.5% of the total inlet flow, and the featherseal flow was set at 0.25% for the low flow conditions and 0.75% for the high flow conditions. There was no aft rim flow used for the thermal field measurements as the aft rim was significantly downstream of the measurements. These results were then compared to thermal profiles taken from the computational predictions.

Experimental Results

The thermal rake measurements near the leading edge of the featherseal for the low flow condition (0.25% featherseal flow) are shown in Figure 5.26a, and for the high flow condition (0.75% featherseal flow) in Figure 5.26b. These figures are shown looking downstream from the combustor simulator (the pressure side of the blades is on the right hand side). The location of the featherseal is indicated in each figure, which is the location of X/P = 0. Negative values of X/P are towards the suction side, and positive values are towards the pressure side. Figure 5.26a shows for the low flow condition near the leading edge of the featherseal, the coolant flow is swept towards the pressure side of the blades. The coolant in the low flow case remains near the platform region, which is beneficial to hub cooling. The additional coolant on the left side of the featherseal is coolant from the front rim leakage.

As the flow out of the featherseal is increased to 0.75%, the thermal rake measurements in Figure 5.26b show this additional cooling is blown into the mainstream. Although the adiabatic effectiveness values above the featherseal are higher than in Figure 5.26a, there is no additional cooling benefit from the increased flow. These thermal rake measurements near the leading edge of the blades provide further data that increasing the featherseal flow does not increase the platform cooling.

Although the coolant from the front part of the featherseal is swept towards the pressure side of the blades, the coolant from the aft of the featherseal is swept towards the suction side of the blades. Figure 5.27a shows the thermal rake measurements along the trailing edge of the featherseal for the low flow condition (0.25% featherseal flow) with 1.5% front rim flow. Though there is not as much coolant on the hub surface, there is a cloud of coolant just above the platform. Because the coolant from the aft section of the featherseal stays on the hub region as it is swept towards the suction side of the blades, the thermal rake measurements of the mainstream did not capture the coolant from the featherseal at that specific location. This coolant above the hub is not blown off coolant from the featherseal. Since the coolant is swept towards the suction side of the blades, the cloud of coolant in Figure 5.27a is actually coolant from upstream in the blade passage that was entrained off the platform by the increased secondary flow fields. Thus, these thermal rake measurements provide support that secondary flow fields in the blade

passage are pulling the featherseal coolant off the hub, creating a vortex of coolant in the mainstream that travels down the blade passage. These thermal rake measurements also support the computational streamlines that show the featherseal coolant is lifted off the platform by the secondary flow fields.

When the flow out of the featherseal is increased from 0.25% to 0.75%, as shown in Figure 5.27b with 1.5% front rim flow, the observed cloud of coolant is higher in the freestream, showing the upstream increases in secondary flows force more coolant into the mainstream. The cloud of coolant visible in Figures 5.27 could be due to the effect of the pressure side leg of the passage vortex. It has been well documented that coolant injection near the vortex lift off region is inefficient as most of the coolant leaves the surface [Friedrichs et al. 1996]. The cloud of coolant visible in Figures 5.27 appears to be a vortex shape, which suggests the cloud shape is a function of the passage vortex.

Just as the thermal rake measurements along the featherseal show the wasted coolant in the freestream, thermal rake measurements along the suction side microcircuit show similar coolant losses. Figure 5.28a shows thermal rake measurements along the suction side microcircuit for a front rim flow of 1.5%, no featherseal flow, and microcircuit flow of 0.4%. Just as the thermal variations along the hub region, there is significantly more coolant from the edges of the microcircuit than from the center. Additionally, since there is little coolant in the middle of the microcircuit exit, warmer freestream air is not blocked by the microcircuit. Thus, there are not the typical cooling advantages common to slot flow because of the non-uniformity of the coolant. Even when the flow through the microcircuit is decreased to 0.2%, as shown in Figure 5.28b, there is still little coolant in the middle of the microcircuit. The thermal rake measurements along the suction side microcircuit, along with the thermal measurements on the hub region, show there is no coolant exiting from the middle of the slot. This non-uniformity does not provide the optimum cooling expected for slot flow. Additionally, the length of the coolant injected into the freestream is comparable to the length of cooling effectiveness on the platform. To provide greater cooling to the platform, the length of cooling effectiveness injected into the freestream should be decreased, possibly by changes in the exit angle of the microcircuit slot.

Computational Results

To compare the experimental thermal rake measurements, we took thermal planes of data from the computational results that matched the same flow conditions of 1.5% front rim flow with 0.25% and 0.75% featherseal flows for the low and high cases, respectively. Figures 5.29a-b show the computational thermal variations for the low and high thermal rake measurements along the front of the featherseal. The location of the actual featherseal is indicated on each image. Just as in the experimental cases, the flow from the featherseal is swept towards the pressure side of the blades near the leading edge. While increases in the experimental cases showed significant increases in mainstream temperatures with increased featherseal flow, Figure 5.29b shows only slight increases in mainstream temperatures with increased featherseal flow. Instead, the computational results seem to indicate there is more of a pitch-wise increase in coolant with increases in featherseal flow. However, overprediction of front rim cooling alters the thermal plane results shown in Figures 5.29 a-b.

Just as both computations and experiments predicted the featherseal flow to be swept towards the pressure side near the leading edge, both predicted the featherseal flow is swept towards the suction side in the trailing edge (Figures 5.30a-b). Because the coolant from the aft section of the featherseal stays on the hub region as it is swept towards the suction side of the blades (shown in computational streamlines in Figures 5.20a-b), the thermal plane at this specific location did not capture the coolant in the mainstream from that specific featherseal location. Both the low and high flow conditions predict a vortex-shaped pattern of cooling in the mainstream, which shows the affects of the upstream secondary flows pulling the featherseal coolant off the hub region. As the coolant is entrained in the stronger secondary flows, the vortex passes down the blade passage. It is this vortex that is observed in the computational and experimental results. Though the computations do not predict as much coolant entrained in this vortex pattern, they still predict the vortex flow in the mainstream above the trailing edge of the featherseal.

Experimental thermal rake measurements were taken along the suction side microcircuit exit to verify the non-uniformity observed in the adiabatic surface measurements. Since the computations did not predict the coolant non-uniformity

observed in the experimental data, computational thermal planes of the microcircuit cooling would not come close to matching the experimental results. One could speculate the computations overpredicted the coolant uniformity because of the size of the microcircuits. The number of nodes required to accurately mesh the entire microcircuits to the same level as the entire hub region would have created a mesh too large for our computational abilities.

Through analysis of the experimental and computational thermal rake measurements, good agreement was achieved with predictions in both the leading edge and trailing edge of the featherseal. Though the magnitudes of temperature were not always correctly predicted, the flow trends and characteristics were similar.

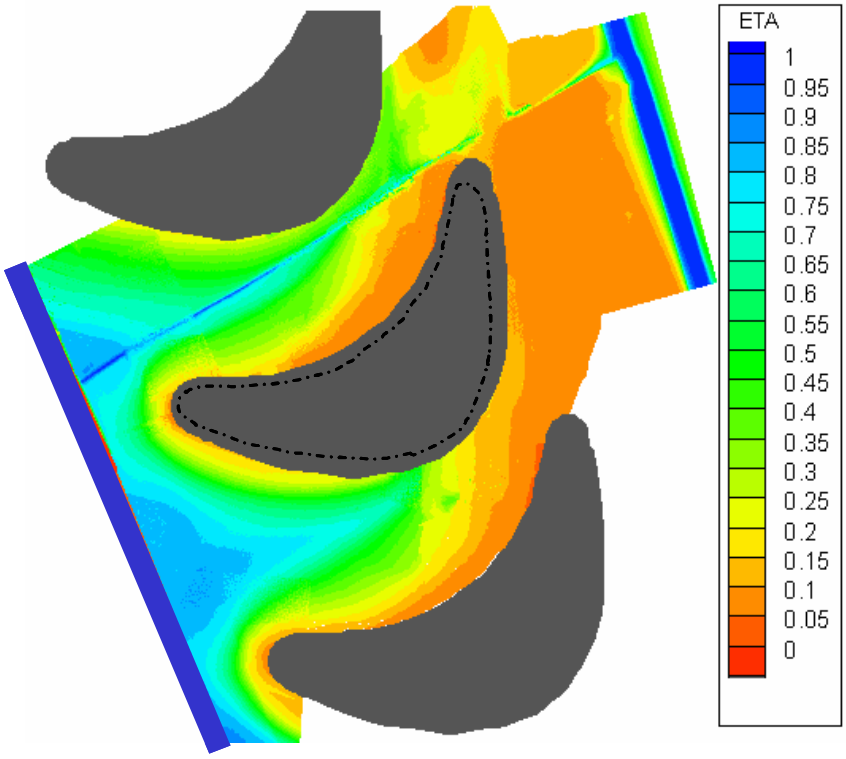

Figure 5.1 Adiabatic effectiveness measurements for the first public case of 1.5% front rim cooling, 0.25% featherseal flow, and 1.5% aft rim flow.

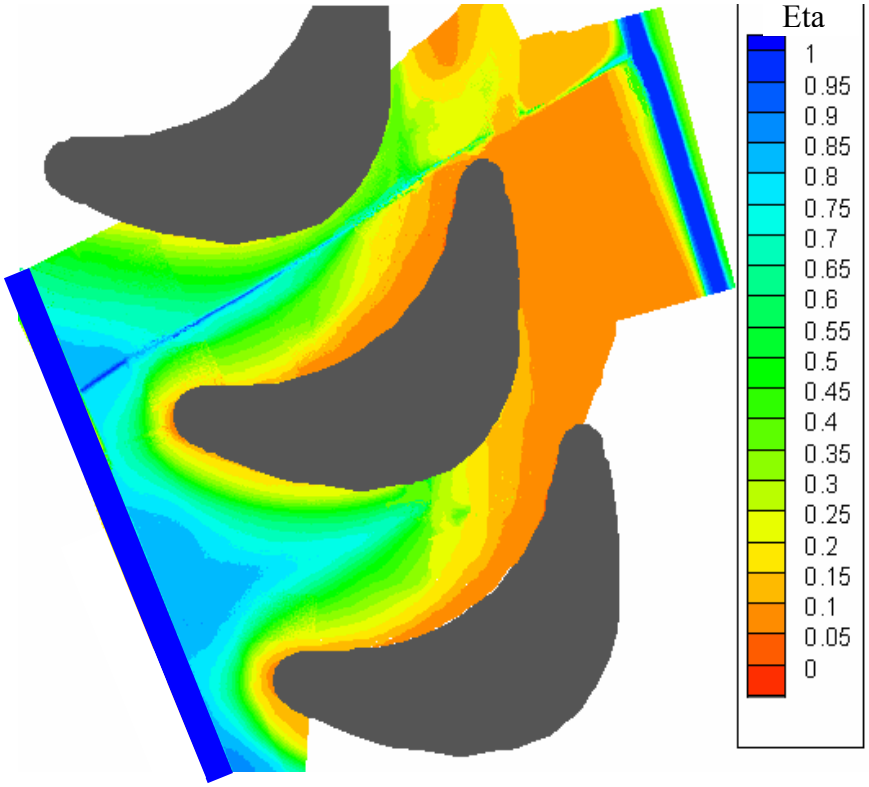

Figure 5.2 Adiabatic effectiveness measurements for the repeat of the first public case of 1.5% front rim flow, 0.25% featherseal flow, and 1.5% aft rim flow.

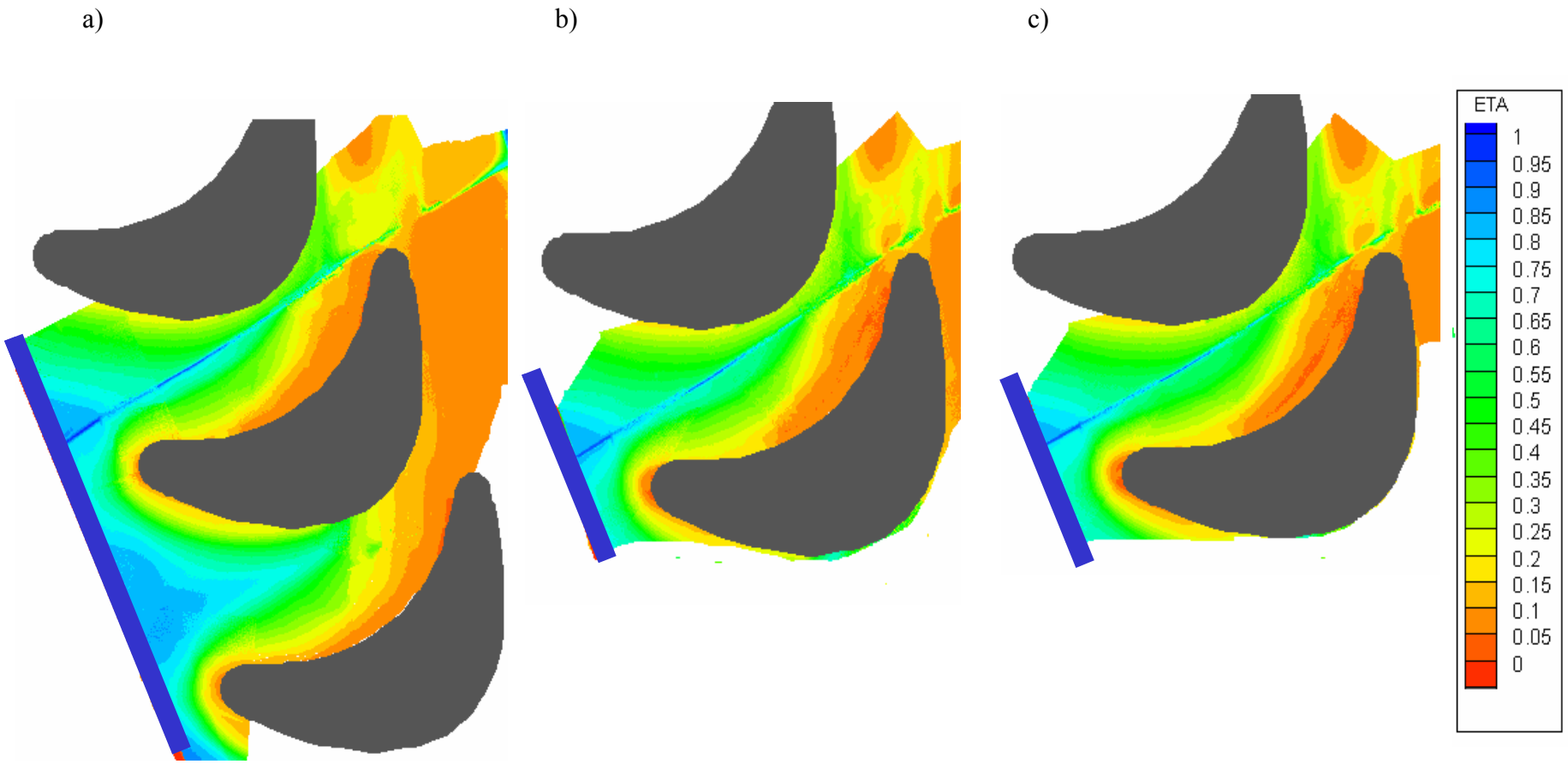

Figure 5.3 Adiabatic effectiveness measurements with the front and aft rim set at 1.5% of the inlet flow, showing increases in the featherseal from a baseline case flow of a) 0.25%, to b) 0.5% and c)0.75% have little affect on the overall cooling of the platform.

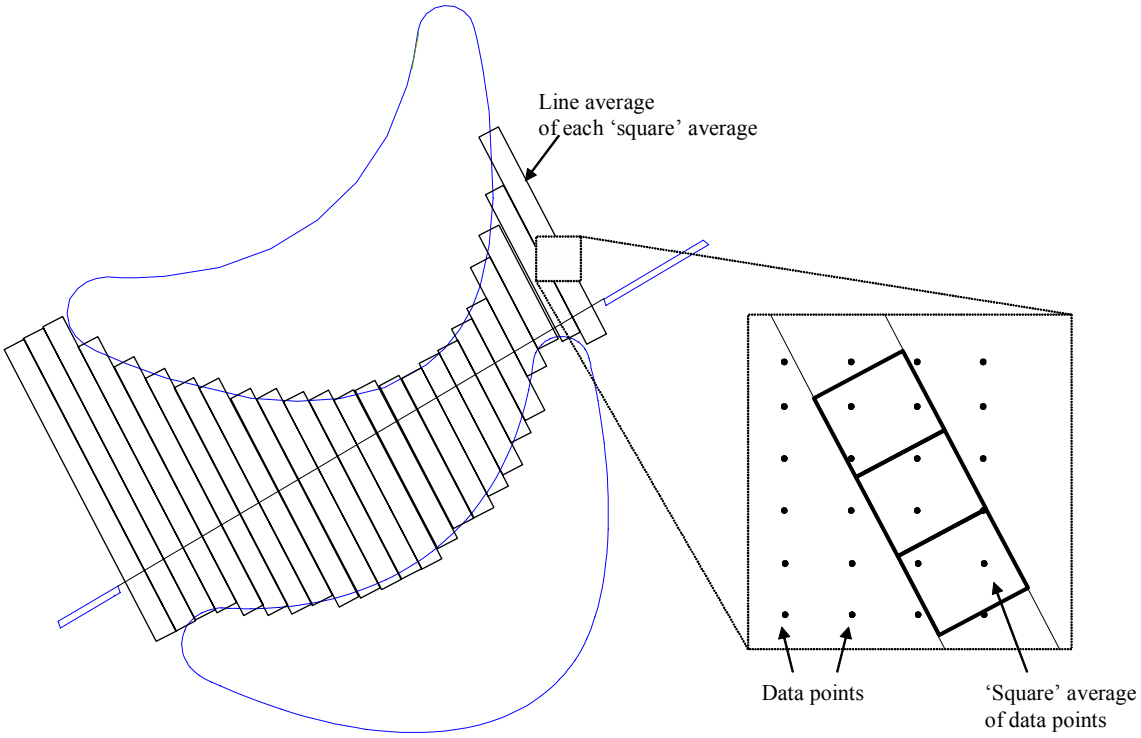

Figure 5.4 Schematic illustrating the calculation of line averaged eta. Data points are first averaged in 'squares', then each 'square' value is averaged in a line perpendicular to the featherseal (size exaggerated for clarity).

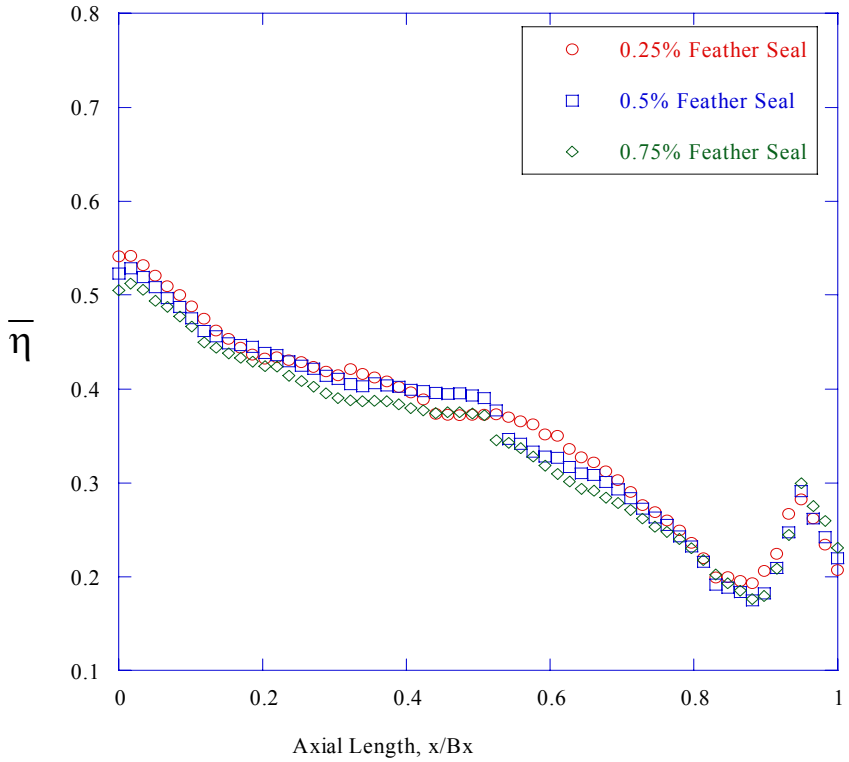

Figure 5.5 Plot of average adiabatic effectiveness values for three featherseal flow conditions with 1.5% front and aft rim cooling.

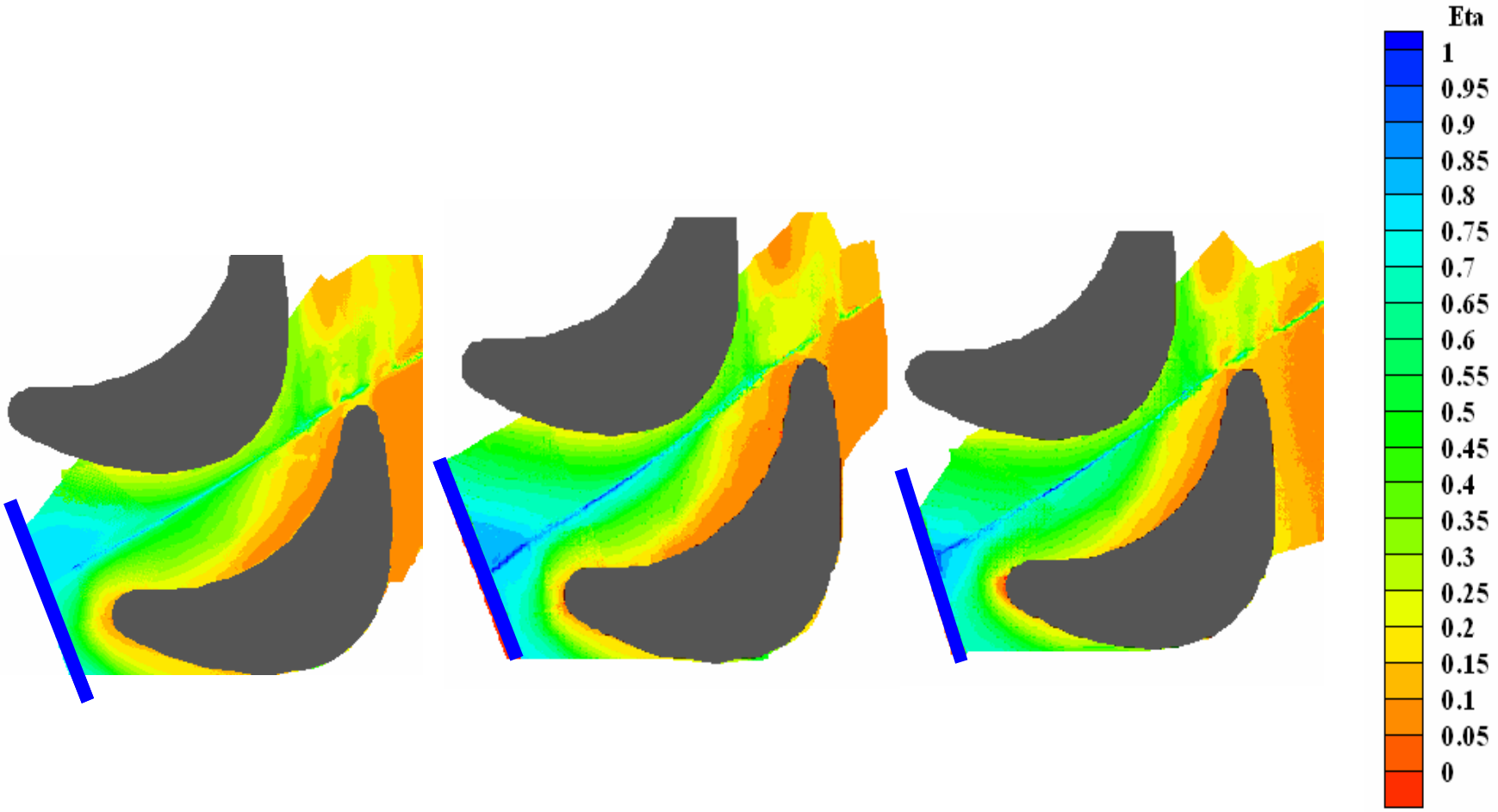

Figure 5.6 Adiabatic effectiveness measurements with the featherseal constant at 0.25%, the aft rim constant at 1.5%, and the front rim leakage at a)0.5%, b)1.5%, and c) 2.0%.

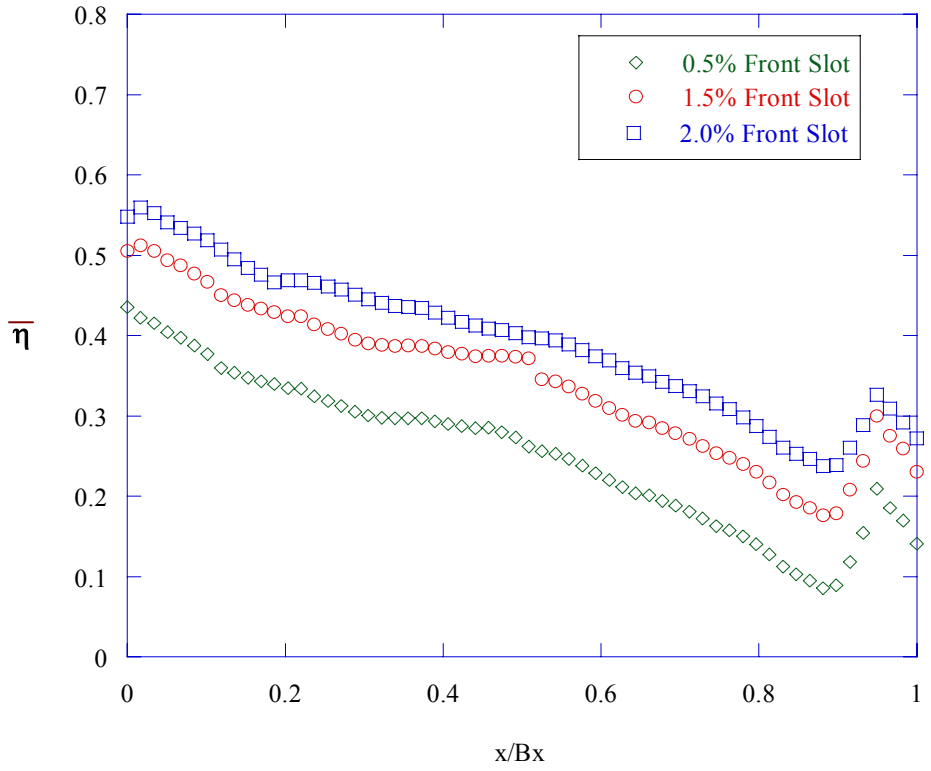

Figure 5.7 Laterally averaged adiabatic effectiveness values showing the benefit of increasing the front rim flow from 1.5% to 2.0% with 0.25% featherseal flow and 1.5% aft rim

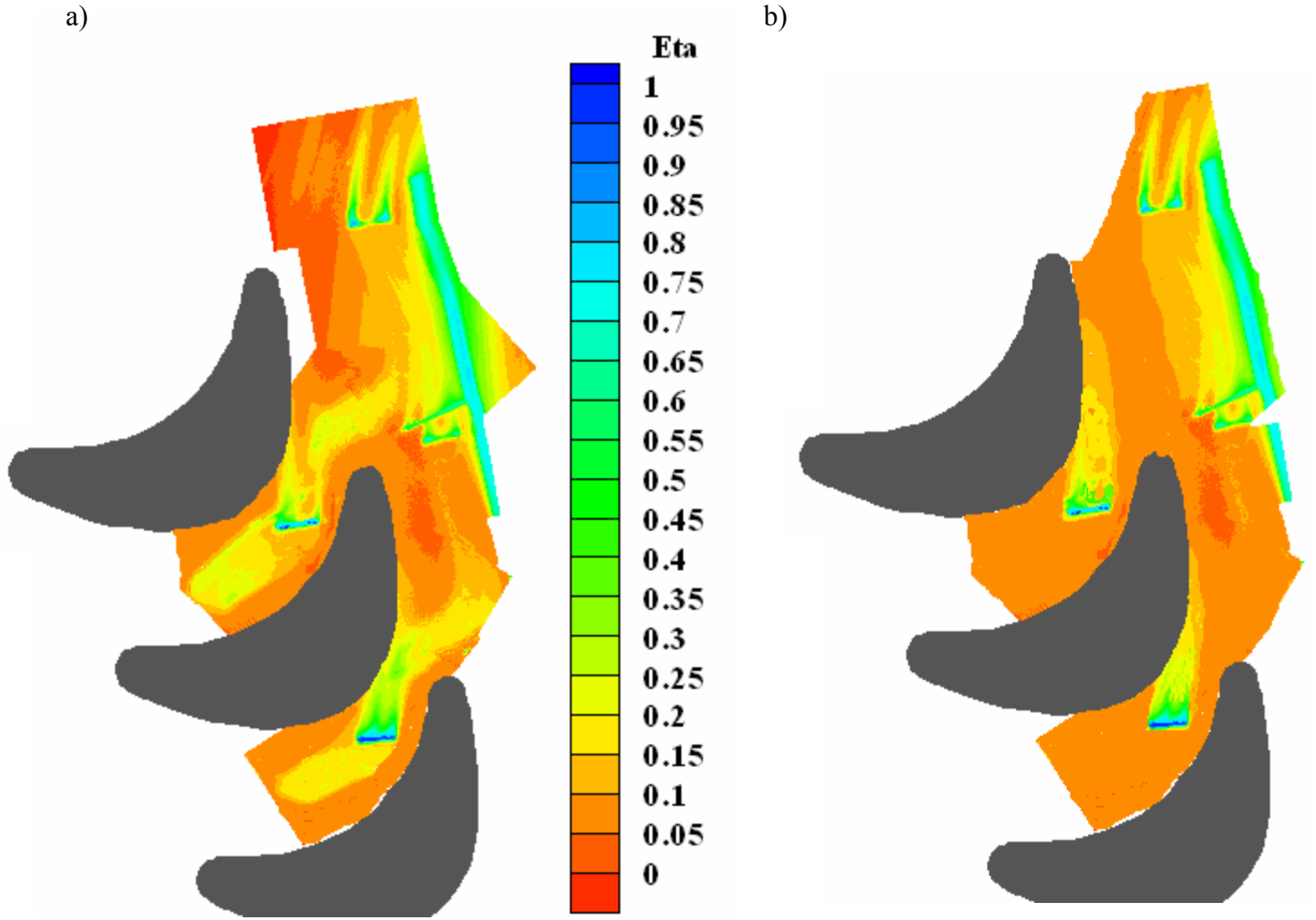

Figure 5.8 Adiabatic effectiveness measurements for the first microcircuit case of only 0.25% microcircuit flow, a)with the conduction error caused by internal cooling in the microcircuits, and b)with the conduction correction.

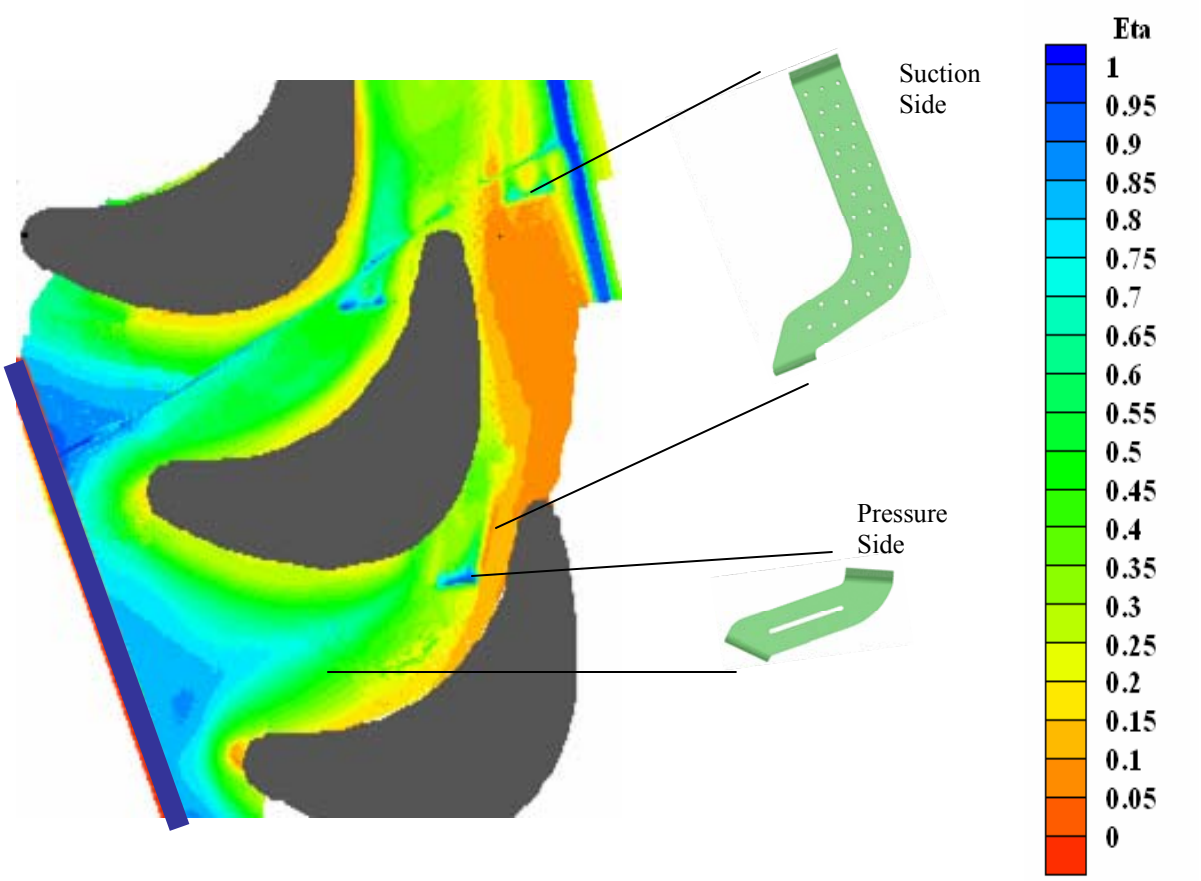

Figure 5.9 Adiabatic effectiveness measurements from microcircuit case with 1.5% front rim flow, 0.25% featherseal flow. 0.25% microcircuit flow and 1.5% aft rim flow. The microcircuits are shown in their approximate size and orientation next to the contour.

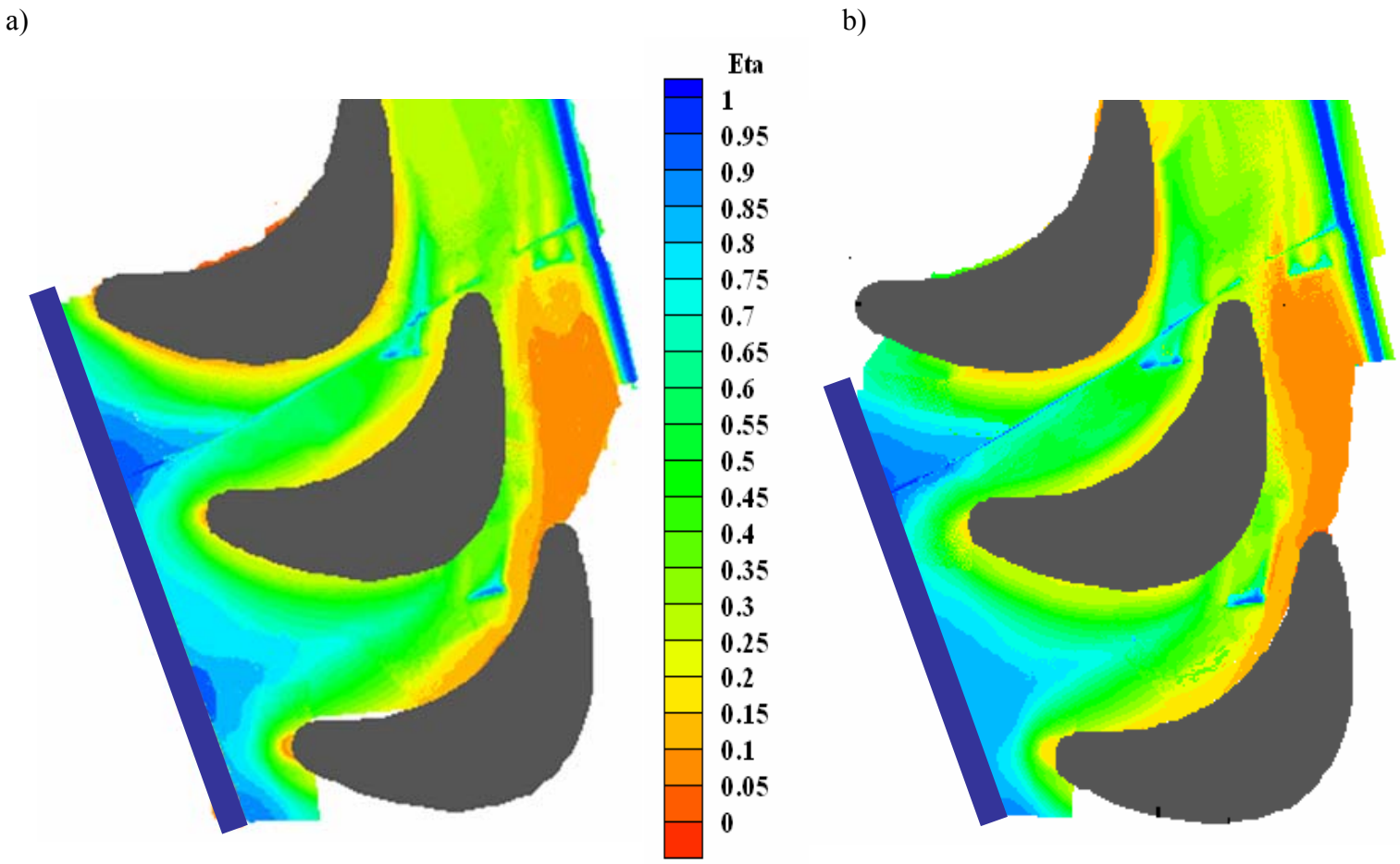

Figure 5.10 Adiabatic effectiveness measurements of microcircuit cases with a) 2.0% front rim, 0.25% featherseal, 0.25% microcircuit, and 1.5% aft rim and b)2.0% front rim, 0.25% featherseal, 0.5% microcircuit, and 1.5% aft rim.

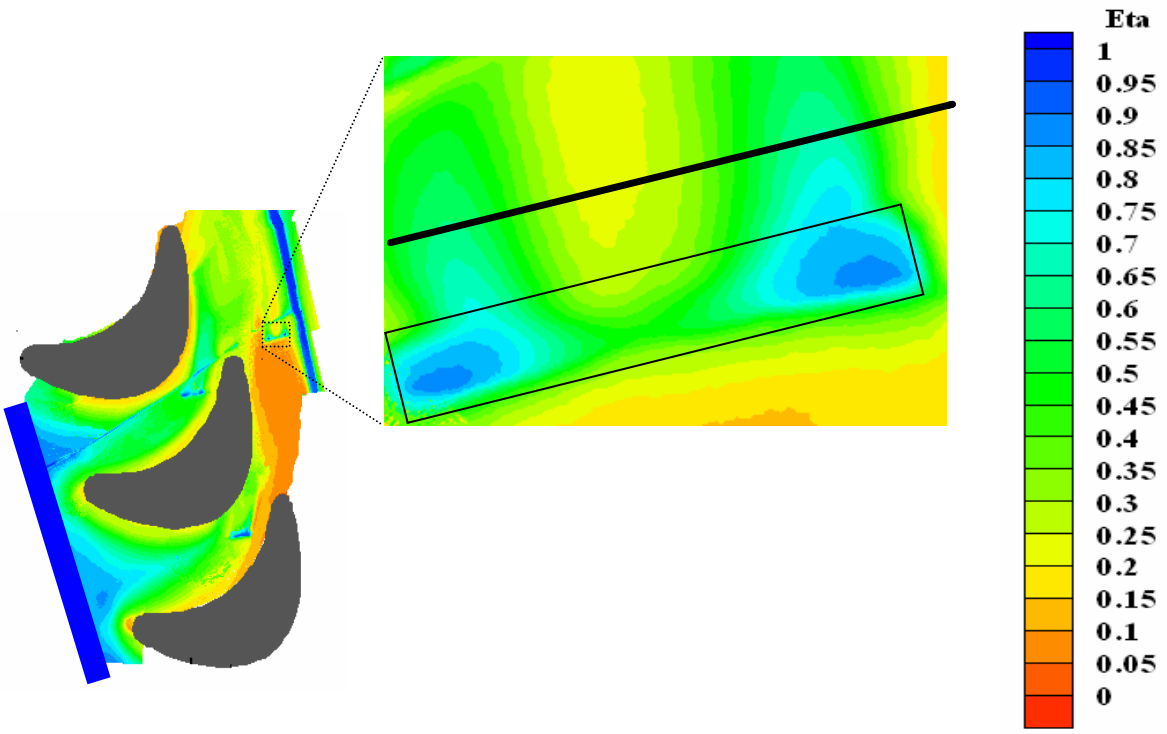

Figure 5.11 Zoom of adiabatic effectiveness measurements around the exit of the suction side microcircuit (slot shown) for 2.0% front rim flow, 0.25% featherseal flow, 0.25% microcircuit flow, and 1.5% aft rim flow.

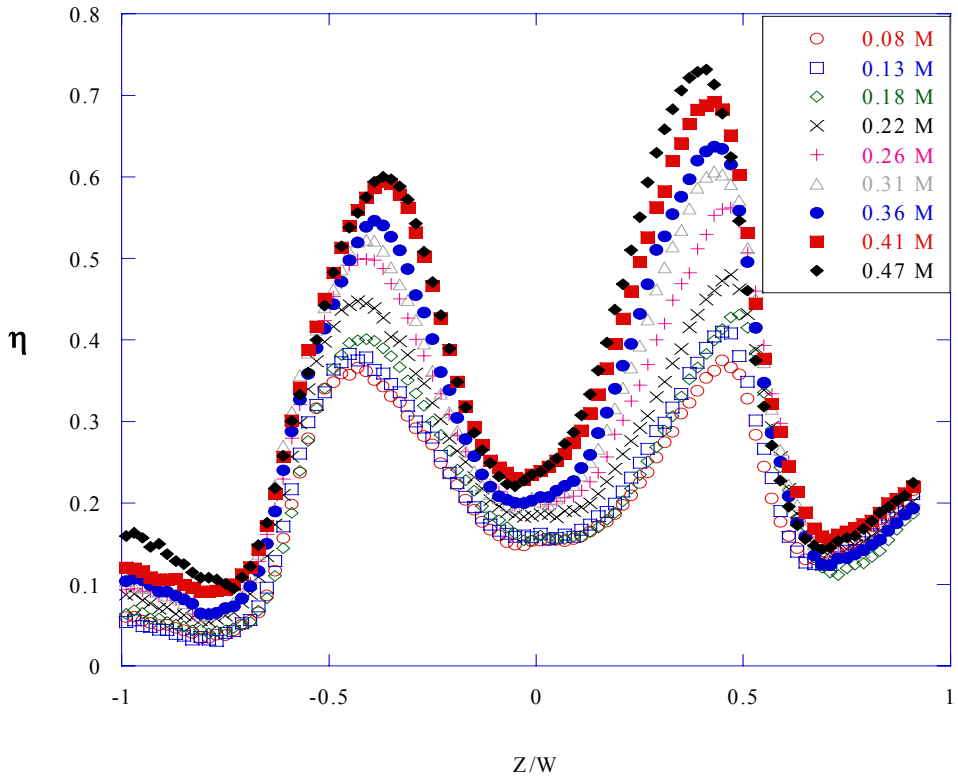

Figure 5.12 Plot of adiabatic effectiveness measurements taken one slot width downstream of the suction side microcircuit exit.

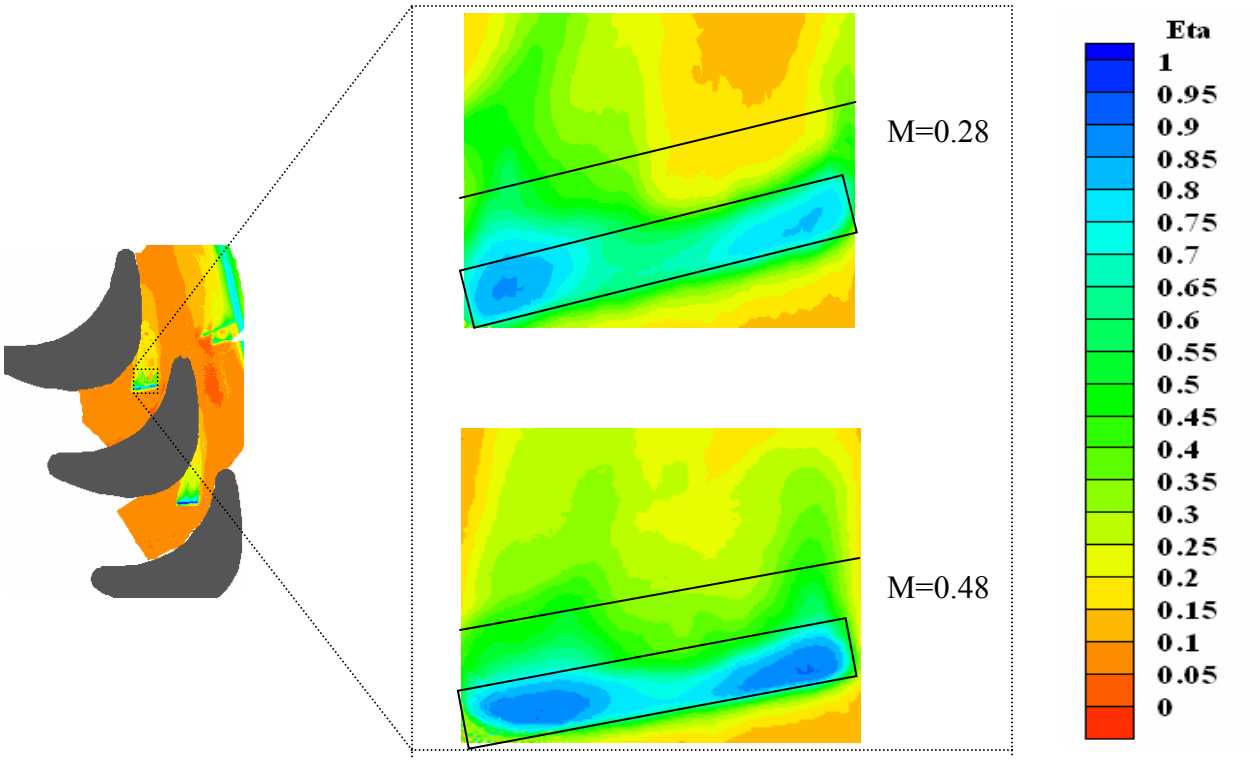

Figure 5.13 Adiabatic effectiveness measurements near the exit of the pressure side microcircuit with no other leakage flow for microcircuit mass flux of M=0.28, and 0.48.

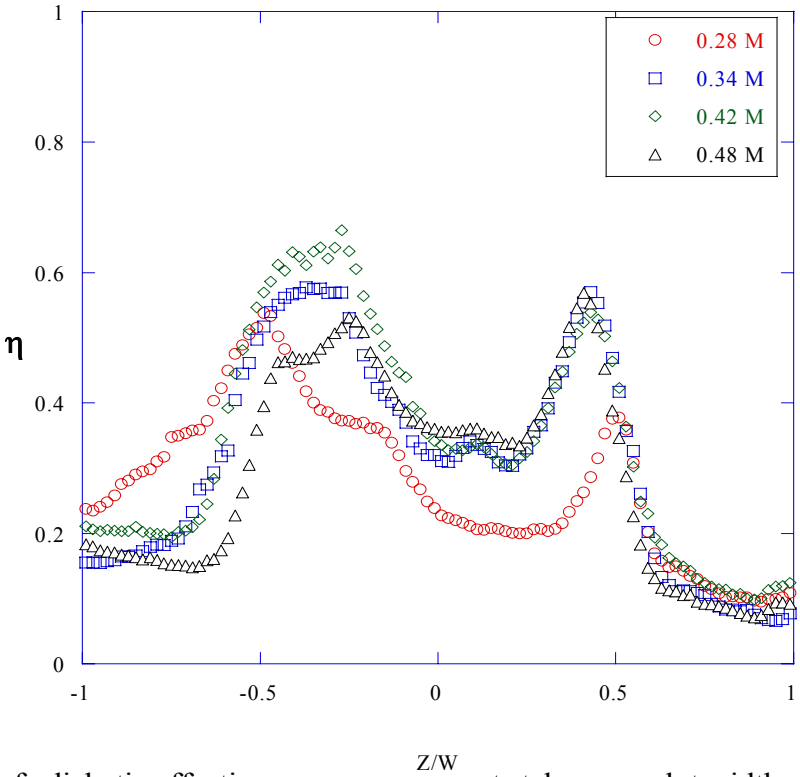

Figure 5.14 Plot of adiabatic effectiveness measurements taken one slot width downstream of the pressure side microcircuit with no featherseal flow.

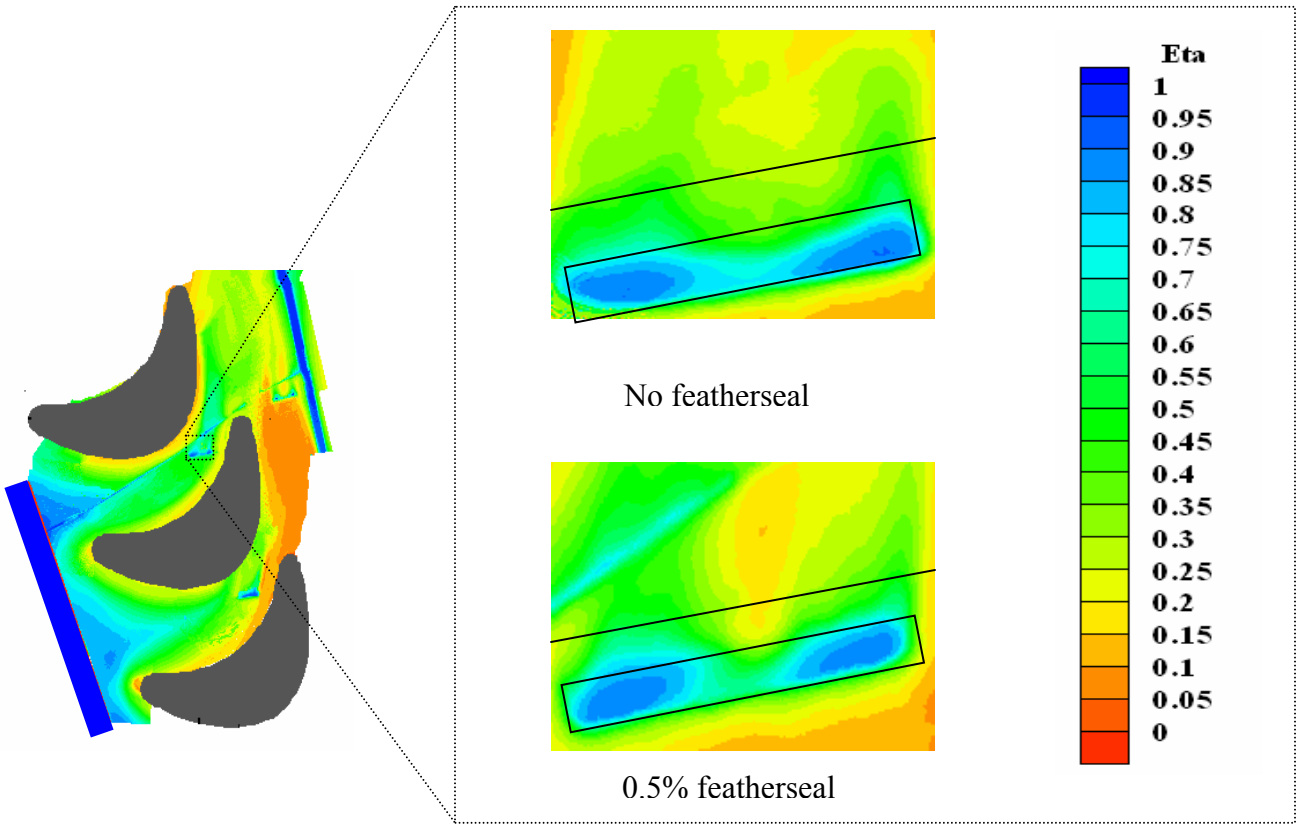

Figure 5.15 Adiabatic effectiveness measurements of the pressure side microcircuit, with 1.5% front and aft rim flow, 0.25% microcircuit flow (0.34 M), a) no featherseal flow, and b) 0.5% featherseal flow.

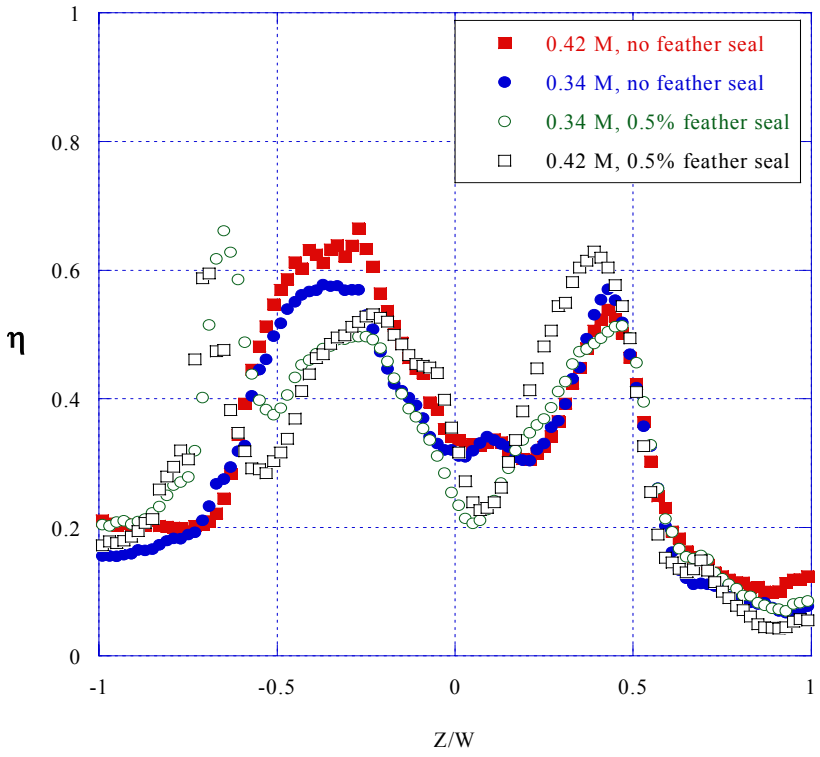

Figure 5.16 Plot of adiabatic effectiveness measurements one slot width downstream, with 1.5% front and aft rim flow, varying the microcircuits from 0.25%-0.4% (0.34 M-0.42 M), and varying featherseal from 0%-0.5%.

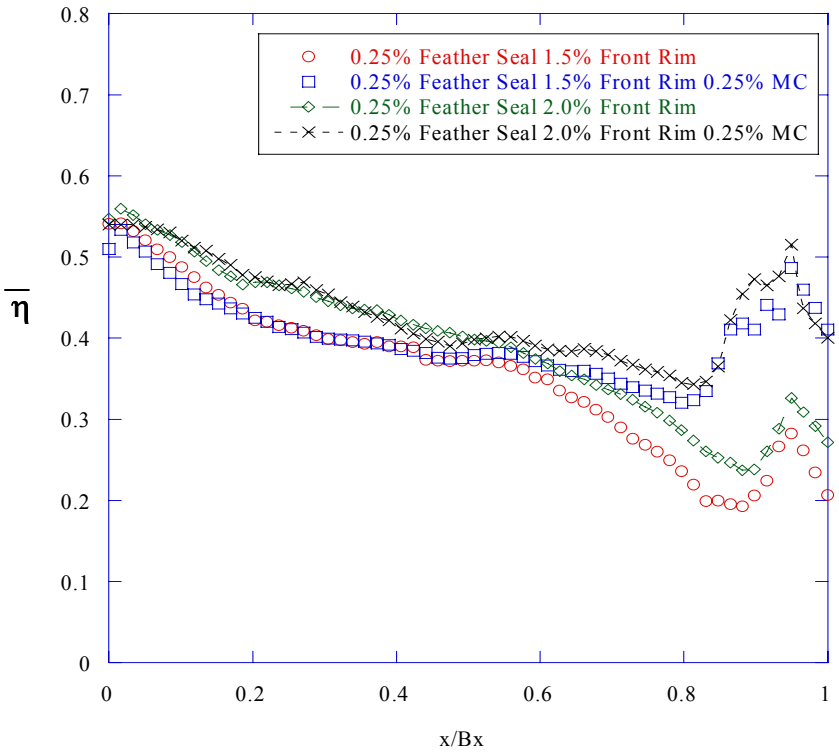

Figure 5.17 Plot of average adiabatic effectiveness measurements for microcircuit and public cases with front rim flows of 1.5%-2.0%, featherseal flows of 0.25%, microcircuit flows of 0.25%, and aft rim flows of 1.5%.

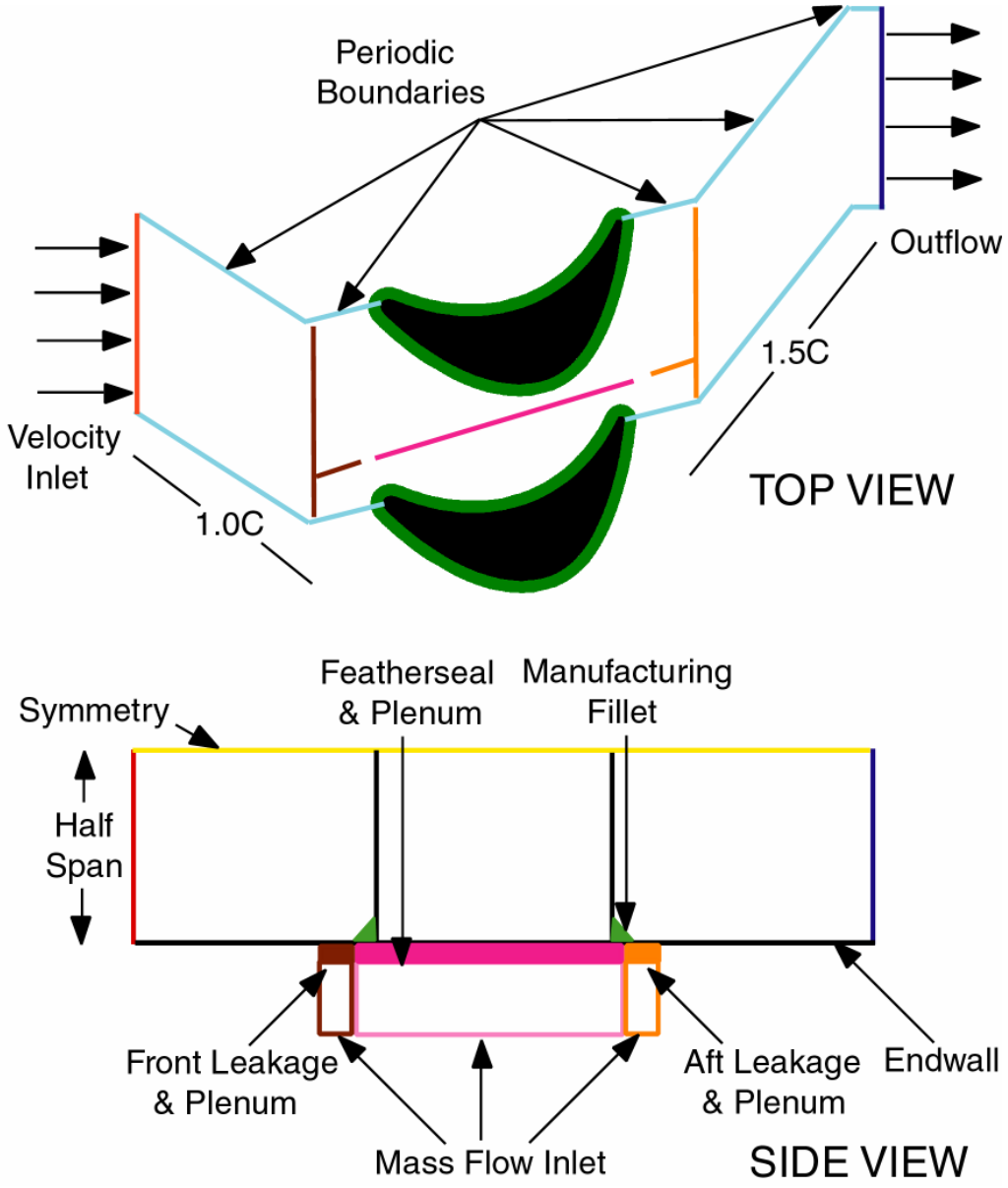

Figure 5.18 Schematic of computational domain from a)top and b) side view, showing the boundary conditions and relative distances modeled [Hohlfeld, 2003].

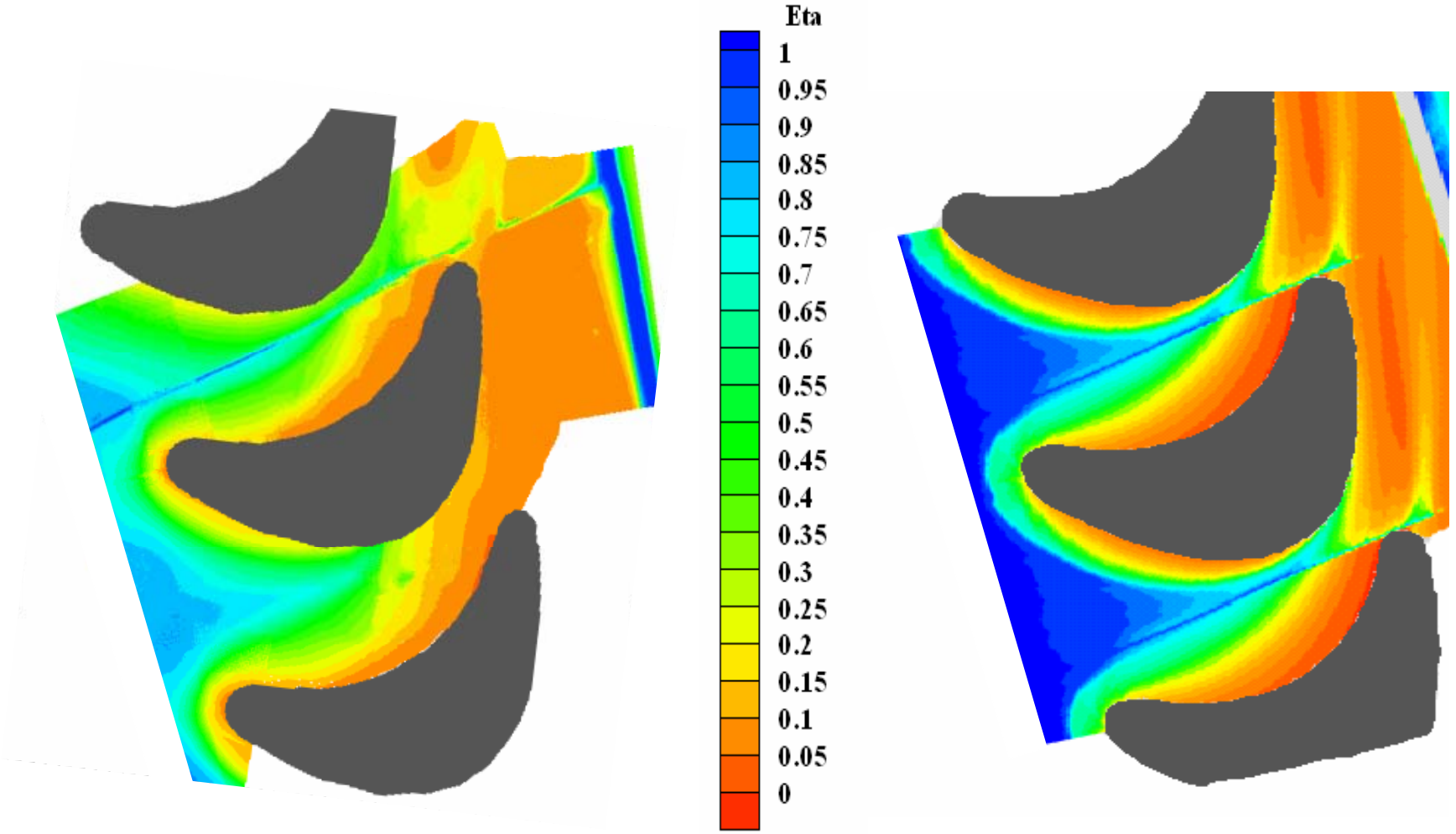

Figure 5.19a-b Adiabatic effectiveness measurements with 1.5% front and aft rim flow and 0.25% featherseal flow for a) experimental test case and b) computational case. The computations overpredict the front rim cooling benefits.

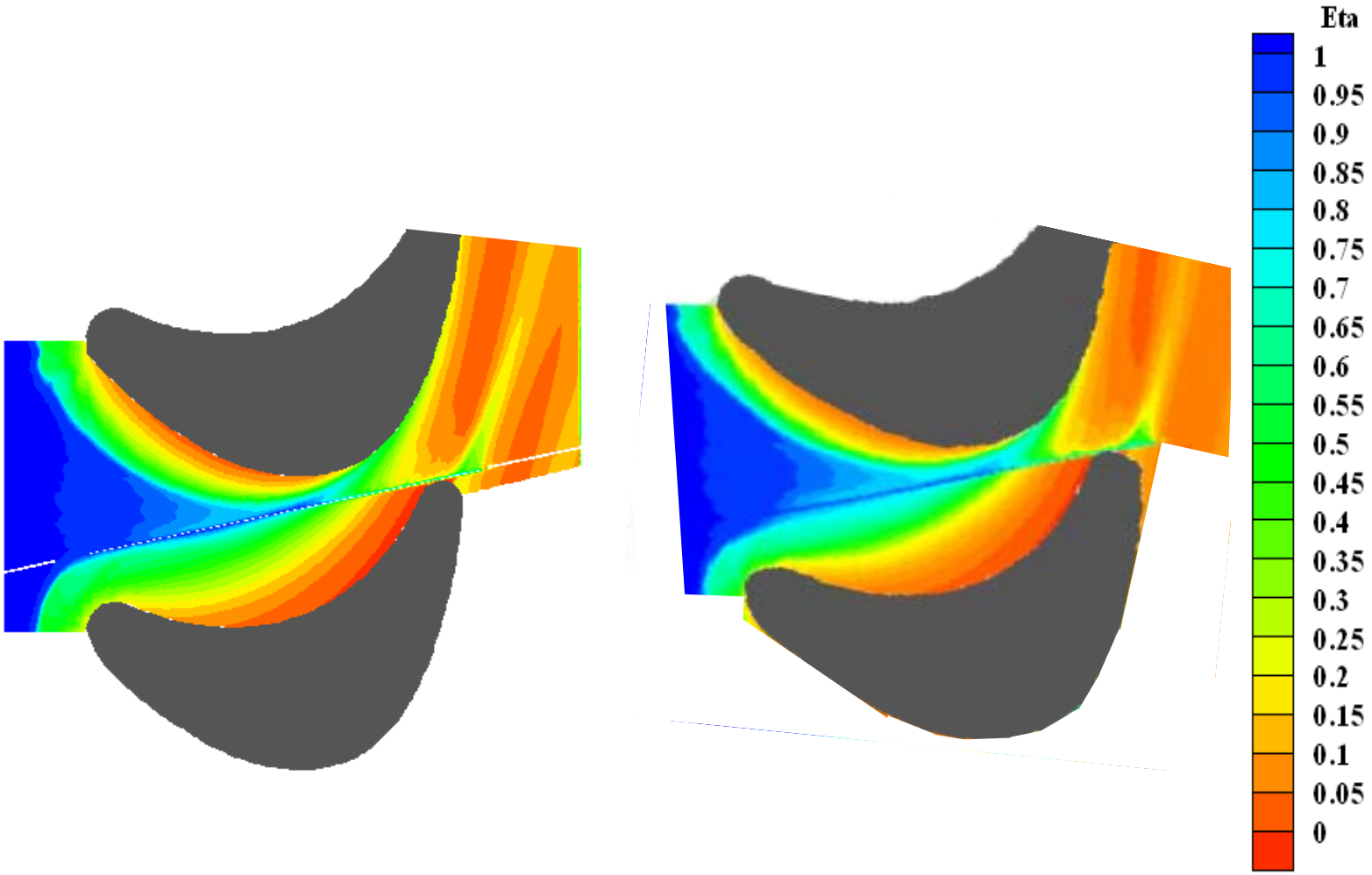

Figure 5.19 c-d. Computational predictions of adiabatic effectiveness for 2.0% front rim flow, 1.5% aft rim flow with a) 0.25% featherseal flow and b) 0.75% featherseal flow.

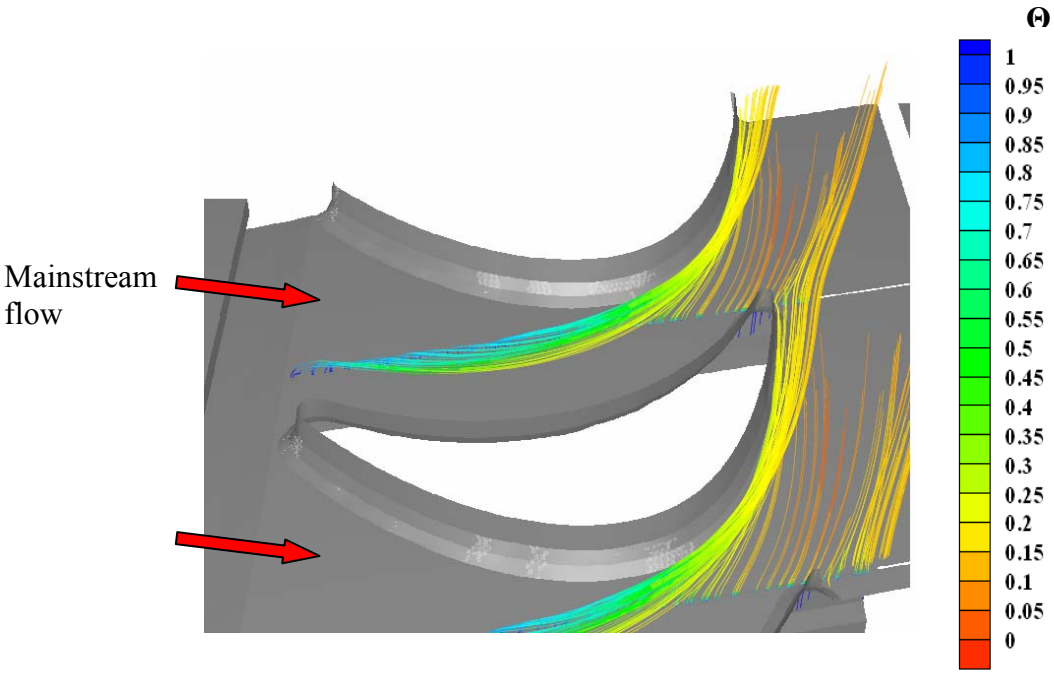

Figure 5.20a Computational predictions of temperature-colored streamlines released from the featherseal for 1.5% front and aft rim flow, and 0.25% featherseal flow.

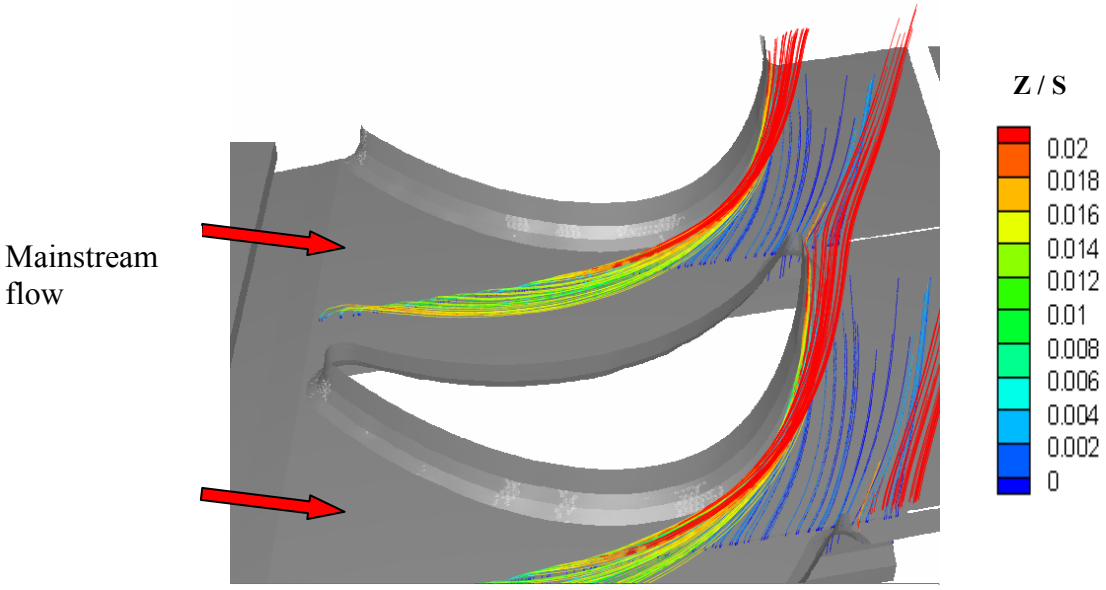

Figure 5.20b. Computational prediction of height of flow out of the featherseal, normalized by the blade span, for 1.5% front and aft rim flow with 0.25% featherseal flow.

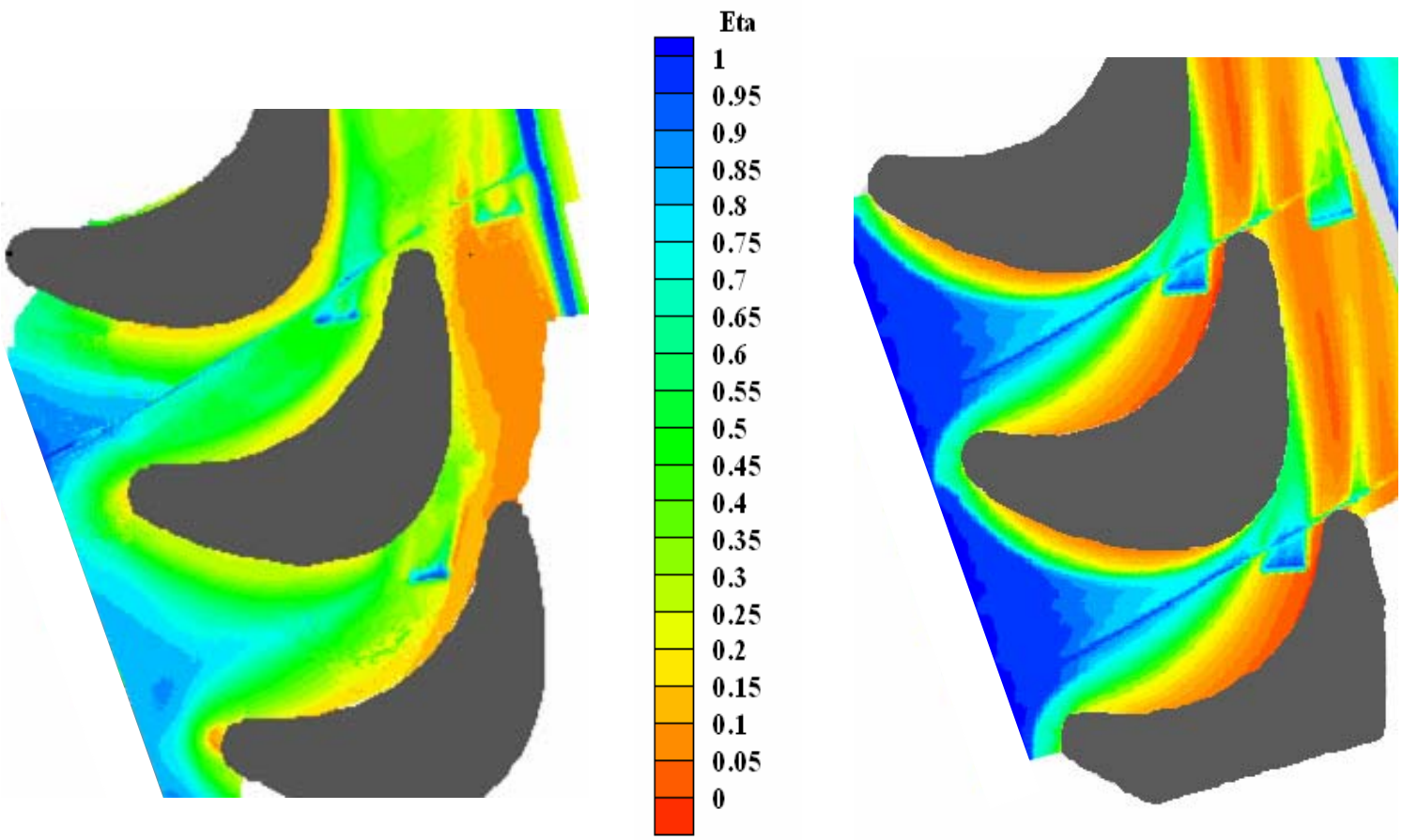

Figure 5.21 Comparison of adiabatic effectiveness measurements between the a)experimental and b)computational predictions for 2.0% front rim flow, 0.25% featherseal flow, 0.25% microcircuit flow, and 1.5% aft rim flow.

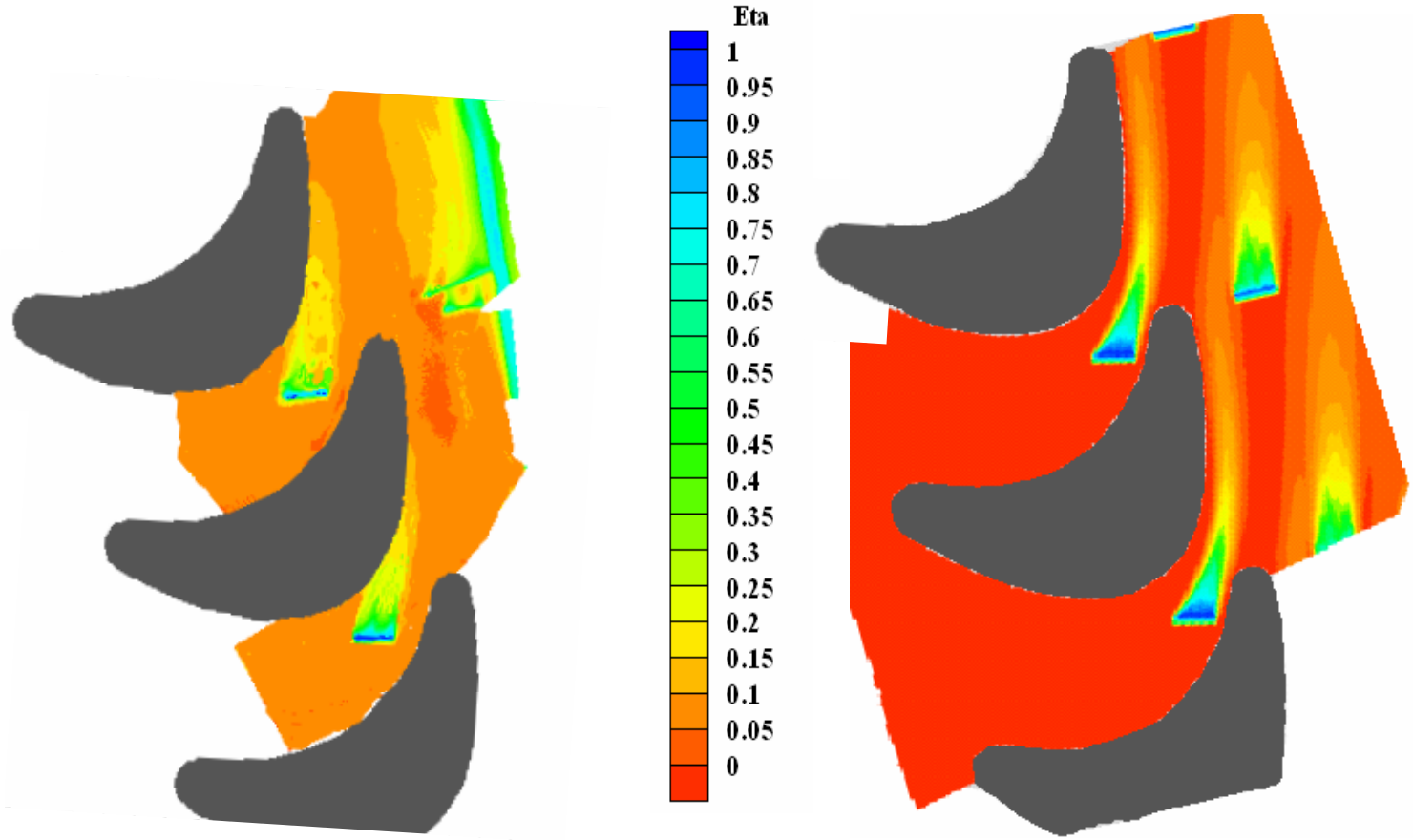

Figure 5.22 Comparison of adiabatic effectiveness measurements between the a)experimental and b)computational predictions for 0.25% microcircuit only case. Though the flow from the experimental model appears to be pulled off the platform into the free stream near the suction side of the blades, the computational model shows the flow stays attached to the platform near the suction side.

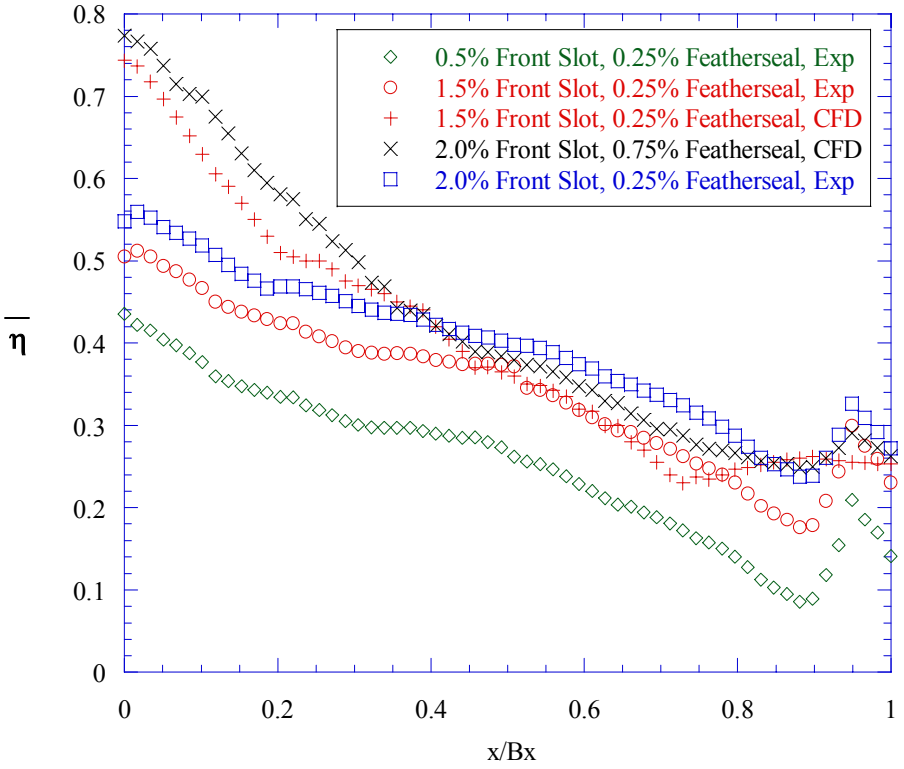

Figure 5.23 Average adiabatic effectiveness for the computational and experimental data.

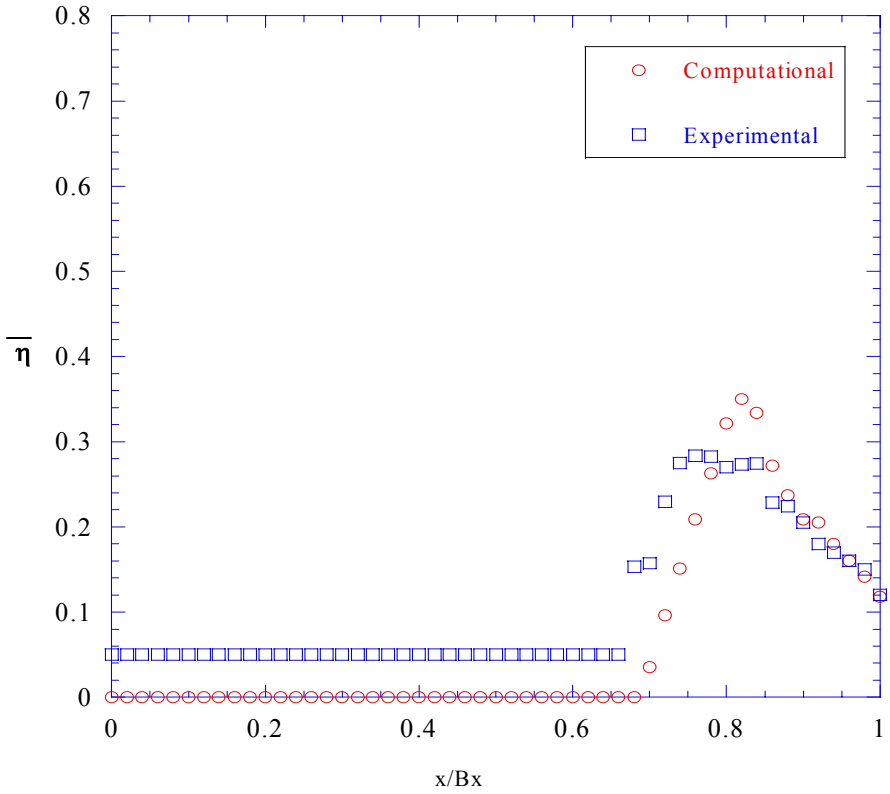

Figure 5.24 Average adiabatic effectiveness for the computational and experimental data of only 0.25% microcircuit flow.

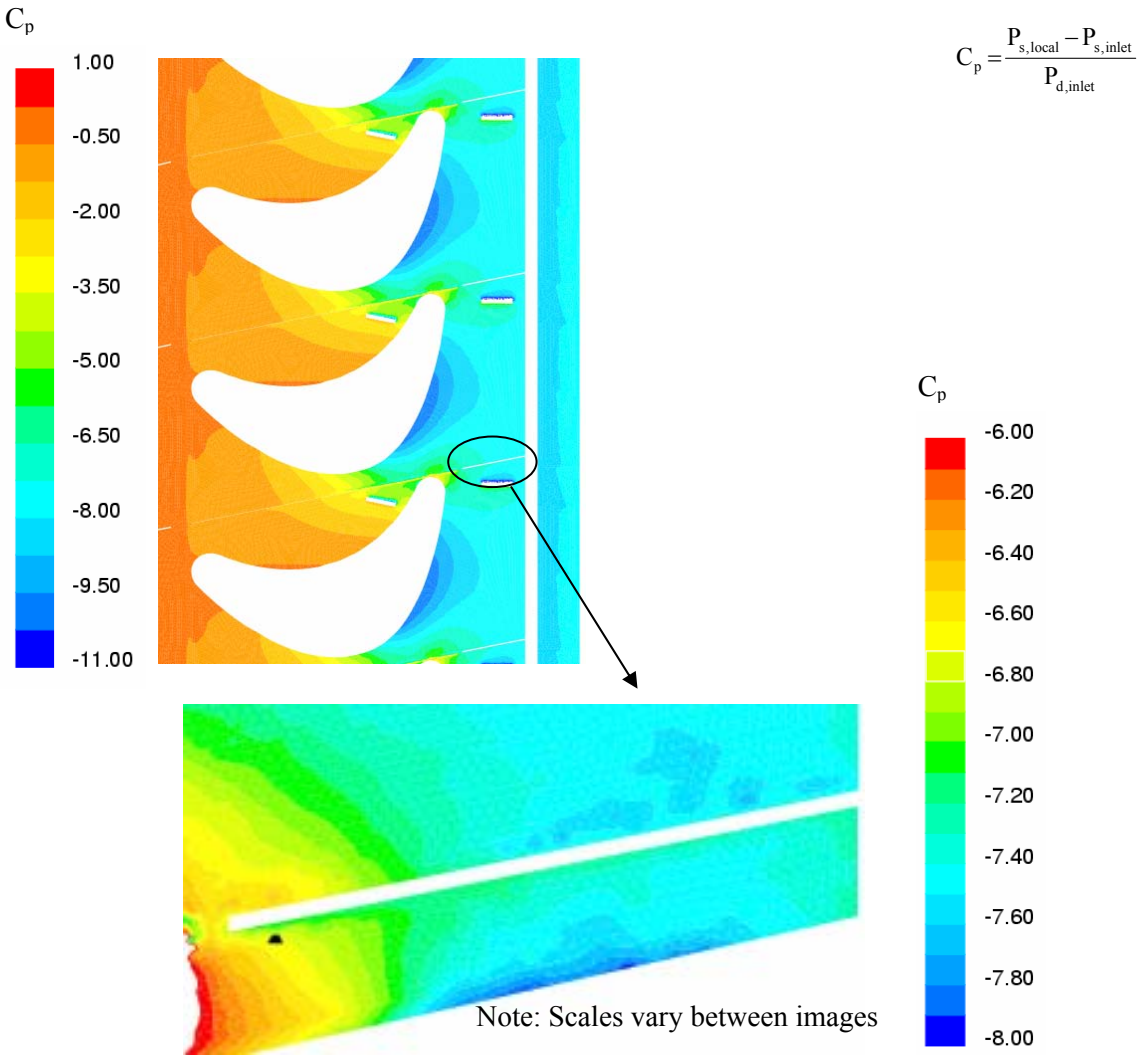

Figure 5.25 Computationally predicted pressure distribution across the hub [Hohlfeld, 2003] for 1.5% front and aft rim flows, 0.25% featherseal flows, and no microcircuit flow.

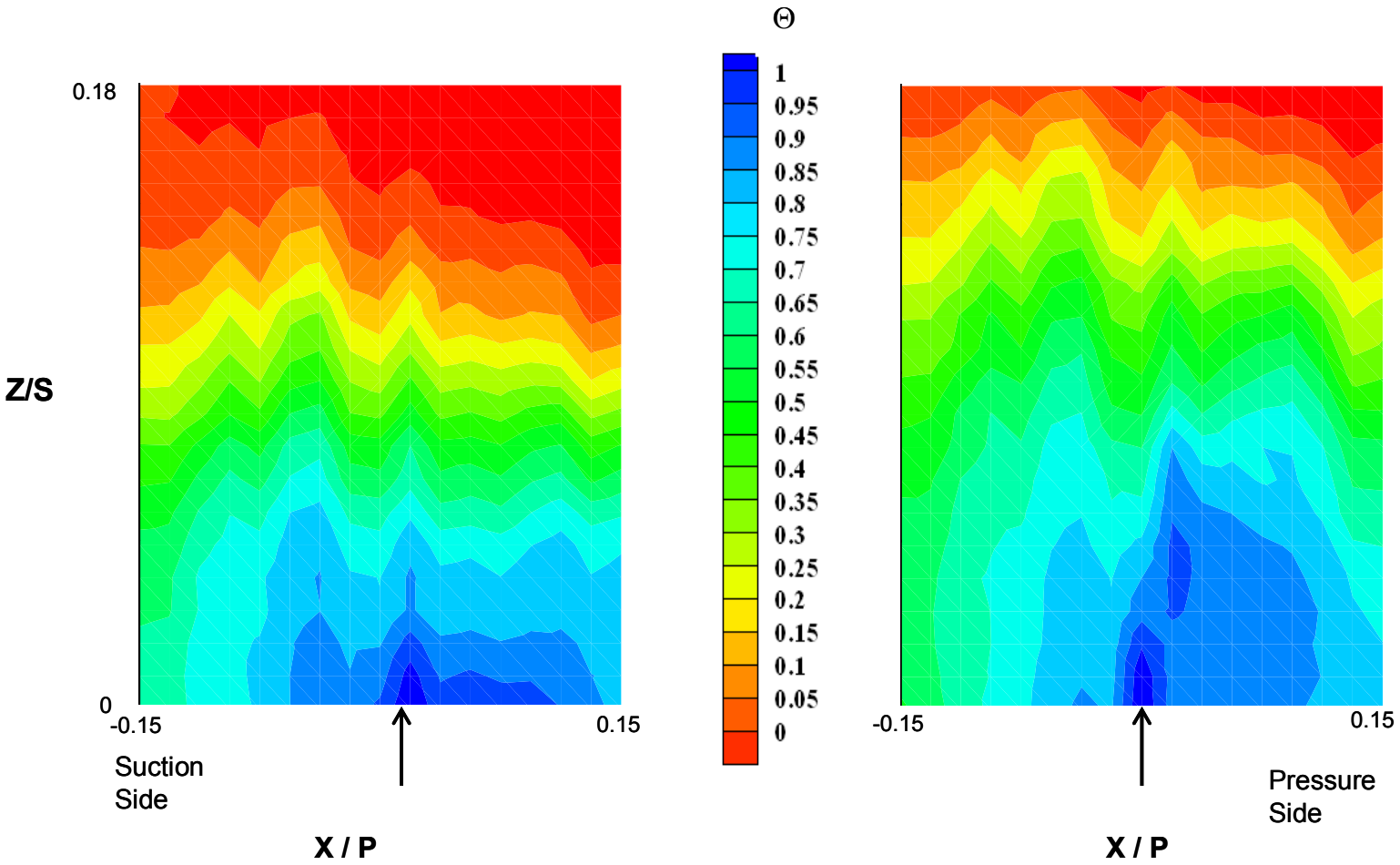

Figure 5.26 Thermal field measurements near the front of the featherseal for 1.5% front and aft rim flows with a)0.25% featherseal flow and b)0.75% featherseal flow.

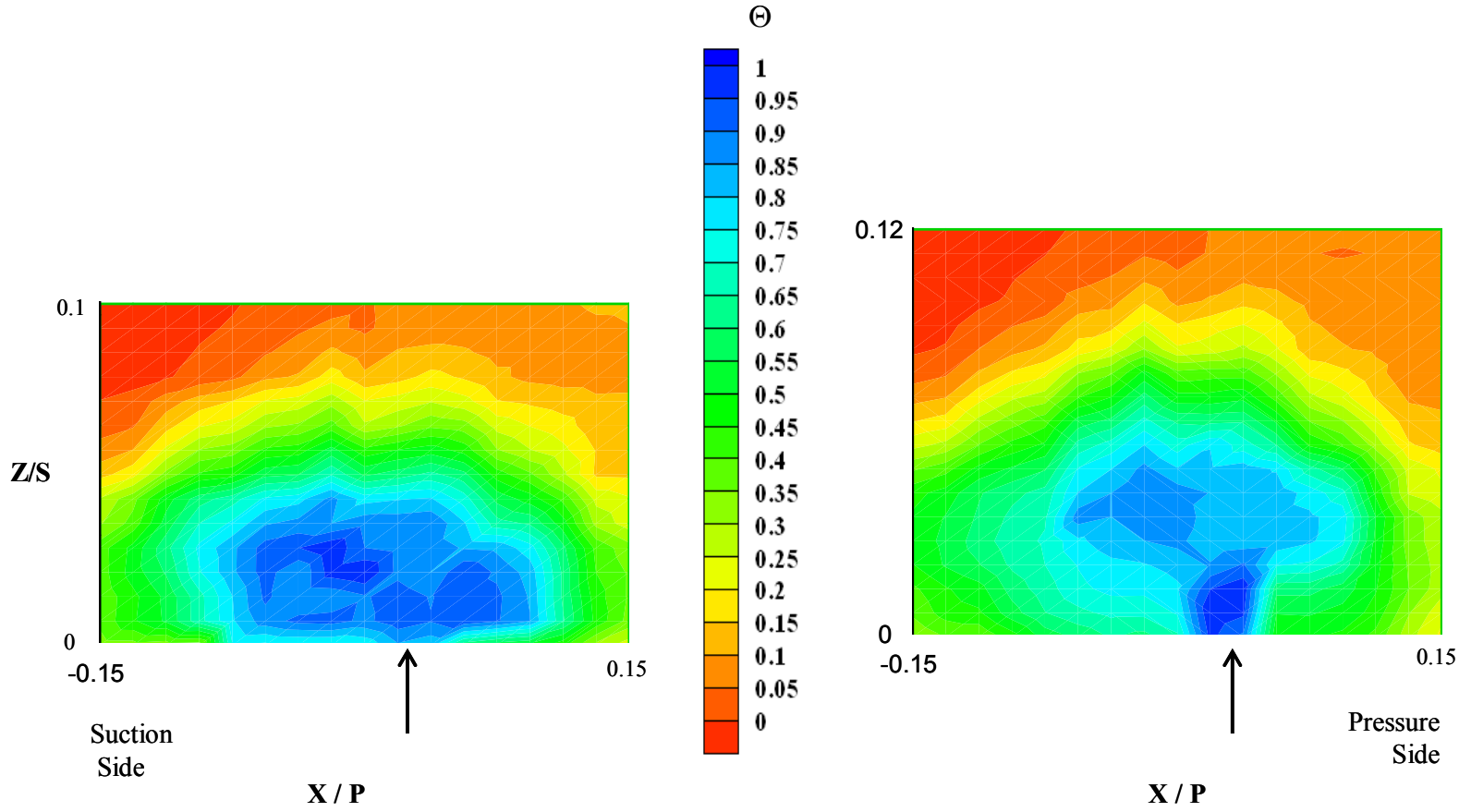

Figure 5.27 Thermal field measurements along the featherseal near the trailing edge with 1.5% front rim flow for a)0.25% and b)0.75% featherseal flow.

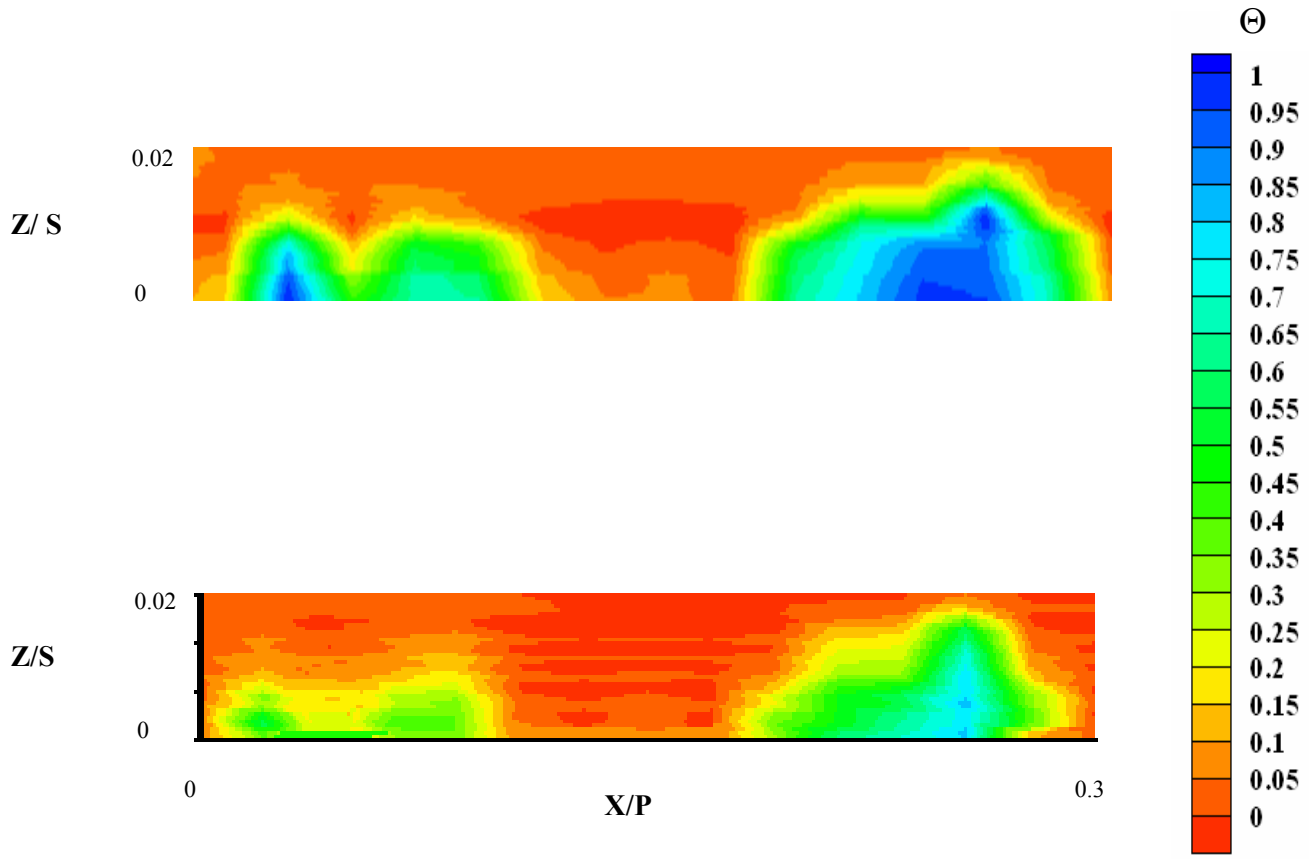

Figure 5.28 a-b Thermal field measurements along the suction side microcircuit exit for flow of a) 0.4% and b)0.2% flow with 1.5% front rim flow, and 0.25% featherseal flow

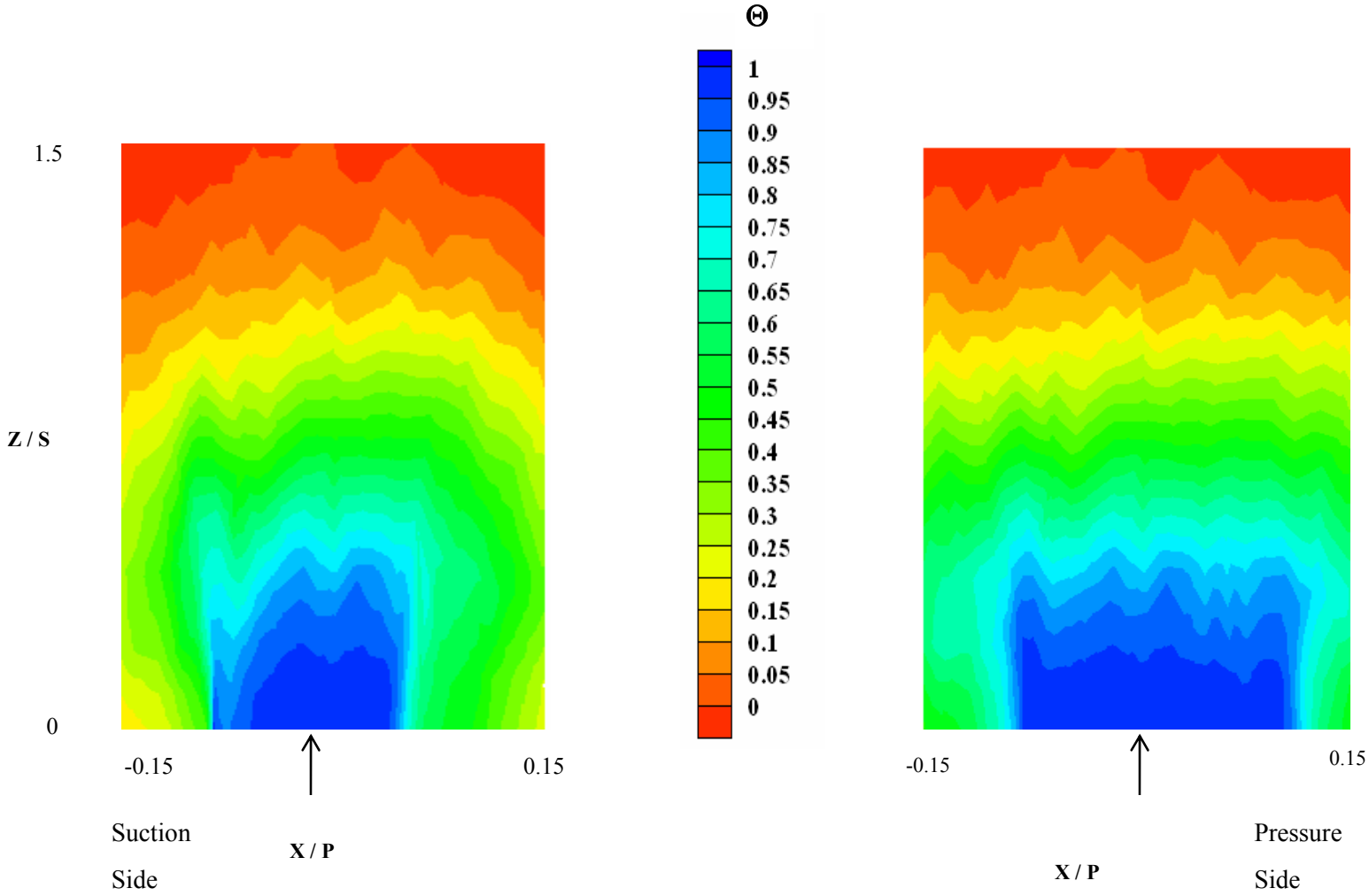

Figure 5.29 a-b. Computational thermal field measurements of the featherseal flow near the leading edge with 1.5% front and aft rim flow for a) 0.25% and b) 0.75% featherseal flow.

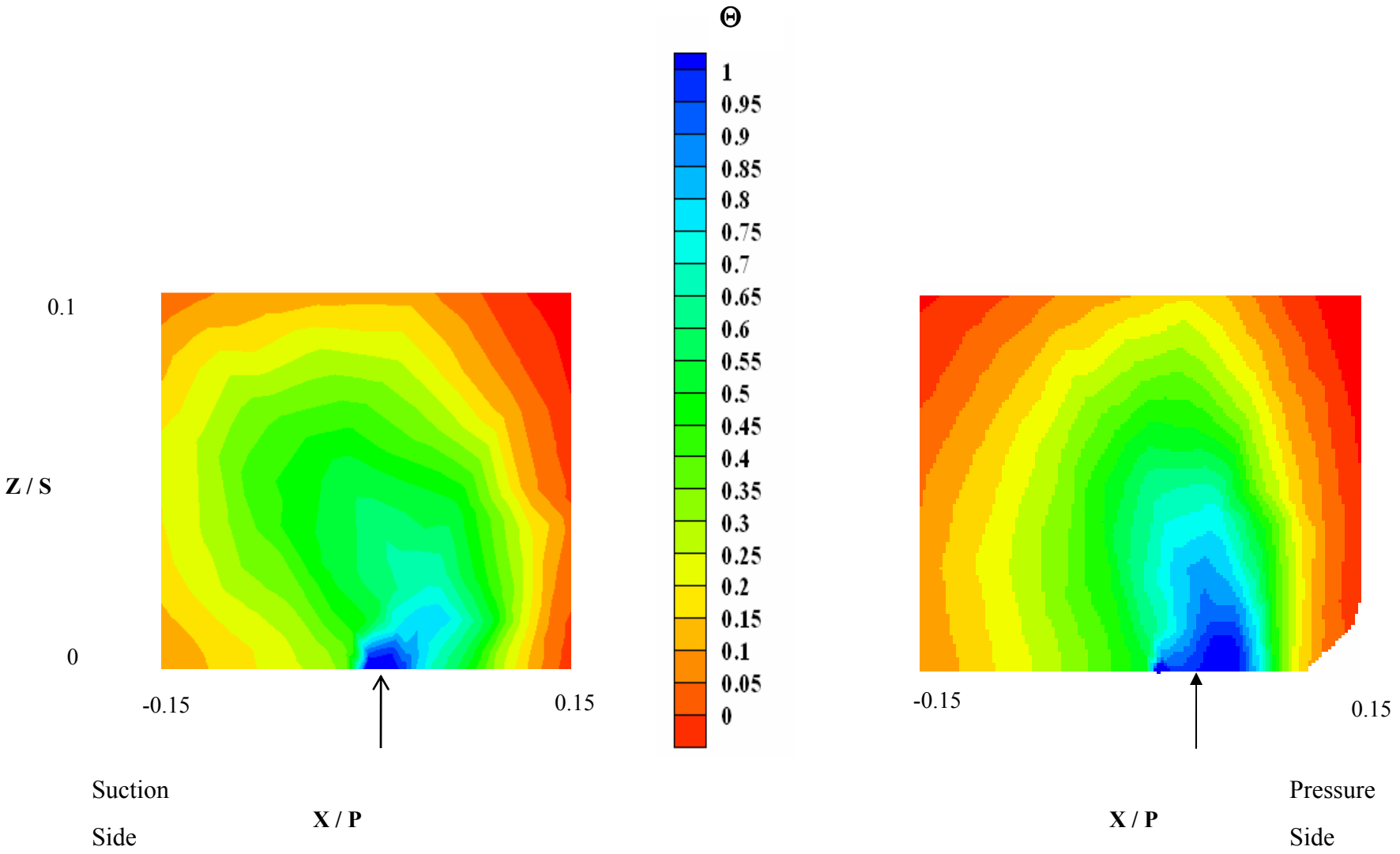

Figure 5.30 a-b. Computational thermal field measurements of the featherseal flow near the trailing edge with 1.5% front and aft rim flow for a) 0.25% and b) 0.75% featherseal flow.

Chapter 6: Conclusions

This thesis reviews the experimental study of cooling benefits of leakage flows along the hub region of gas turbine engines. Prior work concerning hub studies were reviewed in Chapter 2. Though there has been extensive work on hub measurements, especially with a front rim slot cooling, there is no prior work studying the cooling effects from a featherseal slot. Additionally, there is no public literature about any microcircuit designs for the hub. Chapter 3 described the design and construction of the blade cascade used in this research. Calibration of the experimental facilities and test rig were explained in Chapter 4. Chapter 5 presented the results of cooling along the hub region for both the public cases and the microcircuit cases. Comparisons to our computational work and previous work done by Hohlfeld [2003] were made. Additionally, thermal rake measurements of the coolant distribution were made along the featherseal and the exit of one of the microcircuits. In this final chapter, first the conclusions are summarized, and then recommendations for future testing is given.

6.1 Summary of Results

Performed first were the tests on the public cases, which involved coolant leaking from the front rim, featherseal, and aft rim. The resulting temperature distributions across the hub region closely matched many of the results observed in open literature. First, coolant from the front rim provides ample cooling of the platform directly downstream of the slot. Though the front rim flow cooled the hub downstream of this slot, the hub-leading edge intersection was not effectively cooled. Though the effects of the front rim leakage coolant were visible through 50% of the blade passage, little cooling was provided to either sides of the trailing edges of the blades from the front slot cooling. Decreasing the front rim flow significantly reduced the cooling of the hub region, which was visible in both the temperature contours and laterally averaged adiabatic temperature measurements.

Flow from the featherseal provided only slight cooling benefits to the hub region, mostly in the aft part of the featherseal. Towards the leading edge of the featherseal, the inlet angle of the mainstream flow caused coolant to be swept towards the pressure side

of the blades. Farther down the blade passage, near x/Bx=0.7, the pressure differential between the blades overcame the mainstream momentum and swept the featherseal coolant towards the suction side of the blades. At x/Bx=0.7, the featherseal injection caused increased secondary flows, which pulled the featherseal coolant off of the hub region. Near the trailing edge, the crossflow from pressure side to suction side swept the featherseal flow from the featherseal. However, the coolant in the trailing edge remained near the hub region, providing slight cooling to the hub as it blocked the warmer flow being swept from the pressure side of the blades. Momentum flux ratio calculations showed the featherseal momentum remained relatively constant across the entire length of the featherseal.

It was shown that increases in the featherseal leakage flows provided no additional cooling to the hub region. Laterally averaged adiabatic effectiveness values showed that increases in featherseal leakage did not change the hub cooling. This lack of additional hub cooling with increased featherseal flow was also quantified with thermal rake measurements. The thermal rake measurements of the featherseal flow towards the trailing edge also showed effects of the passage leg of the horseshoe vortex typical of turbine blade passages in open literature. Increases in featherseal flow appeared to increase the secondary flow field affects that were observed with both computational and experimental measurements. These results lead us to the conclusion that featherseal flow should be minimized, since the coolant leaking from this location could be better used in other areas.

The initial results from testing of the microcircuits showed their effectiveness in cooling the hub region. Though these experiments were designed to have an adiabatic platform, the microcircuits caused conduction errors as the internal coolant was able to cool that platform. The conduction error was received as positive news from our sponsors that the microcircuits will definitely provide conduction cooling under actual engine conditions.

After accounting for the microcircuit conduction, testing of the leakage flows with the microcircuits produced several interesting results. First, the pressure side microcircuits provided additional cooling to the trailing edge of the suction sides of the

blades. Although the front rim and featherseal flow could not cool this section of the blades, the pressure side location provided additional cooling.

Secondly, the flow out of the microcircuits was not as uniform as computationally predicted. The flow out of both the pressure side and suction side microcircuits was higher towards the sides of the exit slots than in the middle. It was shown that for all levels of coolant flow, the uniformity of coolant from the suction side microcircuit was not improved. This lack of coolant uniformity in the suction side microcircuit exit at both low and high coolant flows was also shown with thermal rake measurements.

Third, unlike the suction side microcircuit, in the pressure side microcircuit there appeared to be an optimal coolant flow, which suggests coolant separates from the platform at higher flows. The flow out of the pressure side microcircuit also appeared more uniform than the suction side microcircuit. The difference in uniformities between the two microcircuits was attributed to the effects of pedestals in the suction side microcircuits that were not in the pressure side microcircuits.

Lastly, we showed the pressure side microcircuit was affected by the featherseal; and conversely, the featherseal was affected by the microcircuit. Comparing pressure side microcircuit flow with and without featherseal flow showed there was decreased coolant uniformity from the slot near the featherseal. The featherseal appeared to act as a blocking wall to the flow coming out of the slot exit closest to the featherseal. Though some of the flow out of the microcircuit was decreased by flow in one section of the featherseal, flow from the microcircuit caused an increase in flow from the featherseal in another section. Directly downstream of the microcircuit exit, the flow from the featherseal increased because the coolant boundary layer from the microcircuit helped the featherseal leakage. This effect of one cooling feature increasing the effectiveness of downstream slot cooling has been documented in open literature [Yu, 1998].

Taking a step back from the specifics of the microcircuit discharge uniformity, this research shows the microcircuits efficiently cool the hub region. In addition to film cooling of the hub near the suction side of the blades, the microcircuits provide ample conduction cooling of the hub region. Though affected by the presence of the other

leakage features, the microcircuits appear to be a viable solution to cooling the hub region compared to the public cases.

6.2 Recommendations for Future Work

The main purpose of this study was to evaluate the adiabatic cooling effectiveness of both leakage flows an microcircuit cooling along the hub region. Naturally, the next step in the analysis of the hub region would be to perform measurements with a heated hub region. Combining the adiabatic wall temperatures from this research with the resulting heated wall temperatures would provide a map of heat transfer coefficients across the hub region. Those measurements would produce the complete boundary conditions required to perform thermal analysis of the microcircuits.

In addition to heated platform measurements, different microcircuit designs should be analyzed. Only the two designs provided by Pratt & Whitney were analyzed in this study. Analysis of different microcircuit designs is presented in Couch [2003] and Prausa [2004]. However, neither of these designs are specifically for hub microcircuits. Perhaps a re-design of the suction side microcircuit could reduce the tooth-shape exit profile of the coolant. In addition to studying different microcircuits, the effects of conduction cooling should be further analyzed. The film cooling from the microcircuits in this thesis should be seen as the best possible case. In reality, as the microcircuits provide conduction cooling, the internal cooling flow will be heated and thus it will be much warmer when exiting the microcircuits.

In addition to further studies involving the microcircuit, more studies should be performed on the front rim and featherseal gaps. Though different flow rates were studied in this research, the gap sizes remained constant. Though increases in flow could cause similar results as an increased gap size, this relation has not been determined experimentally for featherseal leakages. In addition to gap changes, a gap mismatch of the featherseal would cause drastic changes in the flow and temperature distribution along the hub region. The effects of a gap mismatch are analyzed in Cardwell [2005]. By examining the positive and negative effects of gap sizes, featherseal mismatches, additional cooling holes, and new microcircuit designs on platform temperatures, improvements of hub cooling will continue to be made.

References

Aksit, M.F., 2002, "Advanced Seals for Industrial Turbine Applications: Design Approach and Static Seal Developments," *J of Propulsion and Power*, Volume **18**, No. **6**, pp. 1254-1259.

Aunapu, N.V., Volino, R.J., Flack, K.A., and Stoddard, R.M., 2000, "Secondary Flow Measurements in a Turbine Passage with Endwall Flow Modification," *J of Turbomachinery*, **122**, pp. 651-658.

Blair, M.F., 1974, "An experimental Study of Heat Transfer and Film Cooling on Large-Scale Turbine Endwall," *ASME J of Heat Transfer*, vol. 96, pp. 524-529.

Bogard, D., Ethridge, M.L., and Cutbirth, J.M., 2000, "Scaling Performance for Varying Density Ratio Coolants on an AirFoil with Strong Curvature and Pressure Gradient Effects," 2000-GT-239.

Boyle, R.J., and Russel, L.M., 1990, "Experimental Determination of Stator Endwall Heat Transfer," *J of Turbomachinery*, **112**, pp. 547-558.

Burd, S.W., Satterness, C.J., and Simon, T.W., 2000, "Effects of Slot Bleed Injection Over a Contoured Endwall On Nozzle Guide Vane Cooling Performance: Part II - Thermal Measurements," 2000-GT-200.

Burd, S.W., and Simon, T.W., 2000, "Effects of Slot Bleed Injection Over a Contoured Endwall on Nozzle Guide Vane Cooling Performance: Part I – Flow Field Measurements," 2000-GT-199.

Cardwell, N., 2005, Masters Thesis, Dept. of Mechanical Engr., Virginia Polytechnic Institute and State University.

Chung, J.T., and Simon, T.W., 1993, "Effectiveness of the Gas Turbine Endwall Fences in Secondary Flow Control at Elevated Freestream Turbulence Levels," 93-GT-51.

Colban, W.F., Thole, K.A., and Zess, G., 2003 "Combustor Turbine Interface Studies – Part 1: Endwall Effectiveness Measurements," *J of Turbomachinery*, **125**, pp.203-209.

Couch, E.L., 2003, "Measurements of Cooling Effectiveness along the Tip of a Turbine Blade," Masters Thesis, Dept. of Mechanical Engr., Virginia Polytechnic Institute and State University.

Fluent Inc., Fluent User's Guide, Version 6.0, 2002 (Fluent Inc.: New Hampshire).

Fox, R.W., and McDonald, A.T., *Introduction to Fluid Mechanics*, John Wiley & Sons, 1998.

Friedrichs, S., Hodson, H.P., and Dawes, W.N., 1996, "Distribution of Film-Cooling Effectiveness on a Turbine Endwall Measured Using the Ammonia and Diazo Technique," *J of Turbomachinery*, **118**, pp.613-621.

Graziani, R.A., Blair, M.F., Taylor, J.R., and Mayle, R.E., 1980, "An Experimental Study of Endwall and Airfoil Surface Heat Transfer in a Large Scale Turbine Blade Cascade," *ASME J. Eng. Gas Turbine Power*, **102**, pp. 257-267.

Goldstein, R.J., and Spores, R.A., 1988, "Turbulent Transport on the Endwall in the Region Between Adjacent Turbine Blades," *J of Turbomachinery*, **110**, pp. 862-869.

Goldstein, R.J., Wang, H.P., and Jabbari, M.Y., 1995, "The Influence of Secondary Flows Near the Endwall and Boundary Layer Disturbance on Convective Transport from a Turbine Blade," *J of Turbomachinery*, **117**, pp. 657-665.

Hermanson, K.S., and Thole, K.A., 1999, "Effect of Inlet Conditions on Endwall Secondary Flows," AIAA 99-0241

Hohlfeld, E.M. 2003, "Film Cooling Predictions Along the Tip and Platform of a Turbine Blade," Masters Thesis, Dept. of Mechanical Engr., Virginia Polytechnic Institute and State University.

Knost, D.G. 2003, "Predictions and Measurements of Film-Cooling on the Endwall of a First Stage Vane," Masters Thesis, Dept. of Mechanical Engr., Virginia Polytechnic Institute and State University.

Knost, D.G., and Thole, K.A., 2003, " Computational Predictions of Endwall Film-Cooling for a First Stage Vane," GT2003-38252.

Langston, L.S., Nice, M.L., and Hooper, R.M., 1977, "Three-Dimensional Flow within a Turbine Cascade Passage," *ASME Jou of Eng. Power*, **99**, pp. 21-28.

Lethander, A.T., Thole, K.A., Zess, G.A., and Wager, J., 2003, "Optimizing the Vane-Endwall Junction to Reduce Adiabatic Wall Temperatures in a Turbine Vane Passage," GT2003-38940.

Lattime, S.B., and Steinetz, B.M., 2002, "Turbine Engine Clearance Controls Systems: Current Practices and Future Directions," AIAA-2002-3790

Nicklas, M., 2001, "Film-Cooled Turbine Endwall in a Transonic Flow Field: Part II – Heat Transfer and Film-Cooling Effectiveness," *J of Turbomachinery*, **123**, pp. 720-729.

Oke, R.A., Simon, T.W., Burd, S.W., and Vahlberg, R., 2000, "Measurements in a Turbine Cascade Over a Contoured Endwall: Discrete Hole Injection of Bleed Flow," 2000-GT-214.

Prausa, J.N., 2004, “Heat Transfer Coefficient and Adiabatic Effectiveness Measurements for an Internal Turbine Vane Cooling Feature,” Masters Thesis, Dept. of Mechanical Engr., Virginia Polytechnic Institute and State University.

Sharma, O.P., and Buttler, T.C., 1987, “ Reynolds Stresses and Dissipation Mechanisms Downstream of a Turbine Cascade,” *J of Turbomachinery*, **109**, pp. 229-236.

Shih, T.I-P., and Lin, Y.-L., 2002, “Controlling Secondary Flow Structure by Leading-Edge Airfoil Fillet and Inlet Swirl to Reduce Aerodynamic Loss and Surface Heat Transfer,” ASME GT-2002-20529.

Yu, Y., abd Chyu, M.K., 1998, “Influence of Gap Leakage Downstream of the Injection Holes on Film Cooling Performance,” *J of Turbomachinery*, **120**, pp. 541-548.

Zess, G.A., and Thole, K.A., 2001 “Computational Design and Experimental Evaluation of Using a Leading Edge Fillet on a Gas Turbine Engine,” 2001-GT-404

Zhang, L.J., and Jaiswal, R.S., 2001, “Turbine Nozzle Endwall Film Cooling Study Using Pressure Sensitive Paint,” *J of Turbomachinery*, **123**, pp. 730-738.

Appendix A: Blade geometry and pressure tap locations

Table A1. Coordinates of 11X test blades.

x (m)	y (m)	x (m)	y (m)	x (m)	y (m)	x (m)	y (m)
0.135	1.354	0.185	1.382	0.445	1.275	0.513	1.646
0.135	1.346	0.188	1.382	0.447	1.519	0.518	1.643
0.135	1.341	0.193	1.298	0.460	1.542	0.518	1.334
0.137	1.361	0.196	1.382	0.465	1.570	0.521	1.641
0.137	1.334	0.203	1.382	0.467	1.577	0.521	1.336
0.140	1.367	0.206	1.382	0.467	1.283	0.523	1.341
0.140	1.331	0.211	1.382	0.470	1.588	0.523	1.341
0.142	1.323	0.211	1.382	0.470	1.588	0.526	1.638
0.145	1.372	0.211	1.290	0.472	1.595	0.526	1.346
0.147	1.321	0.221	1.382	0.472	1.593	0.528	1.633
0.150	1.374	0.231	1.384	0.475	1.610	0.528	1.354
0.152	1.316	0.231	1.283	0.478	1.626	0.531	1.626
0.152	1.316	0.257	1.384	0.478	1.623	0.531	1.631
0.155	1.377	0.274	1.270	0.478	1.623	0.531	1.626
0.157	1.313	0.282	1.392	0.480	1.636	0.531	1.623
0.160	1.379	0.310	1.400	0.480	1.631	0.533	1.615
0.163	1.311	0.315	1.265	0.485	1.638	0.533	1.361
0.165	1.382	0.333	1.410	0.485	1.298	0.536	1.610
0.168	1.382	0.358	1.422	0.490	1.641	0.536	1.605
0.168	1.308	0.361	1.257	0.493	1.643	0.538	1.595
0.173	1.382	0.378	1.438	0.495	1.306	0.538	1.374
0.173	1.382	0.399	1.453	0.498	1.646	0.541	1.585
0.173	1.306	0.401	1.265	0.503	1.646	0.544	1.565
0.180	1.382	0.417	1.476	0.503	1.313	0.546	1.544
0.180	1.382	0.424	1.267	0.508	1.646	0.549	1.410
0.183	1.303	0.434	1.496	0.511	1.323	0.551	1.499

Table A2. Locations of pressure taps on blades.

	X (m)	Y(m)	S/Smax		X (m)	Y(m)	S/Smax
STAG	0.0000	0.0000	0.0000	P1	0.0016	0.0058	-0.0121
S1	0.0042	-0.0113	0.0183	P2	0.0059	0.0101	-0.0242
S2	0.0128	-0.0200	0.0367	P3	0.0177	0.0120	-0.0485
S3	0.0688	-0.0672	0.1468	P4	0.0349	0.0060	-0.0851
S4	0.1531	-0.1165	0.2936	P5	0.0638	-0.0037	-0.1461
S5	0.2296	-0.1368	0.4130	P6	0.1355	-0.0171	-0.2926
S6	0.2900	-0.1302	0.5048	P7	0.2439	-0.0051	-0.5123
S7	0.3446	-0.0923	0.6058	P8	0.3195	0.0337	-0.6832
S8	0.4056	0.0399	0.8261	P9	0.3681	0.0796	-0.8174
S9	0.4203	0.1117	0.9362	P10	0.3965	0.1192	-0.9151

Appendix B: Dimensions of Front/Aft Plenums

Figure B1. Top View, Front Plenum

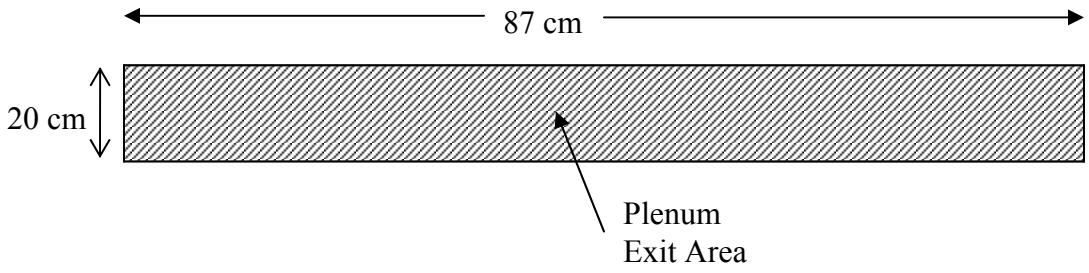

Figure B2. Front View, Front Plenum (slot offset by 1.5 cm on both sides)

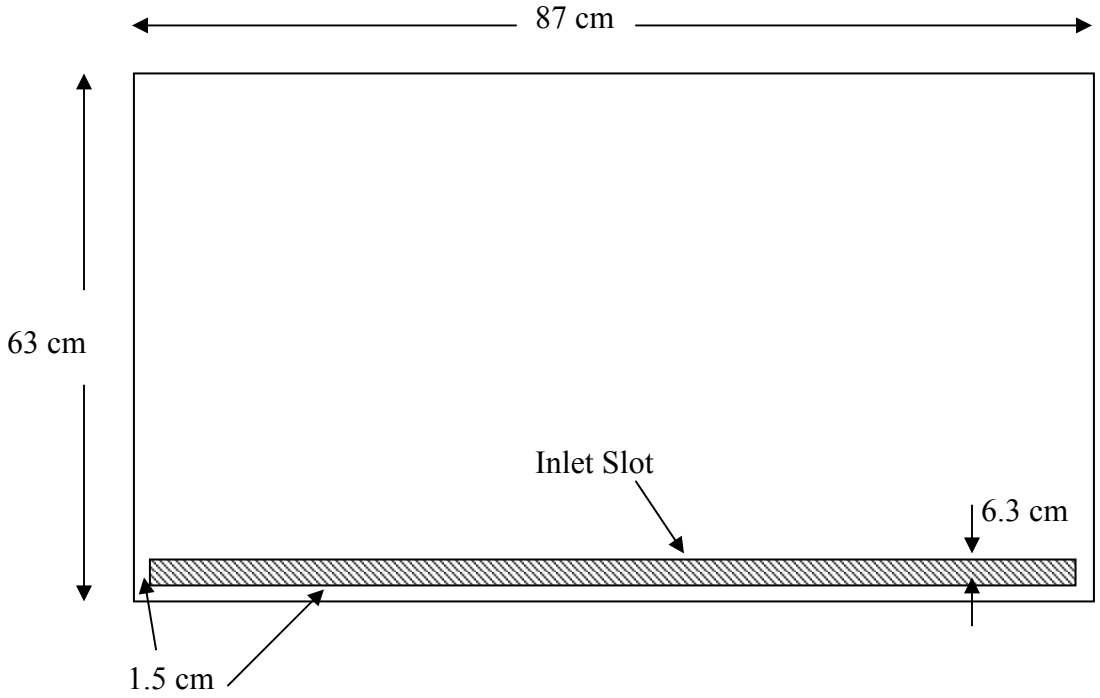

Figure B3. Top View, Aft Plenum

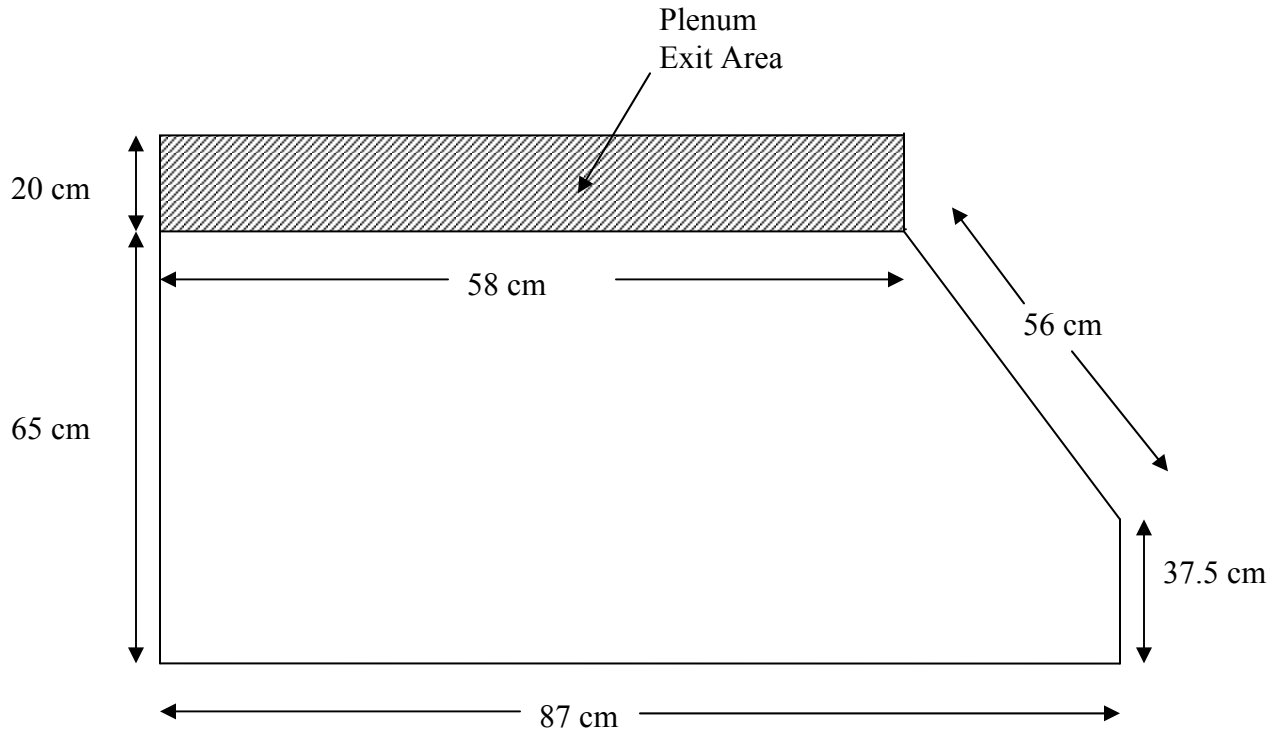

Figure B4. Front View, Aft Plenum

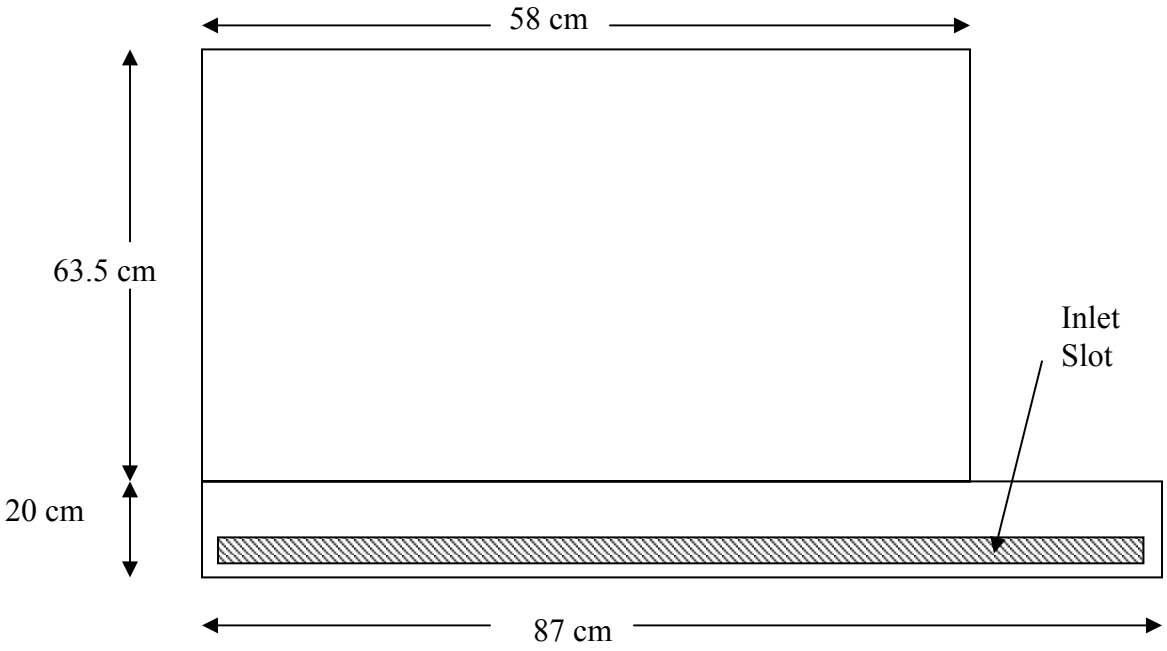

Appendix C: Locations of Thermocouples and Pressure Taps in Plenums

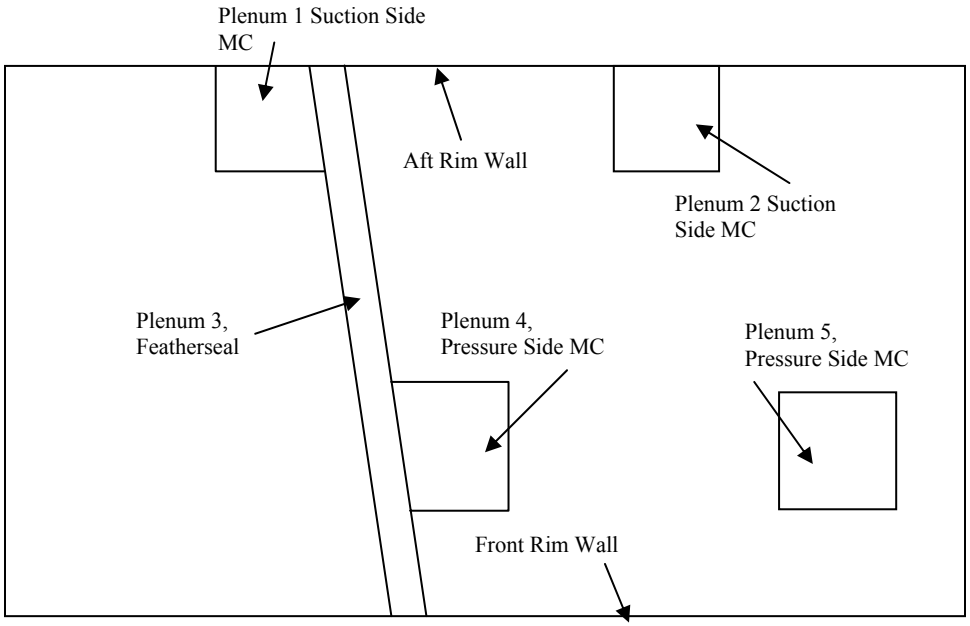

Figure C1. Top view of the plenums. This top view will be used as a template for locating the thermocouples and pressure taps. All taps are placed on the sides of the plenums, and numbered in Figures C2 and C3.

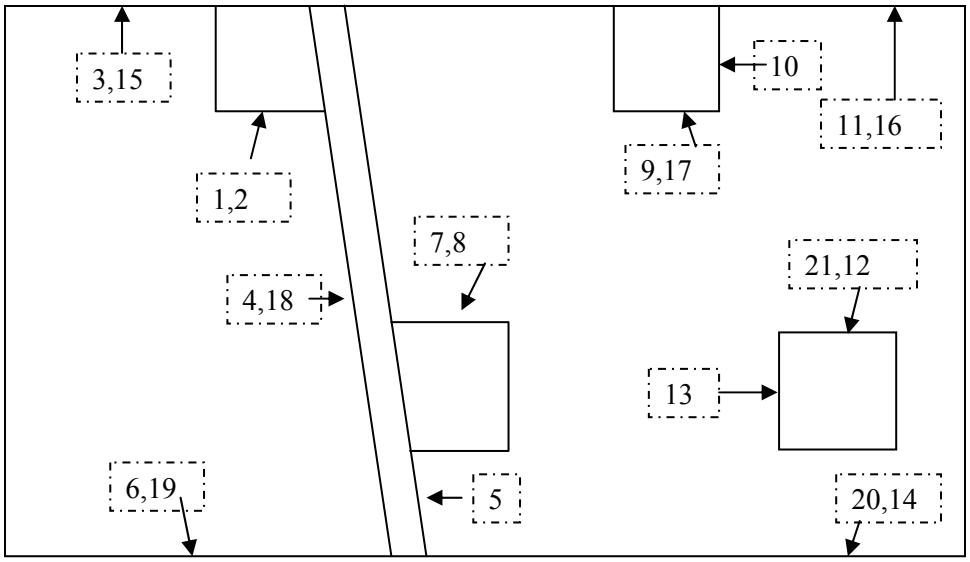

Figure C2. Locations of Pressure Taps on each of the plenums. Each number corresponds to the locations in Table C1.

Table C1. Coordinates of pressure taps corresponding to the numbers in Figure C2.

Pressure Tap #	Location
1	1.95 cm down from platform, 6.3 cm from plenum #3
2	18.4 cm down from platform, 6.3 cm from plenum #3
3	2.54 cm down from platform, 6.3 cm from plenum #1
4	1.95 cm down from platform, 6.3 cm from plenum #1
5	1.95 cm down from platform, 2.54 cm from front rim
6	1.95 cm down from platform, 18.4 cm from plenum #3
7	1.95 cm down from platform, 6.3 cm from plenum #3
8	18.4 cm down from platform, 6.3 cm from plenum #3
9	1.95 cm down from platform, centered on plenum #2
10	1.95 cm down from platform, 6.3 cm from aft rim
11	1.95 cm down from platform, 16.5 cm from plenum #2
12	1.95 cm down from platform, centered on plenum #5
13	1.95 cm down from platform, 43 cm from front rim
14	1.95 cm down from platform, 2.54 cm from plenum #5
15	35 cm down from platform, 8.9 cm from plenum #1
16	35 cm down from platfrom, 17.8 cm from plenum #2
17	35 cm down from platform, centered on plenum #2
18	24 cm down from platform, 16.5 cm from front rim
19	40 cm dowm from platform, 18.4 cm from plenum #3
20	40 cm down from platform, 12.7 cm from plenum #5
21	35 cm down, centered on plenum #5

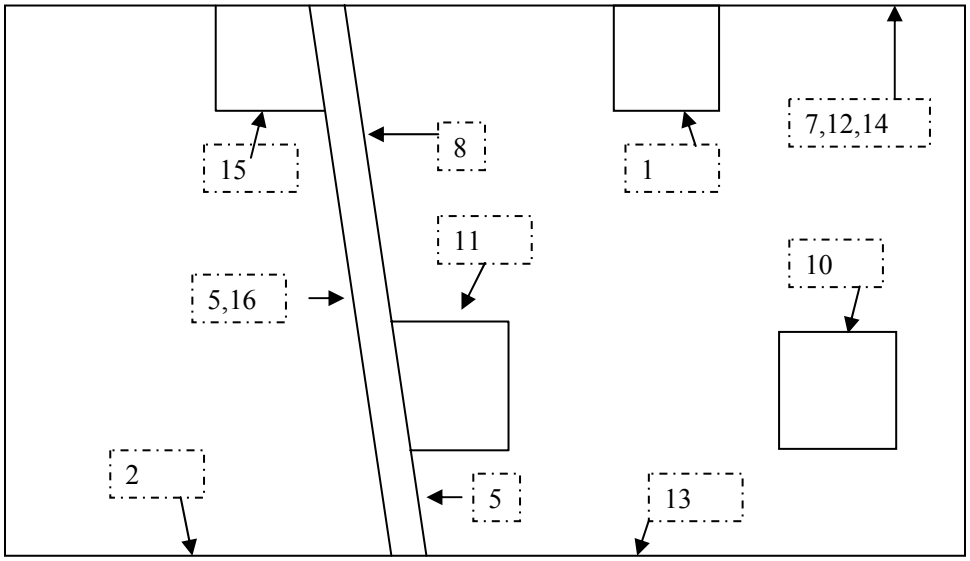

Figure C3. Locations of Thermocouples on each of the plenums. Each number corresponds to the locations in Table C2.

Table C2. Coordinates for thermocouples shown in Figure C3. The thermocouples listed as 'Not In Image' are used in the piping connected to each of the five plenums.

Thermocouple #	Location
1	1.95 cm down from platform, centered on plenum #2
2	1.95 cm down from platform, 7.6 cm from plenum #3
3	Not In Image- Plenum 1 feed pipe
4	Not In Image- Plenum 2 feed pipe
5	1.95 cm down from platform, 13 cm from plenum #1
6	Not In Image- Plenum 3 feed pipe
7	1.95 down from platform, 5.7 cm from plenum #3
8	1.95 cm down from platform, 5.7 cm from aft rim
9	Not In Image- Plenum 4 feed pipe
10	1.95 cm down from platfrom, centered on plenum #5
11	1.95 cm down from platform, 7.6 cm from plenum #3
12	1.95 cm down from platform, 18 cm from featherseal
13	1.95 cm down from platform, 9.5 cm from plenum #5
14	1.95 cm down from platform, 5 cm from plenum #3
15	Not In Image- Plenum 5 feed pipe
16	1.95 cm down from platform, 3.8 cm from front rim

Appendix D: Hole Locations in Top Endwall

Table D1. Coordinates of holes in top plate. Point of reference is corner of top plate connected to the wind tunnel above the blades. X direction is measured from the exit of the combustor simulator, Y direction is perpendicular to test section inlet.

Hole #	X (cm)	Y (cm)
1	32.7	66.7
2	46.5	80.5
3	58.8	88.0
4	67.9	98.9
5	74.3	112.7
6	74.0	128.6
7	73.8	144.6
8	73.8	160.4
9	73.8	176.0
10	73.8	191.6
11	56.4	194.0
12	57.5	173.2
13	61.6	151.9
14	56.8	132.2
15	47.3	120.8
16	28.1	123.3
17	11.4	127.5
18	18.1	107.6
19	35.1	113.2
20	39.5	90.5
21	25.4	87.1

Appendix E Locations of Thermocouples and Markers in Platform

Table E1. Coordinates of thermocouples and pressure taps in platform. Point of reference is corner of platform connected to the wind tunnel near Blade #4. X direction is measured from the exit of the combustor simulator, Y direction is perpendicular to test section inlet. These locations are marked in Figure 3.32.

Thermocouple #	X (cm)	Y (cm)	Marker #	X (cm)	Y (cm)
1	29.0	66.3	1	28.7	54.1
2	46.0	80.5	2	36.8	76.5
3	55.9	87.4	3	53.1	87.4
4	57.9	95.0	4	62.2	98.3
5	74.9	106.9	5	66.8	111.8
6	69.9	116.8	6	84.8	119.1
7	79.2	128.8	7	84.6	122.9
8	67.3	130.8	8	65.8	134.6
9	80.8	147.6	9	65.8	142.7
10	72.4	147.6	10	81.5	150.6
11	81.0	162.3	11	83.3	166.6
12	67.1	158.2	12	83.3	169.9
13	80.5	170.7	13	63.8	181.6
14	73.7	180.1	14	53.3	165.6
15	58.4	181.4	15	69.1	153.9
16	64.0	166.6	16	49.5	129.3
17	57.2	161.0	17	38.4	125.5
18	54.1	133.9	18	43.2	110.7
19	49.8	126.0	19	25.4	107.2
20	43.2	109.5	20	19.1	120.9
21	25.9	119.6	21	1.6	135.4
22	1.6	133.9	22	8.6	115.6
23	9.1	114.0	23	18.3	94.7
24	31.5	86.6	24	49.3	93.2
			25	34.0	83.3

Appendix F: Uncertainty Calculations

Adiabatic Effectiveness Measurements, η

$$\eta = \frac{T_\infty - T_{aw}}{T_\infty - T_c}$$

$$U_\eta = \sqrt{\left(\frac{\partial \eta}{\partial T_{aw}} \cdot u_{T_{aw}}\right)^2 + \left(\frac{\partial \eta}{\partial T_\infty} \cdot u_{T_\infty}\right)^2 + \left(\frac{\partial \eta}{\partial T_c} \cdot u_{T_c}\right)^2}$$

$$\frac{\partial \eta}{\partial T_{aw}} = \frac{1}{T_\infty - T_c}$$

$$\frac{\partial \eta}{\partial T_\infty} = \frac{T_{aw} - T_\infty}{(T_\infty - T_c)^2} + \frac{1}{T_\infty - T_c}$$

$$\frac{\partial \eta}{\partial T_c} = \frac{T_\infty - T_{aw}}{(T_\infty - T_c)^2}$$

High Value of η

Variable	Value	Precision Uncertainty (°C)	Bias Uncertainty (°C)	Total Uncertainty
η	1.00	–	–	0.026 (2.6%)
T_{aw}	27.91	0.313	0.45	0.55
T_∞	50.7	–	–	0.2
T_c	27.9	–	–	0.2

Low Value of η

Variable	Value	Precision Uncertainty (°C)	Bias Uncertainty (°C)	Total Uncertainty
η	0.2	–	–	0.025 (12.5%)
T_{aw}	46.14	0.313	0.45	0.55
T_∞	50.7	–	–	0.2
T_c	27.9	–	–	0.2

Pressure Coefficient Measurements, C_p

$$C_p = \frac{P_{s,local} - P_{s,inlet}}{P_{dynamic}} = \frac{(P_a - P_{s,inlet}) - (P_a - P_{s,local})}{P_{dynamic}} = \frac{\Delta P_{s,inlet} - \Delta P_{s,local}}{P_{dynamic}}$$

$$U_{C_p} = \sqrt{\left(\frac{\partial C_p}{\partial \Delta P_{s,inlet}} \cdot u_{\Delta P_{s,inlet}}\right)^2 + \left(\frac{\partial C_p}{\partial \Delta P_{s,local}} \cdot u_{\Delta P_{s,local}}\right)^2 + \left(\frac{\partial C_p}{\partial P_{dynamic}} \cdot u_{P_{dynamic}}\right)^2}$$

$$\frac{\partial C_p}{\partial \Delta P_{s,inlet}} = \frac{1}{P_{dynamic}}$$

$$\frac{\partial C_p}{\partial \Delta P_{s,local}} = -\frac{1}{P_{dynamic}}$$

$$\frac{\partial C_p}{\partial P_{dynamic}} = \frac{\Delta P_{s,local} - \Delta P_{s,inlet}}{(P_{dynamic})^2}$$

Uncertainties within 0-5 inH2O transducer range:

High Value of C_p = 17.3

Variable	Value	Precision Uncertainty (inH2O)	Bias Uncertainty (inH2O)	Total Uncertainty
C_p	17.3	–	–	1.29 (7.4%)
$\Delta P_{s,inlet}$	0.080	0.021	0.003	0.021
$\Delta P_{s,local}$	5.00	0.021	0.05	0.054
$P_{dynamic}$	0.285	0.021	0.003	0.021

Low Value of C_p = -17.8

Variable	Value	Precision Uncertainty (inH2O)	Bias Uncertainty (inH2O)	Total Uncertainty
C_p	-17.8	–	–	1.33 (7.5%)
$\Delta P_{s,inlet}$	0.080	0.021	0.003	0.021
$\Delta P_{s,local}$	-5.00	0.021	0.05	0.054
$P_{dynamic}$	0.285	0.021	0.003	0.021

Density measurements, ρ

$$\rho = \frac{\Delta P}{287T} \qquad 1.109\,{}^{kg}\!/_{m^3} = \frac{94885\,Pa}{287 * 298K}$$

$$\frac{\partial \rho}{\partial \Delta P} = \frac{1}{287T}$$

$$\frac{\partial \rho}{\partial T} = \frac{-\Delta P}{287T^2}$$

$$U_T = 0.2\,C$$

$$U_P = 800\,Pa$$

$$U_\rho = \sqrt{\left[\left(U_{\Delta P}\right)\left(\frac{\partial \rho}{\partial \Delta P}\right)\right]^2 + \left[\left(U_T\right)\left(\frac{\partial \rho}{\partial T}\right)\right]^2}$$

Based upon given values, $U_\rho = 0.01559\,{}^{kg}\!/_{m^3}$

Velocity Measurements, V

$$V = \sqrt{\frac{2\Delta P}{\rho}} \qquad 9.9\,{}^{m}\!/_{s} = \sqrt{\frac{2(54.8\,Pa)}{1.109\,{}^{kg}\!/_{m^3}}}$$

$$\frac{\partial V}{\partial \Delta P} = {}^{1}\!/_{2}\left(\Delta P\right)^{-0.5}\left(\frac{2}{\rho}\right)^{0.5}$$

$$\frac{\partial V}{\partial \rho} = -{}^{1}\!/_{2}\left(\rho\right)^{-2/3}\left(2\Delta P\right)^{0.5}$$

$$U_{\Delta P} = 2.7\,Pa$$

$$U_\rho = 0.015\,{}^{kg}\!/_{m^3}$$

$$U_v = \sqrt{\left[\left(U_{\Delta P}\right)\left(\frac{\partial V}{\partial \Delta P}\right)\right]^2 + \left[\left(U_\rho\right)\left(\frac{\partial V}{\partial \rho}\right)\right]^2}$$

Based on the given values, $U_V = 0.63\,{}^{m}\!/_{s}$

Mass Flow, m_dot.

$\dot{m} = C_D \rho V A \qquad 0.04 \, {kg}/{s} = 0.6 * 1.109 \, {kg}/{m^3} * 30 \, {m}/{s} * 0.000197 \, m^2$

$$\frac{\partial \dot{m}}{\partial \rho} = C_D V A$$

$$\frac{\partial \dot{m}}{\partial V} = C_D \rho A$$

$$\frac{\partial \dot{m}}{\partial A} = C_d V \rho$$

$U_\rho = 0.01159 \, {kg}/{m}$

$U_V = 0.626 \, {m}/{s}$

$U_A = 4.24 * 10^{-4} \ m^2$

$$U_{\dot{m}} = \sqrt{\left[\left(U_\rho\right)\left(\frac{\partial \dot{m}}{\partial \rho}\right)\right]^2 + \left[\left(U_V\right)\left(\frac{\partial \dot{m}}{\partial V}\right)\right]^2 + \left[\left(U_A\right)\left(\frac{\partial \dot{m}}{\partial A}\right)\right]^2}$$

Based upon the given values, $U_{\dot{m}} = 0.0042 \, {kg}/{s}$

Vita

William W. Ranson was born August 17, 1980 in Richmond, VA to Will an Renée Ranson. He attended the Collegiate School from 1987 to 1998, when he graduated Cum Laude. During this time he became a certified SCUBA diver and a Virginia State licensed fire fighter. In 1998, he entered Virginia Polytechnic Institute and State University as an engineering major. Upon completion of his first year, he began a cooperative education program with E.I. DuPont de Nemours in Richmond, Virginia. While at Virginia Tech he completed five semesters of co-op work at DuPont. Additionally, he joined ASME and Phi Delta Theta, the latter of which he became president. After graduating Magna Cum Laude with a B.S. degree in mechanical engineering in 2003, he joined the Virginia Tech Experimental and Computational Convection Laboratory (VTExCCL) to pursue a M.S. degree in mechanical engineering. Upon graduating Suma Cum Laude with a M.S. in 2004, he rejoined DuPont in the Tyvek® Technical division.

Some of his favorites include:

NFL:	Dallas Cowboys
College Team:	Virginia Tech / University of Richmond
NASCAR:	Kevin Harvick, #29 / Kasey Kahne, #9
Music:	Radiohead
City:	Nice, France
Food:	Steak-Filet Mignon
Dessert:	Doughnuts